

**RADIATION EFFECTS ON MAGNETIC NANOMATERIALS AND  
APPLICATIONS IN NUCLEAR ENERGY**

A Dissertation

Presented in Partial Fulfillment of the Requirements for the

Degree of Doctor of Philosophy

with a

Major in Physics

in the

College of Graduate Studies

University of Idaho

by

Jennifer Anand Sundararajan

December 2014

Major Professor: You Qiang, Ph.D.

**Authorization to Submit Dissertation**

This dissertation of Jennifer Anand Sundararajan submitted for the degree of Doctor of Philosophy with a major in Physics and titled "RADIATION EFFECTS ON MAGNETIC NANOMATERIALS AND APPLICATIONS IN NUCLEAR ENERGY," has been reviewed in final form. Permission, as indicated by the signatures and dates given below, is now granted to submit final copies to the College of Graduate Studies for approval.

Major Professor: \_\_\_\_\_ Date \_\_\_\_\_  
Dr. You Qiang

Committee  
Members: \_\_\_\_\_ Date \_\_\_\_\_  
Dr. Ruprecht Machleidt

\_\_\_\_\_ Date \_\_\_\_\_  
Dr. Leah Bergman

\_\_\_\_\_ Date \_\_\_\_\_  
Dr. Vivek Utgikar

Department  
Administrator: \_\_\_\_\_ Date \_\_\_\_\_  
Dr. Jo Ellen Force

College of Science  
Dean: \_\_\_\_\_ Date \_\_\_\_\_  
Dr. Paul Joyce

**Final Approval and Acceptance**

Dean the College  
of Graduate Studies: \_\_\_\_\_ Date \_\_\_\_\_  
Dr. Jie Chen

## Abstract

Future generation IV nuclear reactors are expected to meet the standards of enhanced safety, minimal waste and economical compatibility. Through Nano-Nuclear Technology, latest engineered-nanomaterials are used for improving the nuclear power performance and safety. This research contributes in part to meet this objective through the understanding of responsibility and stability of magnetic nanomaterials under irradiation by studying changes of nanostructure, magnetic and electrical properties in irradiated nanomaterials. Previous publications have shown fully oxidized nanoparticle structures like Ytria ( $Y_2O_3$ ) and Alumina ( $Al_2O_3$ ) dispersed in commercial Ferritic/Martensitic alloy, also called as Nano Ferritic Alloys (NFA) have improved creep properties, hardness, tensile strength, corrosion resistant, and thermal stability compared with the normal reactor alloys. Since our Fe-based nanoparticles (NPs) like core-shell Fe-Fe oxide, fully oxidized  $Fe_3O_4$ , Ni/Ni-Cr and FeO NPs have proved to alter the radiation effects and radiation resistance behavior, these iron oxide particles could be good candidates for studying the dispersion strengthening phenomena in materials as it promotes grain boundaries and interfacial effects. Based on our primary results obtained from the irradiated Fe- $Fe_3O_4$  core-shell and fully oxidized  $Fe_3O_4$  NPs, we hypothesized that this approach will help us uncover the interfacial behavior between nanomaterials and inter-particle interactions under extreme intense radiation exposure. The combined effect of vacancy formation, atom diffusion under the influence of temperature and breaking of chemical bonds are reported to be the main cause behind the mystery of electron beam induced oxide layer thickening in core-shell iron nanoparticles, which ultimately results in structural changes followed by magnetic property changes. The results obtained from this investigation could help generate data for future scientific assessment in the prediction of material performance in radiation environments and to recommend candidate nanomaterials for development of high sensitive nuclear monitor and detector for safety application in nuclear energy.

## Curriculum Vitae

# Jennifer Anand Sundararajan

1218 S. Main St., Apt. #303, Moscow, ID 83843

208-596-1074, [sund2175@vandals.uidaho.edu](mailto:sund2175@vandals.uidaho.edu)

---

### EDUCATION

<i>Ph.D. (Physics) GPA=3.85</i>	University of Idaho, Moscow, ID, USA	Dec 2014
<i>M.S. (Physics) GPA=3.76</i>	University of Idaho, Moscow, ID, USA	May 2011
<i>B.E. (Mechanical Engineering)</i>	Mepco Schlenk Engineering College, India	May 2009

### WORK EXPERIENCE

**Research Assistant, University of Idaho** (Aug. 2009 – Present, Moscow, ID)

- Worked on the project, ‘Radiation Effects on Nanomaterials & Applications’
- Guided undergraduate and new graduate students in the research lab

**Teaching Assistant, University of Idaho** (Aug. 2009 – Present, Moscow, ID)

- Set-up and taught engineering physics labs
- Held office hours and tutoring hours for undergraduate students

**Web Author, University of Idaho Support Service** (Nov 2013 – Present, Moscow, ID)

- Designed websites for the conference management service
- Created and managed university webpages using Sitecore

**Software Engineer, Cognizant Technology Solutions** (Sep. 2006 – Aug 2009, Chennai, India)

- Tested software and patient data reports for pharmaceutical clients
- Wrote Job Control Language (JCL) & SQL queries for data processing & verification

### INSTRUMENTATION SKILLS

- Magnetron Sputtering System – Gas aggregation technique for nanoparticle synthesis
- Thin film fabrication and Quartz system for thickness measurements
- Vacuum technology - Leak detection and gas flow control
- Transmission Electron Microscopy (TEM), Scanning Electron Microscopy (SEM), Helium Ion Microscope (HIM), Vibrating Sample Magnetometer (VSM), Ion Beam Accelerator
- Two-probe and Van-der Pauw - Electrical conductivity measurement techniques
- Basic knowledge of Cleanroom technology – Photolithography, mask design and etching

### COMPUTER SKILLS

- Proficient: SolidWorks, Microsoft Office, Sitecore-Web Design
- Knowledgeable: Auto CAD, C, JCL, HTML, SQL, Origin
- Operating Systems: Windows 2000/XP/7, Linux-Ubuntu

### TEACHING EXPERIENCE

- As a primary instructor taught engineering physics labs for undergraduate students
- As a TA provided supplemental learning to lectures through tutoring & office hours
- Earned instructor rating, 3.8 out of 4 (5 years) from students
- Evaluated and graded exams and homework
- Communicated openly with students to facilitate learning and personal growth
- As a substitute instructor have led several physics classes including classes over 100 students



## **RESEARCH EXPERIENCE (Aug 2009 – Dec 2014)**

### ***Research title: Radiation-induced property changes in nanoparticle-granular films & future nuclear reactor applications”***

- Investigated the irradiation-induced modification in Fe/Fe-oxide nanoparticle granular films
- Investigated the temperature-induced modifications in Ni and Cr-doped Ni Nanoparticles
- Studied the mechanisms behind the stability & sensitivity of materials under irradiation
- Disseminated research findings in several international conferences and journals
- Reviewed manuscripts for the Journal of Applied Physics
- Designed machine drawings using Solid works and Auto CAD for sputtering system and workshop
- Worked in the national lab user facility, Pacific Northwest National Laboratory (PNNL)
- Wrote proposals as a key user and participant for the use of instruments at PNNL
- Gave seminars in the physics and math department during 2011-13 about the research
- Guided three undergraduate students on three different research projects in the lab

## **RELEVANT COURSES**

- |                        |                                     |                                  |
|------------------------|-------------------------------------|----------------------------------|
| - Techn. of Exp. Phys. | - Nanotech: Processing/Applications | - Radiation Effects on Materials |
| - Electron Microscopy  | - Fundamentals of Nuclear Materials | - Particle & Nuclear Physics     |
| - MEMS Engineering     | - Nuclear Degradation Mechanisms    | - Thermal & Statistical Physics  |

## **AWARDS AND RECOGNITION**

- Alumni Award for Excellence, Fall 2014
- Diane Haynes Memorial Award for Outstanding Graduate Student of the year, 2014
- Runner-up for Outstanding Teaching Assistant of the year, College of Graduate Studies, 2014
- 1st place, Innovation Showcase - Graduate research presentation category, 2013
- 2<sup>nd</sup> place, Idaho Academy of Science-symposium, 2013
- 1<sup>st</sup> place, Idaho Academy of Science-symposium, 2012
- Recognition for outstanding contribution to National Society of Black Engineers
- Nielsen scholarship (\$3500), College of Science for best research student, 2012
- Teaching Assistant of the year, Physics department, 2011

## **PUBLICATIONS**

- W. Jiang, **J.A. Sundararajan**, T. Varga, M.E. Bowden, Y. Qiang, J.S. McCloy, C.H. Henager, Jr. & R.O. Montgomery, “In-situ Study of Nanostructure and Electrical Resistance of Nanocluster Films Irradiated with Ion Beams”, *Advanced Functional Materails*, Published online, 2014. [DOI: 10.1002/adfm.201400553]
- D.T. Zhang, W.T. Geng, M. Yue, W.Q. Liu, Q.M. Lu, J.X. Zhang, Z.H. Guo, W Li, **J.A. Sundararajan**, Y. Qiang, "Magnetic properties and thermal stability of MnBi/SmFeN hybrid bonded magnets", *Journal of Applied Physics*, 115, 17, 17A746, 2014
- **J.A. Sundararajan**, M. Kaur, W. Jiang, J. S. McCloy, and Y. Qiang, “Oxide shell reduction and magnetic property changes in core-shell Fe nanoclusters under ion irradiation”, *Journal of Applied Physics*, 115, 17B507, 2014
- J.S. McCloy, W. Jiang, T.C. Droubay, T. Varga, E.C. Burks, **J. A. Sundararajan**, M. Kaur, Y. Qiang, L. Kovarik, K. Liu, “Ion irradiation of Fe-Fe oxide core-shell nanocluster films: Effect of interface on stability of magnetic properties”, *Journal of Applied Physics*, 114, 083903, 2013
- J.S. McCloy, W. Jiang, **J.A Sundararajan**, Y. Qiang, E. Burks, K. Liu, "Structure and magnetic properties of irradiated Fe-Fe oxide core-shell nanoclusters", *Application of accelerators in research and industry: Twenty-Second International Conference proceedings*, AIP Publishing, 1525, 1, 659-662, 2013

- D.T. Zhang, W.T. Geng, M. Yue, W.Q. Liu, J.X. Zhang, **J.A. Sundararajan**, Y. Qiang, “Crystal structure and magnetic properties of  $Mn_x Bi_{100-x}$  ( $X = 48, 50, 55 \text{ \& } 60$ ) compounds”, *Journal of Magnetism and Magnetic Materials*, 324, 11, 1887–1890, June 2012
- C.M. Wang, D.R. Baer, S.M. Bruemmer, M.H. Engelhard, M.E. Bowden, **J.A. Sundararajan** and Y. Qiang, “Microstructure of the native oxide layer on Ni and Cr-doped Ni nanoparticles”, *Journal of Nanoscience and Nanotechnology*, 11, 8488-8497, 2011
- **J.A. Sundararajan**, T. Schimel, M. Kaur, Y. Qiang, C.M. Wang, D. R. Baer and S.M. Bruemmer, “Heat treatment on Ni and Cr-doped Ni core-shell nanoparticle granular films”, *Proceedings of 2011-11th IEEE International Conf. on Nanotechnology*, IEEE, 0249, 657, 2011
- W. Jiang, J. McCloy, A. Lea, **J.A. Sundararajan**, Q. Yao, and Y. Qiang, “Magnetization and susceptibility of ion-irradiated granular magnetite films”, *Physics Review B*, 83, 134435 (1-8), 2011
- **J.A. Sundararajan**, D.T. Zhang, Y. Qiang, W. Jiang, and J.S. McCloy, “Magnetic stability of  $He^+$  ion irradiated  $FeO+ Fe_3N$  granular films”, *Journal of Applied Physics*, 109, 07E324, 2011

### CONFERENCE PRESENTATIONS

- “Oxide shell reduction and magnetic property changes in Core-Shell Fe nanoclusters, **58<sup>th</sup> MMM meeting**, Denver, Nov 2013.
- “Stability and Response of Core-Shell Magnetic Nanomaterials to Variable Fluence  $Si^{2+}$  ion Irradiation”, **55<sup>th</sup> Idaho Academy of Science Symposium**, March 22, 2013.
- “Mechanism of Ion-Irradiation induced structural and magnetic property changes due to irradiation in nanomaterials”, **INTERMAG**, May 2012.
- “Structural and Magnetic Property Changes under Ion Irradiation in  $Fe/Fe_3O_4$  Core-Shell Nanoparticle Films”, Presented in **54<sup>th</sup> Idaho Academy of Science Symposium**, March 23, 2012.
- “Heavy ion irradiation and magnetic stability of  $Fe_3O_4/Fe_3N$  nanoparticles”, **55<sup>th</sup> annual conference on Magnetism and Magnetic Materials**, November 14-18, 2010. Abstract #GB.014.
- “Magnetic stability of  $FeO/Fe_3N$  nanoparticles under ion irradiation”, **12<sup>th</sup> Annual Meeting of the Northwest Section of the APS**, October 1-2, 2010. Abstract #H3.006.
- “A Debate on the Accuracy of the Results from Transmission Electron Microscopy”, **APS March Meeting 2010**, March 15-19, 2010. Abstract #W15.014.

### PROFESSIONAL ACTIVITIES

- Outreach Chair, Univ. of Idaho - National Society of Black Engineers (NSBE), 2013-2015
- Senator & Representative, Graduate & Professional Student Association, 2013-2015
- Member, University of Idaho Science Outreach Team, 2013-2015
- Committee Member, Student Grant Program (SGP), Fall-2010 to Spring-2012
- Member, American Physical Society (APS)
- Instrument User, Pacific Northwest National Laboratory (PNNL)

### PROFESSIONAL SKILLS

- Positive team member to work with different people in a team and manage diverse situations
- Leadership and presentation skills to help and guide fellow researchers working in the project
- Ability to get involved in research, student associations, and service activities simultaneously
- Teaching, guiding and helping students with different skill sets and knowledge levels
- Community development skills in hosting casual social gatherings
- Presentation skills to disseminate research findings well at scientific conference.

## Acknowledgements

I would like to acknowledge the Department of Physics at the University of Idaho (UI) for allowing me to study and work as a Teaching/Research assistant in the state of Idaho. I would like to thank my advisor Dr. You Qiang for his constant support, tremendous encouragement, valuable advice and timely guidance, which urged me to successfully continue with my studies at graduate level and motivated me to perform research effectively at UI. Without Dr. Qiang's support and guidance I would not have reached this stage in the journey of my education. I owe great thanks to Dr. Weilin Jiang from PNNL and Dr. John McCloy from the Washington State University for their great ideas and collaboration, and their precious help in characterizing our samples using Transmission Electron Microscopy (TEM), Magnetic Force Microscopy (MFM), X-ray Diffraction (XRD) measurements, radiation exposure experiments and magnetic measurements at Environmental Molecular Science Laboratory (EMSL) in Pacific Northwest National Laboratory (PNNL) at Richland, WA through the national user facility projects.

I am grateful to Dr. Indrajit Charit for teaching and giving me an insight into the radiation induced defects in materials and fundamentals of nuclear materials during my study here at UI. I would also like to thank our Ex-department chair Dr. David N. McIlroy for his encouragement and support. I would like to thank all my peers most notably Cami McClure for motivating me in university work and studies.

Special thanks go to our department scientific instrument maker, Mr. John Failla for his technical help in experiment instrumentation during my study at UI. Additionally, I would like to thank my lab colleagues, most notably Dr. Qi Yao, Mr. Ryan Souza and Dr. Maninder Kaur for their support and guidance in using the nanocluster deposition system, Vibrating Sample Magnetometer (VSM) and other equipment in our lab. I would like to convey my special gratitude to Dr. Kaur, a good companion who gave valuable suggestions and guidance when doing experiment and writing manuscripts. I would also like to thank my fellow group members and friends Dr. Dongtao Zhang,

Huijin Zhang (Jin), Tayler Schimel, Kelley Green, Bruce Lee, Paul Bailey, Alex Bowyer, Qian Xie, Cory Ytsma and William Armour for their constant support and cooperation. The time we, I, Dr. Kaur, Dr. Zhang, Jin and Bruce Lee spent together on playing games, fishing, camping, partying and so many other fun activities are memorable and refreshing; the memories will never fade away.

I would like to thank my family members and in particular my sister Jency Pricilla Sundararajan, my brother-in-law Bharathkumar, my wife Lavanya Elangovan for being with me during difficult times in my life and motivating me in my career. I also would like to convey my special love and gratitude to my mom, Fatima Rosary and dad, Sundararajan for their love, patience, support, encouragement and prayers. I am grateful to all my friends in Moscow-Pullman community and Palouse area for their constant support, encouragement and prayers. At this time, I think of all my friends, relatives, and well-wishers in India and around the world, who played a vital role in my life in so many ways and in shaping me to be the person who I am today.

Last but not the least; I thank Almighty God for all His blessings and give Him all the glory.

**This research is supported by DOE-FG02-07ER46386, DOE-FG02-04ER46142 and DOE-AC05-76RL01830 and the Department of Physics at the University of Idaho.**

## Table of Contents

Authorization to Submit Dissertation.....	ii
Abstract.....	iii
Curriculum Vitae.....	iv
Acknowledgements.....	vii
Table of Contents.....	ix
List of Figures.....	xiv
List of Tables.....	xix
Chapter 1: Introduction to Nuclear Energy and Nano-Nuclear Technology.....	1
1.1 The Future of Nuclear Energy.....	1
1.2 Nano-Nuclear Technology.....	3
1.3 Significance of Studying Magnetic Properties.....	5
1.4 Magnetic Nanoparticles for Irradiation Studies.....	7
1.5 Research Scope and Limitations.....	8
1.6 General Overview on All Chapters.....	10
1.7 References.....	12
Chapter 2: Fundamentals of Radiation & Principles of Radiation Detection.....	14
2.1 Introduction.....	14
2.2 Radiation Interaction with Matter.....	14
2.2.1 Neutron Interaction with Matter.....	15
2.3 Neutron Radiation Detection through Ionization.....	16
2.3.1 Commercial Neutron Detectors.....	17
2.3.2 Challenges of Neutron Detection.....	21
2.4 Neutron Radiation Detection through Property Changes.....	22
2.4.1 Radiation Effects on Material Properties.....	22
2.4.2 Radiation Effects and Magnetic Properties.....	26

2.5 Conclusion .....	27
2.6 References .....	28
Chapter 3: Literature Review on Nano-Nuclear Technology .....	29
3.1 Introduction .....	29
3.2 Branches of Nano-Nuclear Technology .....	29
3.2.1 Nanostructured-ODS Materials .....	31
3.2.2 Nano-Scale Coatings .....	34
3.2.3 Nanomaterials for Fission Product Capturing .....	35
3.2.4 Nano-Technology Engineered Fuels .....	38
3.2.5 Nanotechnology Enabled Sensors, Detectors and Monitors .....	40
3.3 Conclusion .....	42
3.4 References .....	43
Chapter 4: Synthesis and Characterization of Thin Films and Granular Films .....	47
4.1 Nanocluster Deposition System .....	47
4.2 Working Principle .....	51
4.3 Synthesis of Granular Films .....	52
4.4 Characterization of Granular Films .....	53
4.4.1 X-Ray Diffraction (XRD) .....	54
4.4.2 Helium Ion Microscopy (HIM) .....	54
4.4.3 Physical Property Measurement System (PPMS) .....	56
4.4.4 Atomic Force Microscopy (AFM) and Magnetic Force Microscope (MFM) .....	56
4.4.5 Transmission Electron Microscope (TEM) .....	57
4.4.6 Scanning Electron Microscope (SEM) .....	58
4.4.7 Energy-Dispersive X-ray Spectroscopy (EDX) .....	59
4.4.8 Vibrating Sample Magnetometer (VSM) .....	60
4.4.9 Van der Pauw Electrical Conductive Measurement .....	61

4.4.10 X-ray Photoelectron Spectroscopy (XPS) .....	63
4.5 Irradiation Experimental Setup .....	63
4.6 References .....	67
Chapter 5: Synthesis, Structure, and Electronic Structure of Pure and Cr-doped Ni Nanoparticles...	68
5.1 Introduction .....	68
5.2 Sample Preparation .....	70
5.3 Results and Discussion.....	73
5.3.1 Structure and Morphology of the Particles .....	73
5.3.2 The Cr distribution .....	78
5.3.3 The electronic structure of the nanoparticles .....	81
5.3.4 General description of the structural features of the nanoparticles .....	85
5.4 Summary .....	87
5.5 References .....	88
Chapter 6: Cr-Doping and Heat-Treatment Effects on Core-Shell Ni Nanocluster Films.....	92
6.1 Introduction .....	92
6.2 Sample Preparation .....	93
6.3 Results and Discussion.....	95
6.4 Summary .....	105
6.5 References .....	106
Chapter 7: Irradiation Effects on Fe-based Nanoparticles and Applications .....	108
7.1 Fe-Based Nanoparticle Granular Films.....	108
7.2 Introduction to Granular Thin Films and Irradiation.....	109
7.3 Synthesis and Characterization of Fe-based Granular Films.....	110
7.4 Fe <sub>3</sub> O <sub>4</sub> Granular Films .....	112
7.4.1 Structural and Magnetic Property Changes of Fe <sub>3</sub> O <sub>4</sub> Granular Films .....	112
7.4.2 Surface Microstructures of Fe <sub>3</sub> O <sub>4</sub> Granular Films .....	114

7.4.3 Magnetic Domains of Fe <sub>3</sub> O <sub>4</sub> Granular Films.....	118
7.5 Fe-Fe <sub>3</sub> O <sub>4</sub> Core-Shell Granular Films .....	120
7.5.1 Structural Property Changes of Core-Shell (CS) Fe-Fe <sub>3</sub> O <sub>4</sub> Granular Films.....	120
7.5.2 Magnetic Property Changes of Core-Shell (CS) Fe-Fe <sub>3</sub> O <sub>4</sub> Granular Films .....	122
7.6 Summary .....	123
7.9 References.....	125
Chapter 8: Oxide Shell Reduction and Magnetic Property Changes in Core-Shell Fe	
Nanoclusters under Ion Irradiation.....	128
8.1 Introduction.....	128
8.2 Sample Preparation .....	129
8.3 Synthesis and Characterization of FeO+Fe <sub>3</sub> N granular films .....	130
8.4 Summary .....	135
8.5 References.....	137
Chapter 9: In-situ Study of Nanostructure and Electrical Resistance of Nanocluster Films	
Irradiated with Ion Beams.....	139
9.1 Abstract.....	139
9.2 Introduction.....	139
9.3 Sample Preparation and Experimental Details.....	142
9.3.1 Van der Pauw Sample Preparation.....	144
9.3.2 In-situ HIM Examination .....	146
9.3.3 In-situ Resistance Measurement.....	147
9.3.4 XRD analysis .....	148
9.4 Results and Discussion.....	149
9.4.1 Structural Evolution in Fe <sub>3</sub> O <sub>4</sub> Nanocluster Film.....	149
9.4.2 Nanostructural Evolution and Phase Transition in Fe-Fe <sub>3</sub> O <sub>4</sub> Core-shell Nanocluster Film.....	154



9.4.3 Response of Fe-Fe <sub>3</sub> O <sub>4</sub> Nanocluster Film Resistivity to Ion Irradiation .....	157
9.5 Future Studies .....	163
9.6 Conclusion .....	164
9.7 References .....	166
Chapter 10: Nanoclusters Embedded Thin Film Matrices and Multi-Layered Films .....	169
10.1 Introduction .....	169
10.2 Experimental Details .....	171
10.3 Result and Discussion .....	172
10.3 Conclusion .....	176
10.4 References .....	177
Chapter 11: Summary and Conclusion .....	178
Appendix A: Sputter yield for different materials .....	180

## List of Figures

Figure 1.1 The evolution of nuclear power from Gen I to Gen IV .....	2
Figure 1.2 The nuclear fuel cycle.....	4
Figure 1.3 Block diagram showing that the microstructural changes directly is related to magnetic properties.....	6
Figure 2.1 Interactions of neutron with matter.....	16
Figure 2.2 Principle of a gas-filled detector.....	18
Figure 2.3 Geiger-Muller counter for radiation detection.....	18
Figure 2.4 Photomultiplier Tube.....	19
Figure 2.5 Principle of a semiconductor detector .....	20
Figure 2.6 Depiction of vacancies and interstitial.....	24
Figure 2.7 Seeger's refined concept of primary damage events in an FCC metal (1958) .....	24
Figure 4.1 Schematic representation of the third generation nanocluster deposition system .....	48
Figure 4.2 Schematic diagrams showing the (a) sputtering region (shaded portion) in a Nickel target and (b) doped chromium spots (shaded portion) in the sputtering area. ....	50
Figure 4.3 Picture showing the nanoparticles deposited on silicon substrate and its cross-sectional view.....	53
Figure 4.4 Schematic of X-ray Diffractometer .....	54
Figure 4.5 Schematic of Helium Ion Microscope .....	55
Figure 4.6 Schematic of Transmission Electron Microscope.....	58
Figure 4.7 Schematic of Scanning Electron Microscope .....	59
Figure 4.8 Schematic of Vibrating Sample Magnetometer.....	61
Figure 4.9 Schematic of the Van der Pauw Sample of Fe-granular film on Silicon Substrates.....	62
Figure 4.10 Schematic representations of the ion accelerator system set up for irradiation experiments. ....	65
Figure 5.1 TEM image showing the different sized Ni nanoparticles prepared using CDS. ....	71
Figure 5.2 Ball and stick model showing the face centered cubic (fcc) structured Ni and the rock salt structured NiO .....	74

Figure 5.3 XRD of pure and Cr-doped Ni nanoparticles. Samples Ni and Ni10Cr were dominated by oxide phase and Ni5Cr is dominated by metallic phase.....	74
Figure 5.4 Representative TEM images showing an overall view of the nanoparticles. (a) Sample Ni, (b) Sample Ni5Cr, and (c) Sample Ni10Cr. The inset within (a), (b), and (c) corresponds to the selected area electron diffraction pattern of the each sample. (d) Matching of the experimental diffraction pattern using sample Ni as a representative case with the calculated patterns of both fcc structured Ni and NiO .....	75
Figure 5.5 Representative TEM images typical showing two types of nanoparticles in the sample Ni5Cr. (a) Core-shell structured particles and (b) fully oxidized particle with a cubed morphology. ....	76
Figure 5.6 HRTEM image showing the lattice image of both core-shell and fully oxidized the fully oxidized particle in sample Ni5Cr. (a) The core-shell structured particle. The thickness of the shell is typically ~ 1.6 nm and note the (111) twin in the fcc structured Ni nanoparticle. (b) The fully oxidized nanoparticle is a single crystal NiO and note the faceting of particle on the (100) planes.....	77
Figure 5.7 HRTEM image showing the lattice image of the fully oxidized particle in sample Ni. Note the trapping of cavity within this fully oxidized particle and faceting of cavity on the (100) planes. ....	77
Figure 5.8 EDS spectra of samples Ni, Ni5Cr and Ni10Cr.....	79
Figure 5.9 EELS spectra obtained from a single oxide particle showing the O K-edge, Cr L2,3-edge, and Ni L2,3-edge .....	80
Figure 5.10 XPS spectra showing the peaks of Cr-2p, Ni-2p and O-1s for samples Ni, Ni5Cr, and Ni10Cr.....	80
Figure 5.11 Detailed comparison of EELS O K-edge obtained from the oxide particle for samples Ni, Ni5Cr and Ni10Cr. All spectra were aligned at the pre-edge peak a at an energy loss position of 532 eV. The peaks intensity a:b is measured and marked in the figures for quantitative analysis of the spectra. ....	83
Figure 6.1 TEM images of (a) CS-Ni (b) CS-Ni5Cr NCs. The inset shows a single CS-Ni NC with ~2 nm oxide layer thickness.....	96
Figure 6.2 XRD pattern for the (a) CS-Ni, (b) CS-Ni5Cr, (c) Heat-Treated CS-Ni and (b) Heat-treated CS-Ni5Cr NC films.....	97
Figure 6.3 EDS spectra for the CS-Ni and CS-Ni5Cr NC films. The insets show the at.% of the elements in films. ....	97
Figure 6.4 Hysteresis loops measured in VSM for CS-Ni and CS-Ni5Cr NC films before and after HT. The inset shows near zero fields.....	98
Figure 6.5 SEM images of the CS-Ni and CS-Ni5Cr NC films on Si substrate before and after HT. ....	100

Figure 6.6 AFM and MFM images of CS-Ni films before and after HT.....	101
Figure 6.7 AFM and MFM images of CS-Ni <sub>5</sub> Cr films before and after HT.....	102
Figure 6.8 Schematic of Cr-doping and HT effect in CS-Ni nanoclusters.....	103
Figure 6.9 I-V curves for the CS-Ni and CS-Ni <sub>5</sub> Cr films before and after HT.....	104
Figure 7.1 Hysteresis loops of a granular Fe <sub>3</sub> O <sub>4</sub> film on Si before and after irradiation to a fluence of 10 <sup>16</sup> Si <sup>2+</sup> ions/cm <sup>2</sup> near room temperature. The inset shows a magnified view near zero.....	113
Figure 7.2 Background subtracted GIXRD patterns for a granular Fe <sub>3</sub> O <sub>4</sub> film on Si before and after irradiation. The pattern intensity for the unirradiated film is multiplied by a factor of 4.....	114
Figure 7.3 High-resolution HIM micrographs of a granular Fe <sub>3</sub> O <sub>4</sub> irradiation.....	115
Figure 7.4 AFM and MFM images for a granular Fe <sub>3</sub> O <sub>4</sub> film on Si before and after film on Si before and after irradiation.....	119
Figure 7.5 Background subtracted GIXRD patterns for a Fe-Fe <sub>3</sub> O <sub>4</sub> core-shell nanocluster film on Si before and after 5.5 MeV Si <sup>+</sup> ion irradiation to 10 <sup>16</sup> Si <sup>+</sup> /cm <sup>2</sup> (~0.95 dpa in the film) at nominal RT.....	120
Figure 7.6 High-resolution HIM micrographs of granular film (a) before and (b) after ion irradiation. The inset to (a) shows a representative TEM image illustrating the core-shell structure.....	121
Figure 7.7 Hysteresis loop for a Fe-Fe <sub>3</sub> O <sub>4</sub> core-shell nanocluster film on Si before and after 5.5 MeV Si <sup>+</sup> ion irradiation to 10 <sup>16</sup> Si <sup>+</sup> /cm <sup>2</sup> (~0.95 dpa in the film) at nominal RT.....	122
Figure 7.8 First-order reversal curves (left) and contour diagram (right) of the irradiated sample. .	123
Figure 8.1 GIXRD pattern for a core-shell Fe-Fe <sub>3</sub> O <sub>4</sub> /Fe <sub>3</sub> N NC film, unirradiated (as-prepared) and irradiated to 10 <sup>15</sup> and 10 <sup>16</sup> ions/cm <sup>2</sup> .....	131
Figure 8.2 Magnetic hysteresis loops for the films Fe-Fe <sub>3</sub> O <sub>4</sub> /Fe <sub>3</sub> N, Fe <sub>3</sub> O <sub>4</sub> , and FeO+Fe <sub>3</sub> N. The inset shows a magnified view near zero fields.....	133
Figure 8.3 Magnetic hysteresis loops for the core-shell Fe-Fe <sub>3</sub> O <sub>4</sub> /Fe <sub>3</sub> N NC film, unirradiated (as-prepared) and irradiated to 10 <sup>15</sup> and 10 <sup>16</sup> ions/cm <sup>2</sup> . The inset shows a magnified view near zero fields.....	134
Figure 8.4 HIM images of the films Fe-Fe <sub>3</sub> O <sub>4</sub> /Fe <sub>3</sub> N (a, b, c), Fe <sub>3</sub> O <sub>4</sub> (i, ii, iii), and FeO+Fe <sub>3</sub> N (I, II, III): unirradiated and irradiated to 10 <sup>15</sup> and 10 <sup>16</sup> ions/cm <sup>2</sup> . The field of view of all images is 3.50 μm. ....	135
Figure 9.1 Cluster-beam deposition system and a schematic drawing for a van der .....	145

Figure 9.2 Helium ion microscope and its working principle.....	146
Figure 9.3 NEC 3.0 MV tandem ion accelerator and +15° beam line for in-situ resistance measurements of nanocluster films under 5.5 MeV Si <sup>2+</sup> and 2.0 MeV He <sup>+</sup> ion irradiation at nominally room temperature and 473 K using van der Pauw four-probe method. The film resistance was determined from the arithmetic average from two reversed-polarity and reciprocal measurements along the horizontal and vertical directions.....	148
Figure 9.4 Selected HIM (operating at 25 kV) snapshots of a nanocluster magnetite Fe <sub>3</sub> O <sub>4</sub> film on a surface-oxidized Si substrate irradiated to various ion fluences: (a) 3.3×10 <sup>16</sup> , (b) 7.6×10 <sup>17</sup> and (c) 1.9×10 <sup>18</sup> He <sup>+</sup> /cm <sup>2</sup> at nominal RT. The images have the same scalar bar and show a significant change in the nanostructure (same area). ....	150
Figure 9.5 HIM (operating at 25 kV) micrographs of the same nanocluster magnetite Fe <sub>3</sub> O <sub>4</sub> film in Fig. 1: (a) as-deposited at nominal RT, (b) annealed at 473 K and (c) at 773 K for 10 hours each in flowing Ar gas environments. The images have the same scalar bar and show a similar nanostructure (different areas). ....	151
Figure 9.6 Selected SEM (operating at 20 kV) snapshots of the same nanocluster magnetite Fe <sub>3</sub> O <sub>4</sub> film in Fig. 1 irradiated to various electron fluences: (a) 4.4×10 <sup>19</sup> , (b) 1.3×10 <sup>21</sup> and (c) 2.6×10 <sup>21</sup> e/cm <sup>2</sup> at nominal RT. The images have the same scalar bar and show a similar nanostructure (same area). ....	152
Figure 9.7 Selected HIM (operating at 30 kV) snapshots of a Fe-Fe <sub>3</sub> O <sub>4</sub> core-shell nanocluster film on a surface-oxidized Si substrate irradiated to various ion fluences: (a) 5.2×10 <sup>16</sup> , (b) 1.1×10 <sup>18</sup> and (c) 2.8×10 <sup>18</sup> He <sup>+</sup> /cm <sup>2</sup> at nominal RT. The images have the same scalar bar and show a dramatic change in the nanostructure (same area). ....	154
Figure 9.8 Typical TEM micrographs of Fe-Fe <sub>3</sub> O <sub>4</sub> core-shell nanoclusters: (a) loosely interconnected nanoparticles and (b) a particle containing a number of grains (circled) surrounded by amorphous material; a grain has a Fe core and Fe <sub>3</sub> O <sub>4</sub> shell, as shown in the inset ...	155
Figure 9.9 (a) Background subtracted GIXRD patterns for a Fe-Fe <sub>3</sub> O <sub>4</sub> core-shell nanocluster film on Si before and after 5.5 MeV Si <sup>+</sup> ion irradiation to 10 <sup>16</sup> Si <sup>+</sup> /cm <sup>2</sup> (~0.95 dpa in the film) at nominal RT. Also shown are the corresponding cross-sectional HIM images of the film (b) before and (c) after the irradiation. The two images have the same scalar bar. ....	156
Figure 9.10 Electrical resistance of a Fe-Fe <sub>3</sub> O <sub>4</sub> core-shell nanocluster film on surface-oxidized Si measured in situ using van der Pauw method as a function of ion fluence during 5.5 MeV Si <sup>2+</sup> ion irradiation at nominal RT. A super exponential decay behavior of the resistance is observed...	157
Figure 9.11 HIM micrographs of the same sample in Fig. 6 (a) before and (b) after 5.5 MeV Si <sup>2+</sup> ion irradiation to 1.5×10 <sup>15</sup> Si <sup>2+</sup> /cm <sup>2</sup> (0.08 dpa at the surface) at nominal RT. The images have the same scalar bar and show a dramatic change in the nanostructure. ....	158
Figure 9.12 GIXRD patterns for the same sample in Fig. 6 (a) before and (b) after 5.5 MeV Si <sup>2+</sup> ion irradiation to 1.5×10 <sup>15</sup> Si <sup>2+</sup> /cm <sup>2</sup> (0.09 dpa in the film) at nominal RT. A phase transition from cubic magnetite Fe <sub>3</sub> O <sub>4</sub> to cubic Wüstite FeO is observed.....	159

Figure 9.13 Electrical resistance of a Fe-Fe <sub>3</sub> O <sub>4</sub> core-shell nanocluster film on surface-oxidized Si measured <i>in situ</i> using van der Pauw method as a function of ion fluence during 5.5 MeV Si <sup>2+</sup> ion irradiation at 473 K. A super exponential decay behavior of the resistance is observed. ....	160
Figure 9.14 (a) HIM micrograph and (b) GIXRD pattern for the same sample in Fig. 9 after 5.5 MeV Si <sup>2+</sup> ion irradiation to 3.4×10 <sup>15</sup> Si <sup>2+</sup> /cm <sup>2</sup> (~0.2 dpa at the surface and in the film) at 473 K. Phase transition is not observed. ....	161
Figure 9.15 Electrical resistance of a Fe-Fe <sub>3</sub> O <sub>4</sub> core-shell nanocluster film on surface-oxidized Si measured <i>in situ</i> using van der Pauw method as a function of ion fluence during 2.0 MeV He <sup>+</sup> ion irradiation at nominal RT. A significant decrease of the resistance is observed within a narrow dose window in the low-dose regime.....	162
Figure 9.16 HIM micrographs for the sample in Figure 9.15 (a) before and (b) after 2.0 MeV He <sup>+</sup> ion irradiation to 8×10 <sup>15</sup> He <sup>+</sup> /cm <sup>2</sup> at nominally RT. A dramatic change in the surface morphology does not occur. ....	163
Figure 9.17 GIXRD patterns for the sample in Figure 9.15 (a) before and (b) after 2.0 MeV He <sup>+</sup> ion irradiation to 8×10 <sup>15</sup> He <sup>+</sup> /cm <sup>2</sup> at nominally RT. Phase transition does not occur. ....	163
Figure 10.1 Room temperature hysteresis loops of Mn <sub>100-x</sub> Bi <sub>x</sub> (x=40, 45, 52) magnets sintered at 287 K. Max. field 2.2 T. <sup>2,3</sup> .....	170
Figure 10.2 Mn-Bi thin film sandwiched in a multilayered metal film (Top). Mn-Bi nanoparticles embedded in a metal thin film matrix (Bottom) .....	170
Figure 10.3 Schematic representation of the nanocluster deposition system with provisions for the synthesis of both thin film and nanoclusters. ....	172
Figure 10.4 SEM images of Ni, Mn-Bi and multilayer Ni/Mn-Bi/Ni thin film deposited on Si substrate at two different scales, 10μm (a,b,c) and 1μm (d,e,f) .....	173
Figure 10.5 Hysteresis loop of (a) Mn-Bi thin film sandwiched between Ni thin films and (b) Mn-Bi nanoparticle sandwiched between Ni thin films .....	174
Figure 10.6 Hysteresis loop of Mn-Bi nanoparticles embedded in Ni thin film matrix.....	174
Figure 10.7 AFM (a, b, c) & MFM (i, ii, iii) images of MnBi Thin film and Ni-MnBi-Ni thin film sandwich.....	175

**List of Tables**

Table 5.1 Sputtering conditions and magnetic properties corresponding to different particle size shown in Figure 5.1 .....	71
Table 5.2 The nominal and measured Cr/Ni atomic ratio as well as the measured lattice constant of the NP .....	75
Table 6.1 Hysteresis data for CS-Ni and CS-Ni5Cr NC Films before and after HT .....	99
Table 8.1 Average grain sizes of different phases in films Fe-Fe <sub>3</sub> O <sub>4</sub> /Fe <sub>3</sub> N, Fe <sub>3</sub> O <sub>4</sub> , and FeO+Fe <sub>3</sub> N before and after irradiation.....	131

## **Chapter 1: Introduction to Nuclear Energy and Nano-Nuclear Technology**

### **1.1 The Future of Nuclear Energy**

We live in the nuclear age, when nuclear power is considered to be one of the most productive and carbon-emission-free power sources. Today, 13-14% of the electricity used worldwide is generated by nuclear power. In United States of America, 20% of electricity is provided by nuclear power and it was predicted by International Atomic Energy Agency (IAEA) that by 2030 the nuclear power capacity could double and will be in high demand. China has 6 nuclear power plants in operation and 20 new reactors under construction, and there is also a considerable number of new reactors being built in South Korea, India, and Russia.<sup>1</sup> Currently the Generation II and Generation III nuclear reactors, which are in use have faced and are facing lot of material damage and safety issues related to high neutron flux and a highly corrosive environment. This includes but is not limited to the cracking of vessel heads and evolution of material fatigue, which has led to the shutdown of the nuclear reactors. The recent nuclear disaster in Japan on March 11<sup>th</sup>, 2011 due to a massive tsunami and earthquake raises huge concern over the safety of the nuclear reactors. Though the existing U.S. nuclear fleet has a remarkable safety and performance record, today many of these reactors are approaching their designed lifetime of 60 years. In its Research and Development Roadmap - Report to Congress dated April 2010, the Department of Energy's (DOE) Office of Nuclear Energy identified four research and development objectives, the top one being "Develop technologies and other solutions that can improve the reliability, sustain the safety, and extend the life of current reactors."<sup>2</sup> For these reasons, the Generation IV nuclear reactors, which are not expected to be in commercial use until 2030, need enhanced safety, minimal wastes and economical compatibility as shown in Figure 1.1; hence, the research on the design of advanced reactors and new builds continues.



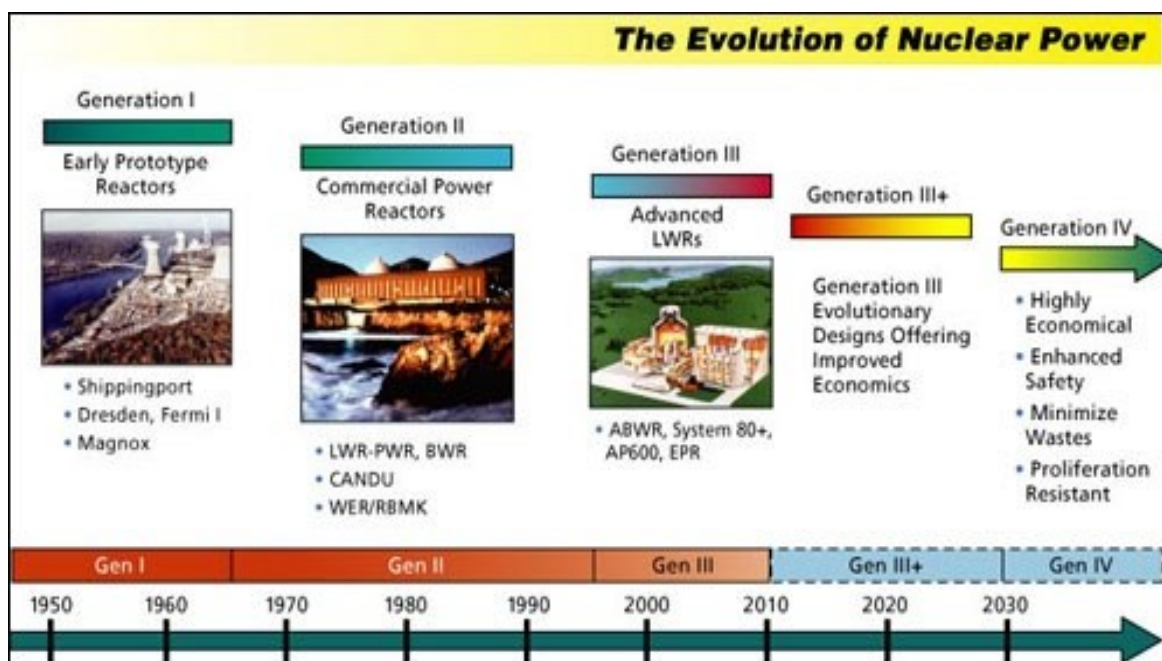


**Figure 1.1** The evolution of nuclear power from Gen I to Gen IV

In order to achieve this objective, an extensive understanding of radiation-induced damages and their effects on materials at the atomic scale is essential. As summarized by P. Hoffmann in the literature review on the subject of ‘core degradation phenomena’, the four main reasons for the nuclear material degradation phenomenon are (i) chemical interactions between core materials, (ii) temperature and heating rates at the core, (iii) material distribution & relocation at melting and (iv) hydrogen formation at quenching.<sup>3</sup> Although, the information provided is certainly beneficial to the scientific community working in this area to focus on the specifics to meet the standards, the accident scenarios are vast and there are still many uncertain issues about materials under irradiation, which should be studied in detail and investigated for future nuclear reactor design and application. Amidst all these uncertainties, in order to come up with such a system which assures safe operation, we are left with no other options except but to approach these issues from all prospective including material property, cooling behavior, melting behavior, melt pathway, mitigation, progression, chemical reactions, temperature effect, oxidation states, cracks, material behavior, steam interactions with material, etc. and more significantly considering the number of scenarios each of these are

subjected to. The Department of Energy has stated in their report “Basic Research Needs for Materials under Extreme Environment” that the behavior of materials under energetic photon and irradiation flux is a high priority area where significant advances in fundamental scientific understanding are needed. This includes the understanding of the atomic basis for defect creation, migration, and annihilation, which help to establish dose limits for materials in radiation fields. These understandings are needed for application in next-generation energy technologies, specifically the design of next-generation fission reactors. Along with that, non-destructive monitoring techniques must be integrated with plant operations to quantify the ‘state of health’ of structural materials in the reactor fleet, and more importantly, to predict their residual safe operating life with the in-situ quantified material properties. These reactors have the option of being designed for inspectability in order to enhance safety.

## **1.2 Nano-Nuclear Technology**

Nano-Nuclear Technology (NNT) deals with the use of latest engineered-nano-materials in each phase of the nuclear fuel cycle to improve the nuclear power performances and safety, bringing new generations of nuclear power units, and a new advanced civilization. During the course of nuclear technological evolution in the history of mankind, numerous lessons were learned through many accidents, some more severe than those registered in the other non-nuclear power plants. In light of these events and the recent Fukushima disaster, a huge responsibility is laid upon the scientific communities to quicken their progresses, which demand for the utmost safety in the future generation nuclear power plants to avoid such disaster. Scientific communities around the world are working towards achieving it in various ways, among which Nano-Nuclear technology is an efficient tool and candidate for achieving the goal of utmost safety and performance. A significant contribution in the NNT area would result in the development of new capabilities that could be useful to nuclear energy, which can help build devices to support the development of sustainable nuclear fuel cycles, to control their effects and its implementation in nuclear power. Ongoing

research of NNT in labs around the world contributes to the improvement of future generation nuclear reactors in safety and performance. A detailed investigation about the on-going research in NNT is discussed in Chapter 2. NNT addresses the issue of performance and safety from various angles and works from different fields to achieve it in every stages of nuclear fuel cycle (Figure 1.2).

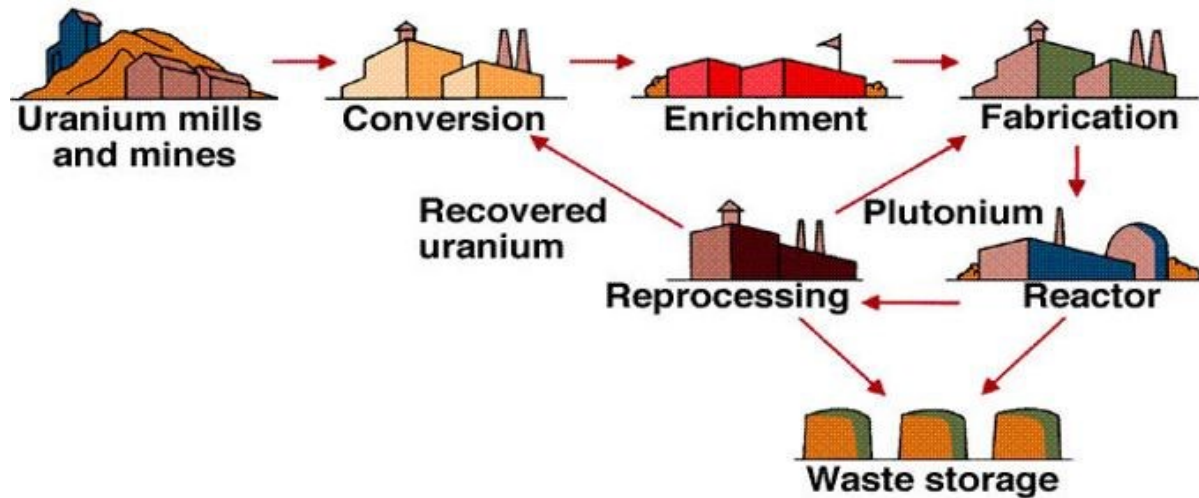


**Figure 1.2** The nuclear fuel cycle

Some of the main focuses are listed below, where the use of nano-particles, nano-structured materials, and/or nano-processes to enhance mechanical, chemical, physical, or thermo-hydraulic properties and performance in nuclear fuel cycle applications, such as:

- i. Nanostructured-ODS Materials* - Reactor (in-core) materials like oxide dispersion strengthened (ODS) materials with nano-scale precipitates that could improve mechanical performance as well as radiation tolerance.
- ii. Nano-Scale Coatings* - Nano-scale coatings that could be included on the exterior or the interior of fuel cladding to improve corrosion resistance and surface hardening, and pellet-clad interactions on the cladding interior.
- iii. Nanomaterials for Fission Product Capturing* - Chemical interaction and separation methods using nano-particles and/or nano-porous materials that can enable techniques to

capture fission product gases either from reprocessing operations or directly within a reactor fuel assembly thereby reducing the potential for releases from normal or accident conditions.

- iv. Nano-Technology Engineered Fuels* - Advanced fuels engineered and/or fabricated with nano-technologies to enable longer service lives, reduce fabrication process losses, and/or reduce the potential for failure in normal or accident conditions including increased fission gas retention, plasticity, radiation tolerance, heat transfer capability, as well as reduced fuel cladding chemical and/or mechanical interactions.
- v. Nano Radiation Sensors, Detectors and Monitors* - Nano-technology enabled sensors, detector and/or in-service monitors that can directly monitor for radiation, temperature, pressure, in situ diagnostics of material properties and mechanical response, corrosion, neutron flux, stress/strain or even chemistry with little effect on system performance with significantly reduced size and weight and increased sensitivity, performance, and functionality.
- vi. Nano Nuclear Waste separation* - Chemical interaction and separation methods using nano-particles and/or nano-porous materials for separating the actinides and other radioactive elements from the nuclear waste for reprocessing and reusing.

### **1.3 Significance of Studying Magnetic Properties**

There has been a considerable interest in developing means of radiation detection, which do not involve direct collection of charge or light as in conventional semiconductor and scintillator detectors, respectively. One possible alternative device design involves remote monitoring of transient or permanent microwave or millimeter-wave reflectivity changes in materials due to photoconductivity, photodielectric, and photomagnetic effects arising from the ionizing radiation.<sup>4</sup> Ionizing radiation creates a transient change in the population of free charge carriers in a material. This change in free carrier population induces changes in magnetic permeability as the free carriers couple with electron spins in magnetic dipoles.<sup>5</sup> It is also well known that neutron irradiation, such

as encountered by metallic structural elements of nuclear reactors, can generate defects that accumulate over the long term, which leads to an increase in hardness and introduces pinning sites for magnetic domain walls.<sup>6</sup> It has been shown in some steels that magnetic changes can be directly correlated with mechanical hardness changes,<sup>7,8</sup> thus potentially offering a non-destructive proxy for radiation-induced mechanical damage. Magnetic permeability decreases have been observed in oxide spinels and garnets after irradiation with x-rays, gamma-rays, and neutrons.<sup>9,10,11</sup> Also, various experiments involving ion irradiation in magnetic oxide garnets, hexaferrites, and spinels have showed substantial changes in magnetization and Mossbauer spectrum due to the creation of paramagnetic channels, which could usually be removed with annealing.<sup>12,13</sup> Hence, whatever be the radiation effect, it directly or indirectly affects the magnetic properties as depicted in the Figure 1.3 and therefore understanding the effects of radiation on magnetism and magnetic permeability becomes more significant.

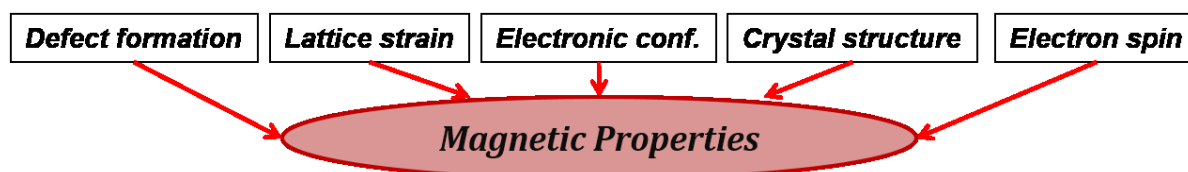


**Figure 1.3** Block diagram showing that the microstructural changes directly is related to magnetic properties

Also, magnetic methods have historically been used to nondestructively monitor changes in structural steels in nuclear reactors.<sup>6</sup> For these reasons, a fundamental understanding of the changes in magnetism on nanomaterials with irradiation will aid in understanding health monitoring of existing reactors as well. Moreover, from the history of space programs, it is evident that the entire community of space exploration has faced a series of radiation-related problems, which include the loss of stored data due to radiation-induced changes in magnetic properties of storage disks. Also, future robotic technologies may involve extreme use of automation in environments with high radiation that might require advanced data storage in a radiation environment. The aforementioned

reasons and discussion makes one point clear: the understanding of radiation-induced modification of magnetic properties needs to be established and developed.

#### **1.4 Magnetic Nanoparticles for Irradiation Studies**

Radiation is a process in which energy emitted by one body travels through a medium or through space, ultimately to be absorbed by another body. This transfer of energy takes place through a carrier based on which the type of radiation can be identified. Ions, electrons, photons, neutrons, and nuclei can carry a huge amount of energy and can cause the following types of radiations: heavy ion irradiation, electron beam irradiation, gamma irradiation, neutron irradiation, alpha irradiation, thermal irradiation and so on. The basic outcome of irradiation is defect formation in the materials. This happens when the above mentioned carriers with incident energy strike the target material atoms. These material atoms have a threshold limit called the threshold displacement energy. When the incident energy is greater than the threshold displacement energy, defects like vacancies and interstitials are created. As it can be seen, at the microscopic level the formation of defects like vacancies and interstitials eventually leads to the formation of voids and cracks. Diffusion of atoms influenced by increase in temperature is also one of the most predominant effects of irradiation, which causes grain/phase boundary shifts. The other outcomes of the irradiation impacts are the displacement spike and thermal spike, which cause huge disturbances of lattice atoms and huge temperature increases in the surrounding lattice sites, thus increasing the hardness of the irradiated material. The details of mechanical irradiation damage are discussed more in books like 'Fundamentals of radiation materials science' by Was G.S.<sup>14</sup> On the other hand, these radiations also alter the electron spin, electronic configuration and structural nature, which largely account for the change in magnetic moments and other magnetic properties. A literature review in chapter 2 deals with the variety of magnetic property changes due to irradiation. Hence, whatever be the radiation-induced defects, they are directly or indirectly linked with the atomic level changes.

Macroscopic level studies have limitations to understanding these atomic level changes. Over the last few decades, nanomaterials like nanoparticles, nanowires and nanotubes have been identified to be the most suitable candidate for study at the atomic level. When it comes to understanding radiation-induced magnetic properties and defects at the atomic level, magnetic nanoparticles are the best choice. This is because of their high sensitivity to irradiation and the flexibility of the studies involved. This can help us to uncover the interfacial behavior and nano-scale interactions under extreme conditions like intense radiation exposure. Specifically, detailed assessments of interfaces between particles, clusters, grains, and particle-matrices can be assessed. This assessment will be helpful in the future for the design of advanced dose sensors or monitors. Applications of such detection and monitoring devices could reduce threats to national security as well as provide integrated health monitoring for next-generation nuclear reactors, spent fuel casks, and other structural materials exposed to continuous irradiation and thermal stress. With the potential renaissance of nuclear energy in the US, novel means for assessing irradiation will be of great benefit to the monitoring of existing power plants and designing of new power plants.

### **1.5 Research Scope and Limitations**

As discussed earlier, owing to these increasing demands of understanding the irradiation-induced modifications in reactor components, this research mainly focuses on the nanostructured-ODS materials and nanotechnology enables sensors, monitors and detectors. This research is mainly based on the hypothesis that, “Fe-based magnetic nanoparticles could help understand the radiation effects and dispersion strengthening phenomena in a better way, and could contribute to the development of radiation sensitive or stable materials for nuclear energy applications.” It addresses the issues or challenges as listed below by specifically studying the changes of magnetic properties, structural properties and electrical conductivity property under irradiation.

- Research of nanocluster for dispersion strengthening & sensor applications is still in their infancy

- Knowledge on nanocluster behavior under irradiation is not fully understood
- Bringing controlled property changes under irradiation is a big challenge
- Controlling particle size and uniform distribution of particles is difficult

As listed below, the objective of this research is to understand the structural, magnetic and electrical material property changes due to irradiation and high temperature exposure, in general, and to develop a fundamental understanding of irradiation-induced modification in the properties of granular magnetic films and composites of metals and dispersed magnetic oxides, in particular.

- To develop a fundamental understanding of the irradiation-induced modifications & the technique of bringing controlled property changes in nanomaterials
- To study the structural, magnetic & electrical-conductivity property changes in nanomaterials under irradiation and heat treatment
- To assess the stability & sensitivity of nanomaterials to irradiation for designing sensors, monitors and long lasting materials to prevent accidents.

The results obtained from this investigation could be useful in the future to generate data for scientific assessment in prediction of the material performance in radiation environments and to recommend candidate compositions for development of novel multifunctional materials. This research investigates several related classes of magnetic materials (magnetic nanoparticles to granular nanocluster films) for their radiation sensitivity and elucidates mechanisms for the susceptibility of irradiation-induced magnetism changes. This research will possibly be able to answer some of the following specific scientific questions: How do cluster size, shape, density and roughness change due to irradiation? What are the factors affecting the change in magnetic properties of nanoparticles due to irradiation? What makes a material able to remain stable and unaltered even under high doses of irradiation? What are the roles of irradiation temperature and dose rate on the structures and magnetic properties of irradiated materials? These questions and more will be addressed by studying in detail the experimental data obtained from measurement tools like



Transmission Electron Microscope (TEM), Grazing-angle Incident X-ray Diffraction (GIXRD), Vibrating Sample Magnetometer (VSM), Physical Property Measurement System (PPMS), Helium Ion Microscope (HIM), Multi-Purpose Diffractometer (MPD), Atomic Force Microscope (AFM) and Magnetic Force Microscope (MFM). Although the basic mechanical defects like vacancy and interstitial formation, void nucleation, and displacement cascade are plausible due to irradiation, this research does not focus on estimating these damages and related factors to relate them to the magnetic property changes. As mentioned before this research is ultimately focused on understanding the structural changes and variation in magnetic behavior due to irradiation. In addition to that, even though nuclear radiation is the real time challenge towards which this research is focused, because of the risks involved in handling it like having residual radioactivity in the irradiated specimens which makes it more difficult and expensive to handle and analysis, and since the neutron source is limited and restricted the research is carried out under the alternate irradiation exposure of  $\text{Si}^{2+}$  ions. The advantages of using  $\text{Si}^{2+}$  ions for irradiation is that Si ions behaves similar to neutrons in terms of defect creation since the efficiency of producing freely migrating defects are almost same for both neutrons (2%) and Si ions (4%).

## **1.6 General Overview on All Chapters**

This chapter lays a foundation for the forthcoming discussion on irradiation-induced and heat-treatment induced changes in magnetic nanoparticles and its applications in nuclear energy. Chapter 2 deals with the fundamentals of radiation, its effects on matter and the principle of radiation detection. Chapter 3 is a literature review on nano-nuclear technology, which presents the research so far in using nanomaterials for nuclear energy applications and how it relates to this research. Chapter 4 explains the experimental setup where synthesis and characterization of the nanoparticles and granular films are discussed. Along with that, the particular equipment used for characterization are discussed in detail. The nature of nickel and Cr-doped nickel nanoparticles and the change of properties under heat treatment are discussed in chapter 5 and 6. Chapter 7 and the following

chapters deal with the radiation and heat treatment effects on iron nanoparticles and its granular films as well as their contribution to NNT and nuclear energy applications. The final chapter gives a summary of this dissertation and its contribution to the field of nano-nuclear technology.

## 1.7 References

1. “Nuclear power - Wikipedia, the free encyclopedia.” [http://en.wikipedia.org/wiki/Nuclear\\_power](http://en.wikipedia.org/wiki/Nuclear_power).
2. “US Department of Energy Nuclear Energy Research and Development Roadmap - Report to Congress.” *Office of Nuclear Energy*, 2010.
3. P. Hofmann, “Current knowledge on core degradation phenomena, a review,” *J. Nucl. Mater.*, vol. 270, no. 1–2, pp. 194–211, Apr. 1999
4. J. S. McCloy, “US Department of Energy Nuclear Energy Research and Development Roadmap - Report to Congress.” *Office of Nuclear Energy*, 2010.
5. S. Zinkle, “Radiation-induced changes in the physical properties of ceramic materials,” *Journal of Nuclear Materials*, vol. 191-194, pp. 58-66, 1992.
6. G. Dobmann, “NDE for material characterization of ageing due to thermal embrittlement, fatigue and neutron degradation,” *International Journal of Materials and Product Technology*, vol. 26, no. 1/2, p. 122, 2006.
7. J. Yi, B. Lee, and H. Kim, “Nondestructive evaluation of isothermally annealed 12% CrMoV steel by magnetic BN measurement,” *Journal of Magnetism and Magnetic Materials*, vol. 130, no. 1-3, pp. 81-91, 1994.
8. K. Ryu, S. Nahm, J. Park, K. Yu, Y. Kim, and D. Son, “A new non-destructive method for estimating the remanent life of a turbine rotor steel by reversible magnetic permeability,” *Journal of Magnetism and Magnetic Materials*, vol. 251, no. 2, pp. 196-201, 2002.
9. K. Hisatake, K. Ohta, N. Ichinose, and H. Yokoyama, “X-ray induced decrease of permeability in YIG single crystals with Pb impurity,” *Physica Status Solidi (a)*, vol. 26, no. 1, p. K79-K82, 1974.
10. K. Hisatake, I. Matsubara, K. Maeda, H. Wakao, T. Fujihara, Y. Kawai and K. Uematsu, “Gamma-ray-induced disaccommodation of permeability in single crystal of yttrium iron garnet,” *Journal of Magnetism and Magnetic Materials*, vol. 112, no. 1-3, pp. 387-388, 1992.
11. V. D. Parkhomenko, S.F. Dubinin, B. N. Goshchitskii, Yu. G. Chukalkin, S.K. Sidorov, V.G. Vologin and V. V. Petrov, “Peculiarities of radiation damage in ferrites with spinel structure,” *Physica Status Solidi (a)*, vol. 38, no. 1, pp. 57-66, 1976.
12. M. Toulemonde, G. Fuchs, N. Nguyen, F. Studer, and D. Groult, “Damage processes and magnetic field orientation in ferrimagnetic oxides  $Y_3Fe_5O_{12}$  and  $BaFe_{12}O_{19}$  irradiated by high-energy heavy ions: A Mössbauer study,” *Physical Review B*, vol. 35, no. 13, pp. 6560-6569, 1987.
13. F. Studer, C. Houpert, D. Groult, J. Fan, A. Meftah, and M. Toulemonde, “Spontaneous magnetization induced in the spinel  $ZnFe_2O_4$  by heavy ion irradiation in the electronic

stopping power regime,” *Nuclear Instruments and Methods in Physics Research Section B: Beam Interactions with Materials and Atoms*, vol. 82, no. 1, pp. 91-102, 1993.

14. G. Was, *Fundamentals of radiation materials science: metals and alloys*. Berlin: Springer, 2007.

## **Chapter 2: Fundamentals of Radiation & Principles of Radiation Detection**

### **2.1 Introduction**

Radiation is a process in which energy emitted by one body travels through a medium or through space, ultimately to be absorbed by another body. Radiation is the energy emitted in the form of microscopic particles or photons. Radiation interacts with matter through the fundamental interactions of our nature, predominantly through the electromagnetic (for charged particles and photons) and strong interactions (for hadrons). Radiation can be broadly classified into ionizing radiation and non-ionizing radiation. In ionizing radiation, the energy carriers interact with a physical medium to produce ion pairs, for example,  $\alpha$ ,  $\beta$ , X,  $\gamma$ -radiation, neutron, proton, pion, muon, etc., which are invisible to human such that the detection of it demands a suitable monitoring instrument. Although, neutrons are neutral particles they do not ionize directly, they produce ions through secondary mechanisms. In non-ionizing radiation, the energy carriers does not produce ion pairs in a physical medium, for example, soft ultra-violet, infra-red, visible light, microwave, radio-frequency, etc.

### **2.2 Radiation Interaction with Matter**

Detection of radiation is based on its interactions with matter and the energy deposited in the matter. The interaction between radiation and matter is accompanied by a number of effects such as the creation of lattice defects (primary and secondary), emission of photons (fluorescent materials), charged particles (electron-ion pairs), liberation of heat and radiation-induced chemical reactions. All these effects can be used to detect radiation, measure particle flux density or intensity and the radiation spectra. Currently, the operation of many measuring devices is based on the ability of radiation to ionize molecules. The basic interaction modes of radiation with matter for detection are excitation and ionization. The ultimate goal is a formation of electron-ion pair inside the working

volume of the detector because at the final stage of detection only electrically charged particles can be registered.

### 2.2.1 Neutron Interaction with Matter

Since neutrons are electrically neutral, they penetrate matter more deeply than electrically charged particles of comparable kinetic energy; therefore they are valuable probes of bulk properties. Neutrons interact with atomic nuclei and magnetic fields from unpaired electrons. The neutrons cause pronounced interference and energy transfer effects in scattering experiments. Unlike an x-ray photon with a similar wavelength, which interacts with the electron cloud surrounding the nucleus, neutrons primarily interact with the nucleus itself. The interactions are either scattering or absorption and have been described by Fermi's pseudo potential. Neutron scattering and absorption cross sections vary widely from isotope to isotope. In general, the neutron-nucleus interactions can be classified into the following

- Inelastic Scattering - (Fig. 2.1(a))
- Elastic Scattering - (Fig. 2.1(b))
- Radiative capture:  $(n, 2n)$ ,  $(n, \alpha)$ ,  $(n, p)$ ,  $(n, \gamma)$  reactions - (Fig. 2.1(c))
- Fission reaction - (Fig. 2.1(d))

Inelastic scattering causes the excitation of a nucleus with subsequent emission of gamma photon and neutron. Elastic scattering occur between fast neutrons and low atomic mass number absorbers (“billiard ball effect”). In radiative capture, for example in  $(n, \gamma)$  reaction, a nucleus with mass  $M$  absorbs a neutron (mass  $m$ ) and form a compound nucleus in its excited state; then goes to the de-excited state by emitting a gamma photon. The nucleus absorbs one neutron and then emits two neutrons gaining recoil energy. For  $(n, 2n)$  reaction, the second neutron can only be ejected if the remaining excitation energy of the nucleus after emission of the first neutron exceed the binding energy of a neutron in the nucleus. In the process, the nucleus will receive a recoil energy,  $T$ . This

type of interaction becomes important when neutron energy is  $> 8$  MeV, which the nucleus of an atom splits into smaller parts (lighter nuclei). The fission process often produces free neutrons and photons (in the form of gamma rays), and releases a very large amount of energy even by the energetic standards of radioactive decay. Fission is caused by fast and thermal neutrons and dissipation of energy causes ionization.

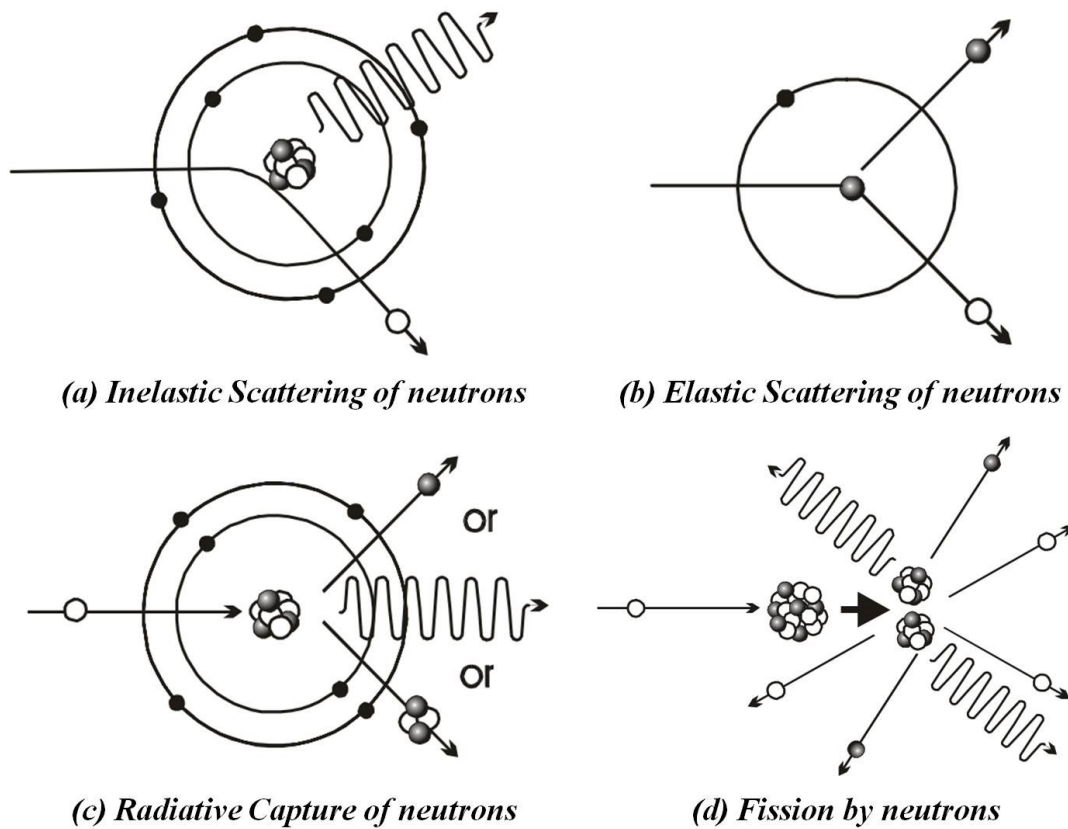


**Figure 2.1** Interactions of neutron with matter

### 2.3 Neutron Radiation Detection through Ionization

Ionization can be caused only through charged particles through Columbic interactions (Electromagnetic Interaction). Since, neutrons are neutral particles they do not ionize directly, they are harder than charged particles to detect directly. Furthermore, their paths of motion are not

affected much by electric and magnetic fields. Hence, neutrons produce ions through secondary mechanisms, which are then detected. Neutrons react with matter through

- i. Elastic scattering producing a recoiling nucleus
- ii. Inelastic scattering producing an excited nucleus, or absorption with transmutation of the resulting nucleus.

Most detection approaches rely on detecting the various reaction products. Inelastic scattering includes the absorptive reactions and activation processes. Low energy neutrons (thermal neutrons) are typically detected indirectly through absorptive reactions. Typical absorber materials used have high cross sections for absorption of neutrons and include helium-3, lithium-6, boron-10, and uranium-235. Each of these reacts by emission of high energy ionized particles, the ionization track of which can be detected by a number of means. In activation processes, neutrons may be detected by reacting with absorbers in a radiative capture, spallation or similar reaction, producing reaction products that then decay at some later time, releasing beta particles or gammas which are then detected. In elastic scattering reactions, neutrons transfer energy to the nucleus of material, creates ions, which is then detected.

### **2.3.1 Commercial Neutron Detectors**

The three commonly used neutron detectors are

1. Gas-Filled neutron Detectors
2. Scintillation neutron detectors
3. Semiconductor neutron detectors

#### **Gas-Filled Neutron Detectors**

Gas-filled detectors operate by utilizing the ionization produced by radiation as it passes through a gas. Typically such a counter consists of two electrodes to which a certain electrical potential is applied. The space between the electrodes is filled with a gas (Figure 2.2).



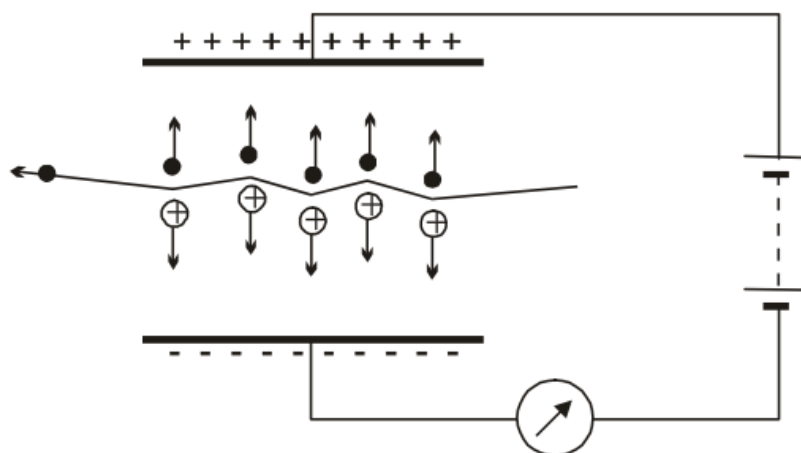


**Figure 2.2** Principle of a gas-filled detector

As we know neutrons do not directly ionize atoms, they are detected indirectly upon producing a charged particle after its reaction with a material in the gas-filled detectors. The gas-filled proportional counter is coated with  $^{10}\text{B}$  on the walls of the  $\text{BF}_3$  gas filled chamber. When neutrons react with  $^{10}\text{B}$  the reaction produces the alphas and the lithium particles as shown below that ionizes the gas and the charged particles are then detected by electrodes and amplified. A typical example of gas-filled neutron detector is Geiger-Muller counter as shown in the Figure 2.3.

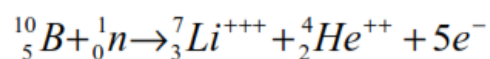


**Figure 2.3** Geiger-Muller counter for radiation detection.

## Scintillation Neutron Detectors

Scintillators are materials - solids, liquids, gasses - that produce sparks or scintillation of light when ionizing radiation passes through them. The first solid material used as a particle detector was a scintillator. The operation of a scintillation counter may be divided into two steps:

1. Absorption of incident radiation energy by the scintillator: electrons are raised to excited states and after subsequent de-excitation the scintillator emits a photon in the visible light range.
2. The photon, emitted from the scintillator, interacts with the photocathode of a photomultiplier tube as shown in Figure 2.4, releasing electrons.

The electrons emitted by the photocathode are guided, with the help of an electric field, towards the first dynode, which is coated with a substance that emits secondary electrons, if electrons impinge upon it. The secondary electrons from the first dynode move towards the second, from there towards the third, and so on. Typical commercial phototubes may have up to 15 dynodes. The production of secondary electrons by the successive dynodes results in a final amplification. The different types of scintillators include: Inorganic crystals, Organic scintillators, Plastic scintillators and Gaseous scintillators.

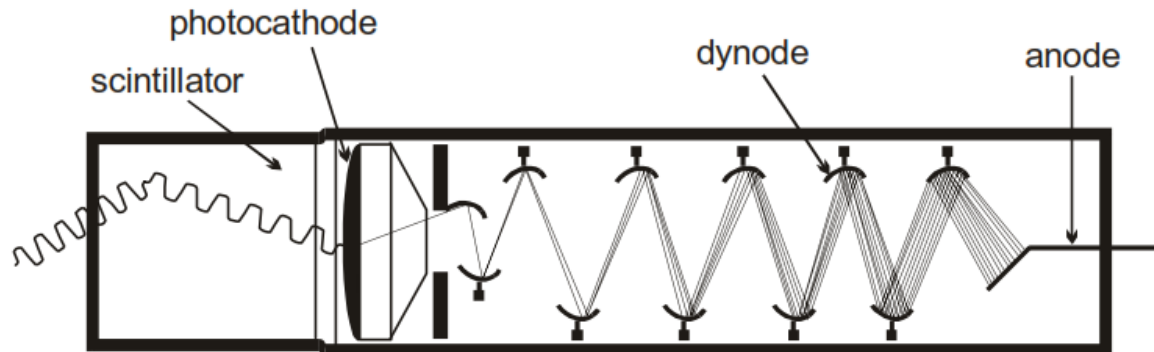


**Figure 2.4** Photomultiplier Tube

## Semiconductor Detectors

Semiconductor detectors are solid-state devices that operate essentially like ionization chambers. The charge carriers in semiconductors are not electrons and ions, as in the gas counters, but electrons and holes.

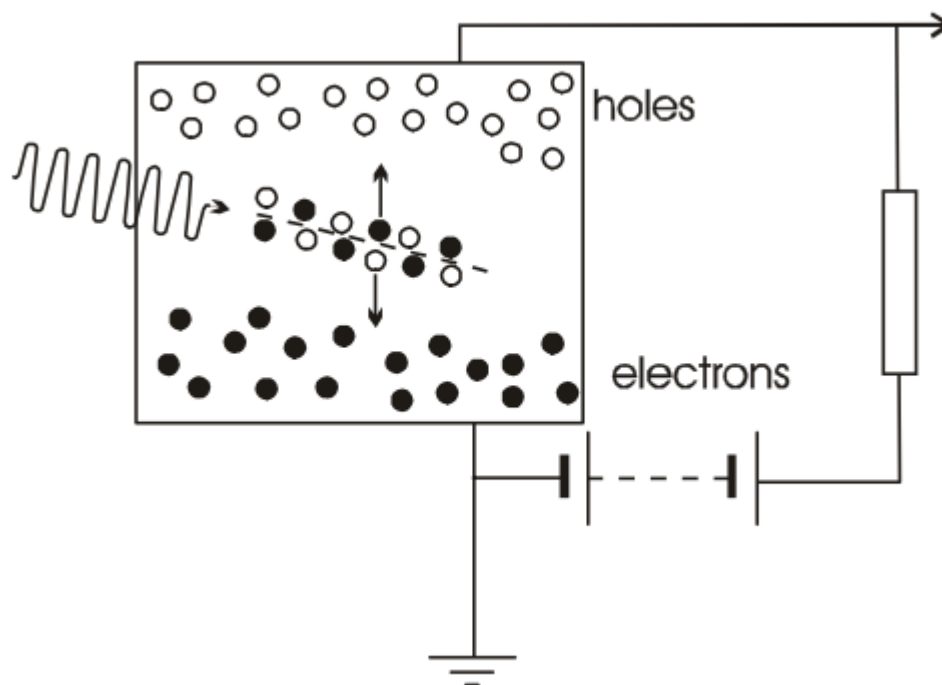


**Figure 2.5** Principle of a semiconductor detector

When an electron moves to the conduction band, an empty state is left in the valence band, which is called a hole. When the electron moves in one direction, a hole moves in the opposite direction. Holes are treated as particles with positive charges:  $+e$ . They contribute to the conductivity in the same way electrons do. Radiation incident upon the semiconducting junction produces electron-hole pairs as it passes through it (Fig. 2.5). Electrons and holes are swept away under the influence of the electric field and, with proper electronics the charge collected produces a pulse that can be recorded.

### 2.3.2 Challenges of Neutron Detection

There are several challenges faced by modern-day neutron detection in an experimental environment among which background noise, high detection rates, neutron neutrality, and low neutron energies are very prominent.

1. The background noise in neutron detection is generally high-energy photons, which aren't easily eliminated by physical barriers.
2. Although, the other sources of noise, such as alpha and beta particles, can be eliminated by various shielding materials, such as lead, plastic, thermo-coal, etc., photons cause major interference in neutron detection.
3. It is uncertain if neutrons or photons are being detected by the neutron detector. Both register similar energies after scattering into the detector from the target or ambient light, and are thus hard to distinguish.
4. Coincidence detection can also be used to discriminate real neutron events from photons and other radiation.
5. In a region of high beam activity, the detector gets hit continuously by neutrons and creates background noise at overwhelmingly high rates which complicates collected data as there will be extreme overlap in measurement, and separate events are not easily distinguished from each other.
6. The main challenge is in keeping detection rates as low as possible and in designing a detector that can keep up with the high rates to yield coherent data which makes is expensive.
7. Neutrons are neutral and thus do not respond to electric fields. This makes it hard to direct their course towards a detector to facilitate detection.
8. Neutrons also do not ionize atoms except by direct collision, so gaseous ionization detectors are ineffective.

9. Detectors relying on neutron absorption are generally more sensitive to low-energy thermal neutrons, and are orders of magnitude less sensitive to high-energy neutrons.
10. Scintillation detectors, on the other hand, have trouble registering the impacts of low-energy neutrons.

## **2.4 Neutron Radiation Detection through Property Changes**

As there are several challenges involved with detecting neutron radiation through ionization due to its complexity and the involvement of large expensive equipment, alternatively neutron radiation detection and monitoring can be achieved through studying the changes in physical properties of the materials exposed to irradiation. The interaction of neutrons through elastic scattering causes primary radiation defects like vacancies and interstitials in the material irradiated, which in turn causes secondary effects resulting in the change of the materials property itself. Although this technique is currently in place in nuclear reactors, where a piece of metal is kept in the reactor for a particular period of time and later removed to study the change in its properties which is a time consuming and difficult-to-handle-material process, live time monitoring, detecting and quick sensing of radiation through property changes is not in place. Therefore it is very important to develop the radiation monitoring and detection devices, which works on the principle of altering the materials properties. This not only gives the benefit of developing better sensor but also helps in investigating the basic mechanisms and process behind the property changes of materials and helps to develop radiation resistant materials.

### **2.4.1 Radiation Effects on Material Properties**

Apart from ionization, interactions of high energy radiation such as  $\alpha$ ,  $\beta$  and  $\gamma$  rays as well as sub-atomic particles, such as electrons, protons, neutrons, with crystal lattices give rise to defects/imperfections such as vacancies, self-interstitials, ionization, electron excitation etc. Ion-atom or atom-atom (neutron-atom) collision are governed by interactions between the electron

clouds, the electron cloud and the nucleus, and between the nuclei. These interactions are described by interatomic potentials, which are basically classified as Coulomb potential, screened Coulomb potential, and Born-Mayer potential. If the distance between the incident particle and target atom is less than the electron shell radius then the interaction is based on Coulomb potential. If the distance is more than the electron shell radius then only weak Van De Waals forces are involved and the interaction can be defined by Born-Mayer potential. If it's between the electron shell radius and the lattice constant then it is screened Coulomb potential. Fission fragments produced as a result of such interaction and neutrons cause the bulk of the radiation damage. Other types of radiation either do not have enough energy or are not produced in sufficient number density to cause any major radiation damage. In a nuclear reactor scenario, the microscopic defects like vacancies and interstitials produced in materials as shown in Figure 2.6 due to irradiation are referred to as radiation damage. The evolution of these defects result in changes in physical, mechanical and chemical properties, and these macroscopic material property changes in aggregate are referred to as radiation effects. Before discussing the effects of radiation on various properties, we need to know how to describe the radiation damage in a quantitative fashion. The time scales in which the damage and effects take place are quite different. While radiation damage events take place within a short time period of around  $10^{-11}$  s or less, the radiation effects occur in a relatively large time scale ranging from milliseconds to months. Radiation effects range from the migration of defects to sinks that takes place in milliseconds to changes in physical dimensions due to swelling etc. with much longer duration.

Following are radiation defects induced by intense nuclear radiation, in particular high energy ( $E \geq 0.1\text{MeV}$ ) neutrons: Vacancies, Interstitials, Impurity atoms - produced by transmutation, Thermal spikes - regions with atoms in high energy states, Displacement spikes - regions with displaced atoms, vacancies, self-interstitials (Frenkel pairs) produced by primary and secondary knock-on atoms, Depleted zones - regions with vacancy clusters (depleted atoms). Voids - large

regions devoid of atoms, Bubbles - voids stabilized by filled gases such as He produced from  $(n,\alpha)$  reactions with B, Ni, Fe etc., Replacement collisions - scattered self-interstitial atoms falling into vacant sites after collisions between moving interstitial and stationary atoms and dissipating their energies through lattice vibrations.

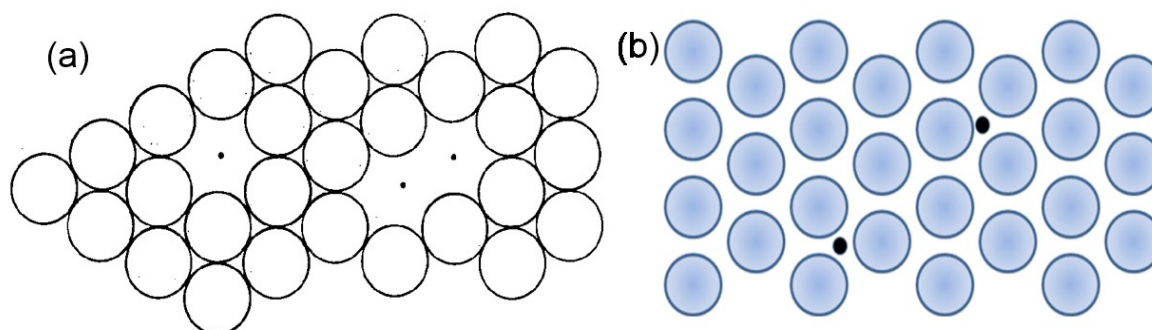


**Figure 2.6** Depiction of vacancies and interstitial

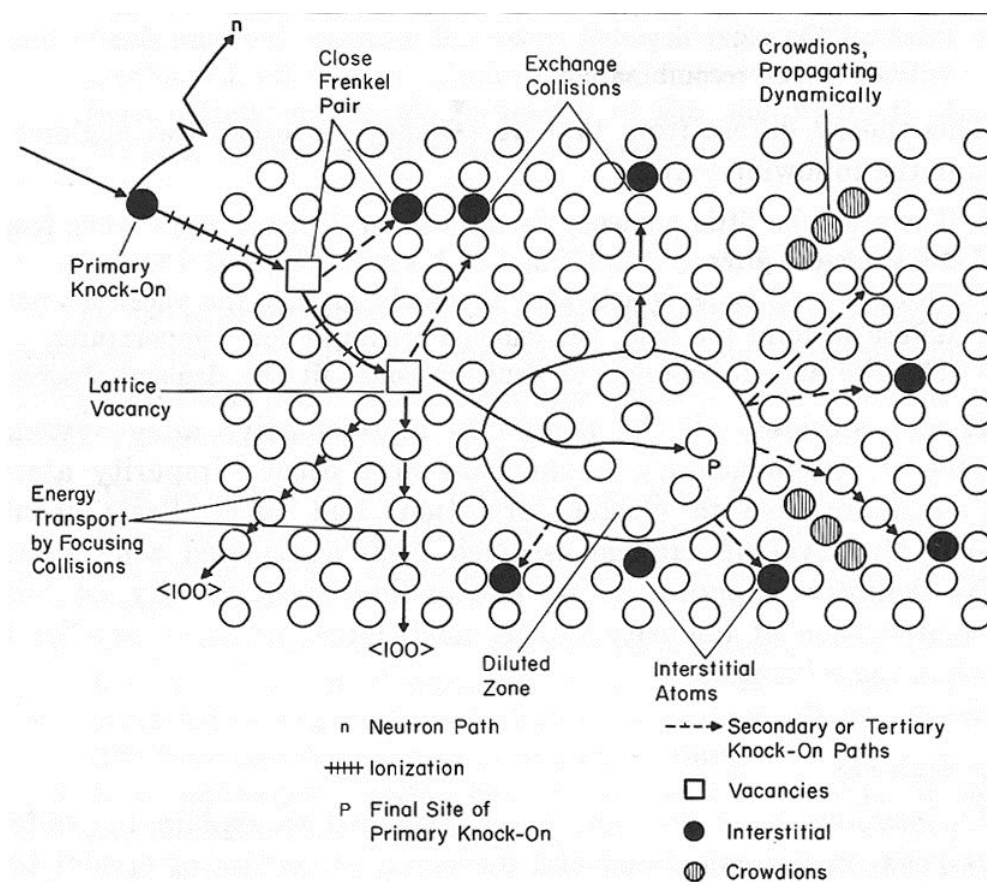


**Figure 2.7** Seeger's refined concept of primary damage events in an FCC metal (1958)

The binding energy of lattice atoms is very small ( $\sim 10-60$  eV) compared to the energy of the impinging particles so that a scattering event between them results in the lattice atom getting knocked off from its position. The atom generally will have such a high energy that it can interact with another lattice atom that will also get knocked off from the lattice position. The atom which was knocked off by the incoming high energy particle is known as 'primary knock-on atom' or PKA which in turn knocks off a large number of atoms before it comes to rest in an interstitial position thereby creating a Frenkel pair in which case the atom is considered to have been 'displaced'. If however the atom is in proximity of a vacancy, it could occupy the vacant lattice position in which case it becomes a 'replacement collision'. Thus in general a PKA can lead to a large number of higher order knock-on atoms (also known as recoil atoms and/or secondary knock-on atoms) resulting in many vacant lattice sites and this conglomeration of point defects is known as 'displacement cascade' (Figure 2.7). A flux of neutrons then results in a large number of PKAs which in turn produce higher order knock on atoms as illustrated in Figure 2.7. If during these collision processes many nuclei go into higher energy states at their lattice position, thermal spike is created. Kinetic aspect in materials is as fundamental and important as atom diffusion. Diffusion can be defined as the effective movement of atoms/molecules relative to their neighbors under the influence of a gradient. The process is assisted by the intrinsic thermal or kinetic energy of atoms. The driving force or the gradient can be of various types. It can be chemical potentials arising from the concentration gradient, or gradients in electrical field, mechanical stresses or even gravitational field. The movement of atoms could be over a large number of interatomic distances (i.e. long range diffusion) or over one or two interatomic distances (i.e. short range diffusion). Although diffusion in liquid and gaseous states is easier to visualize, diffusion of atoms in solids is not so. Diffusion is regarded as one of the most important mechanisms of mass transport in materials. It is again amazing to know how many well-known materials phenomena, and physical property changes are influenced by diffusion. Here are some examples: phase transformations (such as, precipitation), high



temperature creep, high temperature oxidation of metals, metal joining by diffusion bonding, impurity transistors, magnetic property changes, mechanical property changes, grain growth, radiation damage defects and their migration. There are two general ways by which diffusion can be categorized. If one considers diffusion of atoms in a pure metal, the diffusion happens basically between its own lattice atoms. This diffusion is called ‘self-diffusion.’ In the other case, diffusion of alloying elements or impurities may well be occurring in the parent lattice and then the diffusion is termed as ‘hetero-diffusion.’

#### **2.4.2 Radiation Effects and Magnetic Properties**

Energy deposition by ion or neutron irradiation modifies material structure and its physical/chemical properties through defect generation and accumulation (atomic displacements, defect clustering, etc.), amorphization, material decomposition, phase transition, phase segregation, formation of second-phase precipitates and gas species, grain growth, particle aggregation, volumetric change, micro-crack formation, etc. These important microstructural change under neutron irradiation begins with the atomic displacement creating a pair of defects: a self-interstitial and a vacancy, the size of which is known to be the order of several nanometers.<sup>4,5</sup> These defects have a strong interaction with the domain walls. Further modification of the microstructures affects the magnetic properties inevitably. Although, the underlying mechanism for the effects of neutron irradiation on the magnetic characteristics is not comprehensive yet, whatever be the radiation effect, it directly or indirectly affects the magnetic properties as depicted in the Figure 1.8 of Chapter 1 and therefore understanding the effects of radiation on magnetism and magnetic permeability becomes more significant. Material resistance or susceptibility to nuclear radiation depends on its structural stability. It is crucial to study structural changes induced by nuclear irradiation, in particular through magnetic properties, evolution of nanostructures through in-situ methods that provide data to gain physical insights of the basic processes involved in the structural changes.

## **2.5 Conclusion**

This chapter summarizes the principles of radiation including neutron radiation and gives an idea about the existing radiation detection techniques. The signification of detecting radiation through material property changes like magnetic properties are also discussed. Built-in radiation detection and monitoring system in nuclear reactors which are much easy and elegant to work with are so significant to ensure the safety of reactors. Involving nanomaterials and studying in-situ property changes contribute to decode the underlying mechanisms for property changes and helps in successfully creating radiation sensors and monitors thus contributing to the field of nano-nuclear technology. The following chapter gives a summary on the various fields of nano-nuclear technology and the current progress in each of these fields.

## 2.6 References

1. N. Tsoulfanidis, Measurement and Detection of Radiation (Hemisphere Publishing Corporation), Washington 1983
2. G. F. Knoll, Radiation Detection and Measurement (John Wiley & sons) New York 1989
3. [http://en.wikipedia.org/wiki/Neutron\\_detection#Neutron\\_activation\\_detectors\\_civilizationn](http://en.wikipedia.org/wiki/Neutron_detection#Neutron_activation_detectors_civilizationn)
4. O. Akdogan, W. Li, B. Balasubramanian, D. J. Sellmyer, G. C. Hadjipanayis, Adv. Funct. Mater. 2013, 23, 3262.
5. J. S. McCloy, W. Jiang, T. C. Droubay, T. Varga, L. Kovarik, J. A. Sundararajan, M. Kauer, Y. Qiang, E. C. Burks, K. Liu, J. Appl. Phys. 2013, 114, 083903.

## **Chapter 3: Literature Review on Nano-Nuclear Technology**

### **3.1 Introduction**

Nano-Nuclear Technology (NNT) deals with the use of latest engineered-nano-materials on improving the nuclear power performances and safety, bringing advanced materials and technologies for new generations of nuclear power units, and a new advanced civilization. During the course of nuclear technological evolution in the history of mankind, numerous lessons have been learned through many accidents, some more severe than those registered in the other non-nuclear power plants. In light of the recent Fukushima disaster and other similar events, a huge responsibility is laid upon the scientific communities to quicken their progresses, which demand for the utmost safety in the future generation nuclear power plants to avoid such disaster. Scientific communities around the world are working towards achieving it in various ways, among which NNT is an efficient tool and candidate for achieving the goal of utmost safety and performance. A significant contribution in the NNT area would result in the development of new capabilities that could be useful to nuclear energy, which can help build devices to support the development of sustainable nuclear fuel cycles, to control their effects and its implementation in nuclear power. This literature review summarizes the recent and ongoing research in labs around the world on NNT and its capacity for the improvement of future generation nuclear reactors in safety and performance.

### **3.2 Branches of Nano-Nuclear Technology**

Nano-Nuclear Technology addresses the issue of performance and safety from various angles and works from different fields to achieve it. Some of the main focuses are listed below, where the use of nano-particles, nano-structured materials, and/or nano-scale materials, properties, or processes to enhance mechanical, chemical, physical, or thermo-hydraulic properties and performance in nuclear fuel cycle applications, such as:

**Nanostructured-ODS Materials**

- Reactor (in-core) materials like ODS with nano-scale precipitates that could improve mechanical performance as well as radiation tolerance.

**Nano-Scale Coatings**

- Nano-scale coatings that could be included on exterior or interior of fuel cladding to improve corrosion resistance and surface hardening, and pellet-clad interactions on the cladding interior.

**Nanomaterials for Fission Product Capturing**

- Chemical interaction and separation methods using nano-particles and/or nano-porous materials that can enable techniques to capture fission product gases either from reprocessing operations or directly within a reactor fuel assembly thereby reducing the potential for releases from normal or accident conditions.

**Nano-Technology Engineered Fuels**

- Advanced fuels engineered and/or fabricated with nano-technologies to enable longer service lives, reduce fabrication process losses, and/or reduce the potential for failure in normal or accident conditions including increased fission gas retention, plasticity, radiation tolerance, heat transfer capability, as well as reduced fuel cladding chemical and/or mechanical interactions.

**Nano Radiation Sensors, Detectors and Monitors**

- Nano-technology enabled sensors and/or in-service monitors that can directly monitor with enhanced sensitivity for radiation, temperature, pressure, in-situ diagnostics of material properties and mechanical response, corrosion, neutron flux, stress/strain or even chemistry with little effect on system performance with significantly reduced size and weight and increased sensitivity, performance, and functionality.

### 3.2.1 Nanostructured-ODS Materials

Oxide dispersion strengthened alloys (ODS alloys) typically consist of a high temperature metal matrix - such as iron aluminide, iron chromium, iron-chromium-aluminum, nickel chromium or nickel aluminide - with small (5-50 nm) oxide particles of alumina ( $\text{Al}_2\text{O}_3$ ) or Yttria ( $\text{Y}_2\text{O}_3$ ) dispersed within it. ODS alloys exhibit good corrosion resistance and mechanical properties at elevated temperatures. These alloys also show excellent creep resistance, which stems partly from the dispersion of oxide and other particles, and partly from the very large elongated grain structure. The role of ODS-materials for fusion applications was reviewed and concluded by Ukai and Fujiwara<sup>1</sup> and also by Hoelzer<sup>2</sup> that ODS materials are interesting for future nuclear applications and ODS materials have not been considered for High Temperature Reactors (HTRs) so far. Compared with the conventional ODS steels, nanostructured ODS steels shows better performance in radiation resistance, corrosion resistance and tensile strength. With all the promising properties and mechanical stability they are more likely to be considered as serious candidates for future nuclear high temperature applications

Nanostructured ODS alloys have been shown to exhibit excellent creep properties, improved hardness, tensile strength, corrosion resistant, and thermal stability.

- Mechanical creep tests have shown that these alloys offer superior creep properties. For example, a Fe-12Cr-2.5W-0.4Ti-0.25Y<sub>2</sub>O<sub>3</sub> (12YWT) alloy was shown to fail only after 14,500 hours at a very high temperature of 800°C with a 2.3% elongation at a loading stress of 138 MPa. These properties were excellent when compared to a V-4Cr-4Ti alloy that failed after 4,029 hours and 52% elongation also tested at 800°C but at a significantly lower stress of 77 MPa.<sup>3</sup> Y or Y-Ti nanoprecipitates can reduce creep rates by six orders of magnitude at temperatures from 650°C-900°C.<sup>4</sup> The oxide nanoparticles serve for interfacial pinning of moving dislocations. Therefore the creep resistance is improved.

- $Y_2O_3$  is more stable at high temperatures than other oxides like  $Al_2O_3$ ,  $ThO_2$ ,  $SiO_2$ ,  $TiO_2$ , etc. The weight % of  $Y_2O_3$  in ODS alloys is mostly between 0.3 and 0.4 wt.% because only at this % it can maintain both tensile strength and elongation %.<sup>5</sup>
- High temperature strength has been demonstrated by measuring creep response of the ODS alloy in uniaxial tension at 650 °C and 900 °C in an inert atmosphere chamber. Results of tests at 900°C demonstrate that this alloy has creep properties similar to other alloys of similar design and can be considered for use in high temperature fusion power system designs. The alloy selection process, materials production, microstructural evaluation and creep testing are described. Hardness remains very high even following a 1200 °C annealing treatment indicating a highly stable microstructure.<sup>6</sup>
- Experimental ODS steels, 12Y1 (nominally Fe–12Cr–0.25Y) and 12YWT (Fe–12Cr–3W–0.4Ti–0.25 $Y_2O_3$ ) when compared with commercial ODS steels like MA956 (Fe–20Cr–4.5Al–0.33Ti–0.5 $Y_2O_3$ ), MA957 (Fe–14Cr–0.3Mo–1Ti–0.25 $Y_2O_3$ ), and PM 2000 (Fe–19Cr–5.5Al–0.5Ti–0.5 $Y_2O_3$ ) show a significant variation in the yield stress and ultimate tensile strength for tests at room temperature to 800 °C. The 12YWT was much stronger than the 12Y1. Of the commercial steels, MA957 was the strongest with properties similar to those of 12YWT. The MA956 was the weakest of the commercial steels; it was also weaker than 12Y1 below 650 °C. 12YWT had better creep rupture properties than MA956 and MA957 for high stresses and low Larson–Miller values. The reason for the similar tensile and creep behavior of MA957 and 12YWT was concluded to be the distribution of nano-sized particles rich in Y, Ti, and O observed by TEM and atom probe studies on the two steels. Although it was postulated that the excellent long-term, high temperature creep properties of MA956 and PM 2000 was also due to the presence of a fine distribution of nano-size particles, more work is in progress to verify this.<sup>7</sup>

- A new high chromium Ferritic ODS material for high temperature nuclear applications with the chemical composition, Fe–13/18CrWTi ODS has been slightly modified by including nanoclusters to reach the specifications of the materials used for fusion reactors. The microstructure is homogeneous and constituted by very fine grains elongated in the hot extrusion direction and nano-clusters also are observed within the matrix. The mechanical properties show a high tensile strength up to 750 °C with the expected ductility for this type of material.<sup>8</sup>
- ODS materials for structure application in fusion reactor would allow increasing the operating temperature to approximately 650 °C. In order to optimize of metallurgical features to improve high temperature strength and elongation through understanding of contents of Cr and Al the study of ODS steels with Y<sub>2</sub>O<sub>3</sub> content of 0.37wt% have been performed. Tensile test performed on these ODS Ferritic/Martensitic steel between room temperature (RT), 300, 400 and 600 °C shows that dispersion hardening plays a vital role to improve the mechanical properties at elevated temperature, as they are foreseen in the future fusion reactor. It has been successfully demonstrated that it is possible to expand the temperature range for the application of fusion reactor and ODS steels possess high temperature strength by maintaining the ductility even at elevated temperatures.<sup>9</sup>
- Irradiation creep of Ferritic 20% Cr ODS alloys investigated in the temperature range 300–500 °C and microstructural investigations revealed the most interesting finding that size and distribution of nano size dispersoids did show a little influence on the irradiation creep behavior. Moreover, irradiation creep does not show strong temperature dependence. For temperatures up to 500 °C creep and relaxation behavior of components are dominated by irradiation creep. The expected irradiation creep compliances under neutron irradiation to higher doses is lower than under the irradiation conditions in this investigation, and so



irradiation creep can be considered of technical relevance in advanced fast fission reactors and fusion plants.<sup>10</sup>

Thus there are many strong evidences in the publications that the nano structured dispersoids dispersed in the Ferritic/Martensitic steels show improved mechanical properties and radiation resistance based on the size of the particles and distribution of the particles in the matrix. More research has to be done in this area to commercialize and globalize this kind of ODS materials for nuclear applications.

### 3.2.2 Nano-Scale Coatings

A number of literatures have reported that using nanostructured powders as feedstock powders in mechanical milling process, various nanostructured coatings can be successfully synthesized and these coatings exhibits improved performance and mechanical properties compared to the conventional powders.<sup>11</sup> While process parameters and post-sprayed treatment can partially influence mechanical and physical properties of nanostructured coatings, it has been found that nanostructured coatings primly increase hardness,<sup>11,12,13</sup> scratch resistance,<sup>11</sup> reduced coefficient of friction,<sup>12</sup> high fracture toughness,<sup>13</sup> corrosion resistance,<sup>14</sup> and increased thermal stability.<sup>15</sup>

- J. He et al.<sup>11</sup> reported that the average micro-hardness of the nanostructured  $\text{Cr}_3\text{C}_2$ -25 (Ni20Cr) coating, taken on the cross-section, increases from a value of 846 for the conventional  $\text{Cr}_3\text{C}_2$ -25 (Ni20Cr) coating for the nanostructured coating. Hence the nanostructured coating exhibits a 20.5% increase in micro-hardness as compared with the corresponding conventional coating. It has been reported that the hardness of nanostructured materials often exhibits a two- to five-fold increase in hardness compared with that of the conventional materials.<sup>13</sup> Kear and McCandlish also indicated the nanostructured WC-23% Co coatings with a higher hardness than a conventional coating of the same composition.<sup>12</sup> The high hardness of the nanostructured  $\text{Cr}_3\text{C}_2$ -NiCr coatings results primarily from two aspects:

1. Uniformity of microstructure
  2. The intrinsically high hardness of nanostructured phases.
- In related studies on conventional and nanostructured Cr<sub>3</sub>C<sub>2</sub>-25 (Ni20Cr) coatings, the friction coefficient and scratch-resistance of coatings improved in nanostructured coatings.<sup>14</sup> The as-sprayed conventional coating produced an average scratch depth of approximately 100 μm, whereas a depth of around 50 μm was found in the as-sprayed nanostructured coating. Thus, the nanostructured coating exhibits a scratch resistance that is twice that of the conventional one.
  - Coefficient of friction of 0.495 and 0.216 were obtained for the conventional and nanostructured coatings, respectively.<sup>14</sup> Compared with the coefficient of friction in the as-sprayed conventional coating, a reduced coefficient of friction was observed in the as-sprayed nanostructured coating. A decreased friction coefficient was also observed in a nanostructured WC-23% Co coating.<sup>12</sup>
  - In the process of indentation test, at a load of 500 g, a few cracks around the indentation were still observed in the conventional coating, whereas none were present in the nanostructured coating.<sup>11</sup> These results suggest that the nanostructured Cr-NiCr coating possess a higher apparent fracture toughness relative to that of the conventional material.
  - It has also been reported that the presence of nanostructured coating improved the thermal stability of the materials.<sup>15-21</sup>

### 3.2.3 Nanomaterials for Fission Product Capturing

Capturing fission product either from reprocessing operations or directly within a reactor fuel assembly is of prime importance because it can prevent potential danger of material failure and thus can avoid accidents. There is worldwide interest in the effective capture and storage of radioiodine,

as it is both produced from nuclear fuel reprocessing and also commonly released in nuclear reactor accidents.

- Recently in 2012, Dorina F. Sava *et al.*<sup>22</sup> reported the detailed structural evidence of captured molecular iodine ( $I_2$ ), a volatile gaseous fission product, within the metal-organic framework ZIF-8 [zeolitic imidazolate framework-8 or  $Zn(2\text{-methylimidazolate})_2$ ]. Additional tests indicated that extruded ZIF-8 pellets perform on par with ZIF-8 powder and are industrially suitable for  $I_2$  capture.  $I_2$  capture within ZIF-8 was studied with a combination of experiments and molecular simulations. The results suggest that  $I_2$  adsorption is mainly due to favorable interactions with the ZIF-8 framework, which consists of tetrahedrally coordinated Zn atoms linked by 2-methylimidazole. This study acknowledges that ZIF-8 is a highly appropriate capture and interim storage medium for volatile gaseous  $I_2$ . Additionally, the material maintains its high adsorption capacity in extruded pellet form, which is a desired feature, as this is the typical form for porous adsorbents in currently employed separation processes). This study can increase awareness and impact the use of Metal-Organic Framework in the capture of related fission product gases.
- In 2012, K. W. Chapman *et al.*<sup>23</sup> investigated the effective way for capturing  $I_2$  using silver-containing Zeolites Mordenite (MOR). The capture of  $I_2$  by both silver-exchanged and reduced silver MOR was investigated. A differential pair distribution function (d-PDF) study of  $I_2$ -treated silver-containing MOR was used to probe the structure and distribution of the supported AgI (the iodine-capture vehicle). The structure and distribution of the AgI formed when iodine is captured by silver-containing MOR depends on whether the silver is reduced. The reduced  $Ag^0$  stays on the surface of the Zeolite, captures  $I_2$  to form 3 nm AgI nanoparticles and then migrates to the center of the pores and in this case mobility depends on Ag and I. For the unreduced silver-exchanged MOR, since the sub nanometer AgI

clusters is formed inside and confined to the pores. Encouragingly, this may represent a more secure route for radioactive iodine capture, with the possibility of using pore-blocking to further trap the iodine for long-term storage. Separate to the relevance of these materials for radiological gas capture and long-term storage, the data also provide exciting new possibilities in the field of nanoscaled ionic conductors. Previous studies have shown that the progressive reduction in AgI particle size toward the nanoscale not only stabilizes the superionic R-phase but also produces orders of magnitude enhancement in the ionic conductivity. The sub nanometer particles documented here may yield further large gains in conductivity.

- Researchers at Pacific Northwest National Laboratory<sup>24</sup> have developed novel nanoporous functionalized chemisorbents, which shows enhanced properties compared to the conventional chemisorbents. These self-assembled monolayers on mesoporous supports (SAMMS), functionalized with similar reactive surfaces as the conventional resins, can afford exceptional high sorption capacities without significant loss in flow characteristics during large volume sampling. Some of the surface chemistries have been shown to perform well under a wide range of environmental conditions, particularly in waters with high ionic strength.
- B. E. Johnson *et al.*<sup>25</sup> compared the capture performance of novel nanostructured sorbents with the conventional chemisorbents in both fresh, riverine, and saline, oceanic, waters. In most cases, the nanoporous sorbents demonstrated enhanced retention of analytes. Salinity had significant effects upon sorbent performance and was most significant for hard cations, specifically Cs and Ba. In most cases, novel self-assembled monolayers on mesoporous supports (SAMMS) chemisorbents attained higher  $K_D$ . It afforded the high distribution coefficients for ionic forms of Co, Zr, Nb, and Te and also showed excellent retention of the soft metal, Ag. Ionic strength was observed to limit performance of chemisorbents, while

effects due to the presence of natural organics were minimal for all analytes with the exception of Ba.

- Similar to investigation of Dorina F. Sava *et al*, K. W. Chapman *et al*.<sup>26</sup> also investigated the capturing of I<sub>2</sub> within the metal-organic framework ZIF-8. They found out that the release of guest species from within a nanoporous metal-organic framework (MOF) has been inhibited by amorphization of the guest-loaded framework structure under applied pressure.

Thermogravimetric analyses have shown that by amorphizing ZIF-8 following sorption of I<sub>2</sub>, the pore apertures in the framework are sufficiently distorted to kinetically trap I<sub>2</sub> and improve I<sub>2</sub> retention. Pair distribution function (PDF) analysis indicates that the local structure of the captive I<sub>2</sub> remains essentially unchanged upon amorphization of the framework, with the amorphization occurring under the same conditions for the vacant and guest-loaded framework. This mechanical modification through pressure can be applied at any point in a sorption-sequestration process. Consequently, pressure-induced structural changes can be used as a macro scale handle with which to control the nanoscale sorption properties. Specifically, they can be used for increasing hysteresis in the sorption-desorption kinetics, at will, to kinetically trap I<sub>2</sub>. Potential applications, beyond the capture of radioisotopes, include the controlled release of agrochemicals.

Thus the involvement of nanomaterials like nanoporous and nanoparticles for fission product capturing exhibits enhanced capturing behavior and long life.

### **3.2.4 Nano-Technology Engineered Fuels**

The basic research progress in nanomaterials and nanotechnologies for advanced nuclear fuel fabrication, spent nuclear fuel reprocessing, nuclear waste disposal and nuclear environmental remediation is selectively highlighted in this section.

- Wu *et al.*<sup>27,28</sup> synthesized high quality, colloidal uranium oxide nanocrystals by thermal decomposition of uranyl acetylacetonate in a mixture solution of oleic acid (OA), oleylamine (OAm), and octadecene. This synthesis showed characteristic high reaction-yield of 75% and high reproducibility. X-ray powder diffraction confirmed that the nanocrystals were pure uranium-dioxide. The transmission electron microscopy (TEM) showed that periodical pore structures with diameters in the nanometer scale were available within the nanocrystals. It was also found that the size of the nanoparticles and the pore size could be controlled by changing the ratio of the organic additives in the reactions. This work is of high significance because these  $\text{UO}_3$  nanocrystals could be developed as a candidate of potential nano-fuels. The evenly distribute pores might adsorb and accommodate the highly reactive fission products such as iodine which can react with the clad under extreme conditions, and then mitigate fuel-clad or other undesirable chemical interactions. Furthermore, this microstructure can hopefully enhance the thermal and radiation stability of the fuel and consequently improve its burn-up.
- Wang *et al.*<sup>29</sup> synthesized sphere-shaped  $\text{UO}_2$  nanoparticle (100 nm) consisting of 15 nm nanocrystals and single nanorods (diameter 80–100 nm and length 500–1500 nm) under hydrothermal conditions. By adjusting the re-action conditions such as the volume ratio of the solvent and the reducing agent, the size and morphology of the uranium dioxide nanostructures varied to a certain degree. TEM revealed that the  $\text{U}_3\text{O}_8$  nanorods grew along the crystallographic [001] direction. The  $\text{UO}_2$  nanoparticles could be converted to porous  $\text{U}_3\text{O}_8$  aggregates through thermal treatment in air. TEM images also showed the availability of irregular macropores in the aggregates, which were formed from the inter-growth of nanocrystals. It is reasonable to believe that porous aggregates of  $\text{U}_3\text{O}_8$  are more preferred from nuclear fuel point of view. Another merit of porous uranium oxides might lie in their applications in the fabrication of transmutation fuel. Normally, to prevent generation and

diffusion of strong radioactive dust, wet-methods are favored for the fabrication of transmutation fuel. As porous materials show substantial adsorption ability for minor actinides (MA), porous uranium oxides adsorbed with MA can then be directly fabricated into transmutation fuel.

- W-Q Shi *et al.*<sup>30</sup> in their review paper “Nanomaterials and nanotechnologies in nuclear energy chemistry” discussed in detail the various basic research progresses in nanomaterials and nanotechnologies for advanced nuclear fuel fabrication, spent nuclear fuel reprocessing.

### **3.2.5 Nanotechnology Enabled Sensors, Detectors and Monitors**

Nano-technology enabled sensors and/or in-service monitors that can directly monitor for radiation, temperature, pressure, in situ diagnostics of material properties and mechanical response, corrosion, neutron flux, stress/strain or even chemistry with little effect on system performance with significantly reduced size and weight and increased sensitivity, performance, and functionality.

Nanotechnology-based detectors that can discriminate between neutron and gamma radiation and/or have enhanced sensitivity for the detection of fissile materials with very low neutron activation fluxes.

- J. W. Murphy *et al.*<sup>31</sup> investigated on finding the optimal thickness of a semiconductor diode for thin-film solid state thermal neutron detectors. They investigated a coplanar diode/converter geometry, to determine the minimum semiconductor thickness needed to achieve maximum neutron detection efficiency. They kept the semiconductor thickness to a minimum, gamma rejection as high as possible. In this way, we optimize detector performance for different thin-film semiconductor materials. Based on their simulations, they were able to provide a range of diode thicknesses and materials to design an optimal neutron. Diamond and ZnO render the greatest stopping power for charged particles, typically requiring only half the thickness of Si to achieve maximum intrinsic thermal

neutron detection efficiency. They found out that Si possesses the best gamma rejection capability for a given thickness, even greater than that of diamond.

- Detecting radiation based on magnetic properties also has gained more ambience recently and it could be a good non-destructive testing techniques. D. G. Park *et al.*<sup>32</sup> reported that the coercive force of B-H loop showed a slow change up to a neutron dose of  $10^{14}$  n/cm<sup>2</sup> and increased by 15.4% for a  $10^{16}$  n/cm<sup>2</sup> dose sample compared with that of the unirradiated one, related to the domain wall motion hindered by the increased defects. However, the amplitude of Barkhausen noise reflecting the wall motion decreased slowly up to  $10^{14}$  n/cm<sup>2</sup> irradiation, followed by a rapid decrease of 37.5% at  $10^{16}$  n/cm<sup>2</sup>. The results indicate that the Barkhausen noise is more sensitive to the damage of neutron irradiation than conventional magnetic properties, such as maximum induction, coercive force and remanence.
- W. Jiang *et al.*<sup>33</sup> reported that the Fe<sub>3</sub>O<sub>4</sub> nanoparticle granular films, which were initially superparamagnetic, became magnetized following Si<sup>2+</sup> ion irradiation of fluence  $10^{16}$  ions/cm<sup>2</sup>. It was reported that a significant increase in the grain size and a dramatic change in the microstructure were observed and these films represent a new class of semi disordered magnetite materials for study, which could lead to important applications of this type of material in various areas, including radiation detection and monitoring.
- S.Ašmontas *et al.*<sup>34</sup> reported the used of semiconductor nanostructures for microwave and terahertz radiation.
- E. Tupitsyn *et al.*<sup>35</sup> reported the use of single crystals of semiconductor-grade lithium indium selenide (LiInSe<sub>2</sub>) for detecting neutron irradiation. Nuclear radiation devices were fabricated, and alpha particle detection was observed, suggesting particle detection was observed, suggesting that this material could be a candidate for neutron detection application. The crystal showed a high bulk resistivity suitable for nuclear radiation detection. Photocurrent is well pronounced at 445 nm and suggests good generation rate and



mobility of the charge carriers. The LiInSe<sub>2</sub> crystal showed a response to alpha particles radiation and could be a possible candidate for neutron detector. It was reported that further improvement of crystal quality and understanding of defect structure may significantly improve alpha particle detection.

### **3.3 Conclusion**

The creation of various novel nanostructured devices for Nano-Nuclear Technology comes from the tremendous basic research needs for the future advanced nuclear energy system. This review is highlighting a variety of studies that provide new insights into the nanostructures and behaviors of solid-state actinides and novel nanomaterials, which can be used for design and fabrication of new nuclear fuels, fission product capturing, radiation resistant materials like ODS, corrosion resistant nano coatings, nanomaterials for environmental remediation, and radiation detection and sensing. These ranges of approaches will benefit the development of a sophisticated understanding of structure-property relationships in nanoscale clusters. Such an understanding will be incorporated into future attempts to design nanomaterials for specific purposes, such as applications in future advanced fuel cycles. In all, from the above descriptions, we can definitely conclude that nanomaterials and nanotechnologies have diverse potential applications in various aspects of nuclear energy. No doubt, they will play important roles in future advanced nuclear energy systems. However, from the point of view of current international research status, nanomaterials and nanotechnologies in the field of nuclear energy are still in their infancy, there are still huge key scientific issues that should be addressed. With the deepening of the further research work, the advantages of nanomaterials and nanotechnologies will be found out step by step. The contribution of this research to the field of nano-nuclear technology including synthesis, characterization, data analysis and summary are discussed in further chapters.

### 3.4 References

1. Ukai, S. and M. Fujiwara, Perspective of ODS alloys application in nuclear environments. *Journal of Nuclear Materials*, 2002. 307: p. 749-757.
2. D.T. Hoelzer, Contributors: G.R. Odette, M.J. Alinger, D.S. Gelles A.F. Rowcliffe, R.L. Klueh, B.A. Pint, P.J. Mazias: Advanced Alloy Systems, Fusion Materials Science peer review August 27-28, 2001, University of California-Santa Barbara, [http://www.fusionmaterials.pnl.gov/peerreview/hoelzer\\_advanced.pdf](http://www.fusionmaterials.pnl.gov/peerreview/hoelzer_advanced.pdf)
3. R. L. Klueh *et al.*, "Tensile and Creep Properties of an Oxide Dispersion-Strengthened Ferritic Steel," *J. Nucl. Mat.* **307-311**, 773 (2002).
4. A Hirata *et al.*, "Atomic Structure of Nanoclusters in Oxide-Dispersion-Strengthened Steels." *Nature Mat.* **10**, 922 (2011).
5. Ukai et al., *J Nucl. Mater.* 204 (1993) 65-73.
6. D. K. Mukhopadhyay, F. H. Froes, and D. S. Gelles, "Development of oxide dispersion strengthened ferritic steels for fusion," *Journal of Nuclear Materials*, vol. 258–263, pp. 1209–1215, Oct. 1998.
7. R. L. Klueh, J. P. Shingledecker, R. W. Swindeman, and D. T. Hoelzer, "Oxide dispersion-strengthened steels: A comparison of some commercial and experimental alloys," *Journal of Nuclear Materials*, vol. 341, no. 2–3, pp. 103–114, May 2005.
8. Y. de Carlan, J.-L. Bechade, P. Dubuisson, J.-L. Seran, P. Billot, A. Bougault, T. Cozzika, S. Doriot, D. Hamon, J. Henry, M. Ratti, N. Lochet, D. Nunes, P. Olier, T. Leblond, and M. H. Mathon, "CEA developments of new ferritic ODS alloys for nuclear applications," *Journal of Nuclear Materials*, vol. 386–388, pp. 430–432, Apr. 2009.
9. H. K. Yoon and A. Kimura, "High Temperature Strength of Three ODS Ferritic/ Martensitic Steels," *Key Engineering Materials*, vol. 345–346, pp. 1011–1014, 2007.
10. J. Chen and W. Hoffelner, "Irradiation creep of oxide dispersion strengthened (ODS) steels for advanced nuclear applications," *Journal of Nuclear Materials*, vol. 392, no. 2, pp. 360–363, Jul. 2009.
11. J. He and J. M. Schoenung, "Nanostructured coatings," *Materials Science and Engineering: A*, vol. 336, no. 1–2, pp. 274–319, Oct. 2002.
12. [12] B. H. Kear and L. E. McCandlish, "Chemical processing and properties of nanostructured WC-Co materials," *Nanostructured Materials*, vol. 3, no. 1–6, pp. 19–30, Jan. 1993.
13. D. A. Konstantinidis and E. C. Aifantis, "On the 'Anomalous' hardness of nanocrystalline materials," *Nanostructured Materials*, vol. 10, no. 7, pp. 1111–1118, Jan. 1998.
14. J. He, M. Ice, and E. J. Lavernia, "Synthesis of nanostructured Cr<sub>3</sub>C<sub>2</sub>-25(Ni<sub>20</sub>Cr) coatings," *Metallurgical and Materials Transactions A*, vol. 31, no. 2, pp. 555–564, Feb. 2000.

15. L. Hultman and C. Mitterer, "Thermal Stability of Advanced Nanostructured Wear-Resistant Coatings," in *Nanostructured Coatings*, A. Cavaleiro and J. T. M. Hosson, Eds. New York, NY: Springer New York, pp. 464–510.
16. E. J. Lavernia, M. L. Lau, and H. G. Jiang, "Thermal Spray Processing of Nanocrystalline Materials," in *Nanostructured Materials*, G.-M. Chow and N. I. Noskova, Eds. Dordrecht: Springer Netherlands, 1998, pp. 283–302.
17. R. Birringer, "Structure of Nanostructured Materials," in *Nanophase Materials*, G. C. Hadjipanayis and R. W. Siegel, Eds. Dordrecht: Springer Netherlands, 1994, pp. 157–180.
18. Y. Zhang, M. Ishimaru, T. Varga, T. Oda, C. Hardiman, H. Xue, Y. Katoh, S. Shannon, and W. J. Weber, "Nanoscale engineering of radiation tolerant silicon carbide," *Physical Chemistry Chemical Physics*, vol. 14, no. 38, p. 13429, 2012.
19. A. Raveh, I. Zukerman, R. Shneck, R. Avni, and I. Fried, "Thermal stability of nanostructured superhard coatings: A review," *Surface and Coatings Technology*, vol. 201, no. 13, pp. 6136–6142, Mar. 2007.
20. D. Mercier, B. D. Gauntt, and M. Brochu, "Thermal stability and oxidation behavior of nanostructured NiCoCrAlY coatings," *Surface and Coatings Technology*, vol. 205, no. 17–18, pp. 4162–4168, May 2011.
21. A. Fabrizi, M. Cabibbo, R. Cecchini, S. Spigarelli, C. Paternoster, M. Haidopoulos, and P. V. Kiryukhantsev-Korneev, "Thermal Stability of Nanostructured Coatings," *Materials Science Forum*, vol. 653, pp. 1–22, Jun. 2010.
22. D. F. Sava, M. A. Rodriguez, K. W. Chapman, P. J. Chupas, J. A. Greathouse, P. S. Crozier, and T. M. Nenoff, "Capture of Volatile Iodine, a Gaseous Fission Product, by Zeolitic Imidazolate Framework-8," *Journal of the American Chemical Society*, vol. 133, no. 32, pp. 12398–12401, Aug. 2011.
23. K. W. Chapman, P. J. Chupas, and T. M. Nenoff, "Radioactive Iodine Capture in Silver-Containing Mordenites through Nanoscale Silver Iodide Formation," *Journal of the American Chemical Society*, vol. 132, no. 26, pp. 8897–8899, Jul. 2010.
24. G. E. Fryxell, Y. Lin, S. Fiskum, J. C. Birnbaum, H. Wu, K. Kemner, and S. Kelly, "Actinide Sequestration Using Self-Assembled Monolayers on Mesoporous Supports," *Environmental Science & Technology*, vol. 39, no. 5, pp. 1324–1331, Mar. 2005.
25. B. E. Johnson, P. H. Santschi, R. Shane Addleman, M. Douglas, J. D. Davidson, G. E. Fryxell, and J. M. Schwantes, "Collection of fission and activation product elements from fresh and ocean waters: A comparison of traditional and novel sorbents," *Applied Radiation and Isotopes*, vol. 69, no. 1, pp. 205–216, Jan. 2011.
26. K. W. Chapman, D. F. Sava, G. J. Halder, P. J. Chupas, and T. M. Nenoff, "Trapping Guests within a Nanoporous Metal–Organic Framework through Pressure-Induced Amorphization," *Journal of the American Chemical Society*, vol. 133, no. 46, pp. 18583–18585, Nov. 2011.

27. H. Wu, Y. Yang, and Y. C. Cao, "Synthesis of Colloidal Uranium–Dioxide Nanocrystals," *Journal of the American Chemical Society*, vol. 128, no. 51, pp. 16522–16523, Dec. 2006.
28. S. Mantoura, "Uranium dioxide: Nano goes nuclear," *Nature Nanotechnology*, Dec. 2006.
29. Q. Wang, G.-D. Li, S. Xu, J.-X. Li, and J.-S. Chen, "Synthesis of uranium oxide nanoparticles and their catalytic performance for benzyl alcohol conversion to benzaldehyde," *Journal of Materials Chemistry*, vol. 18, no. 10, p. 1146, 2008.
30. W.-Q. Shi, L.-Y. Yuan, Z.-J. Li, J.-H. Lan, Y.-L. Zhao, and Z.-F. Chai, "Nanomaterials and nanotechnologies in nuclear energy chemistry," *Radiochimica Acta*, vol. 100, no. 8–9, pp. 727–736, Aug. 2012.
31. J. W. Murphy, G. R. Kunnen, I. Mejia, M. A. Quevedo-Lopez, D. Allee, and B. Gnade, "Optimizing diode thickness for thin-film solid state thermal neutron detectors," *Applied Physics Letters*, vol. 101, no. 14, p. 143506, 2012.
32. D. G. Park, C. G. Kim, H. C. Kim, J. H. Hong, and I. S. Kim, "Effect of neutron irradiation on magnetic properties in the low alloy Ni-Mo steel SA508-3," *Journal of Applied Physics*, vol. 81, no. 8, p. 4125, 1997.
33. W. Jiang, J. McCloy, A. Lea, J. Sundararajan, Q. Yao, and Y. Qiang, "Magnetization and susceptibility of ion-irradiated granular magnetite films," *Physical Review B*, vol. 83, no. 13, Apr. 2011.
34. Asmontas, S. Vilnius, Kazlauskaitė, V. ; Suziedelis, A. ; Gradauskas, J. ; Sirmulis, E. ; Derkach, V., Microwave Conference, 2009. EuMC 2009. European, Sept. 29 2009-Oct. 1 2009 (1650 - 1653) - Conference Publications
35. E. Tupitsyn, P. Bhattacharya, E. Rowe, L. Matei, M. Groza, B. Wiggins, A. Burger, and A. Stowe, "Single crystal of LiInSe<sub>2</sub> semiconductor for neutron detector," *Applied Physics Letters*, vol. 101, no. 20, p. 202101, 2012.
36. P. Esquinazi, D. Spemann, R. Höhne, A. Setzer, K.-H. Han, and T. Butz, "Induced Magnetic Ordering by Proton Irradiation in Graphite," *Physical Review Letters*, vol. 91, no. 22, 2003.
37. S. Talapatra, P. Ganesan, T. Kim, R. Vajtai, M. Huang, M. Shima, G. Ramanath, D. Srivastava, S. Deevi and P. Ajayan, "Irradiation-Induced Magnetism in Carbon Nanostructures," *Physical Review Letters*, vol. 95, no. 9, 2005.
38. C. Dorleans, J. Stoquert, C. Estournes, J. Grob, D. Muller, J. Guille, M. Richardplouet, C. Cerruti and F. Haas, "Elongated Co nanoparticles induced by swift heavy ion irradiations," *Nuclear Instruments and Methods in Physics Research Section B: Beam Interactions with Materials and Atoms*, vol. 216, pp. 372-378, 2004.
39. J. P. Nozières, M. Ghidini, N. M. Dempsey, B. Gervais, D. Givord, G. Suran and J.M.D. Coey, "Swift heavy ions for magnetic nanostructures," *Nuclear Instruments and Methods in Physics Research Section B: Beam Interactions with Materials and Atoms*, vol. 146, no. 1-4, pp. 250-259, 1998.

40. L. Jacobsohn, J. Thompson, Y. Wang, A. Misra, R. Schulze, and M. Nastasi, "Effects of ion irradiation on cobalt nanocomposite," *Nuclear Instruments and Methods in Physics Research Section B: Beam Interactions with Materials and Atoms*, vol. 250, no. 1-2, pp. 201-205, 2006.
41. J. Ferré, "Irradiation induced effects on magnetic properties of Pt/Co/Pt ultrathin films," *Journal of Magnetism and Magnetic Materials*, vol. 198-199, no. 1-3, pp. 191-193, 1999.
42. P. K. Kulriya, B.R. Mehta, D.K. Avasthi, D.C. Agarwal, P. Thakur, N.B. Brookes, A.K. Chawla and R. Chandra, "Enhancement of ferromagnetism in Pd nanoparticle by swift heavy ion irradiation," *Applied Physics Letters*, vol. 96, no. 5, p. 053103, 2010.
43. C. Gavade, N. L. Singh, D. K. Avasthi, and A. Banerjee, "Effect of SHI on dielectric and magnetic properties of metal oxide/PMMA nanocomposites," *Nuclear Instruments and Methods in Physics Research Section B: Beam Interactions with Materials and Atoms*, vol. 268, no. 19, pp. 3127-3131, 2010.
44. G. H. Jaffari, A. Ceylan, C. Ni, and S. I. Shah, "Enhancement of surface spin disorder in hollow NiFe<sub>2</sub>O<sub>4</sub> nanoparticles," *Journal of Applied Physics*, vol. 107, no. 1, p. 013910, 2010.
45. E. O. Kirkendall and A. D. Smigelskas, "Diffusion of Zinc in Alpha Brass," *AIME Transactions*, vol. 171, pp. 130-142, 1947.
46. A. Heilmann, A. D. Muller, J. Werner, and F. Muller, "Electron beam initiated oxidation and coalescence of metal particles embedded in a plasma-polymer thin film matrix," *Thin Solid Films*, vol. 270, no. 1-2, pp. 351-355, 1995.
47. C. Wang, D. Baer, J. Amonette, M. Engelhard, J. Antony, and Y. Qiang, "Electron beam-induced thickening of the protective oxide layer around Fe nanoparticles," *Ultramicroscopy*, vol. 108, no. 1, pp. 43-51, 2007.
48. C. Wang, D. R. Baer, J. E. Amonette, M. H. Engelhard, J. Antony, and Y. Qiang, "Morphology and Electronic Structure of the Oxide Shell on the Surface of Iron Nanoparticles," *Journal of the American Chemical Society*, vol. 131, no. 25, pp. 8824-8832, 2009.
49. C. M. Wang, D. R. Baer, J. E. Amonette, M. H. Engelhard, Y. Qiang, and J. Antony, "Morphology and oxide shell structure of iron nanoparticles grown by sputter-gas-aggregation," *Nanotechnology*, vol. 18, no. 25, p. 255603, 2007.

## **Chapter 4: Synthesis and Characterization of Thin Films and Granular Films**

### **4.1 Nanocluster Deposition System**

The origin of the cluster source aggregation system dates back to 1990s when Dr. H. Haberland, Dr. You Qiang and other co-workers developed the techniques of combining the magnetron sputtering with gas-aggregation to form a stable cluster beam with a high degree of ionization.<sup>1,2,3,4</sup> After this initial finding, the technique has been adopted in many laboratories worldwide. Dr. You Qiang, being one of the contributors for the initial design, later improved the design and established the third generation nanocluster source-deposition system. The description of the system and cluster preparation techniques can also be found in the published literatures.<sup>5,6,7</sup> This third generation nanocluster source-deposition system has three main chambers: the aggregation chamber, reaction chamber and deposition chamber. Inside the aggregation chamber is the cluster source, or the sputtering gun, which works on the principle of high pressure magnetron sputtering. On sputtering, the target mounted in the sputtering gun releases metal atoms, which aggregate together in chilled-water-cooled aggregation chamber, to form the nanoclusters. The reaction chamber enables nanoclusters to react with the gases. Also, the reaction chamber is connected to the load lock chamber, which helps in loading and unloading the substrates, on which the nanoclusters safely land. The nanoclusters can either be collected in the load lock chamber or the deposition chamber. The advantage of the deposition chamber is that a negative voltage can be applied to the silicon substrate. This voltage accelerates the deposition of the nanoclusters and the charged clusters can be energetically landed on the substrate and deformed to prolate shape, which in turn could exhibit anisotropic behavior. Five different gases, namely Argon (Ar), Helium (He), Nitrogen (Ni), Oxygen (O<sub>2</sub>) and Hydrogen (H<sub>2</sub>) can be supplied into the aggregation and reaction chamber at a time for the benefit of sputtering and reaction with nanoclusters. Argon, Helium, Oxygen and Nitrogen are the most commonly used gases in the cluster source deposition system. Of these gases, Argon and Helium gases serve the purpose of sputtering and aggregation inside the aggregation chamber.

Oxygen and Nitrogen, can be supplied either into the aggregation chamber to form the fully oxidized or fully nitrated nanoclusters or into the reaction chamber to form the core shell nanoparticles. The system produces high purity nanoparticles with narrow size distribution, which can be controlled by the argon/helium gas ratio, pressure inside the aggregation chamber, temperature inside aggregation chamber and aggregation distance. The major factor for the preparation of high purity nanoparticles is that all the chambers are maintained at high vacuum ( $10^{-7}$  Torr) by three Turbo Molecular Pumps-Mechanical pump systems, which constantly create a vacuum, and the gases utilized for sputtering and reactions have ultra-high purity (99.995%). Every chamber is equipped with two pressure gauges, namely low vacuum pressure gauges and high vacuum pressure gauges, which accurately read the pressure inside the chambers. The gas flow rates into the chambers are controlled by a MKS mass flow controller, which can control the flow from 1 sccm to 1000 sccm for Helium and Argon gases. For the Oxygen and Nitrogen gas flow, a mass flow controller (MKS Inc) was used to control the flow from 1 to 200 sccm. A schematic representation of the third generation nanocluster deposition system is shown in Figure 4.1.

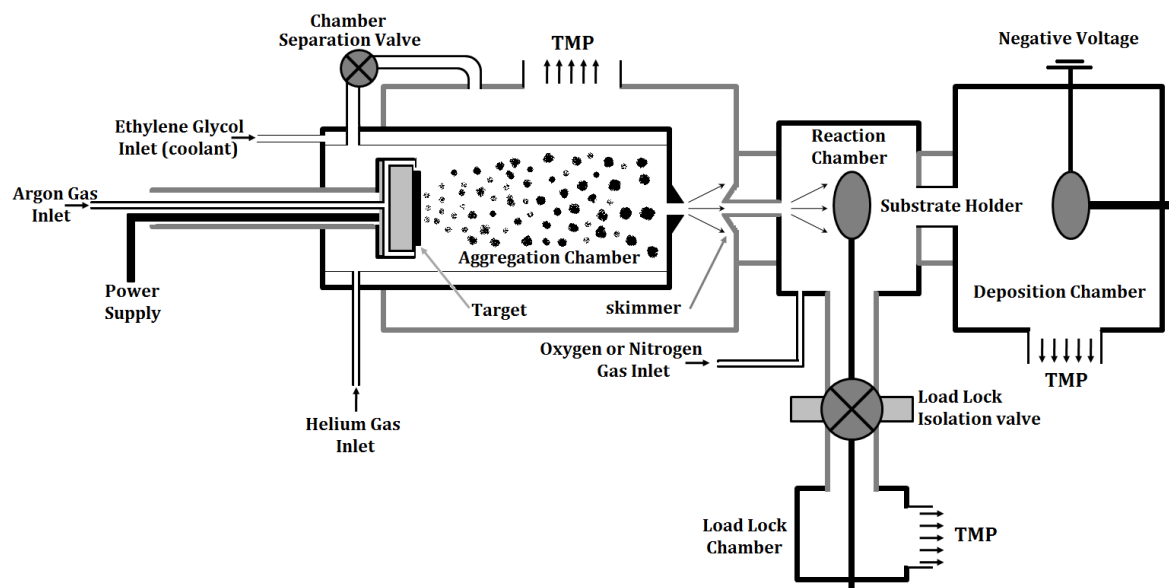


**Figure 4.1** Schematic representation of the third generation nanocluster deposition system

As shown in the Figure 4.1, the sputtering gun is located on the inside of the aggregation chamber. Metallic targets of 3 inches in diameter (76.2 cm) and ~0.3 cm thick with high purity of 5N (99.999%) sit on the circular edge of the gun surface under which two concentric magnets of opposite poles are placed in order to help to direct the path of sputtering. The Argon gas is supplied through the gun into the aggregation chamber. The Helium gas is supplied through an opening at the bottom of the aggregation chamber, which embraces the inside surface layer of the aggregation chamber. The system is cooled by chilled water (5 °C) and Ethylene Glycol cooler (-7 °C), which prevents overheating of the gun and chamber during sputtering. Each target has a life time of around 4 hrs, with good sputtering rate productivity up to 2 hrs. Also, the aggregation chamber is connected with a big Turbo Molecular Pump with a pumping speed of 1000 L/m, which constantly creates high vacuum. Though the aggregation chamber and the external chamber have a valve connecting them to each other that can be opened to suck the gases from the aggregation chamber, it remains closed during sputtering in order to maintain constant high pressure for cluster formation inside aggregation chamber and to create a pressure difference between inside aggregation chamber to the deposition chamber. The pressure difference causes the clusters to travel across the chambers and be deposited in a substrate in the deposition chamber. There is a small opening at the end of the aggregation chamber that can be varied in diameter to increase and decrease the pressure inside the aggregation chamber. Changing the diameter influences on the cluster size. When the pressure is high, it enables more clusters to aggregate, to form bigger size particles. Also, there is a skimmer located just before the reaction chamber, which helps to filter out the smaller particles and focuses the larger particles towards the substrate. The reaction chamber can either be used for the supplying gas to react with the clusters or can be used to collect the clusters in the substrate. The load lock chamber connected to the reaction chamber can be isolated with a valve, which serves the purpose of loading and unloading the samples. The load lock chamber is also connected with a TMP backed up with a mechanical pump. As mentioned earlier, the deposition chamber and the reaction chamber serve the purpose of



collecting the particles. There is no difference in the clusters collected in either of the chambers, except for a negative voltage that can be applied to the substrate in the deposition chamber. This negative voltage accelerates the travelling clusters from the aggregation chamber, which gets deposited to the substrate at high energy, thus deforming the cluster shape from spherical shape to elliptical or prolate shape (foot-ball shape) and enhancing anisotropic behavior in the deposited clusters. The TMP located at the deposition chamber helps to create vacuum in both the reaction and deposition chambers.

Doped nanoclusters can be generated by doping the target exactly on the sputtering region with the required dopant. The Figure 4.2 (a) shows the sputtering area of a 3 inch (76.2 cm) diameter Nickel target, which is along the diameter line of 4 cm and 0.3 cm wide. The dopant (3 spots at angle 120 degree between each) needs to be placed along this area as shown in Figure 4.2 (b), which actually represents 5% doping of Chromium (Cr) in Ni target.

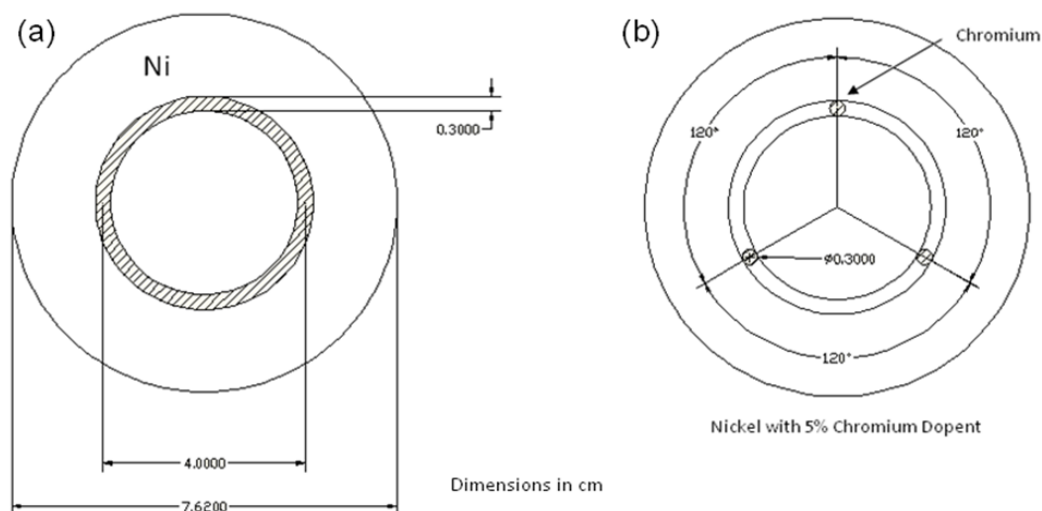


**Figure 4.2** Schematic diagrams showing the (a) sputtering region (shaded portion) in a Nickel target and (b) doped chromium spots (shaded portion) in the sputtering area.

The number of spots and the angle between them depends on the target material, dopant material, percentage of dopant, size of the dopant spot and sputter yield. The sputter yield for

different metals is given in Appendix A. The number of spots can be determined by the dopant area calculation using the formula given below.

$$\frac{A1}{A2} = \frac{X}{(100 - X)} \times \frac{Y2}{Y1} \dots\dots\dots (3.1)$$

Where ‘X’ is the percentage of materials to be doped, ‘A1’ is the sputtering area of the dopant material, ‘A2’ is the sputtering area of the target material, ‘Y1’ is the sputter yield of the dopant material and ‘Y2’ is the sputter yield of the target material. The substrate on which the clusters land can be carefully chosen based on the requirements. A silicon substrate is commonly used for collecting the substrate. Other than this, glass substrates may also be used. The Transmission Electron Microscope (TEM) grids are often used to collect clusters in the reaction or deposition chamber for determining cluster size and shape, and conducting diffraction studies.

#### 4.2 Working Principle

The cluster source has a DC magnetron sputtering gun with a high purity target sitting on the end to which high power (up to 250 W of DC power) is supplied. When the noble gas Argon is supplied to the aggregation chamber and comes into the vicinity of the electric field generated by the gun, it gets ionized. The ionized Ar gases are attracted to the target by the DC bias while the permanent magnet beneath the target surface creates a magnetic field that guides the ions, by Lorentz force, to hit the target with a huge impact. This impact is capable of ejecting the target atoms from the surface, thus the process called sputtering occurs. The highly energetic Ar<sup>+</sup> impact continues as the new neutral Ar atoms come in and the sputtering process continues to eject huge number of target atoms. As these atoms travel along the aggregation chamber, they aggregate with the influence of pressure, temperature, impact of Helium atoms and the distance travelled in the aggregation chamber. The Helium atoms helps in the formation of mono-dispersed (uniform cluster size) nanoclusters, because the energy is transferred from hot metal atoms to the cold Helium gas, which enables the smooth and uniform growth of clusters. Hence, one of the main factors influencing the

cluster growth is the Argon to Helium ratio, the factor which has the greatest influence over the cluster size. The higher the ratio, the greater is the particle size and the smaller is the mono dispersion. The lower the ratio, the smaller is the particle size and the greater is the size distribution. The other factors influencing the cluster size are the power supplied, the aggregation chamber temperature, aggregation distance and the pressure maintained inside the aggregation chamber. The working pressure maintained in the aggregation chamber is normally 1 Torr and the pressure at the deposition chamber is  $10^{-4}$  Torr. This pressure difference causes the clusters to travel the distance in to deposition chamber and become deposited onto the substrate, forming a thin granular film. The thickness of granular film is dependent on the deposition time and varies from nano meter to micro meter based on the duration of deposition. The thickness is almost constant throughout the layer.

### **4.3 Synthesis of Granular Films**

In this research, granular films of Ni and Fe based NPs were created on a silicon substrate with uniform film thickness. In both cases, the target that was placed on the sputtering gun inside the aggregation chamber was allowed to be sputtered. For Fully oxidized Fe NP granular films oxygen gas was supplied into the aggregation chamber to enable instance oxidation of Fe atoms, which aggregate through the low-temperature condensation to form the fully oxidized iron nanocluster (magnetite) and are deposited on to the silicon substrate. In other cases, core-shell NP films were created by allowing either the oxygen gas and/or the nitrogen gas to react with Fe nanoclusters in the reaction chamber.

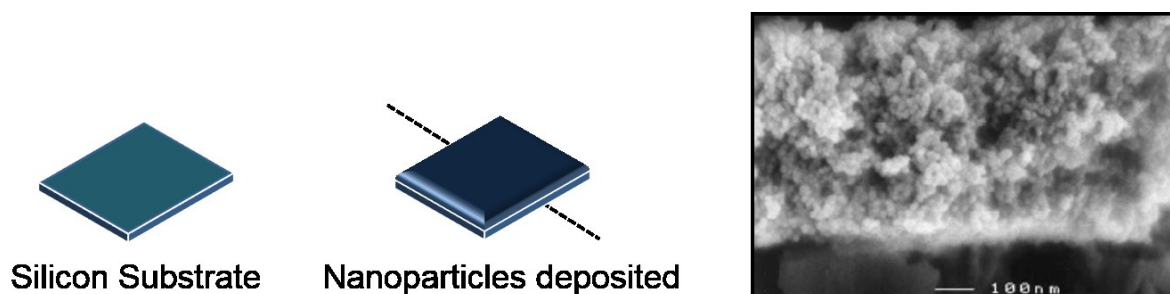


**Figure 4.3** Picture showing the nanoparticles deposited on silicon substrate and its cross-sectional view

The details of sputtering conditions like amount of gas supplied, aggregation temperature, maintained pressure, aggregation distance, supplied power and size of substrates on which the films were deposited are discussed in respective chapters.

#### 4.4 Characterization of Granular Films

Characterization studies were conducted on these granular films before and after exposing the samples to irradiation in order to explore the hidden physical properties and to understand the character behind irradiation-induced property changes. The characterization studies were mainly focused on uncovering the magnetic properties, magnetic interactions, surface property, structural analysis, elemental analysis and cluster size features. Some of the characterization techniques used for the samples are XRD, which provides information regarding the average crystallite size of the sample, Multi-Purpose Diffractometer (MPD), which provided details on the crystal structure of the films, Physical Property Measuring system (PPMS) to measure the magnetic properties and to conduct the Zero Field Cooled-Field Cooled (ZFC-FC) measurement for magnetic susceptibility, HIM for imaging the film microstructures, AFM for the study of surface properties and MFM to measure the magnetic domain interactions. These characterization techniques are discussed in detail below.

#### 4.4.1 X-Ray Diffraction (XRD)

X-ray diffraction technique works on the principle of elastic scattering of X-rays from the electron clouds of the individual atoms in the system. The measurements are based on observing the scattered intensity of an X-ray beam hitting a sample as a function of incident and scattered angle, polarization and wavelength or energy (Figure 4.4). The XRD measurement yields the atomic structure of materials and it is a non-destructive analytical technique, which reveals information about the crystallographic structure, chemical composition, and physical properties of materials and thin films.<sup>8-10</sup> In this research, the XRD measurements were carried out using Grazing-angle Incidence X-Ray Diffraction (GIXRD) technique. GIXRD was performed using a Philips X'pert Multi-purpose Diffractometer (MPD) based on Cu K $\alpha$  radiation. The asymmetric scan ranged from  $2\theta = 10^\circ - 80^\circ$  with a step size of  $0.05^\circ$  and a dwell time of 8s at each step was employed to study the crystallographic phase and average size of the crystalline grains at room temperature. This technique eliminates strong diffraction peaks from the single crystal substrate.

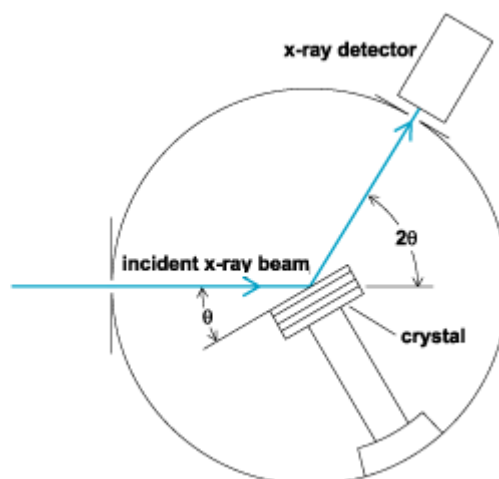


**Figure 4.4** Schematic of X-ray Diffractometer

#### 4.4.2 Helium Ion Microscopy (HIM)

A Scanning Helium Ion Microscope (SHIM or HIM) is an imaging technology similar to the scanning electron microscope, but it has a certain advantage over SEM; its high source brightness,

and the short De Broglie wavelength of the helium ions, which is inversely proportional to their momentum. With a HIM, it is possible to obtain qualitative data not achievable with conventional microscopes, which use photons or electrons as the emitting source and it is based on a scanning helium ion beam. As the helium ion beam interacts with the sample, it does not suffer from a large excitation volume, and hence provides sharp images on a wide range of materials. Also there is no discernible sample damage due to relatively light mass of the helium ion.<sup>8-10</sup> Helium gas is ionized at the source tip that contains three atoms or a trimer. The  $\text{He}^+$  ion beam is extracted and accelerated down to the column where it is focused to a sub-nanometer size for secondary electrons (SE) microscopy, backscattering ion (BI) microscopy, and Rutherford backscattering spectroscopy (RBS).

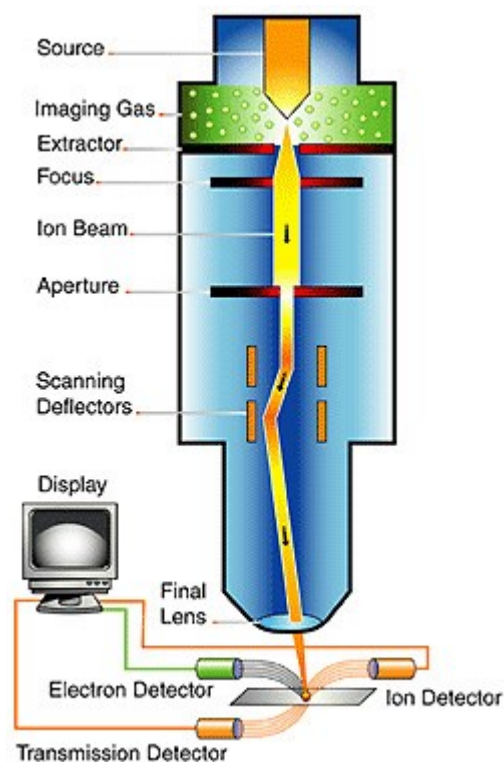


**Figure 4.5** Schematic of Helium Ion Microscope

In this study, the film microstructures of the samples were examined using a Helium Ion Microscope (HIM, Orion Plus, Carl Zeiss SMT, Peabody, MA) before and after irradiation. The schematic of the HIM is shown in (Figure 4.5). High-resolution HIM is an efficient tool to study the

microstructures of the films. This measurement was performed for the film before and after irradiation to study the microstructural changes. This new technique shows advantages over the conventional Scanning Electron Microscopy (SEM) in that it has a larger depth of view, a higher image contrast, a better spatial resolution, and a smaller electronic energy deposition density, among others.

#### **4.4.3 Physical Property Measurement System (PPMS)**

Physical Property Measurement System (PPMS) (Quantum Design INC) enables the measurement of phenomena such as the magneto-caloric effect, magneto-striction and magneto-resistance over a wide range of temperatures at magnetic fields of up to 7 Tesla. PPMS is similar to the Magnetic Property Measurement System (MPMS), which performs DC characterization utilizing a reciprocating sample and SQUID (Superconducting Quantum Interference Device) detection for ultimate resolution at magnetic fields up to 5 Tesla.<sup>8-10</sup> For this study, the magnetic properties were measured for the as-deposited and post-irradiated films using Physical Property Measurement System (PPMS, Quantum Design, San Diego, CA) with the AC Magnetic Susceptibility (ACMS) attachment.

#### **4.4.4 Atomic Force Microscopy (AFM) and Magnetic Force Microscope (MFM)**

Atomic Force Microscopy (AFM), also known as Scanning Force Microscopy (SFM) is a type of scanning probe microscopy, which has a very high-resolution on the order of nanometers. This works on the principle of cantilever deflection where the tip of the cantilever is brought into proximity of a sample surface and the forces between the tip and the sample lead to a deflection of the cantilever according to Hooke's law.<sup>8-10</sup> This deflection is calibrated to give the surface topography, atomic layer, chemical bonding and other details. The surface topography for the unirradiated and irradiated films was studied in this research using the AFM measurement technique. When the AFM is used to measure the magnetic forces by a magnetic tip, it is termed as Magnetic

Force Microscope (MFM). In this study, the MFM technique is used to study the magnetic domains and inter-domain interactions in the unirradiated and irradiated samples. The MFM images were obtained using a Multimode Atomic Force Microscopy (AFM, Digital Instruments, Nanoscope IIIA, Veeco Metrology, Santa Barbara, CA), a cobalt-coated probe tip (MESP, 70 kHz) and a lift height of ~20 nm.

#### **4.4.5 Transmission Electron Microscope (TEM)**

Transition electron microscope (TEM) is analogous to an optical microscopy: the photons are replaced by high energy electrons and the glass lenses by electromagnetic lenses as shown in Figure 4.6. In TEM microscopy technique an electron beam is transmitted through an ultra-thin electron-transparent sample, interacting with the sample and forming an image detected by a sensor such as a CCD camera and an enlarged image is formed using a set of magnetic lenses. The highly energetic incident electrons interact with the atoms in the sample producing characteristic radiation and particles providing information for materials characterization. Information is obtained from both deflected and non-deflected transmitted electrons. Backscattered and secondary electrons, and emitted photons. According to Rayleigh's criterion, the resolution  $W$  of the optical system is given by the following equation:  $W = 0.6\lambda/NA$ , where  $NA$  is the numerical aperture and  $\lambda$  is the wavelength. Therefore, the much smaller wavelength of electrons allows a resolution of about 0.2 nm to be achieved. The particle shape, size distribution, faceting and crystallinity can be obtained using TEM. Here, electron microscopy experiments were conducted on a JEOL 1200 TEM, operating at 120 kV. The samples were prepared by drying the solvent of the MNPs' dispersion onto a 200 mesh copper grid with a carbon coated Formvar film.



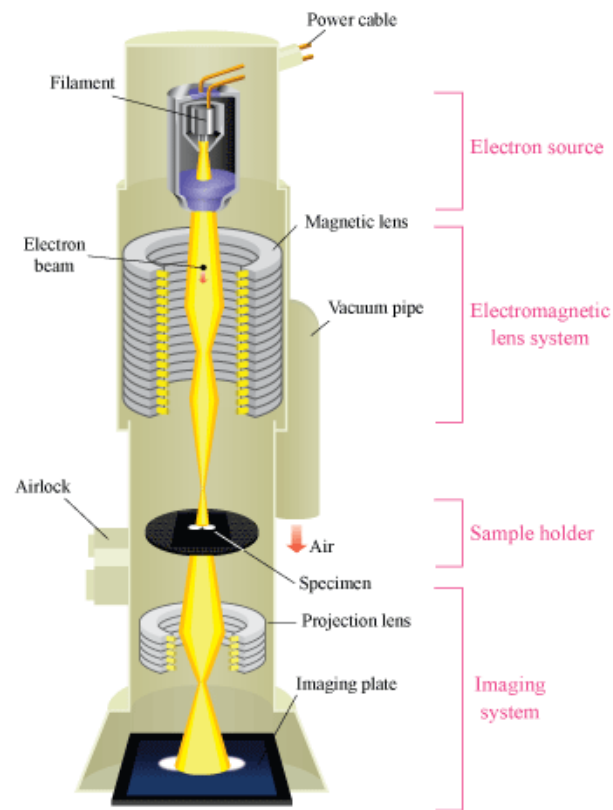


**Figure 4.6** Schematic of Transmission Electron Microscope

#### 4.4.6 Scanning Electron Microscope (SEM)

A scanning electron microscope (SEM) is a type of electron microscope that produces images of a sample by scanning it with a focused beam of electrons. The electrons interact with atoms in the sample, producing various signals that can be detected and that contain information about the sample's surface topography and composition. The electron beam is generally scanned in a raster-scan pattern, and the beam's position is combined with the detected signal to produce an image. SEM can achieve resolution better than 1 nanometer. Specimens can be observed in high vacuum, in low vacuum, in wet conditions (in environmental SEM), and at a wide range of cryogenic or elevated temperatures. The schematic of SEM is shown in Figure 4.7. The most common mode of detection is by secondary electrons emitted by atoms excited by the electron beam. On a flat surface, the plume of secondary electrons is mostly contained by the sample, but on a tilted surface, the

plume is partially exposed and more electrons are emitted. By scanning the sample and detecting the secondary electrons, an image displaying the topography of the surface is created.

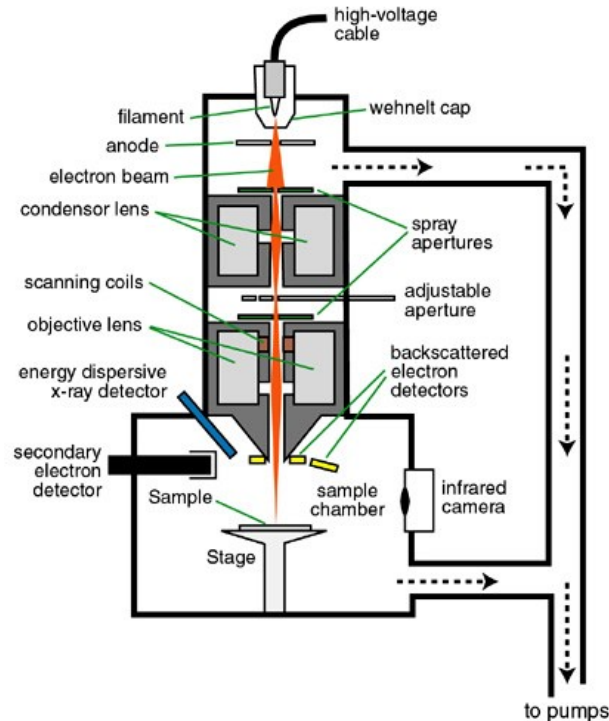


**Figure 4.7** Schematic of Scanning Electron Microscope

#### 4.4.7 Energy-Dispersive X-ray Spectroscopy (EDX)

Energy-Dispersive X-ray Spectroscopy (EDX or EDS) is also called energy dispersive X-ray analysis (EDXA). EDX is a standard procedure for identifying and quantifying elemental composition of specimen areas as small as a few cubic micrometers. The characteristic X-rays are produced when a material is bombarded with electrons in an electron beam instrument, such as transmission electron microscopy (TEM) or scanning electron microscope (SEM). A brief description of the generation of characteristic X-rays is as follows. First the incoming electrons from TEM or SEM knock inner shell electrons out of atoms in the sample. In order to return the atom to its normal state, an electron from an outer atomic shell drops into the vacancy in the inner shell. This drop results in the loss of a specific amount of energy, namely, the difference in energy between the vacant shell and the shell contributing the electron. The energy is given up in the form of

electromagnetic radiation x-rays. Since energy levels in all elements are different, element-specific or characteristic, x-rays are generated. The emitted x-rays are indicative of the element that produced them. The EDX x-ray detector measures the number of emitted x-rays versus their energy. The energy of the x-ray is characteristic of the element from which the x-ray was emitted. A spectrum of the energy versus relative counts of the detected x-rays is obtained and evaluated for qualitative and quantitative determinations of the elements present in the sampled volume.

#### **4.4.8 Vibrating Sample Magnetometer (VSM)**

Magnetic properties were characterized using a DMS 1660 VSM where each pre-weighted sample is placed inside an external magnetic field to get magnetized at room temperature. A hysteresis loop was acquired by applying a scanning magnetic field of 13500 Oe to -13500 Oe. The vibrating sample magnetometer (VSM) was developed in 1956 by S Foner and Van Oosterhart. In a VSM a sample is vibrated in the vicinity of a set of pick-up coils. According to Faraday's laws of magnetic induction, the flux change caused by the moving magnetic sample causes an induction voltage across the terminals of the pickup coils which is proportional to the magnetization of the sample  $V(t) = Cd(f_i)/dt$ , where  $f_i(t)$  represents the changing flux in the pick-up coils caused by the moving magnetic sample. With the calibration, this voltage is proportional to the magnetic moment of the sample. A brief description of VSM is given as follows. The pick-up coils are situated between the pole pieces around the sample (Figure 4.8). Both the signals produced by the permanent magnet vibrating in the pick-up coils and the signal induced in the sample pick-up coils are fed directly into a lock-in amplifier. The permanent magnet signal is used as the reference signal input. The system is calibrated using a single crystal nickel disc whose saturation magnetization is well documented.

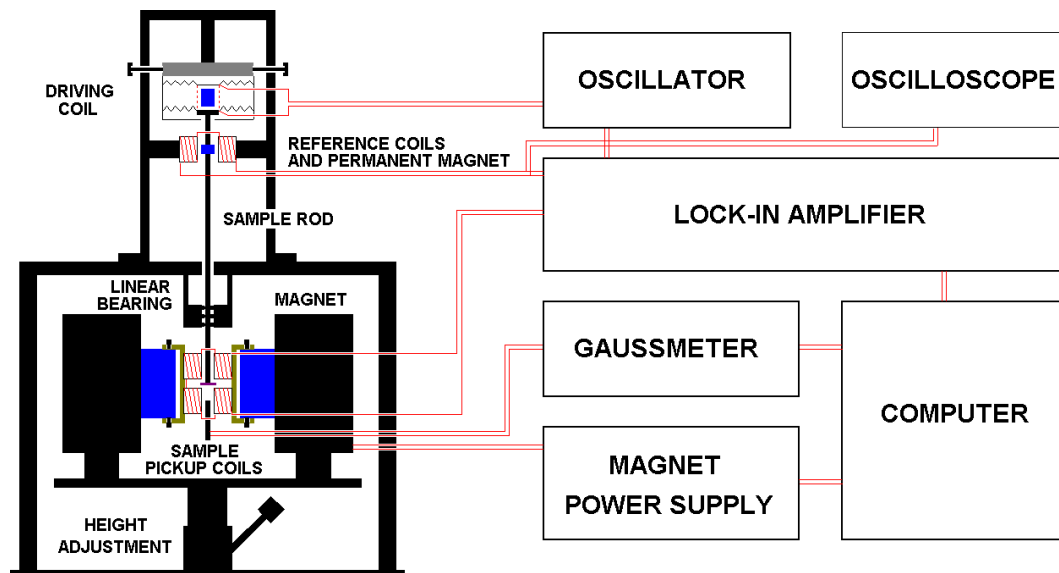


**Figure 4.8** Schematic of Vibrating Sample Magnetometer

If a material is placed within a uniform magnetic field, a magnetic moment will be induced in the sample. In a VSM, a sample is positioned within suitable placed sample, coils, and is made to undergo sinusoidal motion, i.e., mechanically vibrated. The resulting magnetic flux changes induce a voltage in the sample coils that is proportional to the magnetic moment of the sample. The applied field may be produced by an electromagnet or superconducting coils.

#### 4.4.9 Van der Pauw Electrical Conductive Measurement

The van der Pauw method was first propounded by Leo J. van der Pauw in 1958. The method is a technique commonly used to measure the resistivity and the Hall coefficient of a sample. Its power lies in its ability to accurately measure the properties of a sample of any arbitrary shape, so long as the sample is approximately two-dimensional (i.e. it is much thinner than it is wide), solid, and the electrodes are placed on its perimeter. The measurements require that four ohmic contacts be placed on the sample as shown in Figure 4.9.

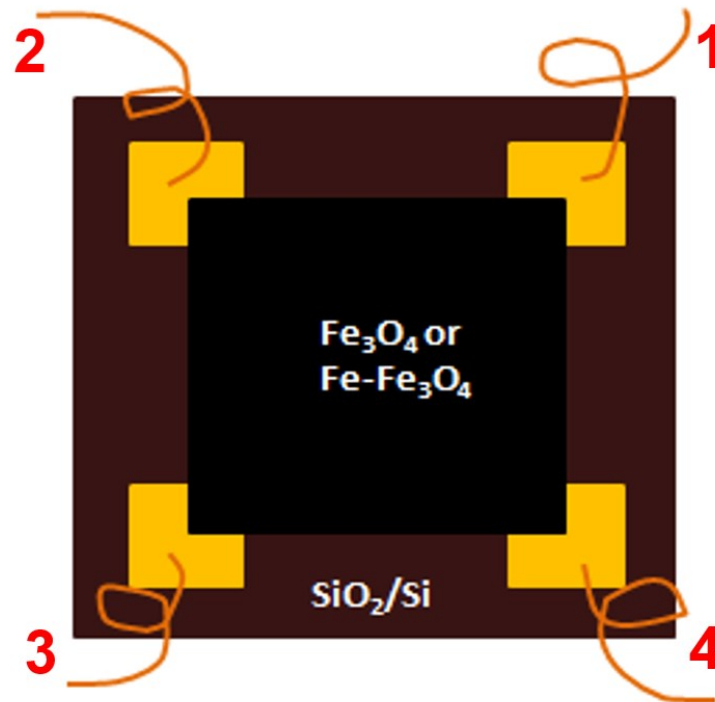


**Figure 4.9** Schematic of the Van der Pauw Sample of Fe-granular film on Silicon Substrates

Certain conditions for their placement need to be met: They must be on the boundary of the sample (or as close to it as possible). They must be infinitely small. Practically, they must be as small as possible; any errors given by their non-zero size will be of the order  $D/L$ , where  $D$  is the average diameter of the contact and  $L$  is the distance between the contacts. In addition to this, any leads from the contacts should be constructed from the same batch of wire to minimize thermoelectric effects. For the same reason, all four contacts should be of the same material. The contacts are numbered from 1 to 4 in a counter-clockwise order, beginning at the top-left contact. The current  $I_{12}$  is a positive DC current injected into contact 1 and taken out of contact 2, and is measured in amperes (A). The voltage  $V_{34}$  is a DC voltage measured between contacts 3 and 4 with no externally applied magnetic field, measured in volts (V). The resistivity  $\rho$  is measured in ohms-metres ( $\Omega\cdot\text{m}$ ). The thickness of the sample  $t$  is measured in meters (m). The sheet resistance  $R_S$  is measured in ohms ( $\Omega$ ). Therefore, it is possible to obtain a more precise value for the resistances  $R_{\{12,34\}}$  and

$R_{\{23,41\}}$  by making two additional measurements of their reciprocal values  $R_{\{34,12\}}$  and  $R_{\{41,23\}}$  and averaging the results.

$$R_{\text{vertical}} = \frac{R_{12,34} + R_{34,12}}{2} \quad R_{\text{horizontal}} = \frac{R_{23,41} + R_{41,23}}{2}$$

#### 4.4.10 X-ray Photoelectron Spectroscopy (XPS)

X-ray photoelectron spectroscopy (XPS) is a surface-sensitive quantitative spectroscopic technique that measures the elemental composition at the parts per thousand range, empirical formula, chemical state and electronic state of the elements that exist within a material. XPS spectra are obtained by irradiating a material with a beam of X-rays while simultaneously measuring the kinetic energy and number of electrons that escape from the top 0 to 10 nm of the material being analyzed. XPS requires high vacuum ( $P \sim 10^{-8}$  millibar) or ultra-high vacuum (UHV;  $P < 10^{-9}$  millibar) conditions, although a current area of development is ambient-pressure XPS, in which samples are analyzed at pressures of a few tens of millibar. XPS is a surface chemical analysis technique that can be used to analyze the surface chemistry of a material in its as-received state, or after some treatment, for example: fracturing, cutting or scraping in air or UHV to expose the bulk chemistry, ion beam etching to clean off some or all of the surface contamination (with mild ion etching) or to intentionally expose deeper layers of the sample (with more extensive ion etching) in depth-profiling XPS, exposure to heat to study the changes due to heating, exposure to reactive gases or solutions, exposure to ion beam implant, exposure to ultraviolet light.

#### 4.5 Irradiation Experimental Setup

As a part of this study, the  $\text{Fe}_3\text{O}_4$  and  $\text{FeO}+\text{Fe}_3\text{N}$  granular thin film samples were subjected to 5.5 MeV  $\text{Si}^{2+}$  ion irradiation to fluence of  $10^{16}$  ions/cm<sup>2</sup> and 2 MeV  $\text{He}^+$  ions irradiations to fluence of  $3 \times 10^{15}$  ions/cm<sup>2</sup> at room temperature. These radiation exposure experiments were carried out in an ‘Ion Accelerator System’ located at Environmental Molecular Science Laboratory (EMSL)

at Pacific Northwest National Laboratory (PNNL), Richland.<sup>11</sup> Detailed description of experimental setup can be found in published literatures.<sup>12,13</sup> The schematic representation of the ion accelerator system setup is shown in Figure 4.10. As depicted in the figure, the radiation setup consists of main parts like the ion source, 3.0 MV electrostatic tandem ion accelerator (NEC model 9SDH-2), injector, analyzing magnets, beam lines, and end stations. The gas is ionized in the source and is allowed to pass through a series of accelerators, which are controlled by the electric fields. The emerging ions, with high kinetic energy, were then directed using beam lines to the end stations and allowed to strike the samples. The Faraday cup serves the purpose of measuring the number of ions or electrons hitting the cup based on the resulting current measured from the metal (conductive) cup, which catches the charged particles in vacuum.

The source contains both Radio Frequency (RF) plasma source and SNICS II (Source of Negative Ions by Cesium Sputtering) ion source. The RF source is dedicated to producing ions from gases. Ions from most other elements are produced from solid sources using Cs<sup>+</sup> sputtering in the SNICS II ion source. Negative ions from either source can be injected into the accelerator by an injector magnet at the system's low-energy beam line. The low-energy beam line is equipped with several other components that include an electrostatic x-y steerer to steer the beam, a beam profile monitor to measure the profile of the ion beam, a Faraday cup for current measurements, and an Einzel lens for focusing. The electrostatic accelerator is equipped with two Pelletron charging chains capable of carrying 300 mA of charging current to the terminal. Since the tandem accelerator provides two stages of acceleration (i.e., negative ion acceleration from the source end to the terminal in the middle and positive ion acceleration from the middle to the high-energy end), the final energy depends on the charge state of the ion. The accelerated ions can be focused through the high-energy beam line using a magnetic quadrupole and a y-axis electrostatic steerer, which are attached to the high-energy beam line. The analyzing (switching) magnet is equipped with seven ports at  $\pm 45^\circ$ ,  $\pm 30^\circ$ ,  $\pm 15^\circ$ , and  $0^\circ$  with respect to the accelerator.

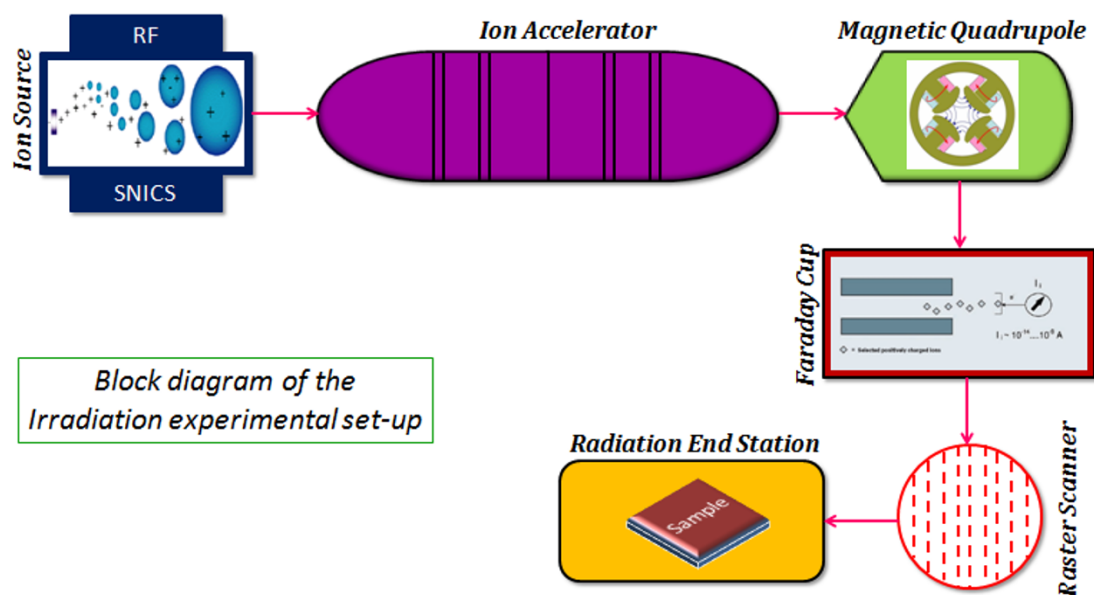
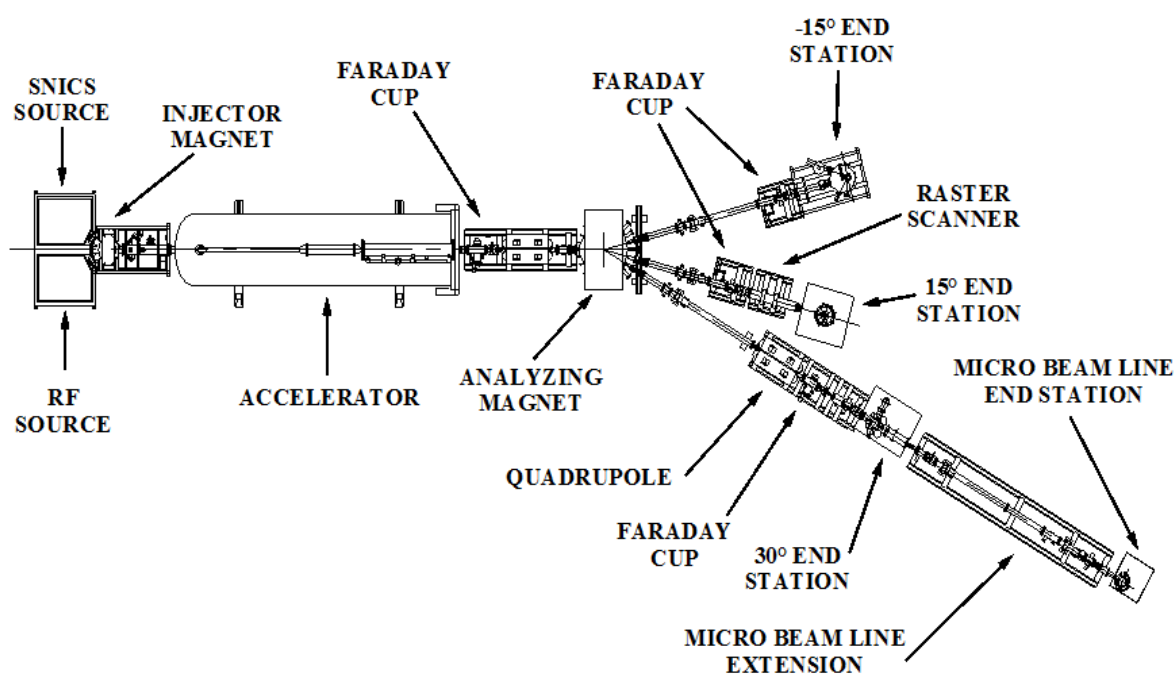


**Figure 4.10** Schematic representations of the ion accelerator system set up for irradiation experiments.

Currently, three beam lines, located at the +30°, +15°, and -15° ports of the analyzing magnet, along with corresponding end stations, have been established for materials modification and



analysis. Turbo pumps are attached to all beam lines and ion sources. Typical base pressure in the low-energy beam line is  $1 \times 10^{-8}$  Torr to  $2 \times 10^{-8}$  Torr, and the mid-to-high  $10^{-9}$  Torr range in the high-energy beam lines. When the ion accelerator is in operation, typical pressures in the high-energy beam lines are in the low-to-mid  $10^{-8}$  Torr range. The  $+15^\circ$  beam line equipped with an NEC raster scanner unit is dedicated to performing ion implantation and irradiation in the samples. The beam rastering system is used to ensure uniform irradiation over an area covering the entire sample surface. All of the three end stations serve their own purposes based on whether they are equipped with most of the standard ion beam analytical capabilities, including Rutherford Back Scattering (RBS), Nuclear Reaction Analysis (NRA), Particle Induced X-Ray Emission (PIXE), Scanning Transmission Ion Microscopy (STIM), Elastic Recoil Detection Analysis (ERDA) and Proton Elastic Scattering Analysis (PESA). Also the samples can be placed in the sample manipulator, which has three axes of rotations (polar, azimuth, and tilt), three axes of translation (x, y, and z), and is interfaced with sample transfer capability and the manipulator has the capability for heating samples to 1300 K or cooling them to 130 K. For this study the  $+15^\circ$  beam line was used to expose the samples to ion irradiations. The advantage of this beam line is it has beam rastering system, sample manipulator and other measurement facilities like RBS, ERDA and NRA.

#### 4.6 References

1. H. Haberland, M. Moseler, Y. Qiang, O. Rattunde, T. Reiners, and Y. Thurner, "Energetic cluster impact (ECI): A new method for thin-film formation," *Surface Review and Letters (SRL)*, vol. 3, no. 1, pp. 887-890, 1996.
2. H. Haberland, M. Mall, M. Moseler, Y. Qiang, T. Reiners, and Y. Thurner, "Filling of micron-sized contact holes with copper by energetic cluster impact," *Journal of Vacuum Science & Technology A: Vacuum, Surfaces, and Films*, vol. 12, no. 5, p. 2925, 1994.
3. H. Haberland, M. Karrais, M. Mall, and Y. Thurner, "Thin films from energetic cluster impact: A feasibility study," *Journal of Vacuum Science & Technology A: Vacuum, Surfaces, and Films*, vol. 10, no. 5, p. 3266, 1992.
4. W. de Heer, "The physics of simple metal clusters: experimental aspects and simple models," *Reviews of Modern Physics*, vol. 65, no. 3, pp. 611-676, 1993.
5. Y. Qiang, Y. Thurner, T. Reiners, O. Rattunde, and H. Haberland, "Hard coatings (TiN,  $Ti_xAl_{1-x}N$ ) deposited at room temperature by energetic cluster impact," *Surface and Coatings Technology*, vol. 100-101, pp. 27-32, 1998
6. Y. Qiang, J. Antony, A. Sharma, J. Nutting, D. Sikes, and D. Meyer, "Iron/iron oxide core-shell nanoclusters for biomedical applications," *Journal of Nanoparticle Research*, vol. 8, no. 3-4, pp. 489-496, 2005.
7. J. Antony, J. Nutting, D. R. Baer, D. Meyer, A. Sharma, and Y. Qiang, "Size-Dependent Specific Surface Area of Nanoporous Film Assembled by Core-Shell Iron Nanoclusters," *Journal of Nanomaterials*, vol. 2006, pp. 1-4, 2006.
8. C. N. R. Rao and K. Biswas, "Characterization of Nanomaterials by Physical Methods," *Annual Review of Analytical Chemistry*, vol. 2, no. 1, pp. 435-462, 2009.
9. Kouros Kalantar-zadeh and Benjamin Fry, *Nanotechnology-Enabled Sensors* (Boston, MA: Springer US, 2008),
10. "Nanomaterials - Wikipedia, the free encyclopedia," <http://en.wikipedia.org/wiki/Nanomaterials>
11. "EMSL: Science: Instruments", <http://www.emsl.pnl.gov/capabilities/viewInstrument.jsp?id=1032>
12. W. Jiang, Y. Zhang, and W. Weber, "Temperature dependence of disorder accumulation and amorphization in Au-ion-irradiated 6H-SiC," *Physical Review B*, vol. 70, no. 16, 2004.
13. W. Jiang and W. Weber, "Multiaxial channeling study of disorder accumulation and recovery in gold-irradiated 6H-SiC," *Physical Review B*, vol. 64, no. 12, 2001.

## Chapter 5: Synthesis, Structure, and Electronic Structure of Pure and Cr-doped Ni

### Nanoparticles

#### 5.1 Introduction

Stainless steel (SS) is a common material used in nuclear reactors which has Ni and Cr content to improve strength, and Ni-based alloys have good high temperature application. Chromium brings resistance to corrosion while nickel offers greater toughness at a specified carbon level. Since Ni and Cr are the major contributors for improved high temperature strength in SS and Ni nanoparticles have been extensively studied for diverse applications over a few decade, utilizing Ni nanoparticles with Cr-doping in SS could positively impact the dispersion strengthening phenomenon in SS. Understanding their structural and electronic properties at nanoscale becomes essential. Although characteristics of Ni-Cr super-alloys are well established, the atomic percentage of Cr in these alloys are usually over 20 at.% and less is known for Cr concentration less than 10 at%. Therefore, in this study Ni and Cr doped Ni core-shell nanoclusters (NCs) are investigated for their structure and electronic properties. It has been very well established that properties and the behavior of nanoparticle of metals and alloys as well as their oxide or compound critically depend on the particle characteristics, such as size, morphology, crystal structure, and the surface characteristics.<sup>1-9</sup> Ni nanoparticles have been extensively studied for applications related to sensors,<sup>10</sup> magnetic recording media,<sup>7</sup> catalysis,<sup>11</sup> magnetic fluids,<sup>12</sup> and biomedical sensing.<sup>13</sup> Ni nanoparticles can be fabricated by either a physical or a chemical method, such as pyrolysis,<sup>14</sup> sputtering,<sup>15</sup> reversedmicelles,<sup>16,17</sup> sonochemical deposition,<sup>18</sup> aqueous and nonaqueous chemical reduction,<sup>19-21</sup> and polyol process.<sup>22-26</sup> The crystal structure, morphology, size and size distribution of the particles greatly depend on the processing parameters and at some degrees can be tailored for a specific structural feature. For example, either the face-centred cubic (fcc) or hexagonal close-packed (hcp) structured Ni nanoparticles can be obtained by adjusting the processing parameters<sup>27-29</sup>.

As similarly with all other metal particles, Ni nanoparticles exposed to air or oxygen-including atmosphere is oxidized instantly, a process normally called initial oxidation.<sup>30</sup> Under the framework of the Cabrera-Mott theory of oxidation of metal,<sup>31</sup> the initial oxidation process of metal can be described as the following: (i) upon initial attachment of oxygen onto the surface of the metal and formation of a thin layer of oxide, (ii) an electron tunnels through the thin oxide layer and (iii) ionizes the oxygen, leading to an electrical field between the metal and the surface of the oxide layer. The electrical field will subsequently drive outward diffusion of the ionized metal.<sup>32,33</sup> As a result of the initial oxidation, metallic nanoparticle exposed to air at room temperature is normally covered by an oxide layer, leading to the formation of metallic core and oxide shell structure. Therefore, the behavior and properties of metallic nanoparticles exposed to air at room temperature is essentially determined by a combination of the metal core and the oxide.<sup>34-36</sup> Contrasted with the understanding of high temperature growth of thick oxide layer, less is known about the initial oxidation process of metal and the structural nature of their product. For example, controlled oxidation of metallic nanoparticles at high temperature enables tailoring of hollow and core-shell structured metal and oxide nanoparticles for specific applications.<sup>37-43</sup> However, it is far more difficulties to know the structural nature of the oxide layer formed on most of metallic particles following the initial oxidation. This is related to the nature of the initial oxidation process, which has three features: (i) the formed oxide layer is normally just a few nm thick, (ii) the initial oxide growth is nearly instantaneous and (iii) most elements present may be oxidized. Depending on the type of migrating lattice defects, the oxide can grow from the metal-oxide interface (oxygen ions are transported inward) or from the oxide-environment interface (metal ions are transported outward). Initial oxidation is the start of a transient phase during which each element present may be oxidized. After this transient stage, a more uniform and often layered oxide structure with a gradient of oxidation states (and sometimes in composition) is formed. Therefore, a great challenge for understanding the

properties of nanostructure particles is the understanding of the oxide shell on the surface of the nanoparticle formed during the initial oxidation.

Although nanoparticles of metal and compounds can be fabricated through chemical route with controlled characteristics, such as composition, size, shape, crystal structure and surface properties, the particle processed by the chemical route is normally stabilized by a layer of surfactant.<sup>3,5,40</sup> This surfactant will inherently modify the oxidation behavior of the otherwise a clean surface. To avoid any modification of a pristine metal surface before exposing to air, the nanoparticle used in this work was processed by a cluster deposition process. In this article we report the structure, morphology, surface characteristics, and electronic structure of the pure and Cr-doped Ni nanoparticles. Microstructure of pure and Cr-doped Ni nanoparticles exposed to air at room temperature were studied using high resolution transmission electron microscopy (HRTEM), selected area electron diffraction, x-ray diffraction (XRD), x-ray photoelectron spectroscopy (XPS) and electron energy-loss spectroscopy (EELS). The results present a comprehensive understanding of the bulk and surface structure of both pure and Cr-doped Ni nanoparticles.

## **5.2 Sample Preparation**

The nickel nanoparticles were synthesized using the cluster deposition system (CDS) in Dr. You Qiang's Laboratory at the University of Idaho. The details of the cluster deposition system can be found in chapter 3 and in the previous papers.<sup>44,45</sup> With this system nanoparticles can be prepared with different particle sizes, ranging from 5 nm to 100 nm and the size variance can be achieved by altering the sputtering conditions like Ar-He ratio, the aggregation distance, and the supplied power. The size of the Ni nanoparticles was determined using Transmission Electron Microscopy (TEM). VSM measurements were also done on each sample to study the magnetic saturation, magnetic coercivity, and magnetic remanence of the particles. The TEM images in Figure 4.1 shows the various particle sizes of Ni nanoparticles that can be attained using the CDS.

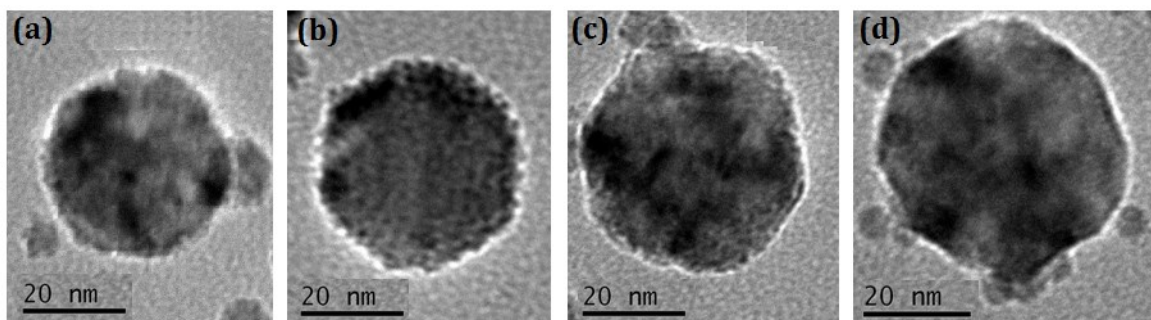


**Figure 5.1** TEM image showing the different sized Ni nanoparticles prepared using CDS.

The gas flow rate of Ar and He and the Ar-He ratio for achieving different particle sizes shown in Figure 5.1 and their corresponding magnetic properties are listed in Table 5.1. The aggregation distance and the supplied power for all the four samples were maintained constant at 288 mm and at 200 W.

**Table 5.1** Sputtering conditions and magnetic properties corresponding to different particle size shown in Figure 5.1

Exp. No	Ar-He Flow (sccm)	Ar-He ratio	Particle Size (nm)	Magnetic Saturation (emu/g)	Remanence (emu/g)	Coercivity (emu/g)
1	450-50	9	~35	25	0.2	10
2	393-41	9.59	~40	33	0.2	9
3	350-35	10	~45	35	1.2	20
4	400-28	14.29	~50	37	0.3	12

In order to prepare the Cr-doped Ni nanoparticles, Cr dopant was added at two nominal concentrations: 5at% and 10at%. Therefore, the pure Ni, 5at% and 10at% Cr-doped samples were correspondingly designated as Ni, Ni5Cr, and Ni10Cr. The deposition process was completed in a nanocluster deposition system, which combines a new kind of sputtering-gas-aggregation cluster beam source with an atom beam from magnetron sputtering. The dopant concentration is controlled by adjusting the relative area of Ni and Cr on the sputtering target. Particles were initially deposited in a source chamber. After deposition they were exposed to ambient air and the expected oxide layer formed on the surface of each nanoparticle. The size of the nanoparticles depend on the He:Ar ratio,

pressure inside the chamber and the distance the clusters travel inside the source chamber. The deposition rate was variable up to 10 mg/h, measured in situ with a rotatable quartz microbalance. It should be realized that the morphology of the particle depends on the material. The general structural features of Fe particles synthesized by this method have been reported in detail in previous publications<sup>34-36</sup>.

The phase of the deposited particles was analyzed using X-ray diffraction (XRD), which is collected on the nanoparticles mounted on a silicon wafer. The analysis utilized a Rigaku D/MAX RAPID II microdiffractometer with a curved imaging plate and a rotating Cr anode operating at 35 kV and 25 mA. An optical prefix consisting of horizontal and vertical mirrors specific to Cr K $\alpha$  provided focused X-rays at the sample position. A collimator (0.1 mm to 0.8 mm) optimized the resolution and signal-to-noise ratio of the diffraction patterns. The incident beam path was purged with He gas to improve X-ray flux at the sample position. The software JADE 8.5 (Materials Data Inc.) was used to analyze X-ray diffraction data.

Particle size, morphology, and crystallographic structural feature of individual particle were analyzed using HRTEM imaging and electron diffraction. These were carried out on a JEOL JEM 2010 microscope with a LaB<sub>6</sub> filament and a specified point-to-point resolution of 0.194 nm. The operating voltage on the microscope was 200 kV. All images were digitally recorded with a slow-scan CCD camera (image size 1024 x 1024 pixels). The actual concentration of the Cr in the Ni particle was analyzed using energy dispersive x-ray spectroscopy (EDS) in a transmission electron microscope (TEM). The EDS spectra were collected using Oxford link system which is attached to the TEM.

In order to check if the Cr is enriched on the surface of the particle, x-ray photoelectron spectroscopy (XPS) is used to analyze the particle. The XPS measurements were carried out using a Physical Electronics Quantum 2000 Scanning ESCA Microprobe system with a focused monochromatic Al K $\alpha$  X-ray (1486.7 eV) source and a spherical section analyzer. The XPS spectra

were collected using a pass energy of 23.5 eV. The spectra were referenced to an energy scale with binding energies for Cu ( $2p_{3/2}$ ) at  $932.67 \pm 0.05$  eV and Au (4f)  $84.0 \pm 0.05$  eV. Binding energies were corrected for sample charging using the C(1s) peak at 284.6 eV for adventitious carbon as a reference. The concentration and distribution depth profile was also analyzed by electron sputtering of the film.

The electronic structure of the surface oxide was analyzed using electron energy loss spectroscopy (EELS) in TEM. The EELS analysis was carried out using Gatan Image Filter (GIF2000), which is post-column attached to the JEOL JEM-2010 TEM. The EELS spectra were acquired in image-coupling mode (with a diffraction pattern on the TEM view screen). A 2-mm entrance aperture and an energy dispersion of 0.2 eV/channel were used. To improve the energy resolution, the LaB<sub>6</sub> filament was operated in an undersaturated condition. This configuration gave an energy resolution of 1.2 eV as measured by the full-width-at-half-magnitude of the zero-loss peak. Each spectrum acquisition time was typically ~10 s. A power-law background was removed from the spectra.

### **5.3 Results and Discussion**

#### **5.3.1 Structure and Morphology of the Particles**

Metallic Ni normally crystallizes in the face centered cubic (fcc) structure and nickel oxide (NiO) exists in the form of rock salt structure as schematically drawn in Figure 5.2. The structure of the particles exposed to air at room temperature was analyzed using XRD and the results were shown in Figure 5.3. It has been found that all three samples are a mix of metallic and oxide phase.

Regardless the Cr dopant concentration, the metallic phase in the nanoparticle can be indexed as the fcc structured Ni and the oxide phase can be indexed as the rock salt structured NiO. Ni and Ni10Cr samples show much similar features on the XRD patterns, which are characterized by a relatively strong and wide peaks related to NiO and as compared with that of Ni5Cr, indicating that both Ni



and Ni10Cr samples were dominated by a relatively high concentration of NiO and the overall particle size is smaller than that in the sample Ni5Cr.

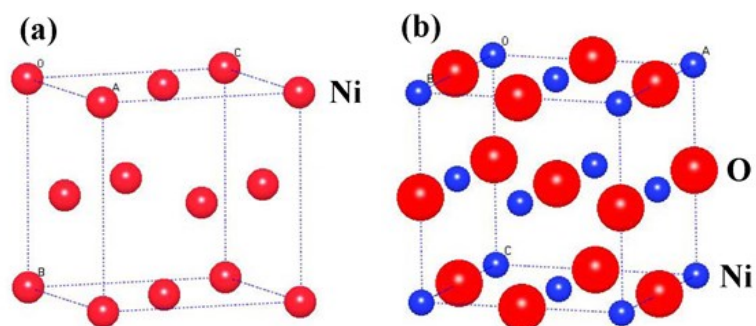


**Figure 5.2** Ball and stick model showing the face centered cubic (fcc) structured Ni and the rock salt structured NiO

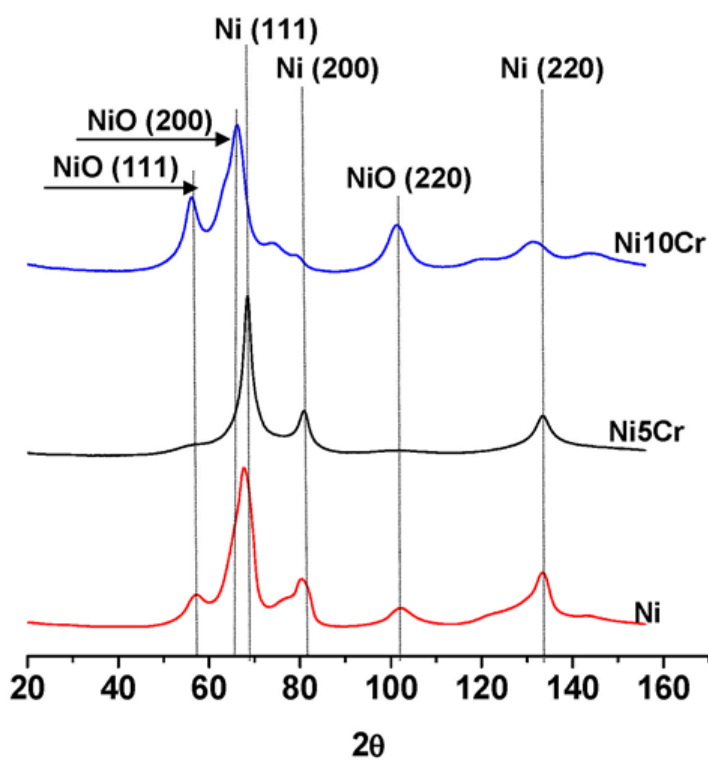


**Figure 5.3** XRD of pure and Cr-doped Ni nanoparticles. Samples Ni and Ni10Cr were dominated by oxide phase and Ni5Cr is dominated by metallic phase.

Quantitative analysis of the lattice parameters of both metal and oxide are summarized in Table 5.2. Ni has an atomic size of 1.35 Å and Cr corresponds to 1.40 Å.

**Table 5.2** The nominal and measured Cr/Ni atomic ratio as well as the measured lattice constant of the NP

Sample ID	Nominal Cr dopant conc. at%	Cr:Ni atomic ratio by EDS	Cr:Ni atomic ratio by XPS	Lattice constant of alloy (Å)		Lattice constant of oxide (NiO) (Å)	
				Measured	Literature	Measured	Literature
Ni	0	0	0	3.528	3.524	4.172	4.177
Ni5Cr	5	3.81:96.19	3.77:96.23	3.527	3.524	N/A	N/A
Ni10Cr	10	5.58:94.42	4.71:95.29	3.583	3.524	4.160	N/A

The ionic radii of Ni is 0.55 Å, the ionic radii of Cr is ranging from 0.55 to 0.80 Å depending on the valence state. Therefore, the addition of Cr into the lattice of both Ni and NiO will not be expected to induce significant change of the lattice constants. In addition, related to the small size of the nanoparticle, the diffraction peak broadening makes it hard for measuring such a small change of lattice constant. At this sense, the estimation of the lattice constant with the addition of Cr is believed not significant.

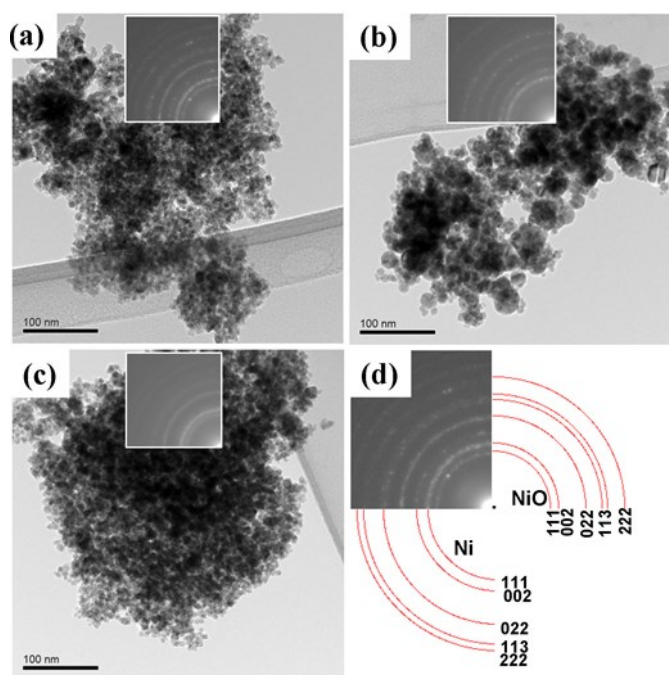


**Figure 5.4** Representative TEM images showing an overall view of the nanoparticles. (a) Sample Ni, (b) Sample Ni5Cr, and (c) Sample Ni10Cr. The inset within (a), (b), and (c) corresponds to the selected area electron diffraction pattern of the each sample. (d) Matching of the experimental diffraction pattern using sample Ni as a representative case with the calculated patterns of both fcc structured Ni and NiO

The structural features derived from the XRD diffraction analysis are consistently supported by the TEM imaging and electron diffraction analysis. Figure 5.4(a) shows the general morphology of the particles for all three samples along with the correspondingly selected area electron diffraction pattern. Overall, the particle size in samples Ni and Ni10Cr (Figure 5.4(a&b)) are smaller than that in sample Ni5Cr. All three samples show similar features on the selected area electron diffraction pattern, which is a superposition of fcc structured Ni and rock salt structured NiO, which is representatively matched with the calculated diffraction patterns as shown in Figure 5.4(d).

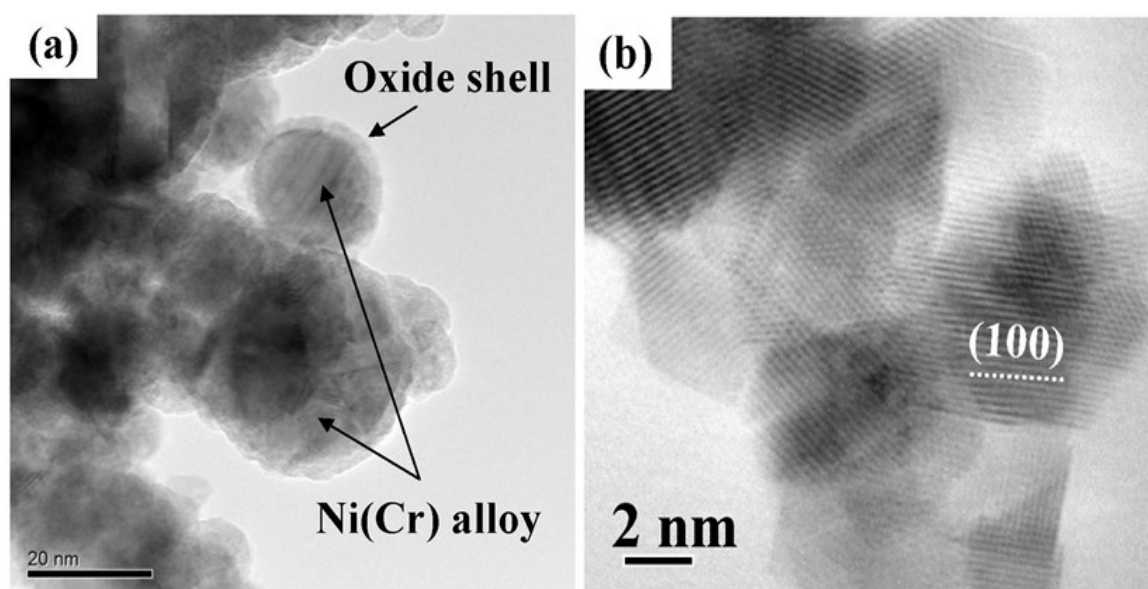


**Figure 5.5** Representative TEM images typical showing two types of nanoparticles in the sample Ni5Cr. (a) Core-shell structured particles and (b) fully oxidized particle with a cubed morphology.

High magnification TEM imaging reveals that all three samples are similarly featured by a mix of two types of particles. The relatively large particle shows a core-shell structure, featuring a Ni metal core covered by an oxide layer as illustrated in Figure 5.5(a). Formation of the oxide is the consequence of the surface oxidation of the Ni nanoparticles when they are exposed to air at room temperature. At the same time, there exists a large collection of small and cube-shaped particles (Figure 5.5(b)), which show high proportion in the samples Ni and Ni10Cr. HRTEM imaging reveals that the metal particle is slightly faceted on the (111) planes and normally possesses (111)

twins within the particles as representatively shown in Figure 5.6(a) for the case of sample Ni5Cr. The oxide shell covering the metal particle is pretty thin with a typical thickness of  $\sim 1.6$  nm (Figure 5.6(a)). No specific crystallographic orientation relationship between the surface layer and the metal core can be identified. HRTEM imaging indicates that the small and cube-shaped particle is a fully oxidized NiO particle, featuring a single crystal and faceting on the (100) planes (Figure 5.6(b)).

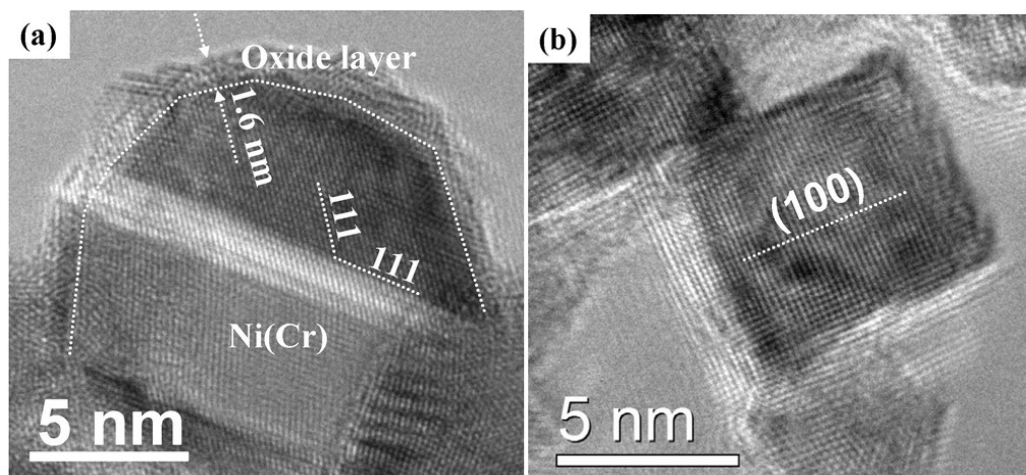


**Figure 5.6** HRTEM image showing the lattice image of both core-shell and fully oxidized the fully oxidized particle in sample Ni5Cr. (a) The core-shell structured particle. The thickness of the shell is typically  $\sim 1.6$  nm and note the (111) twin in the fcc structured Ni nanoparticle. (b) The fully oxidized nanoparticle is a single crystal NiO and note the faceting of particle on the (100) planes.

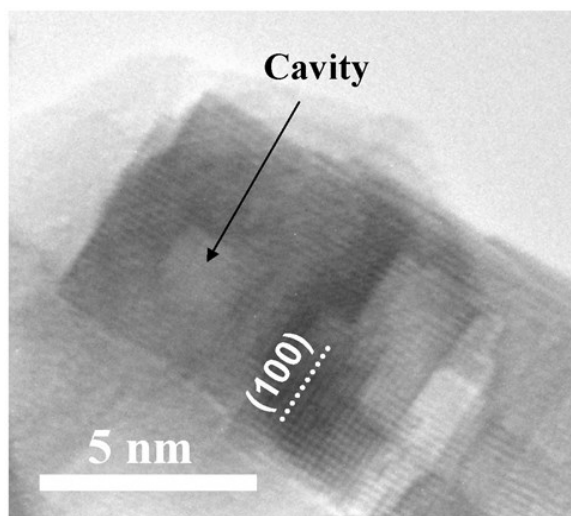


**Figure 5.7** HRTEM image showing the lattice image of the fully oxidized particle in sample Ni. Note the trapping of cavity within this fully oxidized particle and faceting of cavity on the (100) planes.

There exists a critical size of  $\sim 6$  nm, below which the particle is fully oxidized and above which the particle forms a core-shell structure. Furthermore, cavity can also be noticed in some of the fully oxidized particle and the cavity is also faceted on the (100) planes as representatively shown in Figure 5.7 for the sample Ni. It is far more interesting to note that the fully oxidized NiO nanoparticle corresponds to a single crystal and is faceted on the (100) planes. It has been observed that the iron oxide nanoparticle formed by oxidation of Fe at room temperature is characterized by a multi-domain structure and shows a spherical morphology.<sup>35,36</sup> This likely indicates that during the oxidation of Ni in air at room temperature, it is subject to significant re-arrangement of atoms within the oxide. Furthermore, it has been noticed that the oxide layer formed on Fe is about 3 nm, while for Ni, it is only about 1.6 nm. The critical particle size for complete oxidation of Fe is  $\sim 8$  nm, which contrasts with the dimension of  $\sim 6$  nm for Ni. The morphological and structural differences between the oxide layer formed on Ni and Fe nanoparticles are closely related to the differences in the electronegativity between Ni and Fe for oxidation. It would be expected that the oxidation rate of Fe is much faster than that for Ni.

### 5.3.2 The Cr distribution

Three critical questions that need to be addressed in the Cr doped Ni nanoparticles. (1) The dopant concentration is targeted as Cr:Ni = 5:95 in atomic ratio for sample Ni5Cr, and Cr:Ni = 10:90 in atomic ratio for sample Ni10Cr. However, what is the true concentration of Cr indeed doped in the particle? (2) The spatial distribution of the Cr, does the Cr form solid solution with the Ni lattice or does it segregate to the surface of the particle, or does it exist as a Cr-based separate phase? (3) What is the effect of initial oxidation on the distribution of the Cr, does Cr preferentially oxidize to form Cr<sub>2</sub>O<sub>3</sub>? The actual Cr concentration is analyzed by EDS at two different scales. At a large scale, the electron beam was spreaded overall a large area, covering a large agglomeration of particles. The result of this analysis reflects the overall composition of the particle. At a finer scale, the electron beam is focused on to a single particle, which gives the composition of single particle.

The EDS analysis indicates that at both scales the Cr:Ni ratio consistently falls to Cr:Ni = 3.81:96.19 for sample Ni5Cr and Cr:Ni = 5.58:94.42 for sample Ni10Cr (Figure 5.8).

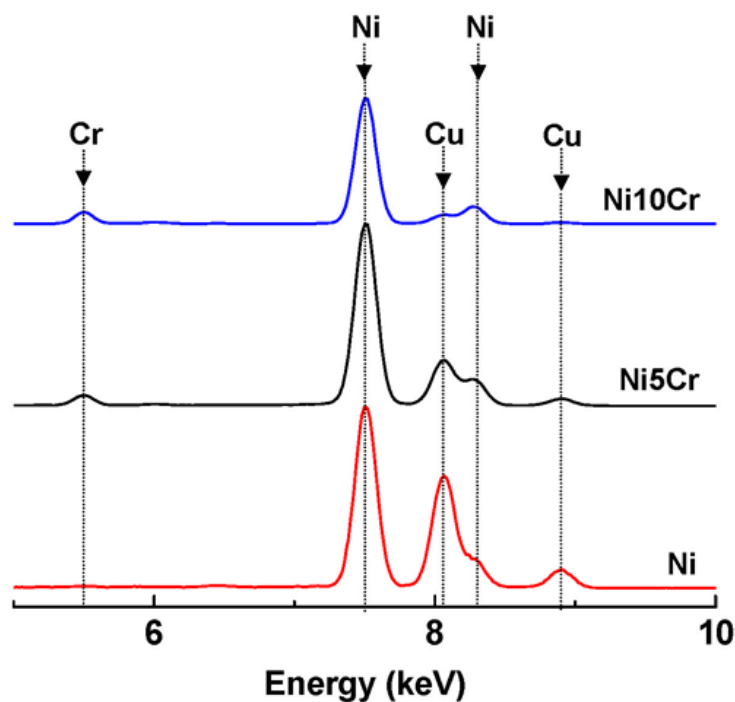


**Figure 5.8** EDS spectra of samples Ni, Ni5Cr and Ni10Cr

Apparently, the actual concentration of Cr is less than what has been initially targeted. The EDS analysis indicates that the Cr dopant is uniformly distributed on a single particle scale for both sample Ni5Cr and Ni10Cr. This is also further confirmed by EELS analysis of individual particle as shown in Figure 5.9. For EELS analysis, the slightly overlapping of the Cr  $L_{2,3}$  edge with the O K-edge makes it complicated from the background removal. Therefore, no attempt was made to quantify the Cr/Ni ratio using the EELS spectra. However, due to the high spatial resolution of EELS, it has been noticed that all the particles analyzed by EELS is composed of both Cr and Ni. XRD, electron diffraction analysis and HRTEM imaging all collectively indicate that no secondary phase of either pure Cr or corundum structured  $\text{Cr}_2\text{O}_3$  was formed, demonstrating that the Cr is indeed distributed in the lattice of Ni to form a solid solution.

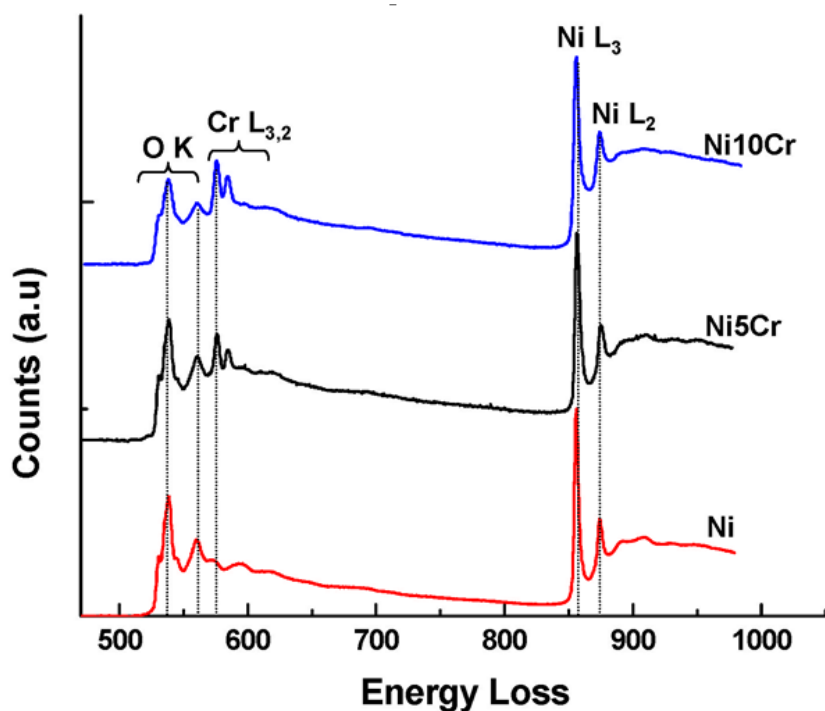


**Figure 5.9** EESL spectra obtained from a single oxide particle showing the O K-edge, Cr L2,3-edge, and Ni L2,3-edge

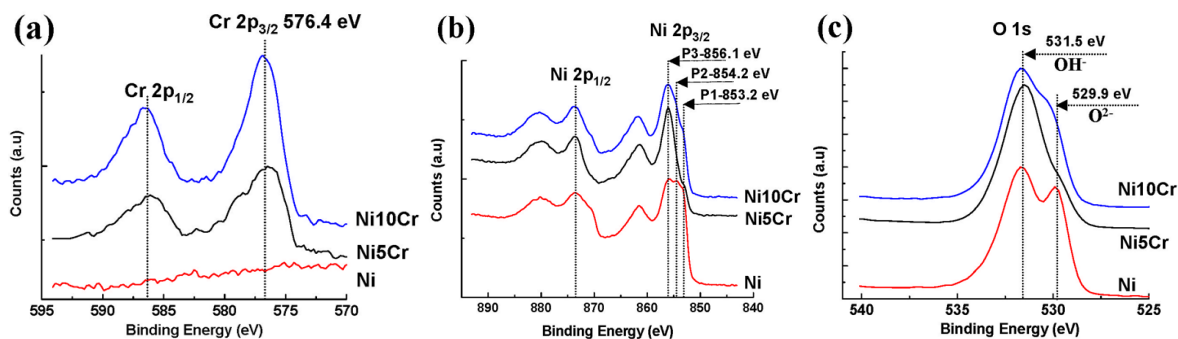


**Figure 5.10** XPS spectra showing the peaks of Cr-2p, Ni-2p and O-1s for samples Ni, Ni5Cr, and Ni10Cr

Due to short escape distance of photoelectrons, the XPS signal mostly reflects the composition of surface of the particles. Therefore, possible segregation of the Cr on the surface of the particle was identified using XPS analysis. Figure 5.10 shows the representative XPS spectra of Cr 2p, Ni 2p, and O 1s. XPS quantification in terms of Cr:Ni atomic ratio is summarized in Table 5.1. It is apparent that the Cr:Ni atomic ratio obtained by XPS is approximately consistent with that

obtained by EDS. Therefore, it is confirmed that the oxide layer is a uniform structure with Cr as similarly as in the bulk composition. Above analysis clearly indicates that the Cr at a concentration of ~ 5 at% forms solid solution with Ni lattice. Room temperature exposure of the Cr-doped Ni nanoparticle in air does not lead to the preferential oxidation Cr to form  $\text{Cr}_2\text{O}_3$ . This is markedly contrasted with the case of high temperature oxidation of Ni-Cr superalloy for which the Cr is preferentially oxidized to form  $\text{Cr}_2\text{O}_3$ , subsequently preventing further oxidation of Ni.<sup>46,47</sup> However, this type of superalloy normally contains about ~20at% Cr, which is far more than what has been incorporated in the nanoparticle in the present work.

### 5.3.3 The electronic structure of the nanoparticles

XPS and EELS not only provide information with respect to the chemical composition of the sample, but also give the electronic structure of the samples. Furthermore, XPS and EELS provide complementary information regarding the density of state of both valence band (XPS) and conduction band (EELS). XPS is a very surface sensitive techniques and the information provided by XPS is mostly relevant with the surface structure of the sample. The Ni 2*p* XPS of both pure and Cr-doped Ni nanoparticles is shown in Figure 5.10(b). The spectra composed of two edges split by spin-orbit coupling as  $2p^{1/2}$  and  $2p^{3/2}$ . Apparently, the Ni  $2p^{3/2}$  edge shows significant differences for the pure Ni and Cr-doped Ni particles. The Ni  $2p^{3/2}$  edge is composed of three peaks labeled as P1, P2 and P3 in Figure 5.10(b). Chang et al<sup>48</sup> has observed similar structural features on Ni film exposed to 1 atm high purity oxygen for 2 hours. Based on the features of XPS spectra obtained on both Ni oxidized at room and high temperature and NiO<sup>48-55</sup>, it can be generally concluded that P1 located at binding energy of 853.2 eV corresponds to the Ni metal peak, P2 located at binding energy of 854.2 eV is contributed by  $\text{Ni}^{2+}$ , and P3 located at binding energy of 856.1 eV is associated with either  $\text{Ni}^{3+}$  or defect  $\text{Ni}_2\text{O}_3$ <sup>52,53,56</sup> corresponding to the excited  $3d$  states with the  $3d^7$  electron configuration<sup>57,58</sup> or  $\text{Ni}(\text{OH})_2$ .<sup>54,55</sup> It can be seen from Figure 5.10(b) that the pure Ni particle shows peaks associated with metallic Ni,  $\text{Ni}^{2+}$  and  $\text{Ni}^{3+}$  or  $\text{Ni}(\text{OH})_2$  in approximately equal intensity. With



the addition of Cr dopant, the peak associated with the metallic Ni is suppressed, which is especially true for the sample Ni5Cr.

Based on HRTEM imaging, it can be seen that the oxide shell formed on the surface of the nanoparticle is pretty thin, with a typical thickness of  $\sim 1.6$  nm as shown in Figure 5.10(a). Consistent with this observation is the results of Railsback et al.<sup>38</sup>. They have observed that Ni nanoparticles synthesized by a chemical route and exposed to air at room temperature is covered by an oxide layer with a thickness ranging from 1.3 nm to 3.9 nm.<sup>38</sup> This thickness is approximately comparable with the Ni 2p photoelectron escape distance of approximately 1  $\sim$  2 nm. Therefore, the existence of the Ni metal peak is related to the thin nature of the oxide layer formed on the Ni nanoparticle. Similarly, Chang et al has observed that following the exposure of Ni film at room temperature in oxygen for 2 hours, they still can see a strong metallic peak on the XPS of Ni 2p and they attribute this to a slow oxidation kinetics of Ni based on both theoretical and experimental work.<sup>51,59</sup>

The O 1s XPS spectrum shows two significant peaks as shown in Figure 5.10(c). The peak located at a binding energy of  $\sim 529.9$  eV is associated with  $O^{2-}$ .<sup>53,55</sup> The other peak with a binding energy of  $\sim 531.5$  eV corresponds to  $OH^-$ .<sup>53,55</sup> and this peak appears to be dominant features for all three samples. Considering the features of both the O 1s and the Ni 2p XPS spectra as shown in Figure 5.10, it can be generally concluded that the peak P3 in the Ni  $2P^{3/2}$  edge is associated with  $Ni(OH)_2$ . Given the fact that XPS is a surface sensitive tool, it can be seen that both pure Ni and Cr-doped Ni nanoparticles that exposed to air is covered by a  $Ni(OH)_2$  layer on the very top of the particle surface.

EELS spectra represents excitation of core electron to unoccupied orbitals. Contrary to the XPS that maps the density of state of valence band, EELS maps the density of state of conduction band. Furthermore, the primary electrons used in EELS transmit through the sample, EELS gives the electronic structure of the whole particles, rather than only the surface region. Given the fact that

all particles were covered by a native oxide layer as discussed in previous sections, it is informative to measure the fine structural feature of the EELS on O K-edge. For EELS measurement, the electron beam was focused on the oxide layer. Figure 5.11 shows the representative EELS O K-edge of both pure and Cr-doped Ni particles. The O K-edge shows four peaks, which are labeled *a*, *b*, *c*, and *d* in Figure 5.11. To exclude the uncertainty regarding the absolute energy scale, the spectra shown in Figure 5.11 are all aligned with the pre-edge peak *a* at 532 eV. Overall, the O K-edge shows the typical features of the NiO as reported in literatures.<sup>60-63</sup> Qualitatively, the heights and the positions of these four peaks can be used to obtain information about the electronic structure and the coordination chemistry of the absorbing O atoms including information about 1) the valence state of Ni, 2) the average and distribution of the interatomic distances between the absorbing O and its nearest and next-nearest neighbors, 3) the nature of the Ni-O bond (degree of covalency vs. ionicity), and 4) coordination number.

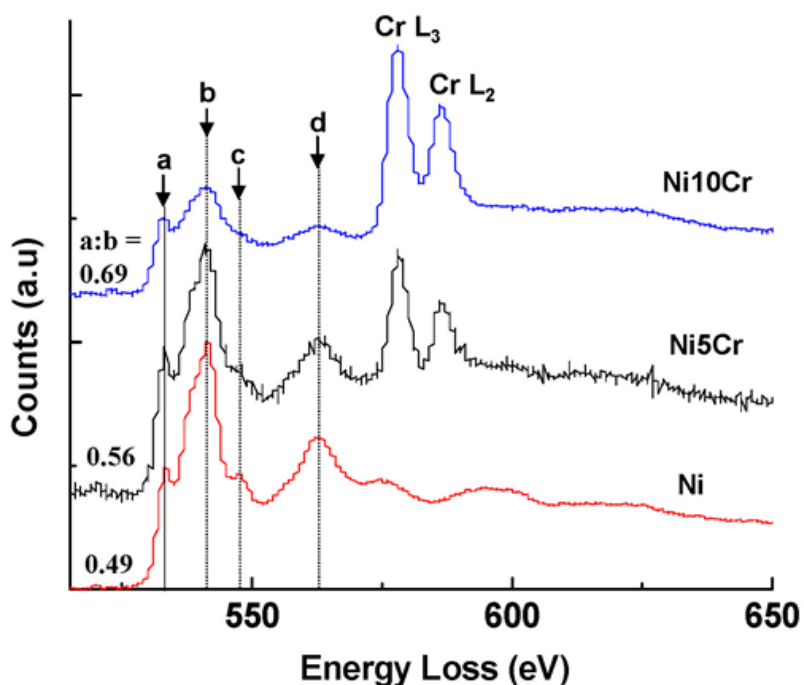


**Figure 5.11** Detailed comparison of EELS O K-edge obtained from the oxide particle for samples Ni, Ni5Cr and Ni10Cr. All spectra were aligned at the pre-edge peak *a* at an energy loss position of 532 eV. The peaks intensity *a*:*b* is measured and marked in the figures for quantitative analysis of the spectra.

Kanda et al<sup>60</sup> have calculated the EELS spectra of O K-edge for NiO, which provide fundamental insights in terms of atomic orbitals and electron transitions on the understanding of the observed EELS spectra. The pre-peak *a* is located at ~532 eV, which can be interpreted as a transition from the O 1*s* core state to the unoccupied states of O 2*p* hybridized with the metal 3*d* states. Therefore, the intensity of the pre-peak *a* will reflect the unoccupied 3*d* state in the metal atoms available for mixing with the O 2*p* states, as well as the cation-oxygen bond length. To quantitatively understand the effect of the ratio of each peak, the intensity ratio of peak *a* to peak *b* is measured. For the pure Ni particle sample, the *a*:*b* = 0.49, which is consistent with the values of 0.43 and 0.55 measured in the paper of Mitterbauer et al<sup>63</sup>, 0.50 in the papers of Kurita et al<sup>61</sup> and Koyama et al.<sup>62</sup> This also indicates that the oxide formed on the Ni metal particle is dominated by NiO as indicated by XRD, electron diffraction analysis, and HRTEM imaging as described in previous sections.

The intensity ratio of peak *a* to peak *b* for the Cr doped sample is measured to be ~ 0.56 and 0.69 for samples Ni5Cr and Ni10Cr, respectively, which is apparently larger than that of NiO. Cr has an electronic structure [Ar]3*d*<sup>5</sup>4*s*<sup>1</sup>, while Ni has an electronic structure [Ar]3*d*<sup>8</sup>4*s*<sup>2</sup>. Therefore, it would be expected that substitution of Cr for Ni in the NiO will lead to a higher prepeak *a* as compared with that of pure NiO.<sup>64</sup> The electronic structural information also provides evidence that Cr is indeed dissolved in the lattice of NiO, which is consistent with general chemical composition analysis and structural information obtained based on XRD, electron diffraction, and HRTEM imaging.

From the electronic transition point of view, peak *b*, *c*, and *d* are generally attributed to the transition of the O 1*s* electron to O 2*p* unoccupied states hybridized with cations (Ni and Cr) unoccupied 4*s* and 4*p* states. From the point of view of scattering resonance, it is known that the position of the resonance energy, *E*, and the radius of the scattering shell, *R*, satisfies the relationship:  $E \cdot R^2 = \text{constant}$ .<sup>65-67</sup> Therefore, the resonance energy position scales inversely with the

square of the radius of the scattering shell. Therefore, with the alignment of the prepeak a, any relative shift of peak b, c, and d on energy scale will correspond to the change of the distance of absorbing oxygen to the surrounding cations. It can be seen that the peak b, c, and d are all aligned at the same position on the energy scale for pure and Cr-doped samples. This indicates that there is no substantial bond length change following the partial substitution of Cr for Ni in the lattice of NiO.

### 5.3.4 General description of the structural features of the nanoparticles

A combination of XRD, electron diffraction, HRTEM imaging, XPS, and EELS measurement provide key information regarding the morphology, structure, dopant distribution, surface species and electronic structure of both pure and Cr-doped Ni particles. Both pure and Cr-doped Ni nanoparticle deposited by sputter deposition process shows no distinctive faceting on a specific crystallographic plane under the current deposition conditions. Air exposure of the nanoparticles at room temperature leads to the formation of an oxide layer on the metal particle surface. The oxide particle is the rock salt structured NiO. Furthermore, the very top surface of the oxide layer is hydrolyzed and dominated by Ni(OH)<sub>2</sub>. Therefore, the Ni nanoparticle exposed to air is featured by core-shell structure of three layers: Ni core-NiO layer-Ni(OH)<sub>2</sub> surface species. The oxide layer with a typical thickness of ~ 1.6 nm. There exists a critical size of ~ 6 nm for pure Ni and Cr-doped sample below which the particle is fully oxidized. The fully oxidized particle is a single crystal and faceted on the (100) plane of the NiO. Cavities as a result of vacancy condensation have also been noticed in some of the fully oxidized NiO particle. Mechanism on the formation of nanoscale void in the center of the oxidized nanoparticles is associated with process of Kirkendall Effect<sup>68</sup> by which the outward diffusion rate of Ni is much larger in the oxide layer than the inward diffusion rate of oxygen. This process has been recently explored for tailoring of either single or bi-metallic hollow structured nanoparticles.<sup>39</sup> However, it has also been noticed that exposure of the NiO nanoparticle under electron beam also lead to the formation of cavities. Therefore, it is appropriate to distinguish possible artifacts introduced during the TEM imaging.<sup>69</sup>

Cr dopant at the level of 5 at% was found to form solid solution with Ni lattice and the initial oxidation does not lead to the preferential oxidation Cr to form  $\text{Cr}_2\text{O}_3$ . This is markedly contrasted with the situation of high temperature oxidation of Ni-Cr superalloy. It is a very well known phenomenon that the oxidation resistance of superalloy is relied on preferential oxidation of Cr to form a  $\text{Cr}_2\text{O}_3$  layer, which prevents the oxidation of the underlying Ni.<sup>47,70</sup> Furthermore, it is known that for the high temperature oxidation of Ni-Cr, the oxidation rate shows dependence on the Cr concentration. Andreev et al<sup>71</sup> reported that for Ni-Cr alloy with 10 at% Cr, the high temperature oxidation rate of the alloy is increased due to the high self-diffusivity of NiO lattice. Based on the TEM imaging, the critical dimension for complete oxidation of the nanoparticle to form NiO for both pure and Cr-doped Ni nanoparticles is consistently falls to the value of  $\sim 6$  nm, indicating that the addition of Cr at the level of 5at% into the lattice of Ni show no detectable differences on the oxidation rate of the Ni at room temperature.

It is known that the behavior and properties of nanoparticles depend on their process method, handling history, and the environment in which the nanoparticles exist.<sup>72</sup> For example, the amount of  $\text{CeO}_{1.5}$  in  $\text{CeO}_{2-x}$  nanoparticles is a strong function of the particular synthesis methods used to make these particles.<sup>73-75</sup> Therefore, it is likely that the structure and electronic structures we observed for the core-shell structured Ni nanoparticles and the fully oxidized nanoparticles are specific to these types of nanoparticles prepared by the present method. Ni nanoparticles prepared by other processes and having different handling histories may exhibit different structures. It is also very interesting to note that the Ni nanoparticle that is fully oxidized is a single crystalline NiO and shows faceting on the (100) planes. This is markedly contrasted with the case of Fe nanoparticle. For the case of Fe nanoparticle, the small and fully oxidized particle normally exhibits a multi-domain structure.<sup>35,36,69</sup>

## 5.4 Summary

Air passivated pure and Cr-doped Ni nanoparticles with a size ranging from several nanometer to several ten nanometers show distinctive structural feature of three layered structures: a metal core covered by an oxide layer of  $\sim 1.6$  nm and the very surface of the oxide layer is hydrolyzed to form  $\text{Ni(OH)}_2$ . There exists a critical size of  $\sim 6$  nm. For particles smaller than this critical size, the overall particles are fully oxidized to form rock salt structured NiO single crystal, which is faceted on the (100) surface. Cavity can also be seen in the fully oxidized particle, which is a direct result of the outwards diffusion of Ni through the oxide layer. For particle larger than this critical size, it possesses a core-shell structure. Cr at the level of  $\sim 5$  at% has been found to form solid solution with the Ni lattice. The initial oxidation does not lead to preferential oxidation of Cr to form  $\text{Cr}_2\text{O}_3$ . The following chapter discusses the heat treatment and doping effect on the Ni nanoparticles.

## 5.5 References

1. V. R. Stamenkovic, B. Fowler, B. S. Mun, G. F. Wang, P. N. Ross, C. A. Lucas, and N. M. Markovic, *Science* **315**, 493-497 (2007).
2. S. E. Habas, H. Lee, V. Radmilovic, G. A. Somorjai, and P. Yang, *Nature Materials* **6**, 692-697 (2007).
3. Y. Xia, Y. J. Xiong, B. Lim, and S. E. Skrabalak, *Angewandte Chemie-International Edition* **48**, 60-103 (2009).
4. Y. G. Sun and Y. N. Xia, *Science* **298**, 2176-2179 (2002).
5. S. H. Sun, H. Zeng, D. B. Robinson, S. Raoux, P. M. Rice, S. X. Wang, and G. X. Li, *Journal of the American Chemical Society* **126**, 273-279 (2004).
6. S. Peng, C. Wang, J. Xie, and S. H. Sun, *Journal of the American Chemical Society* **128**, 10676-10677 (2006).
7. S. H. Sun, C. B. Murray, D. Weller, L. Folks, and A. Moser, *Science* **287**, 1989-1992 (2000).
8. G. S. Chaubey, C. Barcena, N. Poudyal, C. B. Rong, J. M. Gao, S. H. Sun, and J. P. Liu, *Journal of the American Chemical Society* **129**, 7214 (2007).
9. C. Desvaux, C. Amiens, P. Fejes, P. Renaud, M. Respaud, P. Lecante, E. Snoeck, and B. Chaudret, *Nature Materials* **4**, 750-753 (2005).
10. Z. K. Wang, M. H. Kuok, S. C. Ng, D. J. Lockwood, M. G. Cottam, K. Nielsch, R. B. Wehrpohn, and U. Gosele, *Phys. Rev. B* **89**, 27201 (2002).
11. J. Park, E. Kang, S. U. Son, H. M. Park, M. K. Lee, J. Kim, K. W. Kim, H. J. Noh, J. H. Park, C. J. Bae, J. G. Park, and T. Hyeon, *Advanced Materials* **17**, 429 (2005).
12. M. P. Pileni, *Advanced Functional Materials* **11**, 323-336 (2001).
13. K. B. Lee, S. Park, and C. A. Mirkin, *Angewandte Chemie-International Edition* **43**, 3048-3050 (2004).
14. S. L. Che, K. Takada, K. Takashima, O. Sakurai, K. Shinozaki, and N. Mizutani, *Journal of Materials Science* **34**, 1313-1318 (1999).
15. G. B. Thompson, R. Banerjee, X. D. Zhang, P. M. Anderson, and H. L. Fraser, *Acta Materialia* **50**, 643-651 (2002).
16. D. H. Chen and S. H. Wu, *Chemistry of Materials* **12**, 1353 (2000).
17. M. Mandal, S. Kundu, T. K. Sau, S. M. Yusuf, and T. Pal, *Chemistry of Materials* **15**, 3710-3715 (2003).
18. S. Ramesh, Y. Koltypin, R. Prozorov, and A. Gedanken, *Chemistry of Materials* **9**, 546-551 (1997).

19. S. H. Wu and D. H. Chen, *Chemistry Letters* **33**, 406-407 (2004).
20. O. Margeat, C. Amiens, B. Chaudret, P. Lecante, and R. E. Benfield, *Chemistry of Materials* **17**, 107-111 (2005).
21. M. Green and P. O'Brien, *Chemical Communications*, 1912-1913 (2001).
22. L. K. Kurihara, G. M. Chow, and P. E. Schoen, *Nanostructured Materials* **5**, 607-613 (1995).
23. N. Chakroune, G. Viau, C. Ricolleau, F. Fievet-Vincent, and F. Fievet, *Journal of Materials Chemistry* **13**, 312-318 (2003).
24. G. M. Chow, J. Ding, J. Zhang, K. Y. Lee, D. Surani, and S. H. Lawrence, *Applied Physics Letters* **74**, 1889-1891 (1999).
25. H. Yin and G. M. Chow, *Journal of the Electrochemical Society* **149**, C68-C73 (2002).
26. P. Toneguzzo, G. Viau, O. Acher, F. Guillet, E. Bruneton, F. Fievet-Vincent, and F. Fievet, *Journal of Materials Science* **35**, 3767-3784 (2000).
27. Y. Z. Chen, D. L. Peng, D. P. Lin, and X. H. Luo, *Nanotechnology* **18**, 505703 (2007).
28. Y. Z. Mi, D. S. Yuan, Y. L. Liu, J. X. Zhang, and X. Yong, *Materials Chemistry and Physics* **89**, 359-361 (2005).
29. C. N. Chinnasamy, B. Jeyadevan, K. Shinoda, K. Tohji, A. Narayanasamy, K. Sato, and S. Hisano, *Journal of Applied Physics* **97**, 10J309 (2005).
30. E. Fromm, *Kinetics of Metal-Gas Interactions at Low Temperature: Hydriding, Oxidation, Poisoning* (Springer, Berlin, Heidelberg, New York, 1998).
31. N. Cabrera and N. F. Mott, *Rep. Prog. Phys.* **12**, 163-184 (1948-1949).
32. S. Linderoth, S. Morup, and M. D. Bentzon, *J. Mater. Sci.* **30**, 3142-3148 (1995).
33. K. K. Fung, B. X. Qin, and X. X. Zhang, *Mater. Sci. Eng.* **A286**, 135-138 (2000).
34. C. M. Wang, D. R. Baer, J. E. Amonette, M. H. Engelhard, J. Antony, and Y. Qiang, *J. Am. Chem. Soc.* **131**, 8824-8832 (2009).
35. C. M. Wang, D. R. Baer, J. E. Amonette, M. H. Engelhard, J. Antony, and Y. Qiang, *Nanotechnology* **18**, 255603 (2007).
36. C. M. Wang, D. R. Baer, L. E. Thomas, J. E. Amonette, J. Antony, Y. Qiang, and G. Duscher, *J. Appl. Phys.* **98**, 094308 (2005).
37. R. Nakamura, J. G. Lee, H. Mori, and H. Nakajima, *Philosophical Magazine* **88**, 257-264 (2008).



38. J. G. Railsback, A. C. Johnston-Peck, J. W. Wang, and J. B. Tracy, *Acs Nano* **4**, 1913-1920 (2010).
39. Y. Yin, R. M. Riou, C. K. Erdonmez, S. M. Hughes, G. A. Somorjari, and A. P. Alivisatos, *Science* **304**, 711-714 (2004).
40. Y. Yin and A. P. Alivisatos, *Nature* **437**, 664-670 (2005).
41. H. J. Fan, M. Knez, R. Scholz, D. Hesse, K. Nielsch, M. Zacharias, and U. Gosele, *Nano Letters* **7**, 993-997 (2007).
42. H. J. Fan, U. Gosele, and M. Zacharias, *Small* **3**, 1660-1671 (2007).
43. J. Svoboda, F. D. Fischer, and D. Vollath, *Acta Materialia* **57**, 1912-1919 (2009).
44. J. Antony, Y. Qiang, D. R. Baer, and C. M. Wang, *J. Nanoscience and Nanotechnology* **6**, 568-572 (2006).
45. Y. Qiang, J. J. Antony, A. Sharma, J. Nutting, D. Sikes, and D. Meyer, *J. Nanoparticles Res.* **8**, 489-496 (2006).
46. A. Atkinson, *Rev. Mod. Phys.* **57**, 437-470 (1985).
47. P. Y. Hou and J. Stringer, *Oxidation of Metals* **34**, 299-321 (1990).
48. C. L. Chang, S. K. R. S. Sankaranarayanan, D. Ruzmetov, M. H. Engelhard, E. Kaxiras, and S. Ramanathan, *Physical Review B* **81**, 085406 (2010).
49. V. Biju, *Materials Research Bulletin* **42**, 791-796 (2007).
50. M. A. Vanveenendaal and G. A. Sawatzky, *Physical Review Letters* **70**, 2459-2462 (1993).
51. A. R. Kortan and R. L. Park, *Physical Review B* **23**, 6340-6347 (1981).
52. M. Tomellini, *Journal of the Chemical Society-Faraday Transactions I* **84**, 3501-3510 (1988).
53. B. P. Payne, A. P. Grosvenor, M. C. Biesinger, B. A. Kobe, and N. S. McIntyre, *Surface and Interface Analysis* **39**, 582-592 (2007).
54. P. R. Norton, R. L. Tapping, and J. W. Goodale, *Surface Science* **65**, 13-36 (1977).
55. N. Kitakatsu, V. Maurice, C. Hinnen, and P. Marcus, *Surface Science* **407**, 36-58 (1998).
56. G. K. Wertheim and S. Hufner, *Physical Review Letters* **28**, 1028-1031 (1972).
57. W. Low, *Physical Review* **109**, 247-255 (1958).
58. R. Newman and R. M. Chrenko, *Physical Review* **114**, 1507-1513 (1959).
59. S. Sankaranarayanan and S. Ramanathan, *Physical Review B* **78**, 085420 (2008).

60. H. Kanda, M. Yoshiya, F. Oba, K. Ogasawara, H. Adachi, and I. Tanaka, *Physical Review B* **58**, 9693-9696 (1998).
61. H. Kurata, E. Lefevre, C. Colliex, and R. Brydson, *Physical Review B* **47**, 13763-13768 (1993).
62. Y. Koyama, T. Mizoguchi, H. Ikeno, and I. Tanaka, *J. Phys. Chem. B* **109**, 10749-10755 (2005).
63. C. Mitterbauer, G. Kothleitner, W. Grogger, H. Zandbergen, B. Freitag, P. Tiemeijer, and F. Hofer, *Ultramicroscopy* **96**, 469-480 (2003).
64. F. M. F. Groot, M. Grioni, J. C. Fuggle, J. Ghijsen, G. A. Sawatzky, and H. Petersen, *Phys. Rev. B* **40**, 5715-5723 (1989).
65. Z. Y. Wu, S. Gota, F. Jollet, M. Pollak, M. Gautier-Soyer, and C. R. Natoli, *Phys. Rev. B* **55**, 2570-2577 (1997).
66. C. A. Ashley and S. Doniach, *Phys. Rev. B* **11**, 1279 (1975).
67. F. W. Kutzler and D. E. Ellis, *Phys. Rev. B* **29**, 6890-6900 (1984).
68. A. D. Smigellkas and E. O. Kirkendall, *AIME* **171**, 130 (1947).
69. C. M. Wang, D. R. Baer, J. E. Amonette, M. H. Engelhard, M. J. Antony, and Y. Qiang, *Ultramicroscopy* **108**, 43-51 (2007).
70. H. V. Atkinson, *Oxidation of Metals* **24**, 177-197 (1985).
71. Y. Y. Andreev and A. A. Shumkin, *Protection of Metals* **42**, 221-226 (2006).
72. D. R. Baer, J. E. Amonette, M. H. Engelhard, D. J. Gaspar, A. S. Karakoti, S. Kuchibhatla, P. Nachimuthu, J. T. Nurmi, Y. Qiang, V. Sarathy, S. Seal, A. Sharma, P. G. Tratnyeke, and C. M. Wang, *Surf. Interface Anal.* **40**, 529-537 (2008).
73. F. Zhang, S. W. Chan, J. E. Spanier, E. Apak, Q. Jin, R. D. Robinson, and I. P. Herman, *Applied Physics Letters* **80**, 127-129 (2002).
74. L. Wu, H. J. Widemann, A. R. Moodenbaugh, R. F. Klie, Y. Zhu, D. O. Welch, and M. Suenaga, *Phys. Rev. B* **69**, 125415 (2004).
75. S. Tsunekawa, R. Sivamohan, S. Ito, A. Kasuya, and T. Fukuda, *Nanostruct. Mater.* **11**, 141-147 (1999).

## Chapter 6: Cr-Doping and Heat-Treatment Effects on Core-Shell Ni Nanocluster Films

### 6.1 Introduction

With nanomaterials and nanostructures gaining popularity in recent years to be used in different applications and fields like bio-medicine, data storage, and waste water treatment,<sup>1-3</sup> fine tuning of the synthesis process of nanomaterials becomes very essential to meet the challenge of attaining desired surface morphology, stoichiometry, electrical and magnetic properties for specific applications. It has been found that dispersion strengthening through particles and precipitates in commercial alloys exhibit good corrosion resistance and mechanical properties even at elevated temperatures.<sup>4-5</sup> Apart from the commercial oxide dispersion strengthened (ODS) alloys, dispersion of nano-sized clusters in the alloy matrix, also called as Nano Ferritic Alloys (NFA) has been found to show radiation and high temperature strength.<sup>6</sup> It is well known that, properties and behavior of such nanoparticles of metals and alloys as well as their oxide or compound critically depend on the particle characteristics, such as size, morphology, crystal structure, and the surface characteristics.<sup>7,8,9</sup> Presence of impurities or dopants and exposure to aggressive environment like elevated temperature or pressure in these nanomaterials were known to have caused changes in magnetic and structural properties of metal nanoparticles.<sup>10,11,12</sup> Therefore, it is significant to impose desired properties by engineering such nanoparticles and to understand their behavior separately before dispersing them in alloys. In nuclear reactors and gas turbines, materials exposed to high temperature results in degradation of material properties. The generation-IV nuclear reactor like Supercritical-water-cooled reactor (SCWR), Sodium-cooled fast reactor (SFR), and Lead-cooled fast reactor (LFR) are expected to have an operating temperature between 500 °C and 800 °C, which is much higher than the operating temperature of current generation nuclear reactors.<sup>13,14</sup> Hence, high temperature strength is required in Gen-IV reactor materials. Although, the expectations are high for using the NFA in the Gen-IV reactors, much investigation is needed in this area. Stainless steel (SS) is a common material used in nuclear reactors which has Ni and Cr content to improve strength, and Ni-based alloys have

good high temperature application. Chromium brings resistance to corrosion while nickel offers greater toughness at a specified carbon level. Since Ni and Cr are the major contributors for improved high temperature strength in SS and Ni nanoparticles have been extensively studied for diverse applications over a few decade,<sup>15,16</sup> utilizing Ni nanoparticles with Cr-doping in SS could positively impact the dispersion strengthening phenomenon. In Chapter 4 the synthesis, structure and electronic structure of the Ni and Cr-Ni nanoparticles were discussed. This chapter helps in understanding these property changes at nanoscale under high temperature as it is essential for applications. Although characteristics of Ni-Cr super-alloys are well established, the atomic percentage of Cr in these alloys are usually over 20 at.% and less is known for Cr concentration less than 10 at%. Therefore, in this study Ni (CS-Ni) and 5 at.% Cr doped Ni (CS-Ni5Cr) core-shell nanoclusters (NCs) are investigated for their behavior under heat-treatment (HT) at 600 °C. In this chapter we report the core-shell Nickel (CS-Ni) and 5% Chromium-doped core-shell Nickel (CS-Ni5Cr) nanocluster (NC) films prepared by a nanocluster deposition system and the heat-treatment (HT) induced magnetic, structural and electrical property changes. Both the films were heat-treated at 600 °C for 30 min under a constant flow of Argon gas. The presence of antiferromagnetic Cr in the as-prepared CS-Ni5Cr film is found to reduce the saturation magnetization. Interestingly, after HT Cr contributes to the enhancement of saturation magnetization in CS-Ni5Cr films. Growth in magnetic domain and increase in magnetic interaction after HT are observed. Particle size growth and aggregation after HT are inferred and the average particle size increased in both the films. The electrical conductivity of the films is in conformity with the surface morphology of the films. The Cr-doping and HT methods are reported as effective methods to bring controlled property changes in Ni based films.

## 6.2 Sample Preparation

The CS-Ni and CS-Ni5Cr films in this study were prepared by the state-of-the-art cluster deposition system, which combines magnetron sputtering with gas aggregation technique as

described in details in our previous reports<sup>17,18</sup> and by carefully allowing the nanoclusters to deposit on the silicon substrate. By controlling the sputtering power, aggregation distance, He to Ar gas flow rate, pressure and the temperature inside the aggregation chamber, the cluster size growth inside the aggregation chamber was controlled. By allowing the clusters leaving the aggregation chamber to combine with oxygen gas in the reaction chamber, the desired core-shell nanocluster films were obtained.<sup>19</sup> The Ni atoms were sputtered from a nickel target inside the aggregation chamber at a power of 200 W by supplying 400 sccm (standard cubic centimeters per minute) of Ar gas and 30 sccm of He gas. These Ni atoms aggregate under the influence 1.4 Torr pressure and -5 °C aggregation temperature to form Ni NCs as they travelled a distance of 288 mm in the aggregation chamber. These NCs were then allowed to react with 2 sccm oxygen in the reaction chamber, to form the desired CS-Ni NCs with core as Ni and shell as NiO, which were subsequently deposited on a Si wafer in the deposition chamber to form CS-Ni NC film. The same procedure was followed to prepare the CS-Ni5Cr film except here a Cr doped Ni target was used. Cr dopant was added at a nominal concentration of 5% and the concentration was controlled by adjusting the relative area of Ni and Cr on the sputtering target. For the films in this study, a total of 0.119 mg of CS-Ni and 0.134 mg of CS-Ni5Cr nanoparticles were uniformly deposited over silicon substrates with an area of 8 mm × 8 mm. The thickness of the deposited films of CS-Ni and CS-Ni5Cr were found to be 291 nm and 288 nm based on the theoretical specific densities of Ni (8.9 g/cm<sup>3</sup>), O (1.14 g/cm<sup>3</sup>) and Cr (7.2 g/cm<sup>3</sup>). Some nanoclusters were collected in Transmission Electron Microscope (TEM) grids to study the particle sizes and nanostructures. These samples were heat-treated in a Lindberg mini furnace up to 600 °C in 15 minutes at a heating rate of 39 °C/s and then maintained at a constant temperature of 600 °C for the 30 minutes. The heat-treated samples were allowed to cool down in the furnace to room temperature. Throughout the whole HT process a constant argon gas flow of 4 liters per minute (LPM) was maintained to avoid oxidation of the films. The measurements were done before and after doping, and before and after HT in all these samples, to investigate the changes in

the structural, magnetic and electrical properties. Transmission Electron Microscope (TEM) images were taken in JEOL 2010J 200 keV analytical TEM with Angstrom-scale resolution. Energy-Dispersive X-ray Spectroscopy (EDS) measurements were carried out in Zeiss Supra 35 variable-pressure SEM having 1 nm resolution. The magnetic measurements were carried out in the DMS 1660 Vibrating Sample Magnetometer (VSM) at magnetic fields between -1.35 to 1.35 Tesla. X-Ray diffraction (XRD) measurements were performed in Siemens D5000 Powder X-ray Diffractometer with Solex solid-state detection system and Cu radiation. The surface morphology and magnetic domain images were taken by Atomic Force Microscope (AFM), Magnetic Force Microscope (MFM).

### 6.3 Results and Discussion

A TEM images in Figure 6.1 shows that the average particle size of both CS-Ni and CS-Ni5Cr films to be around ~20 nm. The inset of Figure 6.1(a) shows a single CS-Ni NC with ~2 nm thick NiO layer formed on the surface. This thin oxide layer is formed at the surface when oxygen released in the deposition chamber of the cluster deposition system reacts with the NCs at room temperature. Figure 6.2 (a, b) shows the XRD pattern of the as-prepared CS-Ni and CS-Ni5Cr films. It confirms the presence of Ni and NiO phases with the crystal planes of Ni (111) and NiO (200) slightly shifted. Ni has a face centered cubic (FCC) structure and NiO has a rock salt structure. The nanoclusters of the CS-Ni and CS-Ni5Cr films sit one over the other and are loosely connected forming a porous NC film on the Si substrates. This porous structure exposes the silicon at the base to the X-ray during XRD measurement and consequently leading to the detection of silicon peak in the XRD pattern for these two films. Although the elements in these films are dominated by the presence of NiO and Ni, there is no evidence in the XRD pattern for the presence of any phases of Ni-Cr or the corundum structured  $\text{Cr}_2\text{O}_3$ . Unlike the alloys having more than 10% of Cr, which oxidizes Cr and form a protective layer of  $\text{Cr}_2\text{O}_3$  to prevent further oxidation of metal, this Ni NC film with 5% of Cr does not form any  $\text{Cr}_2\text{O}_3$  phase.

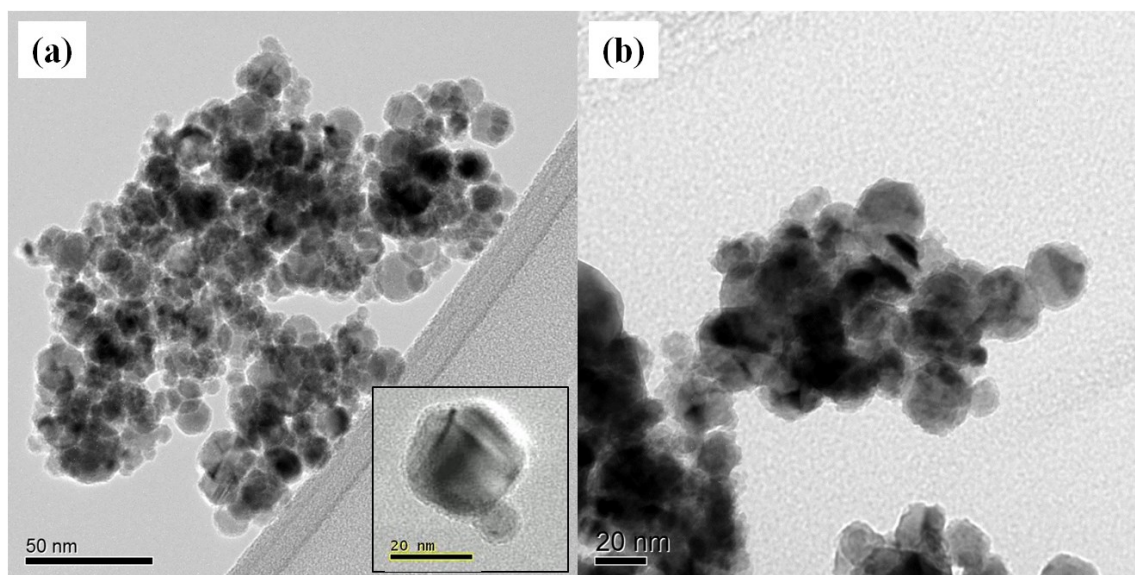


**Figure 6.1** TEM images of (a) CS-Ni (b) CS-Ni<sub>5</sub>Cr NCs. The inset shows a single CS-Ni NC with ~2 nm oxide layer thickness.

Although Cr is not detected in the XRD pattern, the presence of Cr is confirmed by the EDS measurement. Figure 6.3 shows the EDS spectra of the CS-Ni and CS-Ni<sub>5</sub>Cr films. It is confirmed from the area scan and point scan of EDS that 3.76 at.% of Cr is present in the CS-Ni<sub>5</sub>Cr film. Since there is evidence from the EDS measurement for the presence of Cr and since from XRD results there is no Cr<sub>2</sub>O<sub>3</sub> phase in the sample, consequently it follows that the Cr should be distributed as interstitial solutes in the Ni and NiO solid solution in these films. It has been confirmed from our previous study that in similar samples Cr is uniformly distributed as solute atoms forming a solid solution with the Ni lattice in the core of the CS-Ni<sub>5</sub>Cr NCs and no Cr enrichment is observed on the surface oxide (NiO) layer.<sup>20</sup> Even after the HT there was no evidence from XRD for the formation of any new phases of Ni-Cr or Cr<sub>2</sub>O<sub>3</sub> confirming that Cr is still dispersed as solutes or segregated as precipitates within the Ni lattice.

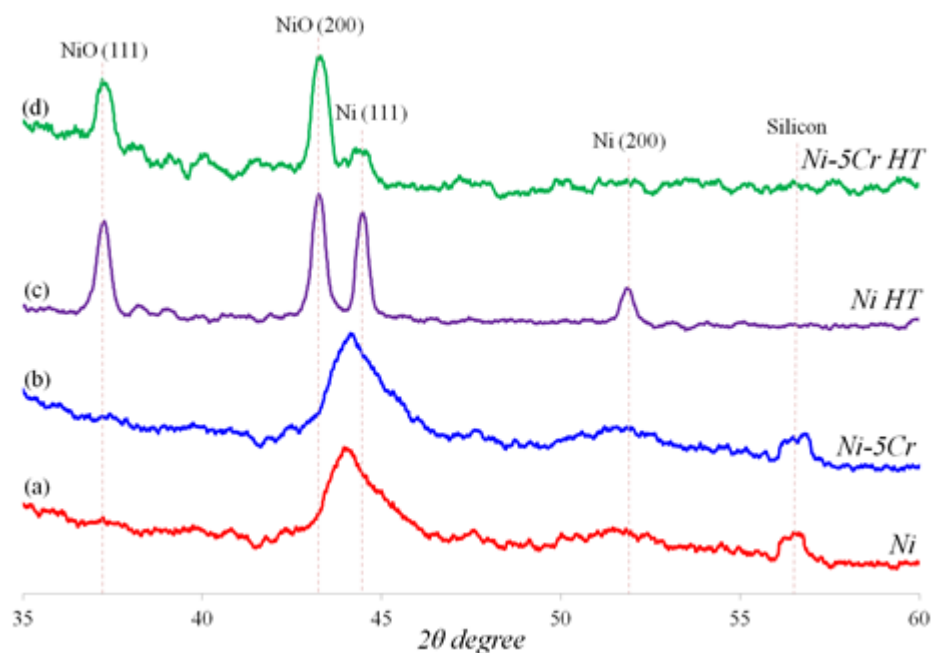


**Figure 6.2** XRD pattern for the (a) CS-Ni, (b) CS-Ni5Cr, (c) Heat-Treated CS-Ni and (b) Heat-treated CS-Ni5Cr NC films.

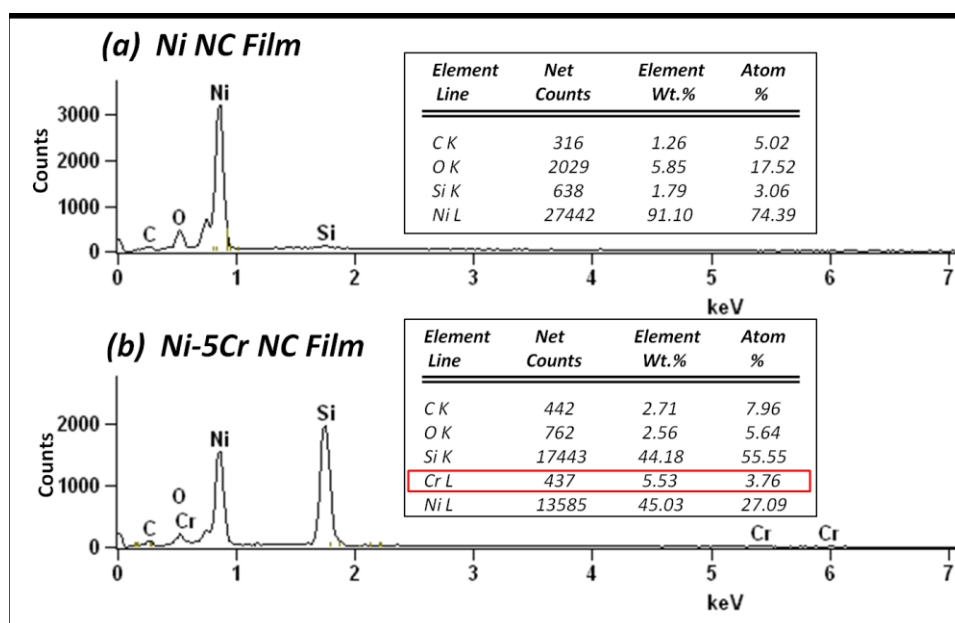


**Figure 6.3** EDS spectra for the CS-Ni and CS-Ni5Cr NC films. The insets show the at.% of the elements in films.

Figure 6.4 shows the hysteresis loops corresponding to the CS-Ni and CS-Ni5Cr films deposited on the silicon substrates. The saturation magnetization ( $M_s$ ) values for CS-Ni and CS-



Ni5Cr films are found to be about 22 emu/g and 8 emu/g. The drop in  $M_s$  in CS-Ni5Cr films is attributed to the uniform distribution of the antiferromagnetic Cr, which couples with the ferromagnetic Ni through exchange integration. Our previous study on Cr doped Fe nanoclusters confirms that the drop in  $M_s$  is due to the ferromagnetic-antiferromagnetic exchange coupling.<sup>21</sup> Although the magnetic remanence ( $M_r$ ) in both the films are almost the same, which is  $\sim 0.20$  emu/g, the coercivity ( $H_c$ ) values of CS-Ni (5 Oe) and CS-Ni5Cr (10 Oe) are different. The  $H_c$  in the CS-Ni5Cr film is almost double than that of the CS-Ni film because of the addition of 5 at.% Cr dopant in the Ni samples. This is due to the antiferromagnetic-ferromagnetic interaction (AFI), which takes more energy to nullify the remanent magnetization in the sample. The hysteresis loops of heat-treated CS-Ni and CS-Ni5Cr films show tremendous effect on the enhancement of magnetic saturation, magnetic remanence and coercivity.

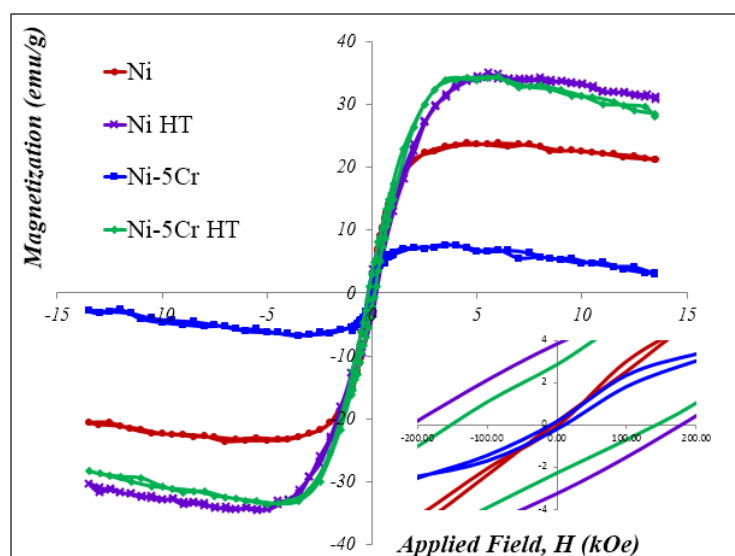


**Figure 6.4** Hysteresis loops measured in VSM for CS-Ni and CS-Ni5Cr NC films before and after HT. The inset shows near zero fields.

Table 6.1 summarizes the magnetic properties of the CS-Ni and CS-Ni5Cr films before and after HT. Although the changes in  $M_r$  and  $M_s$  in both films are similar after the HT, the change in  $M_s$  of these films suggest that the effect of AFI in the CS-Ni5Cr film no longer dominates. Because after HT both the films reaches almost the same  $M_s$  and both the films exhibits almost the same

ferromagnetic behavior. This suggests that the signal due to the AFI in the CS-Ni5Cr sample is no longer strong compared to the strong ferromagnetic interaction (FI) from Ni. Therefore it can be concluded that Cr is no longer uniformly distributed in the nanoclusters aggregates, instead should have been segregated as precipitates. It's also clear that the aggregation of nanoclusters has led to the growth and domination of ferromagnetic domains of Ni. After HT CS-Ni5Cr film exhibits magnetic properties similar to that of the heat-treated CS-Ni NC film, which can be well understood from the SEM, AFM and MFM imaging.

**Table 6.1** Hysteresis data for CS-Ni and CS-Ni5Cr NC Films before and after HT

<i>Data</i>	<i>Ni NP film</i>		<i>5Cr-Ni NP film</i>	
	<i>Before</i>	<i>After</i>	<i>Before</i>	<i>After</i>
<b>Ms (emu/g)</b>	22	35	8	36
<b>Mr (emu/g)</b>	0.16	3.5	0.2	3.6
<b>Hc (Oe)</b>	4	195	8	210

The SEM images (Figure 6.5) show that in CS-Ni film after HT, aggregation of particles is observed, but the aggregation of nanoclusters in the CS-Ni5Cr film is large in comparison with the CS-Ni film such that it forms island like structures on the surface of the film. It is obvious that the presence of Cr in CS-Ni5Cr film has a strong influence on the structural and magnetic behavior unlike the CS-Ni NC film, which does not have any Cr content in it. It is also evident here that based on the elemental composition of the films the level of nanocluster aggregation differs. While the structural changes from the SEM images verify the change in magnetic properties, the AFM and MFM images give insight to the growth of particles, magnetic domain and magnetic interaction.

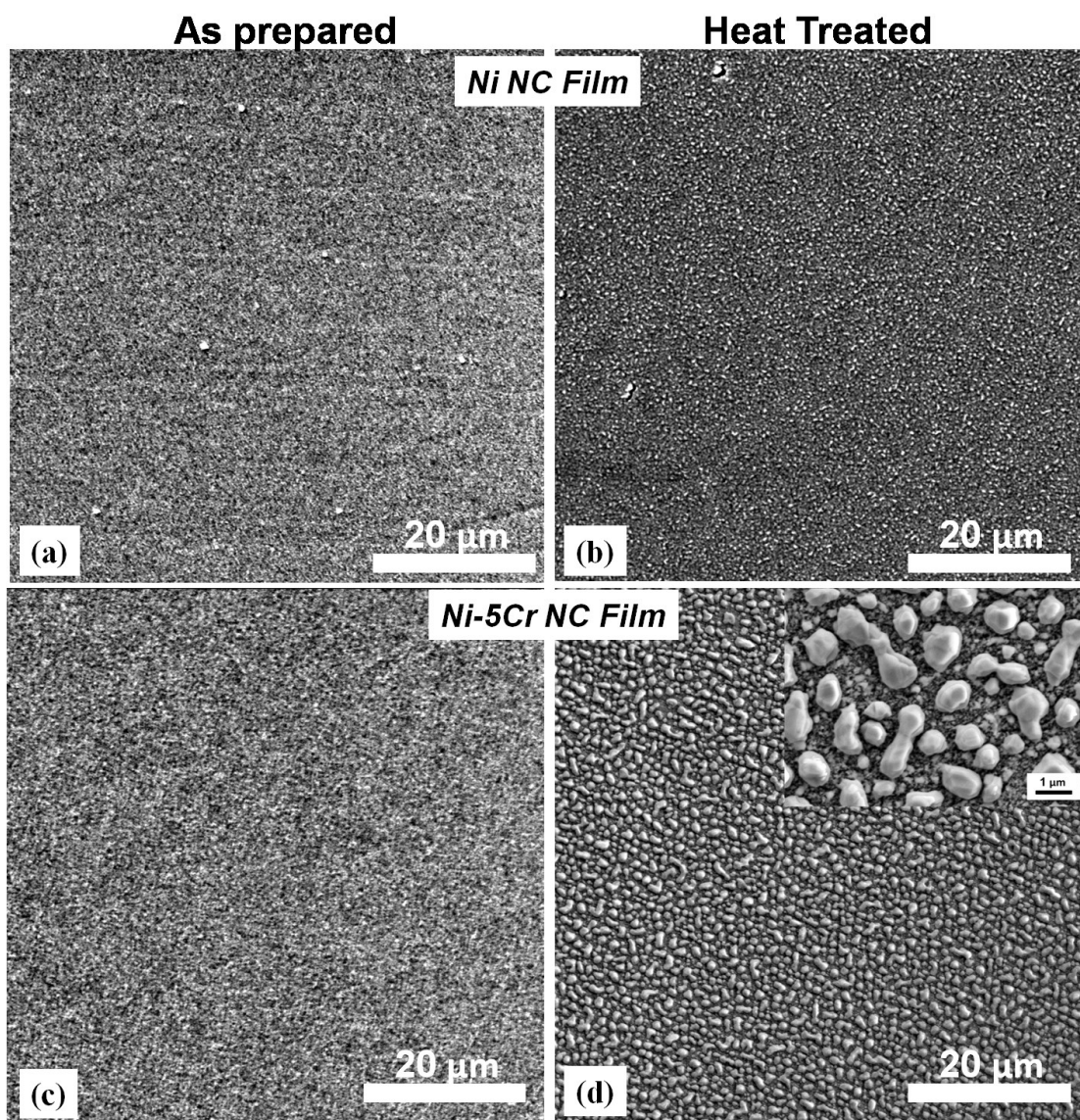


**Figure 6.5** SEM images of the CS-Ni and CS-Ni5Cr NC films on Si substrate before and after HT.

The AFM images in Figure 6.6 (a, b) confirm that the cluster size of the CS-Ni films has grown almost double the size after HT and the loosely connected particles are now in close vicinity with each other. The dark shades of the MFM image (Figure 6.6(c)) again confirm that FI is weak in the as prepared CS-Ni film since the particles are loosely connected and the ferromagnetic Ni cores are far away from each other as they are separated by the antiferromagnetic NiO layer.

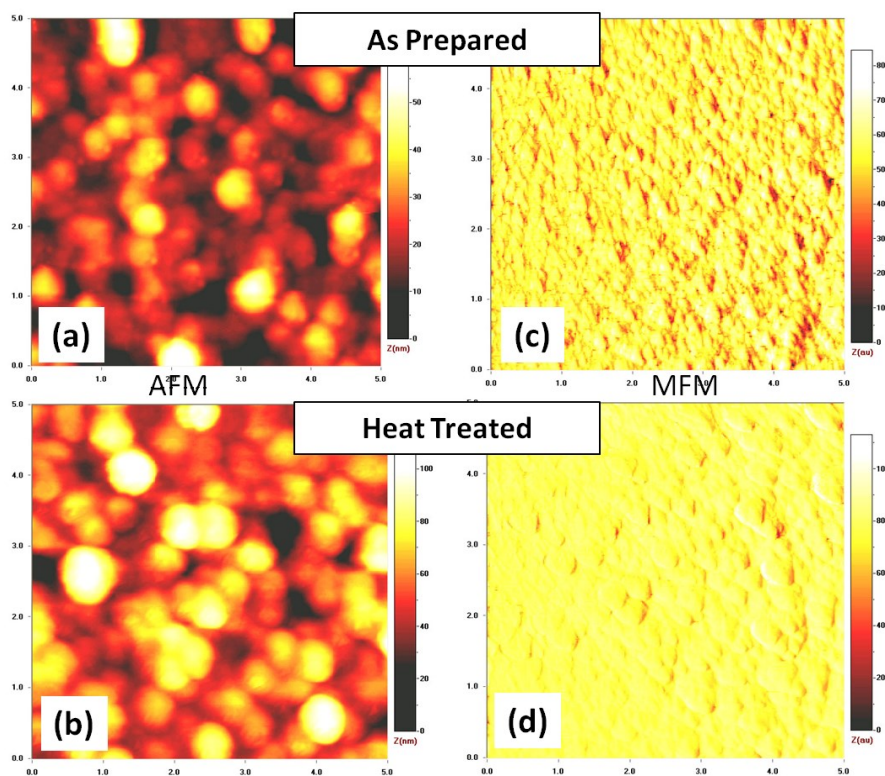


**Figure 6.6** AFM and MFM images of CS-Ni films before and after HT.

The coupling of ferromagnetic Ni core and the antiferromagnetic NiO shell contributes to the reduction of FI in CS-Ni films. However after HT, as the Ni core in particles come in close vicinity with each other the magnetic domains grow larger and the FI is improved in the heat-treated CS-Ni film. The AFM and MFM images of CS-Ni5Cr film in Figure 6.7 show the effect of Cr-doping in the structural and magnetic properties of these films. The appearance of dark shades in the MFM images of CS-Ni5Cr film before HT is in conformity with the presence of uniformly distributed antiferromagnetic Cr and the domination of the AFI between Cr and Ni. However, after HT there is growth of magnetic domains and disappearance of dark shades, which confirms the strong FI, unlike the AFI before HT. These results explain the contribution of magnetic domain growth and magnetic interaction for the enhancement of magnetic properties in CS-Ni and CS-Ni5Cr films.

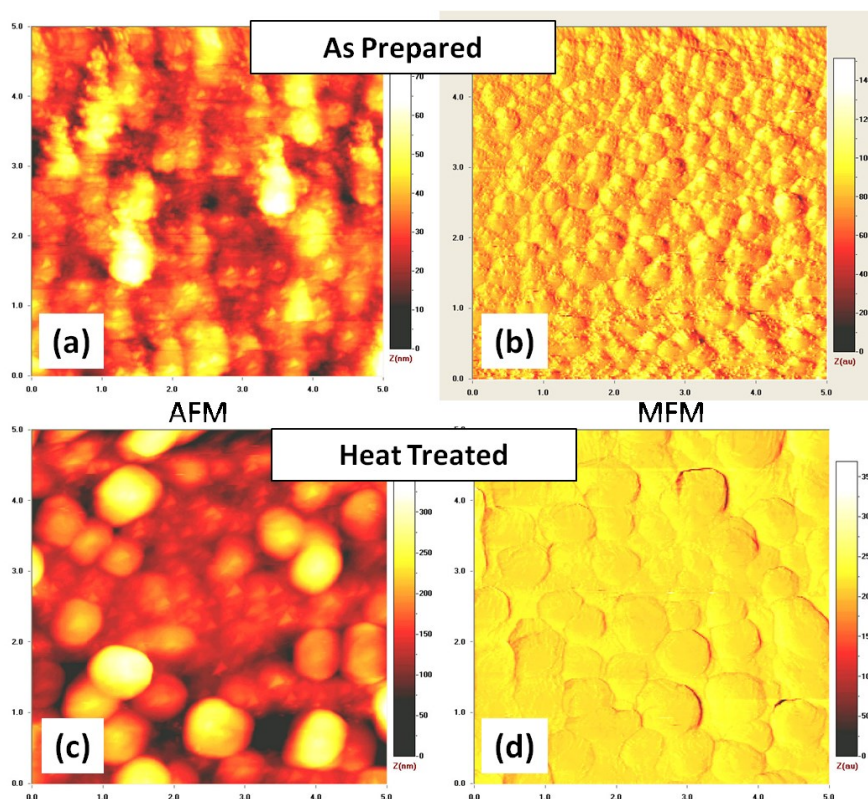


**Figure 6.7** AFM and MFM images of CS-Ni5Cr films before and after HT.

The level of enhancement of magnetization in each of these films is different due to the differences in the elemental composition. In other words, Cr as a dopant has acted as an agent for particle aggregation causing property changes. Inference from the AFM images is in conformity with the SEM images showing the particle size growth and the formation of island like structures in the CS-Ni5Cr films after HT.

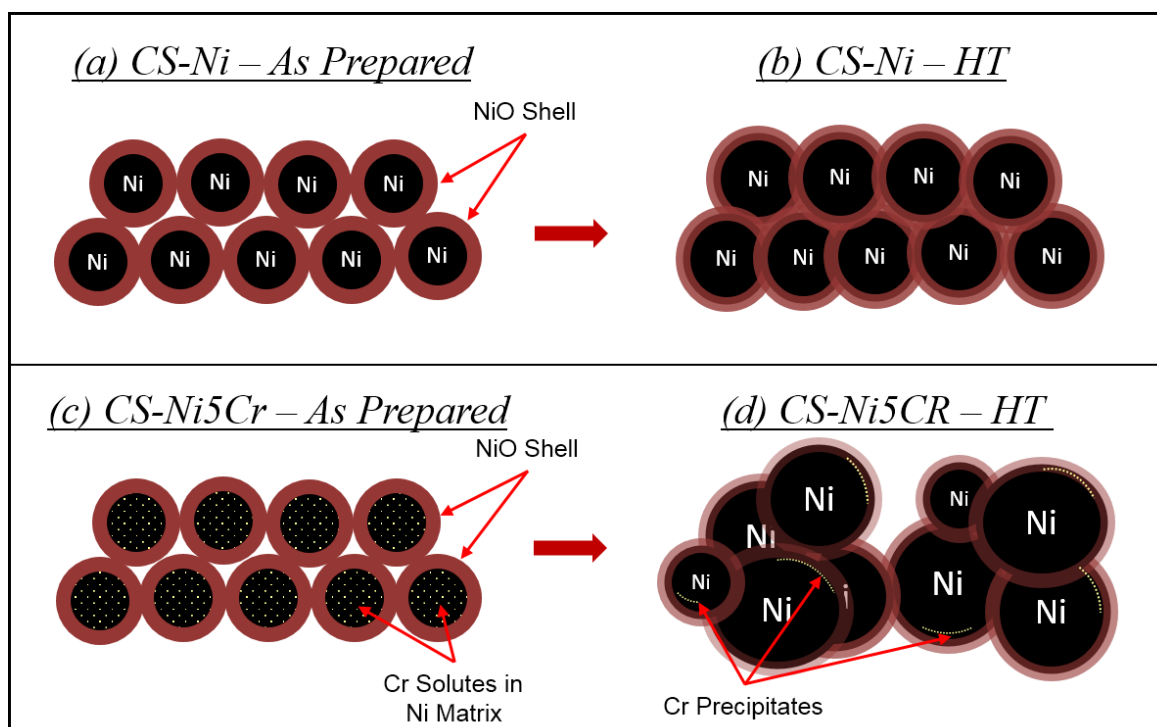


**Figure 6.8** Schematic of Cr-doping and HT effect in CS-Ni nanoclusters.

The schematic for the behavior of the CS-Ni NCs under the effect of Cr-doping and HT is shown in Figure 6.8. The as-prepared CS-Ni NCs are loosely connected through the antiferromagnetic NiO layer, which causes drop in  $M_s$ . The electrical conductivity of the film can also be deterred since NiO is a semi-conductor. However, after the HT the particles grow and merge with each other. The particles are no longer connected through the NiO layer but are directly connected through the diffused Ni atom from the core. This behavior can cause the weakening of AFI, strengthening of the FI and improvement of conductivity. In the CS-Ni<sub>5</sub>Cr, the uniformly distributed Cr in the Ni core forms AFI to drop the  $M_s$ , but improve the conductivity through Cr. After HT the segregation of Cr as precipitates enables the effective aggregation of Ni atoms to form island like structures. Although formation of island like structures leaves dis-connectivity in the heat-treated CS-Ni<sub>5</sub>Cr film, the presence of Cr segregates and Ni aggregates could still contribute to the better conduction of the film.



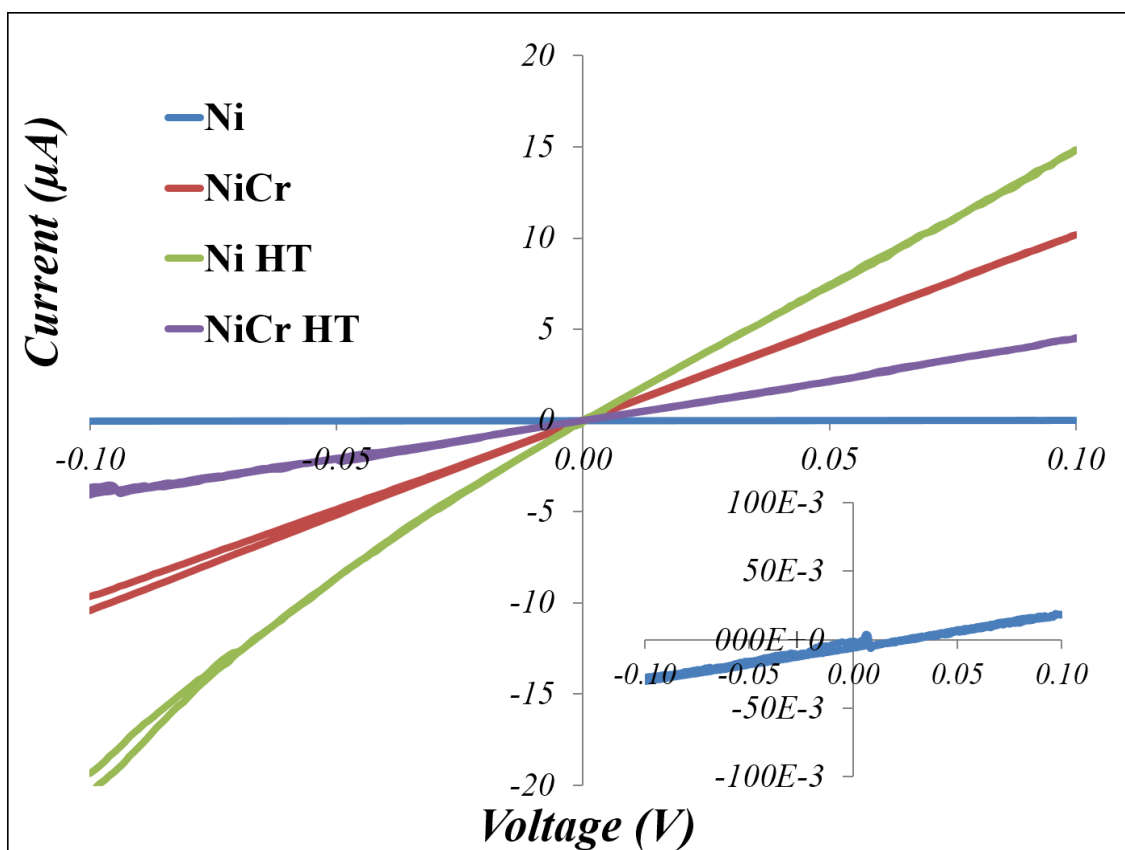


**Figure 6.9** I-V curves for the CS-Ni and CS-Ni5Cr films before and after HT.

The electrical conductivity of the CS-Ni and CS-Ni5Cr films before and after HT can be understood from the I-V curves shown in Figure 6.9. Some of the I-V curve loop is open because the electrons could take different path depending on the least resistant path and the surface morphology of the films. CS-Ni film show low conductivity of 0.06 S/m (slope=0.24) because the clusters are connected loosely and through the NiO semi-conductor layer. In CS-Ni5Cr film the conductivity (64.76 S/m) (slope=101.4) increases due to the presence of uniformly distributed Cr solute atoms in Ni and NiO solid solution. The conductivity of heat-treated CS-Ni film is the highest (102.37 S/m, slope=166.5) among the other films due to the aggregation of the clusters that favors the easy transfer of electrons. However, the conductivity of heat-treated CS-Ni5Cr film (30.44 S/m, slope=42.873) decreases because the formation of the island like structures reduces contact points as discussed before (Figure 6.5d) and the easy transfer of electrons.

## 6.4 Summary

Based Core-shell Ni NCs were studied for the effects of Cr-doping and HT. Cr-doping in Ni nanoclusters did not form any secondary phases in Ni instead stays as solutes in the Ni/NiO solid solution. Upon HT, effective changes of structure, magnetic properties and electrical conductivity occurred and a shift from strong AFI to FI was observed. The presence of Cr is found to be the major influence behind these changes. The observed changes in electrical conductivity of the films confirms to the changes in structural and magnetic properties. Cr-doping and HT methods could be effectively used to achieve desired property control in Ni based alloys to meet specific application standards. In addition to Ni, Fe is a major content in the nuclear reactors. Also with these Fe nanoparticles, Fe oxides and different phases of Fe with N or O can be prepared and investigated for the effect of radiation and its effects.



## 6.5 References

1. X. X. Zhang, G. H. Wen, S. Huang, L. Dai, R. Gao, and Z. L. Wang 2001 *J. of Mag. and Magnetic Materials*, **231** 9
2. J. Hu, G. Chen, and I. M. C. Lo 2006 *Journal of Environmental Engineering* **132** 709
3. J. Hu, G. Chen, and I. M. C. Lo 2005 *Water Research* **39** 4528
4. D. A. McClintock, M. A. Sokolov, D. T. Hoelzer, and R. K. Nanstad 2009 *J. of Nuclear Materials* **392** 353
5. D. K. Mukhopadhyay, F. H. Froes, and D. S. Gelles, 1998 *J. of Nuclear Materials* **258** 1209.
6. J. Chen and W. Hoffelner 2009 *J. of Nuclear Materials* **392** 360
7. Y. Sun, and Y. Xia 2002 *Science* **298** 2176
8. S. Peng, C. Wang, J. Xie, and S. Sun, 2006 *J. Am. Chem. Soc* **128**, 10676
9. S. Sun, C. B. Murray, D. Weller, L. Folks, and A. Moser 2000 *Science* **287** 1989
10. J. Yang, B. Feng, Y. Liu, Y. Zhang, L. Yang, Y. Wang, M. Wei, J. Lang, and D. Wang 2009 *J. of Alloys and Compounds* **467** L21
11. S. Chen, J. Y. Huang, Z. Wang, K. Kempa, G. Chen, and Z. F. Ren 2005 *Applied Physics Letters* **87** 263107
12. S. Kumar, Y. J. Kim, B. H. Koo, and C. G. Lee 2010 *J. of Nanoscience and Nanotechnology* **10** 7204
13. T. Allen, J. Busby, M. Meyer, and D. Petti 2010 *Mater. Today* **13** 14
14. K. L. Murty and I. Charit, 2008 *J. Nucl. Mater.* **383** 189
15. Z. Wang, M. Kuok, S. Ng, D. Lockwood, M. Cottam, K. Nielsch, R. Wehrspohn, and U. Gosele 2002 *Phy. Rev. L* **89**
16. J. Park et al., 2005 *Advanced Materials* **17** 429
17. Y. Qiang, J. Antony, A. Sharma, J. Nutting, D. Sikes and D. Meyer 2006 *J. of Nanoparticle Research* **8** 489
18. J. Antony, Y. Qiang, D. R. Baer, and C. M. Wang 2006 *J. Nanoscience and Nanotechnology* **6** 568
19. M. Kaur, J.S. McCloy, W. Jiang, Q. Yao, and Y. Qiang 2012 *J. Phys. Chem. C* **116** 12875.
20. C.-M. Wang, D. R. Baer, S. M. Bruemmer, M. H. Engelhard, M. E. Bowden, J. A. Sundararajan, and Y. Qiang 2011 *J. Nanosci. Nanotechnol.* **11** 8488

21. M. Kaur, Q. Dai, M. Bowden, M. Engelhard, Y. Wu, J. Tang, and Y. Qiang 2013 *Appl. Phys. Lett.* **103** 202407.

## Chapter 7: Irradiation Effects on Fe-based Nanoparticles and Applications

### 7.1 Fe-Based Nanoparticle Granular Films

Iron is the fourth most abundant element in the Earth's crust (5% of Earth's mass) and it tops in saturation magnetization ( $\sim 210$  emu/g) among its ferromagnetic neighbors Nickel ( $\sim 58$  emu/g) and Cobalt ( $\sim 64$  emu/g). Because of its abundance, iron is being used effectively in a variety of applications that include nuclear reactors and nuclear power plants. Because of its fascinating behaviors as a nanoparticle, it is also being used in variety of research fields like magnetic recording, bio-medical applications etc. Even though this element is abundant, it never exists in its pure form in nature. It exists mostly as iron oxide everywhere from the earth's core to its surface. A pure iron exposed to air will be instantly oxidized by the process called initial oxidation to form a protective oxide layer on the metal. This phenomenon was first explained by Cabrera and Mott in the years 1948 and 1949.<sup>1</sup> As explained by Cabrera and Mott, the two reasons behind this oxidation are (1) tunneling of electrons from the metal surface to the oxide surface, setting up an electric field and (2) this electric field driving the core metal atoms to the surface for the oxide layer formation. The formed oxide layer remains stable, serving as a strong shield around the core iron metal, preventing further oxidation. Even in nuclear reactors, the major elemental composition of nuclear grade Stainless Steels (SS) is Iron. Iron is not the only metal to possess this characteristic; every metal that is exposed to atmosphere has a thin oxide layer on its surface and in case of SS alloy it is  $\text{Cr}_2\text{O}_3$ . Upon irradiation, the first impact is to the oxide layer and the damage starts from this oxide layer or the oxide layer film on the top of iron core. It is, therefore, essential to study the radiation impact on the oxide layer film. In this chapter, the superparamagnetic granular magnetite ( $\text{Fe}_3\text{O}_4$ ) films having an average grain size of 3 nm are investigated, for their structural and magnetic properties due to  $\text{Si}^{+2}$  ion irradiation. It was found that these films were magnetized following 5.5 MeV  $\text{Si}^{2+}$  ion irradiation to a fluence of  $10^{16}$  ions/cm<sup>2</sup> near room temperature, exhibiting a superparamagnetic to ferromagnetic transition after the irradiation. This change in the magnetic properties is attributed to

irradiation induced grain growth and structural modifications that lead to magnetic anisotropy. The irradiation has also resulted in an increase of the average grain size 3 nm to 23 nm, which was confirmed by the XRD. The dramatic change in the microstructure, as a result of particle aggregation and material condensation, is discussed in this chapter. The MFM results, which are discussed, confirm that the increase in magnetic domain size in the irradiated film is in the range of tens to several hundreds of nanometers. In the near-zero-field cooling process (ZFC), evidence is found that shows bipolar interactions between the nanoparticles in both the unirradiated and irradiated films. Data fits for the in-phase alternating current magnetic susceptibility ( $\chi$ ) of the unirradiated film indicate that the blocking temperature is  $\sim 150$  K, depending on frequency. Unusual behavior of susceptibility observed above Verwey temperature<sup>25</sup> ( $\sim 75$  K) for the irradiated film is also discussed in detail in this chapter.

## 7.2 Introduction to Granular Thin Films and Irradiation

Magnetic nanostructured materials, including thin films and multilayer structures, have attracted considerable attention in recent years because of new science<sup>2</sup> and interesting properties.<sup>3,4</sup> Most of the studies conducted are driven primarily by advances in the synthesis of complex structures and motivated by demands for higher-density information recording media. To this date very few irradiation studies have been conducted for granular films, in part because of the limited availability of the films. Some of the radiation studies conducted include the radiation impact on bulk graphite and composite thin films. The 2.25 MeV proton irradiation in graphite was found to have induced magnetic ordering and this was attributed to spontaneous magnetization from hydrogenated carbon atoms.<sup>5</sup> In addition to other thin films with various compositions (Co/Fe,<sup>6</sup> Co/Cu,<sup>7</sup> FePt<sup>8</sup> and NiFe<sup>9</sup>), extensive irradiation studies on Co/Pt<sup>10,11,12</sup> multilayer structures have been reported and it was found that irradiation modified magnetic properties, including a reduction in coercivity and remanent magnetization, loss of magnetic anisotropy, and transition of easy axis, through defect production, lattice strain release, interface roughening, and atomic mixing at the

interface. In this study we report the radiation exposure on this unique iron oxide thin granular film. Generally, magnetic properties of granular films are expected to be susceptible to nuclear radiation because of the large area of surface and interface susceptible to exposure. A slight change in bond distance and angles or the coordination number at surfaces and interfaces of nanostructures could dramatically affect the magnetic behavior.<sup>13</sup> Understanding the modification of the magnetic properties of granular films under irradiation can provide scientific assessment and prediction of the material performance in radioactive environments. The scientific foundation to be developed could also help control magnetic properties and design advanced devices. This chapter reports the radiation response of granular magnetite ( $\text{Fe}_3\text{O}_4$ ) films near room temperature. Magnetite composition was chosen as a model material in this study for the following two reasons. First, there are extensive experimental and theoretical reports on the magnetic properties of bulk, mono-crystalline, polycrystalline and granular films of  $\text{Fe}_3\text{O}_4$ , and second, the technique for preparation of high-quality granular  $\text{Fe}_3\text{O}_4$  films is well established. In addition to ion irradiation, near-zero-field cooling also has been used to study the magnetic properties of the films.

### **7.3 Synthesis and Characterization of Fe-based Granular Films**

Fe-based granular films of core-shell (CS) Fe- $\text{Fe}_3\text{O}_4$  and fully oxidized  $\text{Fe}_3\text{O}_4$  nanoparticles used in this study were prepared using a state-of-the-art nanocluster deposition system<sup>14</sup>; a detailed discussion about this is found in chapter 3. The nanoparticles were formed in the aggregation chamber, where sputtered Fe atoms were fully oxidized by supplying oxygen into the aggregation chamber and were allowed to aggregate through low-temperature condensation. A high-transmission mass selector integral to the system was used to achieve a narrow particle size distribution (~5%). The selected nanoparticles landed softly onto a Si (100) substrate at room temperature in the deposition chamber. For the film used in this study, a total of 0.344 mg  $\text{Fe}_3\text{O}_4$  nanoparticles was uniformly deposited over an area of  $4 \times 8 \text{ mm}^2$ , corresponding to an areal density of  $1.075 \times 10^{-3} \text{ g/cm}^2$  or film thickness of  $\sim 2.07 \text{ }\mu\text{m}$  based on the theoretical specific gravity of  $5.197 \text{ g/cm}^3$  for

$\text{Fe}_3\text{O}_4$ . To make the CS Fe-  $\text{Fe}_3\text{O}_4$  the Fe atoms were sputtered at a power of 200 W from a Fe target placed on the magnetron gun in the aggregation chamber by supplying 350 standard cubic centimeters per minute (sccm) of Ar gas and 50 sccm of He gas were allowed to react with 3 sccm oxygen by supplying the gases into a second chamber, the reaction/deposition chamber, to form the desired CS nanoparticles. After reacting with oxygen, the particles were deposited onto a Si substrate in this same chamber to form the granular film, which was an aggregate of nanoparticles. A total of 0.274 mg nanoparticles were uniformly deposited over an area of  $6 \times 4 \text{ mm}^2$  Si substrate for the sample discussed here. The actual linear thickness is greater because of the film porosity. The unirradiated film or a similarly prepared film having a comparable grain size and microstructure is used for comparison with the irradiated sample. The granular film was irradiated at normal incidence with 5.5 MeV  $\text{Si}^{2+}$  ions to a fluence of  $10^{16}$  ions/ $\text{cm}^2$  near room temperature using a 3.0 MV electrostatic tandem accelerator, as explained in chapter 3. A beam rastering system was used to ensure uniform irradiation over an area of  $12.5 \times 12.5 \text{ mm}^2$  covering the entire sample surface. Typical ion flux was on the order of 0.01 ( $\text{Si}^{2+}/\text{nm}^2$ )/sec and the increase of the sample temperature during the irradiation was less than 50 K. Computer simulations with the Stopping and Range of Ions in Matter (SRIM) code<sup>14</sup> were carried out to estimate the ion projected range in the film. Based on the theoretical specific gravity of  $\text{Fe}_3\text{O}_4$ , the ion projected range under the irradiation condition is  $\sim 2.1 \mu\text{m}$  with a FWHM of  $\sim 0.3 \mu\text{m}$ . Thus, the implanted Si peaked near the film/substrate interface in this study.

The magnetic properties were measured for the as-deposited and post-irradiated films using Physical Property Measurement System (PPMS, Quantum Design, San Diego, CA). Following irradiation, the sample was placed in the same manner under zero fields for remanence measurement at room temperature. Hysteresis measurement with an external field applied parallel to the sample surface was followed starting from 10 kOe. The crystal structure of the film was analyzed using the Philips X'pert Multi-Purpose Diffractometer (MPD) based on fixed  $\text{Cu K}_\alpha$  radiation ( $\lambda = 0.154187$

nm). Grazing-angle incidence x-ray diffraction (GIXRD) was employed to study the crystallographic phase and average size of the crystalline grains at room temperature. This technique eliminates strong diffraction peaks from the single crystal substrate. The film microstructures were examined using a HIM before and after irradiation. In addition, Magnetic Force Microscopy (MFM) was used to study the magnetic domains in the unirradiated and irradiated samples.

## **7.4 Fe<sub>3</sub>O<sub>4</sub> Granular Films**

### **7.4.1 Structural and Magnetic Property Changes of Fe<sub>3</sub>O<sub>4</sub> Granular Films**

As discussed in chapter 2, the enhancement of ferromagnetic behavior was observed in our superparamagnetic samples. Figure 7.1 shows the hysteresis loops for a granular Fe<sub>3</sub>O<sub>4</sub> film before and after Si<sup>2+</sup> ion irradiation, where the diamagnetic signal from the Si substrate has been subtracted. Before irradiation, the film does not possess any detectable magnetic remanence and coercivity at room temperature. The magnetization of the unirradiated film is not saturated at the maximum applied field of 10 kOe, where the corresponding value is ~8.2 emu/g. After irradiation, the film is magnetized with a remanence of 9.4 emu/g at room temperature. This magnetization was induced by the irradiation only. Hysteresis measurement was performed subsequently with the magnetic field parallel to the sample surface and the irradiated film showed a coercivity of 250 Oe and an unsaturated magnetization of 56 emu/g at ~10 kOe as shown in Figure 7.1. The remanent magnetization showed no change with the parallel and perpendicular hysteresis measurement, which is completely a different magnetization behavior that is exhibited in this case. In order to understand the change in the magnetic properties of the irradiated granular Fe<sub>3</sub>O<sub>4</sub> film, a number of characterizations have been performed to study the microstructures and magnetic domains. The increase in coercivity is clearly attributed to the grain growth and is discussed in sections below. The enhancement of magnetization should be more likely due to the enhancement of magnetic interactions between the magnetic domains in the irradiated samples and is discussed below.

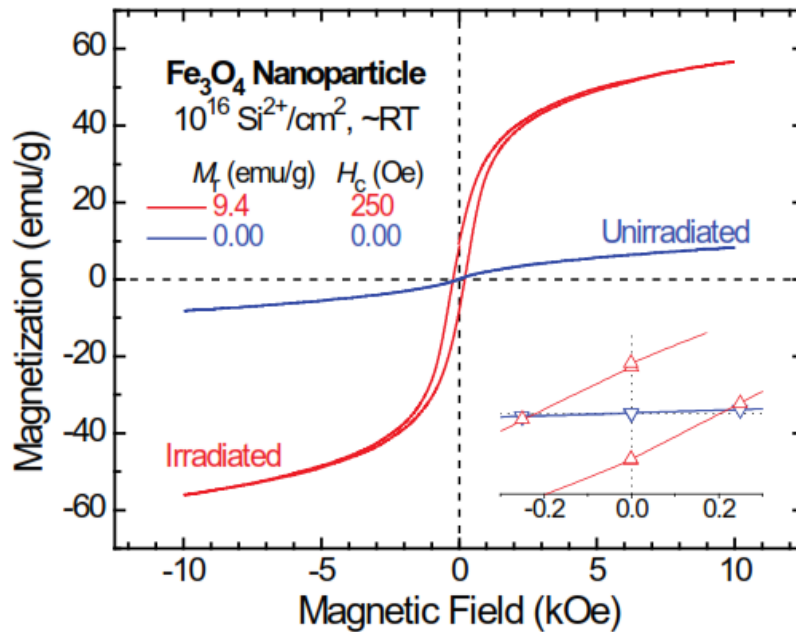


**Figure 7.1** Hysteresis loops of a granular Fe<sub>3</sub>O<sub>4</sub> film on Si before and after irradiation to a fluence of  $10^{16} \text{ Si}^{2+}$  ions/cm<sup>2</sup> near room temperature. The inset shows a magnified view near zero.

Figure 7.2 shows GIXRD patterns for the unirradiated and irradiated films, where the pattern intensity for the unirradiated sample was multiplied by a factor of four. The data indicates that the film is a single-phase cubic magnetite (Fe<sub>3</sub>O<sub>4</sub>) prior to irradiation. Neglecting the small lattice strain, the average grain size,  $s$ , was estimated using Scherrer formula<sup>16</sup>:

$$s = K \times \lambda / [\text{FW}(S) \times \cos \theta] \dots \dots \dots (7.1)$$

where  $\text{FW}(S)$  is the specimen broadening (peak FWHM subtracted from the instrument broadening),  $\theta$  is the peak position, and  $K$  is the shape factor of the average crystallite and is taken as 0.9 in the estimation. Using Eq. (7.1), the average grain size for the unirradiated film was determined to be  $3 \pm 1$  nm based on the well-resolved (400) peak. Following irradiation, even though the diffraction peaks from all the observable planes become much sharper, the crystalline phase (cubic Fe<sub>3</sub>O<sub>4</sub>) remains unchanged, as shown in Figure 7.2 confirming the fact that there is a tremendous growth in the grain size. The average grain size for the irradiated film was estimated again to be  $23 \pm 1$  nm based on the (400) peak. The grain shrinkage or growth can induce amorphization or crystallization



at the surface/interface of crystalline particles depends on material composition, irradiation temperature and dose rate of ion irradiation and can result in grain shrinkage or growth. Studies in the past have confirmed the fact of grain boundary amorphization<sup>17,18</sup> or crystallization<sup>19,20</sup> for different ceramic materials under ion irradiation. The significant increase in the Fe<sub>3</sub>O<sub>4</sub> grain size in this study could be attributed to radiation-enhanced epitaxial growth and possibly coalescence of smaller crystalline grains. The epitaxial growth is an oriented overgrowth of crystalline material upon the surface of another crystal of different chemical composition but similar structure. The coalescence of smaller grains could be due to ‘Ostwald Ripening’ where the grains break and aggregate with the neighboring grains resulting in grain growth.

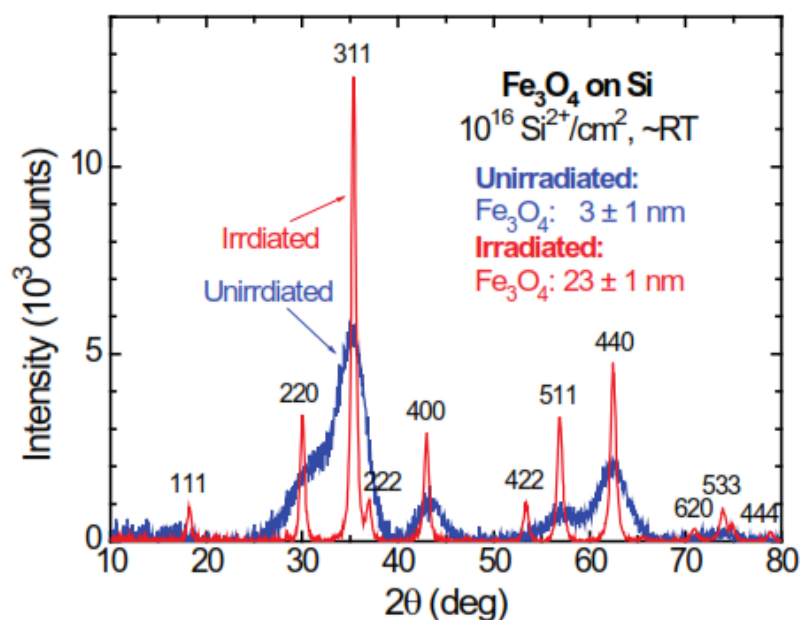


**Figure 7.2** Background subtracted GIXRD patterns for a granular Fe<sub>3</sub>O<sub>4</sub> film on Si before and after irradiation. The pattern intensity for the unirradiated film is multiplied by a factor of 4.

#### 7.4.2 Surface Microstructures of Fe<sub>3</sub>O<sub>4</sub> Granular Films

Studying the surface microstructures of films reveals important details about grain growth, which may help researchers, solve its underlying mysteries. Since the granular film in this study is susceptible to electronic energy absorption, only a small amount of electronic energy may be deposited near the surface during the structural examination. The high-resolution HIM micrographs

for the film before and after irradiation are shown in Figure 7.3. As shown in Figure 7.3 (a), the unirradiated film exhibits clearly that the nanoparticles are loosely interconnected with each other in the film. Also it is evident that the nanoparticles have a typical size of  $\sim 10$  nm and each may contain several crystalline grains having  $\sim 3$  nm size with different orientations. Even though the film is highly porous with a large surface area, after irradiation, the film becomes much denser, as shown in Figure 7.3 (b), which may be a result of grain growth and particle aggregation. The resulting structure is complex with varied particle sizes ranging from 30 and 50 nm. Clearly, the surface roughness is reduced significantly and the constituent nanoparticles are networked more tightly. Adhesion of the  $\text{Fe}_3\text{O}_4$  film to the Si substrate is also found to be much stronger. It should be noted that the structural modification is mainly a result of electronic energy deposition of the 5.5 MeV  $\text{Si}^{2+}$  ions during irradiation. Nuclear energy deposition that generates atomic displacements becomes important only near the film/substrate interface just before the implanted Si ions reach their projected range.

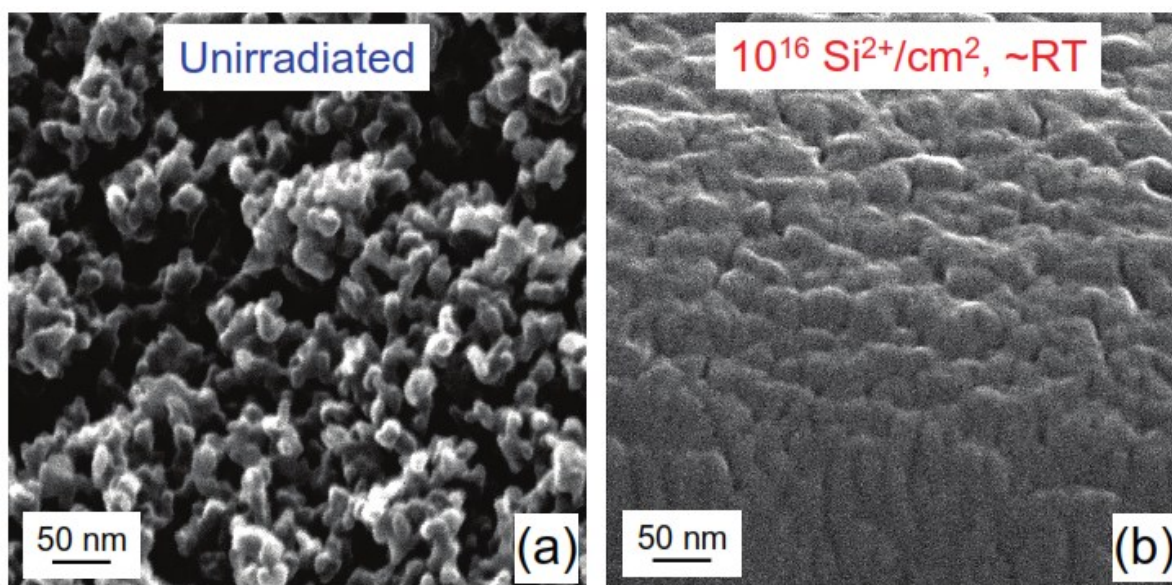


**Figure 7.3** High-resolution HIM micrographs of a granular  $\text{Fe}_3\text{O}_4$  irradiation.

The unirradiated Fe<sub>3</sub>O<sub>4</sub> granular film contains particles with size ~10 nm and it is well known that each particle can contain several grains in it. The grain size for the unirradiated sample was estimated to be ~3 nm using Eq. 7.1. After irradiation both the particle size and grain size are found to have increased. This change in the grain/particle size and an alteration in the interatomic and electronic configurations at the grain/particle surface and interface can be the reason behind change in magnetic properties. It is also known that each grain has a single magnetic domain that is relatively free to rotate. When an external field is applied, the magnetic moments of the individual grains and particles tend to align with the field to minimize the system energy, which leads to magnetic anisotropy and magnetization of the film. Once the external field is removed, thermal randomization of the moment orientation occurs; resulting in vanishing magnetization (no coercivity and remanence) and this behavior is paramagnetic. If single domain particles exhibit similar behavior then they are superparamagnetic. The unirradiated Fe<sub>3</sub>O<sub>4</sub> film consisting of loosely interconnected particles are identified to have small domains with a larger moment and it is superparamagnetic.

Due to ion radiation process, energy is deposited into the material through both elastic and inelastic interactions between the energetic ions and electrons/nuclei in the material. As predicted by SRIM,<sup>15</sup> elastic collisions that produce atomic displacements are important only near the film/substrate interface in this study. On the other hand inelastic interactions lead to electron excitation and ionization of the target atoms throughout the entire thickness of the film. Local heating along the ion track was already reported in chapter 2 and in this case due to inelastic collision a large amount of the primary ion energy is eventually coupled to phonons, which induces local heating along the ion track. As a result of the local temperature increase, the inelastic process can enhance epitaxial re-crystallization at the amorphous-crystalline interface and promote coalescence of small crystalline grains and it can be evidently seen from Figure 7.3 (b). As grain grows, nanoparticles aggregate and magnetic domain expands due to ion beam enhanced energy. Nucleation and growth of magnetic domains could take place at defects, such as grain boundaries.

Domain rotation could be associated with the radiation-induced modification of the interatomic and electronic structures at the grain/particle surface. The resulting larger grain (~23 nm in size) is expected to still have a single magnetic domain because the formation of a flux-closure configuration is energetically unfavorable at this small size. The critical size for superparamagnetic in magnetite at room temperature is known to be 17 – 20 nm for low-frequency susceptibility measurements<sup>21</sup> but is smaller for shorter measurement times (9 nm for Mossbauer measurements).<sup>22</sup> The resulting larger grain (~23 nm in size) is expected to still have a single magnetic domain because the formation of a flux-closure configuration is energetically unfavorable at the small size. Domain wall motion proceeds as the grain grows and neighboring particles interact, leading to a much larger size than the particle dimension (see MFM data below). However, the distribution of the moment orientation is largely random at room temperature. A majority of the magnetic moments cancel themselves in the film, but a complete cancellation does not occur because of the structural inhomogeneity and imperfection with complex grain boundaries and different grain sizes that may create some high-energy barriers. These energy barriers must be overcome in order to rotate the local moment. At room temperature, thermal energy is not high enough to activate the rotation process. Thus, a small remanence in the film emerges. When an external field is applied, domains tend to align with and reinforce the external field. In the magnetization process, domain wall pinning is evident since the loop as shown in Figure 7.1 is not a perfect square. Domain rotation and possible nucleation and growth at structural defects are expected to be the main mechanisms although wall propagation cannot be completely ruled out. The same remanent magnetization remains once the external field is removed because the atomic structure of the film is not affected during the magnetization and demagnetization processes. An opposite field must be applied ( $H_c = 250$  Oe) to completely cancel the magnetization in the film. The observed behavior of the irradiated film is characteristic of ferromagnetic materials.

From the discussion above, it is apparent that the granular  $\text{Fe}_3\text{O}_4$  film underwent a superparamagnetic to ferromagnetic phase transition during the ion irradiation. For multilayer structures, changes in magnetic properties due to ion irradiation are quite different. A previous study on thin Pt/Co/Pt/ $\text{Al}_2\text{O}_3$  films<sup>2</sup> reported a reduction in the magnetocrystalline anisotropy, spin orientation transition from easy axis out-of-plane to easy axis in-plane, and a ferromagnetic to paramagnetic transition at progressively higher doses of  $\text{He}^+$  ion irradiation. The physical interpretations were based on lattice relaxation, ion-beam mixing, and interface roughening. Similar effects of  $\text{Ga}^+$  ion irradiation on a Co/Pt multilayer was also reported.<sup>23</sup>

#### **7.4.3 Magnetic Domains of $\text{Fe}_3\text{O}_4$ Granular Films**

A combination of AFM and MFM measurements were carried out in order to study the magnetic domains and examinations of the unirradiated and irradiated films. The surface topography for the unirradiated and irradiated films is shown in Figures 7.4 (a) and (c), respectively. Evidence of cluster size growth and magnetic interactions are clearly depicted in the figures below. The spatial resolution under the experimental condition was  $\sim 50$  nm. The magnetic force gradient was measured based on the resonant frequency shift. The resonant vibration frequency of the cantilever is  $\sim 80$  kHz and the detection limit for the frequency shift is  $\sim 0.1$  Hz. During the MFM scanning over the same AFM area, the cantilever was lifted  $\sim 10$  nm from the surface while keeping the same surface contour determined from the AFM. Since the atomic force has a short range, the long-range magnetic force is dominant at a distance of 10 nm. The MFM images shown in Figure 7.4 (b) and (d) for the unirradiated and irradiated films, respectively, are the result of the measured MFM contrast subtracted from the AFM topographic effects in a proper manner. Except for some artifacts (dots and strips) in Figure 7.4 (b), the area shows a uniform contrast for the unirradiated sample, suggesting that the magnetic domains in the unirradiated film are too small to be resolved, which is well expected since the domain size is  $\sim 3$  nm or a little larger. After irradiation, the MFM image of the film is shown in Figure 7.4 (d).

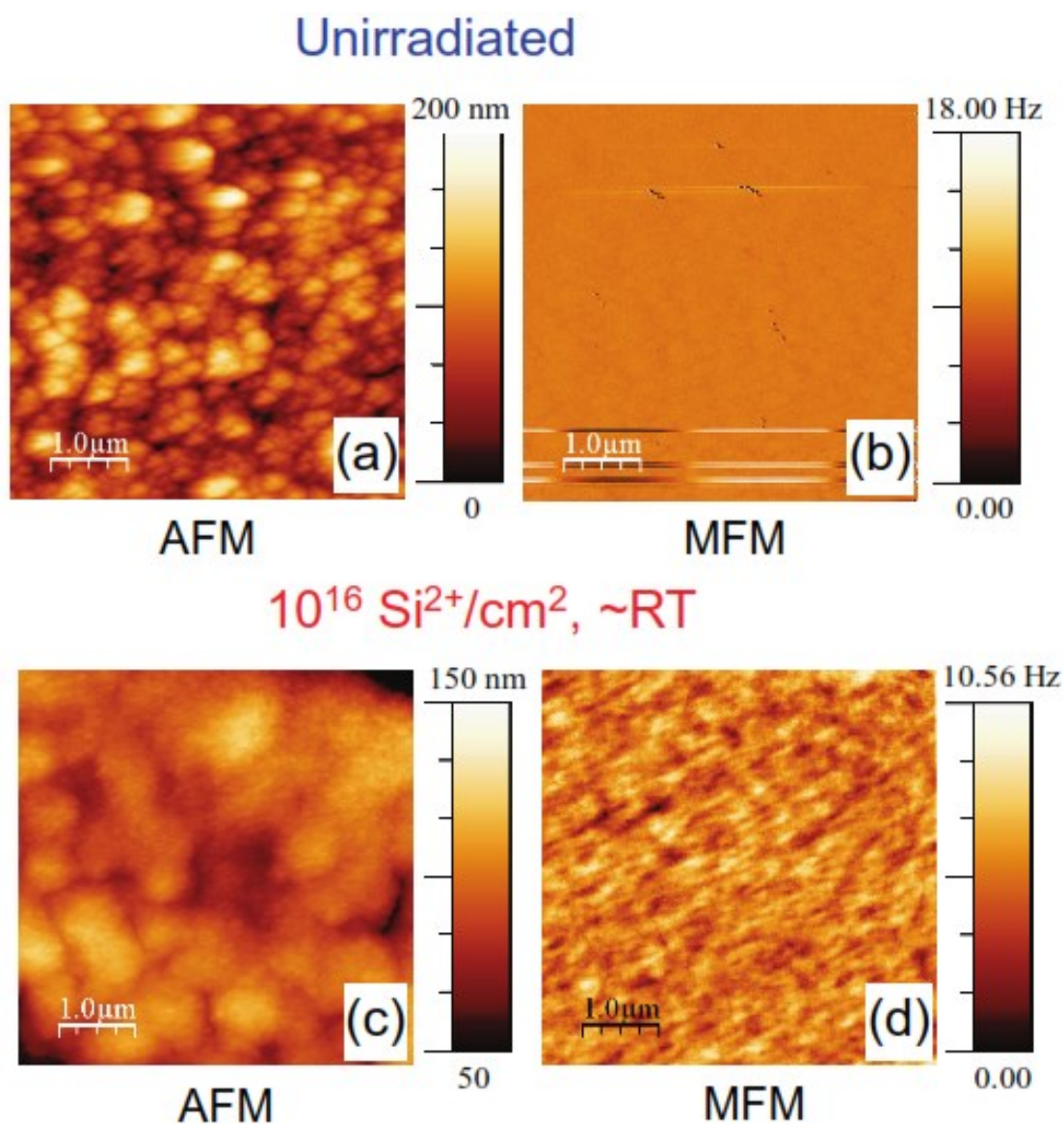


**Figure 7.4** AFM and MFM images for a granular  $\text{Fe}_3\text{O}_4$  film on Si before and after film on Si before and after irradiation.

A clear contrast is observed, where the brighter area represents a larger frequency shift, thus a larger magnetic gradient. From Figure 7.4 (d), the magnetic domain size is on the order of tens to hundreds of nanometers. Since the average size of the crystalline grains with single magnetic domains in the irradiated film is only 23 nm, domain expansion is expected during the ion irradiation, as discussed above.

## 7.5 Fe-Fe<sub>3</sub>O<sub>4</sub> Core-Shell Granular Films

### 7.5.1 Structural Property Changes of Core-Shell (CS) Fe-Fe<sub>3</sub>O<sub>4</sub> Granular Films

The granular films were analyzed using GIXRD and the data are shown in Figure 7.5 for the CS Fe-Fe<sub>3</sub>O<sub>4</sub> sample M1-D before and after Si<sup>2+</sup> ion irradiation. GIXRD data indicate that the films consist of two-phases, Fe and Fe oxide, both before and after irradiation, but that the oxide changes from Fe<sub>3</sub>O<sub>4</sub> (magnetite) before irradiation to FeO (Wüstite) after irradiation. The average grain size is estimated using the Scherrer equation, as previously described for these systems.<sup>24</sup> Average grain size for the unirradiated film was  $8 \pm 1$  nm for the Fe core, based on the well-resolved Fe(110) peak, and  $2 \pm 1$  nm for the Fe<sub>3</sub>O<sub>4</sub> shell, based on the Fe<sub>3</sub>O<sub>4</sub>(311). These values are typical and have been confirmed on similar samples by transmission electron microscopy (TEM).<sup>25</sup> Following irradiation, the crystalline Fe core size remains unchanged, but the oxide shell becomes FeO and grows to a thickness of  $17 \pm 1$  nm based on the FeO (200) peak.

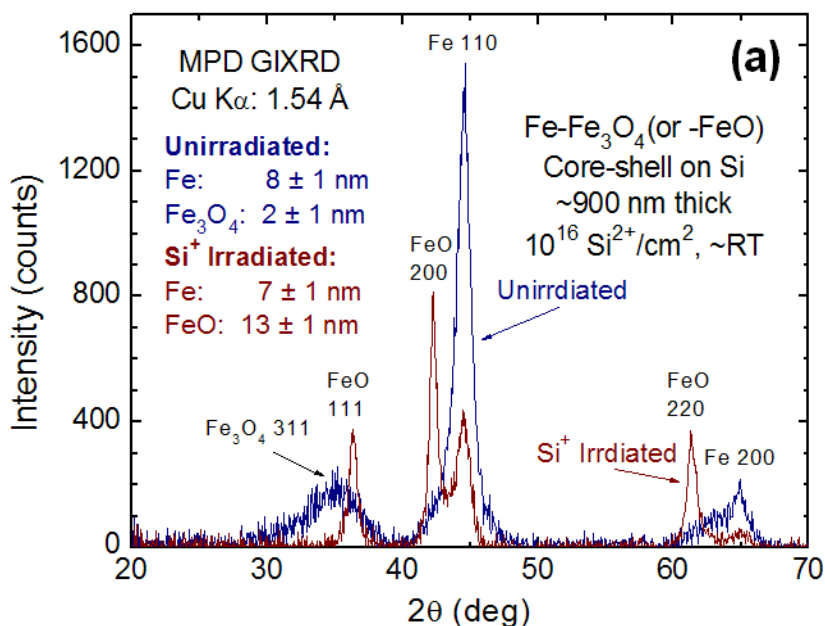


**Figure 7.5** Background subtracted GIXRD patterns for a Fe-Fe<sub>3</sub>O<sub>4</sub> core-shell nanocluster film on Si before and after 5.5 MeV Si<sup>+</sup> ion irradiation to  $10^{16}$  Si<sup>+</sup>/cm<sup>2</sup> ( $\sim 0.95$  dpa in the film) at nominal RT



Figure 7.6 shows the HIM images of the films before and after irradiation. The unirradiated film exhibits loosely interconnected nanoparticles, similar to those observed for other Fe/Fe<sub>3</sub>O<sub>4</sub> core-shell<sup>25</sup> and Fe<sub>3</sub>O<sub>4</sub> clusters.<sup>24</sup> Particles are observed to have a typical size of ~10 nm and are agglomerated at various scales. The overall film is highly porous with large surface and interface areas. Irradiation leads to grain growth and particle aggregation as described previously for Fe<sub>3</sub>O<sub>4</sub> nanoclusters,<sup>2</sup> resulting in a densified continuous film. In areas where few nanoclusters are present on the Si surface, irradiation leads to formation of islands, as shown in Figure 7.6.

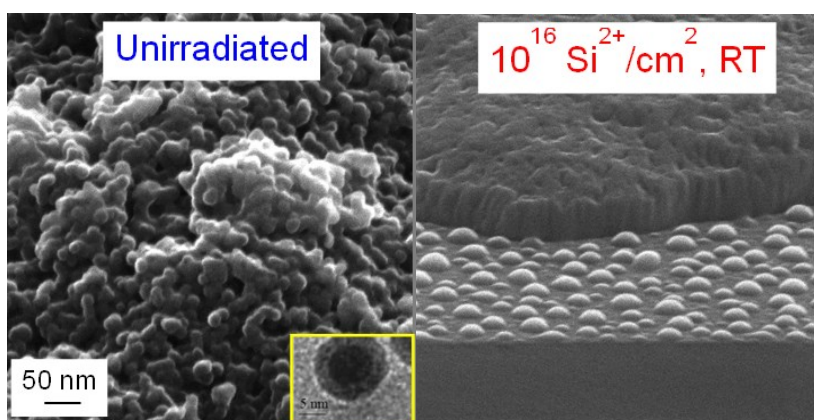


**Figure 7.6** High-resolution HIM micrographs of granular film (a) before and (b) after ion irradiation. The inset to (a) shows a representative TEM image illustrating the core-shell structure.

Changes in surface morphology and composition are attributed to irradiation driven processes for grain growth in the nanostructures. In this core-shell iron-iron oxide nanoparticle granular film system, the average particle size increases probably as a result of the coalescence of the loosely packed particles. Grain growth under ion irradiation in this study could also occur due to ion beam-induced epitaxial crystallization.<sup>26</sup> The change of phase from Fe<sub>3</sub>O<sub>4</sub> to FeO is known to take place due to thermal decomposition<sup>27</sup> or reduction by process gases,<sup>28</sup> where temperature increase plays a vital role in phase change. In our case, the phase transition is likely a dynamic process induced by the highly energetic (5.5 MeV) Si<sup>2+</sup>-ions. Additional studies are required to better understand the physical and chemical processes. Some additional studies done to investigate the unique structural changes in CS Iron-Iron oxide nanoparticles are discussed in Chapter 8.



### 7.5.2 Magnetic Property Changes of Core-Shell (CS) Fe-Fe<sub>3</sub>O<sub>4</sub> Granular Films

Figure 7.7 shows the hysteresis loops, taken at 300 K, for the film before and after Si<sup>2+</sup> ion irradiation. It can be seen that the remanence increases ~14% upon irradiation, from 14.5 to 16.5 emu/g. Coercivity increases 25% from 44.8 Oe to 55.9 Oe. Additionally, the saturation magnetization decreases by ~14% after irradiation, from 89.4 to 76.6 emu/g. This reduction in saturation is expected since the shell changes from a ferrimagnetic material (Fe<sub>3</sub>O<sub>4</sub>) to an antiferromagnetic material (FeO). Figure 7.8 shows the family FORCs and the corresponding distribution for the irradiated sample.

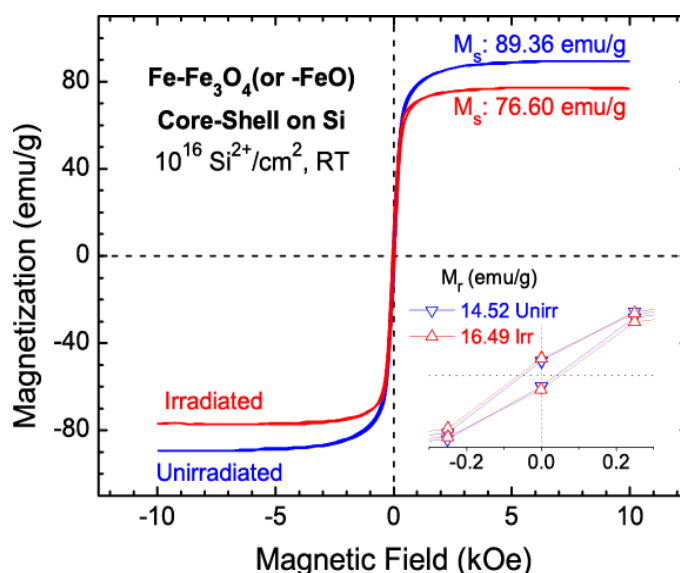


**Figure 7.7** Hysteresis loop for a Fe-Fe<sub>3</sub>O<sub>4</sub> core-shell nanocluster film on Si before and after 5.5 MeV Si<sup>+</sup> ion irradiation to  $10^{16}$  Si<sup>+</sup>/cm<sup>2</sup> (~0.95 dpa in the film) at nominal RT.

The FORC distribution is a sharp ridge along the local coercivity ( $H_c$ ) axis, with little spread along the bias field ( $H_b$ ) or interaction axis. The peak coercivity values of 25-50 Oe correspond closely to the major loop coercivity. The lack of bias field spreading indicates that the Fe cores are behaving as single domain particles nearly independently of one another, with the FeO shell minimizing interaction between them. The low coercivity is a size effect of the small Fe cores. The FORC distribution is a sharp ridge along the local coercivity ( $H_c$ ) axis, with little spread along the bias field ( $H_b$ ) or interaction axis. The peak coercivity values of 25-50 Oe correspond closely to the

major loop coercivity. The lack of bias field spreading indicates that the Fe cores are behaving as single domain particles nearly independently of one another, with the FeO shell minimizing interaction between them. The low coercivity is a size effect of the small Fe cores.

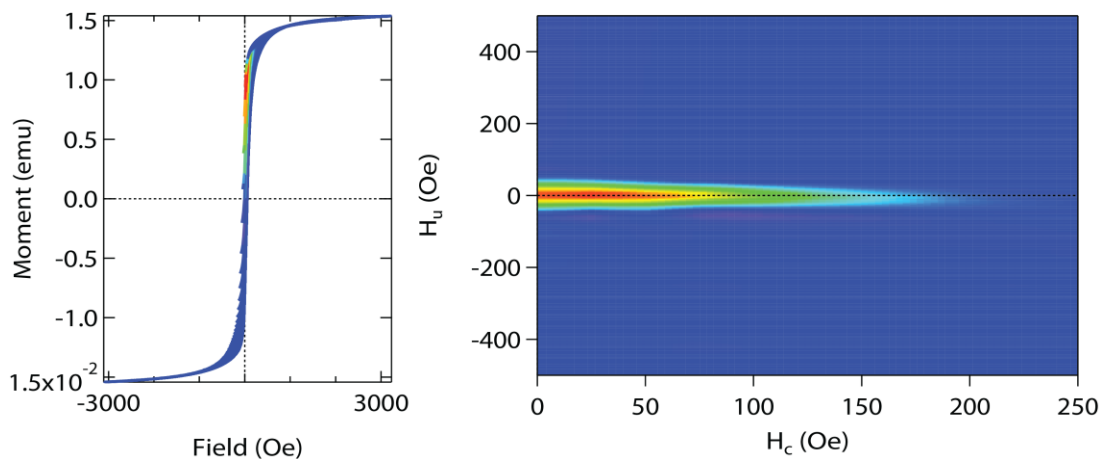


**Figure 7.8** First-order reversal curves (left) and contour diagram (right) of the irradiated sample.

In similar samples,<sup>24,25</sup> a distribution of particle sizes is seen, with some below the superparamagnetic (SPM) threshold. Only those particles above this size threshold will contribute to the coercivity, and the small distribution of  $H_c$  seen in FORC is likely a consequence of size and anisotropy distribution. Though anisotropy suggests that the threshold size for room temperature SPM in Fe should be 13 nm,<sup>29</sup> these particles are much smaller, yet remain magnetized at room temperature. This can be explained as being due to the influence of the oxide shell stabilizing the core moments, as seen also in Co-CoO particles.<sup>30</sup> Alternatively, some particles may be larger than others, or a few particles cluster together to have a bigger interaction volume, such that they behave as ferromagnets rather than superparamagnets.

## 7.6 Summary

This chapter reports the silicon ion irradiation effects on the Fe-based nanoparticle granular films, namely fully oxidized ( $\text{Fe}_3\text{O}_4$ ) and core-shell ( $\text{Fe-Fe}_3\text{O}_4$ ) nanoparticle granular films.

Superparamagnetic to ferromagnetic transition of the  $\text{Fe}_3\text{O}_4$  granular film after 5.5 MeV  $\text{Si}^{2+}$  ion

irradiation to fluence of  $10^{16}$  ions/cm<sup>2</sup> was observed and the underlying magnetic behaviors due to irradiation were explored. The remanent magnetization of the film changes from 0 to 9.36 emu/g at room temperature. For the irradiated sample, the saturation magnetization increases to 45.64 emu/g and coercivity increases to 250 Oe. The Fe<sub>3</sub>O<sub>4</sub> average grain size is increased from 3 to 23 nm as a result of the irradiation. A dramatic change in the microstructures of irradiated film occurs, featuring particle aggregation and material condensation. The magnetic domains have a size of tens to hundreds of nanometers. The change in the magnetic property of the granular Fe<sub>3</sub>O<sub>4</sub> film is attributed to the irradiation-induced grain growth and an alteration of the interatomic and electronic configurations at the grain/particle surface and interface, which lead to magnetic domain growth, reorientation, and occurrence of magnetic anisotropy. There are bipolar interactions between the particles in both the unirradiated and irradiated films. The films represent a new class of semi-disordered magnetite materials for study, which could lead to important applications of this type of material in various areas, including radiation detection and monitoring.

CS Fe-Fe<sub>3</sub>O<sub>4</sub> Nanocluster film on silicon substrates, which consist of 8 nm Fe cores with 2 nm Fe<sub>3</sub>O<sub>4</sub> shells upon ion irradiation converts the Fe<sub>3</sub>O<sub>4</sub> shell to a FeO with a shell thickness increase by about a factor of two, and the film become denser as shown by helium ion microscopy. Upon irradiation, the saturation magnetization decreases due to the antiferromagnetic FeO core. First-order reversal curve measurements show that the individual Fe cores exhibit small coercivity and are isolated from one another by the antiferromagnetic oxide shells, despite being a part of the continuous film. Understanding the behavior of core-shell iron nanoparticles, including the interface effect and grain boundary effect may contribute to the radiation resistant materials and its application. The irradiation-induced oxide phase change and magnetic behavior due to the antiferromagnetic shell is distinct from previously reported nanocluster systems of this type and this phenomenon is investigated further in Chapter 8.

## 7.9 References

1. N. Cabrera and N. F. Mott, "Theory of the oxidation of metals," *Reports on Progress in Physics*, vol. 12, no. 1, pp. 163-184, 1949.
2. C. Boeglin, E. Beaurepaire, V. Halté, V. López-Flores, C. Stamm, N. Pontius, H.A. Dürr and J.Y. Bigot, "Distinguishing the ultrafast dynamics of spin and orbital moments in solids," *Nature*, vol. 465, no. 7297, pp. 458-461, 2010.
3. H. Bernas, *Materials science with ion beams*. Berlin: Springer, 2010.
4. D. H. Reich, "Preface: Proceedings of the 53rd Annual Conference on Magnetism and Magnetic Materials, Austin, Texas, November 2008," *Journal of Applied Physics*, vol. 105, no. 7, p. 07A101, 2009.
5. P. Esquinazi, D. Spemann, R. Höhne, A. Setzer, K.-H. Han, and T. Butz, "Induced Magnetic Ordering by Proton Irradiation in Graphite," *Physical Review Letters*, vol. 91, no. 22, 2003.
6. K. Zhang, K. Lieb, M. Marszalek, V. Milinovic, and V. Tokman, "Ion beam mixing of Co/Fe multilayers: Magnetic and structural properties," *Thin Solid Films*, vol. 515, no. 2, pp. 700-704, 2006.
7. M. C. Sung, D.G. You, H.S. Park, J.C. Lee, S.Y. Je, I.S. Kim, J. Lee, C.N. Whang, S. Im, K. Jeong, T.G. Kim, J.S. Yang and J.H. Song, "Modification of magnetic properties of epitaxial Co/Cu multilayers by 1 MeV C<sup>+</sup> irradiation," *Journal of Applied Physics*, vol. 90, no. 4, p. 2036, 2001.
8. D. Ravelosona, C. Chappert, V. Mathet, and H. Bernas, "Chemical order induced by ion irradiation in FePt (001) films," *Applied Physics Letters*, vol. 76, no. 2, p. 236, 2000.
9. S. I. Woods, S. Ingvarsson, J. R. Kirtley, H. F. Hamann, and R. H. Koch, "Local magnetic anisotropy control in NiFe thin films via ion irradiation," *Applied Physics Letters*, vol. 81, no. 7, p. 1267, 2002.
10. C. Chappert, H. Bernas, J. Ferré, W. Kottler, J.P. Jamet, Y. Chen, E. Cambriil, T. Devolder, F. Rousseaux, V. Mathet and H. Launois, "Planar Patterned Magnetic Media Obtained by Ion Irradiation," *Science*, vol. 280, no. 5371, pp. 1919-1922, 1998.
11. C. T. Rettner, S. Anders, J. E. E. Baglin, T. Thomson, and B. D. Terris, "Characterization of the magnetic modification of Co/Pt multilayer films by He<sup>+</sup>, Ar<sup>+</sup>, and Ga<sup>+</sup> ion irradiation," *Applied Physics Letters*, vol. 80, no. 2, p. 279, 2002.
12. G. J. Kusinski, K. M. Krishnan, G. Denbeaux, G. Thomas, B. D. Terris, and D. Weller, "Magnetic imaging of ion-irradiation patterned Co/Pt multilayers using complementary electron and photon probes," *Applied Physics Letters*, vol. 79, no. 14, p. 2211, 2001.
13. P. Allongue and F. Maron, "Electrodeposition and chemical bath deposition of functional nanomaterials," *MRS Bulletin*, vol. 35, no. 10, pp. 761-770, 2010.

14. Y. Qiang, J. Antony, A. Sharma, J. Nutting, D. Sikes, and D. Meyer, "Iron/iron oxide core-shell nanoclusters for biomedical applications," *Journal of Nanoparticle Research*, vol. 8, no. 3-4, pp. 489-496, 2005.
15. J. F. Ziegler, J. P. Biersack, and U. Littmark, "Stopping and Range of Ions in Solids," *Pergamon, New York*, 1985.
16. B. D. Cullity and S. R. Stock, "Elements of X-Ray Diffraction," *3rd edition, Prentice Hall, New Jersey*, p. 170, 2001.
17. W. Jiang, H. Wang, I. Kim, I.T. Bae, G. Li, P. Nachimuthu, Z. Zhu, Y. Zhang and W. Weber,, "Response of nanocrystalline 3C silicon carbide to heavy-ion irradiation," *Physical Review B*, vol. 80, no. 16, 2009.
18. W. Jiang, H. Wang, I. Kim, Y. Zhang, and W. J. Weber, "Amorphization of nanocrystalline 3C-SiC irradiated with Si<sup>+</sup> ions," *Journal of Materials Research*, vol. 25, no. 12, pp. 2341-2348, 2010.
19. J. Lian, J. Zhang, F. Namavar, Y. Zhang, F.Lu, H. Haider, K. Garvin, W. J. Weber and R.C. Ewing, "Ion beam-induced amorphous-to-tetragonal phase transformation and grain growth of nanocrystalline zirconia," *Nanotechnology*, vol. 20, no. 24, p. 245303, Jun. 2009.
20. Y. Zhang, W. Jiang, C.M. Wang, F. Namavar, P.D. Edmondson, Z. Zhu, M. H. Engelhard, F. Gao, J Lian and W.J. Weber ,*Submitted*, 2010.
21. H.-U. Worm, "On the superparamagnetic-stable single domain transition for magnetite, and frequency dependence of susceptibility," *Geophysical Journal International*, vol. 133, no. 1, pp. 201-206, 1998.
22. J. L. Dormann, D. Fiorani, and E. Tronc, "Advances in Chemical Physics," *John Wiley and Sons*, vol. XCVIII, p. 283, 1997.
23. R. Hyndman, P. Warin, J. Gierak, J. Ferré, J. N. Chapman, J.P. Jamet, V. Mathet and C. Chappert, "Modification of Co/Pt multilayers by gallium irradiation—Part 1: The effect on structural and magnetic properties," *Journal of Applied Physics*, vol. 90, no. 8, p. 3843, 2001.
24. W. Jiang, J. S. McCloy, A. S. Lea, J. A. Sundararajan, Q. Yao and Y. Qiang, "Magnetization and susceptibility of ion-irradiated granular magnetite films", *Phys. Rev. B* 83 (13), 134435 (2011).
25. M. Kaur, J. S. McCloy, W. Jiang, Q. Yao and Y. Qiang, " Size Dependence of Inter- and Intracluster Interactions in Core–Shell Iron–Iron Oxide Nanoclusters", *J. Phys. Chem. C*, 116 (23), 12875-12885 (2012).
26. W. Jiang, L. Jiao and H. Wang, "Transition from Irradiation-Induced Amorphization to Crystallization in Nanocrystalline Silicon Carbide", *J. Amer. Ceram. Soc.*, 94 (12), 4127-4130 (2011).

27. M. J. Benitez, D. Mishra, P. Szary, G. A. B. Confalonieri, M. Feyen, A. H. Lu, L. Agudo, G. Eggeler, O. Petravic and H. Zabel, " Structural and magnetic characterization of self-assembled iron oxide nanoparticle arrays", *J. Phys. Cond. Matt.*, 23 (12), 126003 (2011).
28. Z. Swiatkowska-Warkocka, K. Kawaguchi, H. Wang, Y. Katou and N. Koshizaki, " Controlling exchange bias in Fe<sub>3</sub>O<sub>4</sub>/FeO composite particles prepared by pulsed laser irradiation", *Nanoscale Res. Lett.*, 6 (1), 226 (2011).
29. G. Bertotti, *Hysteresis in Magnetism: for physicists, materials scientists, and engineers*, edited by I. Mayergoyz, San Diego: Academic Press, 1998.
30. J. Nogués, V. Skumryev, J. Sort, S. Stoyanov and D. Givord, "Shell-Driven Magnetic Stability in Core-Shell Nanoparticles ", *Phys. Rev. Lett.*, 97 (15), 157203 (2006)

## Chapter 8: Oxide Shell Reduction and Magnetic Property Changes in Core-Shell Fe

### Nanoclusters under Ion Irradiation

#### 8.1 Introduction

As discussed in chapter 6, the behavior of oxide shell reduction and phase change in core-shell nanoclusters is unique and therefore the reason behind this phenomenon is investigated in this chapter. As we know, nanomaterials and nanostructures have gained popularity in recent years because of their interesting properties and promising applications in various fields.<sup>1-5</sup> Synthesis of such nanomaterials with desired properties for commercial use has been a great challenge for nanotechnology industries for more than two decades. It has been shown that particle-irradiation can be used as a method to bring desired property changes in nanomaterials.<sup>6-8</sup> These irradiation-induced property changes vary as a function of irradiation dose,<sup>9</sup> ion energy,<sup>10</sup> duration of exposure,<sup>11</sup> and material composition/structure under irradiation.<sup>12</sup> Changes in structural and magnetic properties due to oxidation are some of the notable behavior observed in nanomaterials due to ion irradiation.<sup>13-16</sup> Surface morphology, stoichiometry and magnetic properties of these nanomaterials must be carefully controlled and tuned for each application. Hence, it is very important to study the irradiation effects on nanomaterials at an atomic level. In our previous studies, we reported the irradiation-induced structural and magnetic property changes on fully oxidized Fe<sub>3</sub>O<sub>4</sub> nanocluster (NC) films<sup>17</sup> and core-shell (CS) Fe-Fe<sub>3</sub>O<sub>4</sub> NC films<sup>18,19</sup> irradiated with 5.5 MeV Si<sup>2+</sup> ions to a fluence of 10<sup>16</sup> ions/cm<sup>2</sup>. On a separate report, FeO+Fe<sub>3</sub>N NC films showed that their structure and magnetic property were not subjected to a noticeable change under He<sup>+</sup> ion irradiation to a relatively low dose.<sup>20</sup> Reduction of oxide phases was observed in the core-shell NC films,<sup>18,19</sup> but fluence-dependence of this effect and the possibility of reduction in the mixed oxide/nitride shells have not yet been reported. Here, we report the fluence-dependence reduction behavior in a Fe-based CS Fe-Fe<sub>3</sub>O<sub>4</sub>/Fe<sub>3</sub>N NC film with mixed oxide/nitride shells. These NC films were deposited on Si substrates to thickness of ~0.5 micrometers using a NC deposition system. The films were irradiated at room temperature with 5.5

MeV  $\text{Si}^{2+}$  ions to ion fluences of  $10^{15}$  and  $10^{16}$  ions/cm<sup>2</sup>. It was found that the irradiation induced grain growth, Fe valence reduction in the shell, and crystallization or growth of  $\text{Fe}_3\text{N}$ , although the film retained its Fe-core and its ferromagnetic properties after irradiation. The nature and mechanism of oxide shell reduction and composition dependence after irradiation were further studied by synthesizing additional NC films of  $\text{Fe}_3\text{O}_4$  and  $\text{FeO}+\text{Fe}_3\text{N}$  and irradiating them under the same conditions with 5.5 MeV  $\text{Si}^{2+}$  ions to fluences of  $10^{15}$  and  $10^{16}$  ions/cm<sup>2</sup> to better understand the reduction behavior in these films. The presence of nanocrystalline Fe is found to be a major factor for the oxide shell reduction. The surface morphologies of these films show dramatic changes in the microstructures due to cluster growth and agglomeration as a result of ion irradiation.

## 8.2 Sample Preparation

The NC films in this study were prepared by the state-of-the-art cluster deposition system, which combines magnetron sputtering with gas aggregation technique as described in details in our previous reports.<sup>21,22</sup> By controlling the sputtering power, aggregation distance, He to Ar gas flow rate and the temperature inside the aggregation chamber, the cluster size formed inside the aggregation chamber was determined. By allowing the clusters leaving the aggregation chamber to combine with oxygen and nitrogen gas in the reaction chamber at right proportion, the desired nanocluster films were obtained.<sup>23</sup> The Fe atoms were sputtered from an iron target placed on the magnetron sputtering gun inside the aggregation chamber at a power of 200 W by supplying 350 sccm (standard cubic centimeters per minute) of Ar gas and 50 sccm of He gas. These Fe atoms on the surface of pure Fe NCs were allowed to react with 6 sccm oxygen and 6 sccm of nitrogen gas, supplied simultaneously in the reaction chamber, to form the desired CS  $\text{Fe}-\text{Fe}_3\text{O}_4/\text{Fe}_3\text{N}$  NC, which were subsequently deposited on a Si wafer in the deposition chamber to form NC films. The separate  $\text{Fe}_3\text{O}_4$  NC films were prepared by allowing 3 sccm of oxygen to react with Fe atoms in the aggregation chamber. The  $\text{FeO}+\text{Fe}_3\text{N}$  NC films were prepared using the same procedure as reported in the previous work.<sup>20</sup> Ion irradiation of these NC films was performed using a 3.0 MV electrostatic



tandem accelerator (NEC 9SDH-2 pelletron, Middleton, WI). All the films were irradiated uniformly near room temperature at normal incidence with 5.5 MeV  $\text{Si}^{2+}$  ions to two different fluences of  $10^{15}$  and  $10^{16}$  ions/cm<sup>2</sup> under vacuum maintained at the lower end of  $10^{-7}$  Torr. Grazing Incidence X-ray Diffraction (GIXRD) was performed using a Philips X'pert Multi-purpose Diffractometer (MPD) based on Cu K $\alpha$  radiation. The asymmetric scan ranged from  $2\theta = 20^\circ - 80^\circ$  with a step size of  $0.05^\circ$  and a dwell time of 6 sec at each step. Magnetic hysteresis loops of the films were measured using a vibrating sample magnetometer (VSM) up to a maximum field of 1.35 Tesla. The surface morphologies of the films before and after irradiation were examined to study microstructural changes using a helium ion microscope (HIM, Orion Plus, Carl Zeiss SMT, Peabody, MA) at an operating voltage of 25 kV.

### 8.3 Synthesis and Characterization of FeO+Fe<sub>3</sub>N granular films

Figure 8.1 shows the GIXRD patterns of the CS Fe-Fe<sub>3</sub>O<sub>4</sub>/Fe<sub>3</sub>N NC film, unirradiated (as-prepared) and irradiated to fluences of  $10^{15}$  and  $10^{16}$  ions/cm<sup>2</sup>. The major peaks from the GIXRD pattern confirm the existence of Fe in the core with Fe<sub>3</sub>O<sub>4</sub> in the shell of the unirradiated sample. Iron nitride is also likely to be present in the shell, but XRD cannot detect it probably due to its small size or amorphous phase. After irradiation of the film to a fluence of  $10^{15}$  ions/cm<sup>2</sup>, grain growth in the Fe core and the oxide shell takes place, as listed in Table 8.1. It is observed that under the irradiation, a portion of Fe<sub>3</sub>O<sub>4</sub> underwent a reduction reaction from Fe<sup>3+</sup> to Fe<sup>2+</sup> valence state to form FeO phase and probably the amorphous iron nitride underwent crystallization. Iron nitride could exist in an amorphous state in the as-deposited sample and crystallize under ion irradiation.<sup>24</sup> Prolonged exposure of irradiation up to fluence of  $10^{15}$  ions/cm<sup>2</sup> either led to the crystallization of amorphous iron nitride or growth of Fe<sub>3</sub>N crystal to be detected in XRD and further irradiation up to fluence of  $10^{16}$  ions/cm<sup>2</sup> led to the formation of a new phase Fe<sub>4</sub>N. Even after irradiation of the sample to  $10^{16}$  ions/cm<sup>2</sup>, the film retained its Fe core with only a slight increase in the grain size and retained its ferromagnetic behavior. Though FeO (Wustite) phase forms at high temperatures (560 –

570 °C),<sup>25</sup> it can also be stable at room temperature when mixed with other phases.<sup>26</sup> FeO samples in this study remains stable because it co-exists with the Fe<sub>3</sub>O<sub>4</sub> and Fe<sub>3</sub>N as a composite.

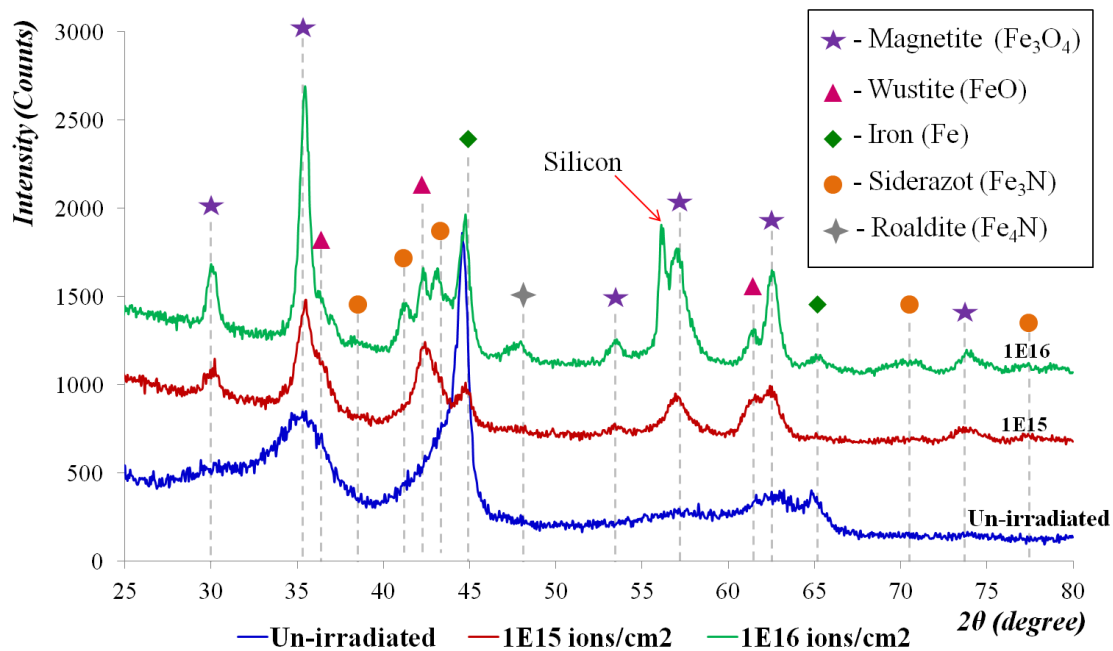


**Figure 8.1** GIXRD pattern for a core-shell Fe-Fe<sub>3</sub>O<sub>4</sub>/Fe<sub>3</sub>N NC film, unirradiated (as-prepared) and irradiated to 10<sup>15</sup> and 10<sup>16</sup> ions/cm<sup>2</sup>.

**Table 8.1** Average grain sizes of different phases in films Fe-Fe<sub>3</sub>O<sub>4</sub>/Fe<sub>3</sub>N, Fe<sub>3</sub>O<sub>4</sub>, and FeO+Fe<sub>3</sub>N before and after irradiation.

No.	Sample Name	Phases	Grain size		
			Unirradiated	Irradiated to 1E15 Si <sup>2+</sup> /cm <sup>2</sup>	Irradiated to 1E16 Si <sup>2+</sup> /cm <sup>2</sup>
1	Core-Shell Fe-Fe <sub>3</sub> O <sub>4</sub> /Fe <sub>3</sub> N Film	Fe	9 nm	12 nm	12 nm
		Fe <sub>3</sub> O <sub>4</sub>	5 nm	9 nm	17 nm
		Fe <sub>3</sub> N	Undetectable	4 nm	15 nm
		FeO	Not present	8 nm	31 nm
		Fe <sub>4</sub> N	Not present	Undetectable	9 nm
2	Fully Oxidized Fe <sub>3</sub> O <sub>4</sub> Film	Fe <sub>3</sub> O <sub>4</sub>	3 nm	9 nm	15 nm
3	FeO+Fe <sub>3</sub> N Film	Fe <sub>3</sub> O <sub>4</sub>	Not present	13 nm	16 nm
		Fe <sub>3</sub> N	7 nm	11 nm	15 nm
		FeO	7 nm	11 nm	16 nm

In order to investigate the mechanisms of the reduction process in the CS Fe-Fe<sub>3</sub>O<sub>4</sub>/Fe<sub>3</sub>N NC film under ion irradiation, two additional NC films of Fe<sub>3</sub>O<sub>4</sub> and FeO+Fe<sub>3</sub>N were also made and studied under the same irradiation conditions as for the CS films. As listed in Table I, in both the Fe<sub>3</sub>O<sub>4</sub> and FeO+Fe<sub>3</sub>N NC films no reduction reactions were observed after ion irradiation. However, oxidation of some portion of FeO occurred in the FeO+Fe<sub>3</sub>N film to form Fe<sub>3</sub>O<sub>4</sub> at fluence of 10<sup>15</sup> ions/cm<sup>2</sup>, resulting in a combined phase of Fe<sub>3</sub>O<sub>4</sub>+FeO+Fe<sub>3</sub>N, which is similar to that of the shell phase in the CS film. This oxidation reaction is in contrast to the reduction reaction observed in the CS films. Oxidation of metal under irradiation is a common phenomenon and it is not surprising in the case of FeO+Fe<sub>3</sub>N film. Extended exposure of Fe<sub>3</sub>O<sub>4</sub>+FeO+Fe<sub>3</sub>N film to fluence 10<sup>16</sup> ions/cm<sup>2</sup> resulted in a slight increase in grain sizes of each phases and with no occurrence of any reduction reaction. Since no reduction reaction occurs in the phase of Fe<sub>3</sub>O<sub>4</sub>, FeO+Fe<sub>3</sub>N or Fe<sub>3</sub>O<sub>4</sub>+FeO+Fe<sub>3</sub>N, it is evident that only in the presence of Fe core will the iron oxides reduce. K. J. Kim *et al.*<sup>27</sup> and Stir *et al.*<sup>28</sup> reported the reduction from Fe<sub>3</sub>O<sub>4</sub> to FeO and from FeO to Fe in thin films and powders when nanocrystalline Fe is present. The results obtained from this study confirm the reduction reaction in the CS Fe-Fe<sub>3</sub>O<sub>4</sub>/Fe<sub>3</sub>N films with a mixed-phase shell in the presence of nanocrystalline Fe core that could serve as a catalyst. The mechanisms behind the reduction reaction in these samples are still under investigation. However, the hypothetical mechanism for this reduction reaction is the irradiation-induced defect creation and the irradiation-induced heating that induces defect migration (diffusion). It is plausible that the irradiation of Si<sup>2+</sup> ions with 5.5 MeV incident energy could create Fe and O vacancies/interstitials<sup>29,30</sup> and these oxygen interstitials could diffuse to the surface where it can combine to form O<sub>2</sub> and removed.<sup>31,32</sup> Therefore this mechanism involving atomic diffusion of O and/or Fe, have resulted in the reduction of Fe<sub>3</sub>O<sub>4</sub> to FeO in the CS Fe-Fe<sub>3</sub>O<sub>4</sub>/Fe<sub>3</sub>N film. This kinetic process could be activated and enhanced by ion irradiation that produces atomic displacements, ionization and heat.

The magnetic hysteresis loops of the unirradiated films of CS Fe-Fe<sub>3</sub>O<sub>4</sub>/Fe<sub>3</sub>N, Fe<sub>3</sub>O<sub>4</sub> and FeO+Fe<sub>3</sub>N are shown in Figure 8.2. The Fe<sub>3</sub>O<sub>4</sub> NC film is superparamagnetic with an average grain size less than 3 nm, which is consistent with our previous report,<sup>17</sup> where a transition from superparamagnetic to ferromagnetic behavior was also observed due to coalescence and aggregation of NCs. The CS Fe-Fe<sub>3</sub>O<sub>4</sub>/Fe<sub>3</sub>N film has high saturation magnetization due to the Fe core, a coercivity of 220 Oe and remanence of 5 emu/g. In the FeO+Fe<sub>3</sub>N film, due to the presence of anti-ferromagnetic FeO phase, a decrease in the saturation magnetization is observed.

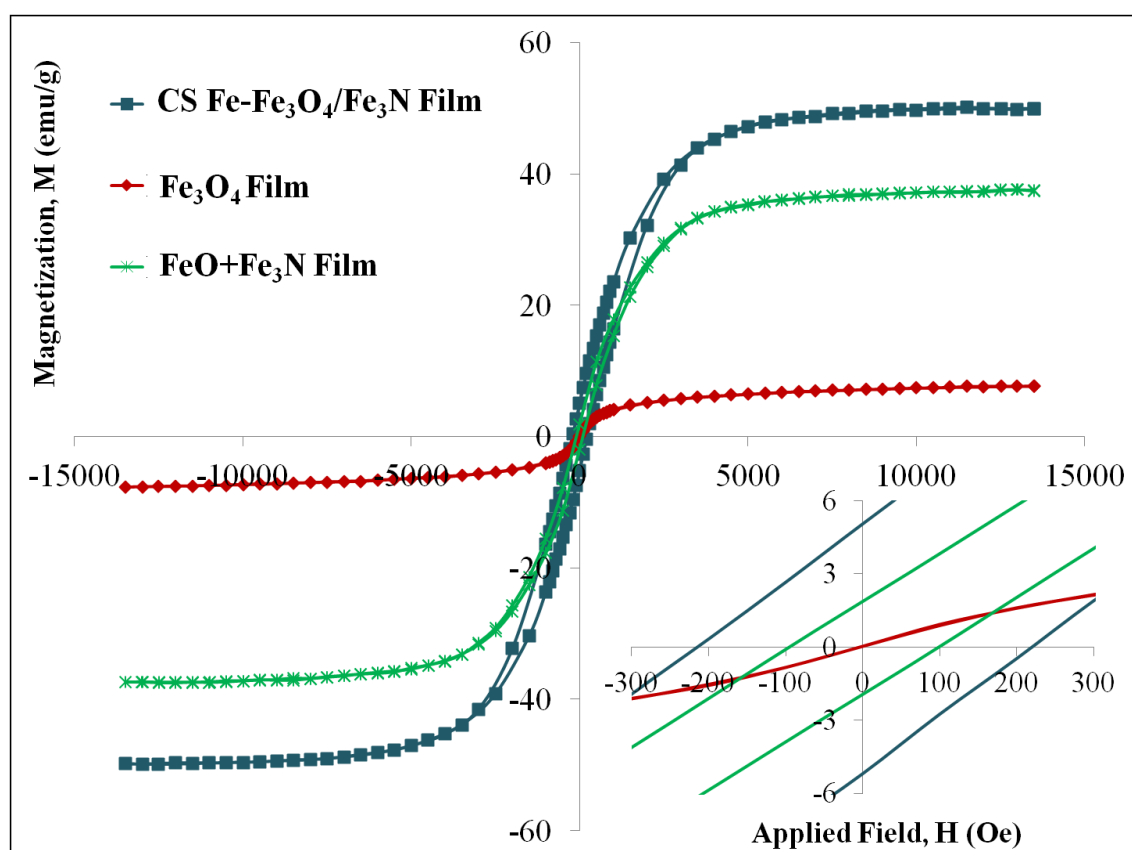


**Figure 8.2** Magnetic hysteresis loops for the films Fe-Fe<sub>3</sub>O<sub>4</sub>/Fe<sub>3</sub>N, Fe<sub>3</sub>O<sub>4</sub>, and FeO+Fe<sub>3</sub>N. The inset shows a magnified view near zero fields.

Figure 8.3 shows the magnetic hysteresis loops for the core-shell Fe-Fe<sub>3</sub>O<sub>4</sub>/Fe<sub>3</sub>N NC film, unirradiated (as-prepared) and irradiated at 10<sup>15</sup> and 10<sup>16</sup> ions/cm<sup>2</sup>. As mentioned earlier, since the CS Fe-Fe<sub>3</sub>O<sub>4</sub>/Fe<sub>3</sub>N film retained its Fe core and its ferromagnetic properties even after irradiation up to 10<sup>16</sup> ion/cm<sup>2</sup>. At the fluence of 10<sup>15</sup> ions/cm<sup>2</sup>, the formation of anti-ferromagnetic FeO causes the

$M_s$  to drop but not that much because of the simultaneous crystallization of ferromagnetic  $Fe_3N$ . Prolonged irradiation up to  $10^{16}$  ions/cm<sup>2</sup> led to grain grown and aggregation of particles contributing to the increase of  $M_s$  and  $H_c$ . In addition to that, the formation of  $Fe_4N$  phase at  $10^{16}$  ion/cm<sup>2</sup> stands as the major reason behind the increase of  $M_s$ , since  $Fe_4N$  compound naturally has a very high saturation magnetization (184 emu/g) close to that of Fe.<sup>33</sup>

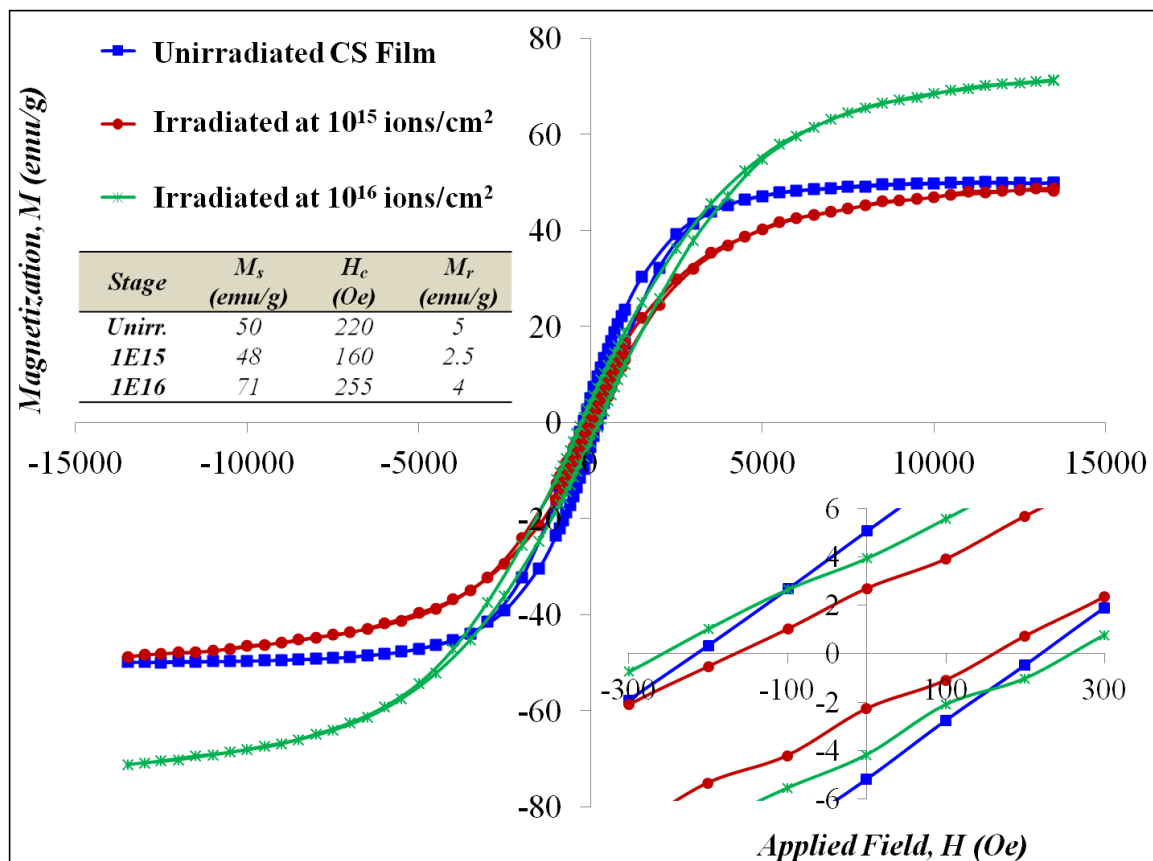


**Figure 8.3** Magnetic hysteresis loops for the core-shell Fe- $Fe_3O_4/Fe_3N$  NC film, unirradiated (as-prepared) and irradiated to  $10^{15}$  and  $10^{16}$  ions/cm<sup>2</sup>. The inset shows a magnified view near zero fields.

Grain growth and aggregation behavior is supported by Figure 8.4, which shows the HIM images of the unirradiated and irradiated films of CS Fe- $Fe_3O_4/Fe_3N$ ,  $Fe_3O_4$  and FeO+ $Fe_3N$ . Particle aggregation in all the films is observed. Each particle may contain a few nanocrystalline grains.<sup>17</sup> Higher ion fluence results in a denser film and a smoother surface. Different film compositions show different surface morphologies after ion irradiation.

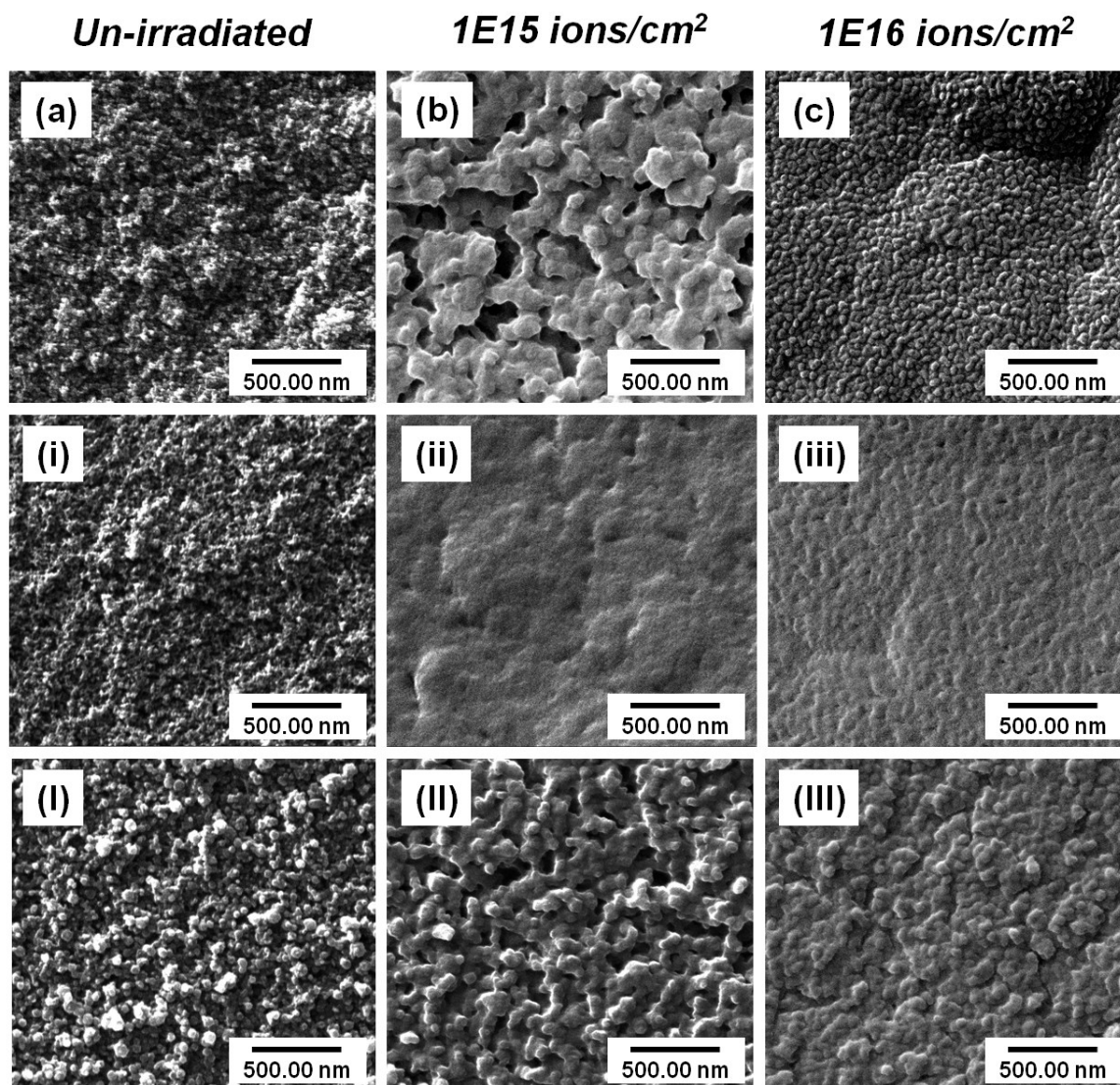


**Figure 8.4** HIM images of the films Fe-Fe<sub>3</sub>O<sub>4</sub>/Fe<sub>3</sub>N (a, b, c), Fe<sub>3</sub>O<sub>4</sub> (i, ii, iii), and FeO+Fe<sub>3</sub>N (I, II, III): unirradiated and irradiated to 10<sup>15</sup> and 10<sup>16</sup> ions/cm<sup>2</sup>. The field of view of all images is 3.50 μm.

#### 8.4 Summary

Core-shell Fe-Fe<sub>3</sub>O<sub>4</sub>/Fe<sub>3</sub>N nanocluster films were prepared using a nanocluster deposition system. GIXRD confirms the presence of Fe<sub>3</sub>O<sub>4</sub> phase in the shell of unirradiated CS film with iron nitride phase undetected due to its amorphous state or small size. A reduction of Fe<sub>3</sub>O<sub>4</sub> to FeO and crystallization of iron nitride or growth of Fe<sub>3</sub>N occur after 5.5 MeV Si<sup>2+</sup> ion irradiation. Similar

reduction behavior was not observed in other films of  $\text{Fe}_3\text{O}_4$ ,  $\text{FeO}+\text{Fe}_3\text{N}$  or  $\text{Fe}_3\text{O}_4+\text{FeO}+\text{Fe}_3\text{N}$ . The reduction is attributed to the presence of the nanocrystalline Fe core that possibly serves as a catalyst. The core-shell  $\text{Fe}-\text{Fe}_3\text{O}_4/\text{Fe}_3\text{N}$  film retained its Fe core and its ferromagnetic nature even after irradiation. HIM study shows cluster aggregation in the films, resulting in surface smoothing and material densification. In order to investigate the property changes while the samples are subject to irradiation in-situ studies are important. These studies help in understanding the actual mechanisms and the contributing factors for the radiation-induced property changes in nanomaterials. Chapter 9 deals with such in-situ studies on the Fe nanoparticle and its composites.

## 8.5 References

1. X. Zhang, G. Wen, S. Huang, L. Dai, R. Gao, and Z. L. Wang, *J. of Magnetism and Magnetic Materials*, **231**, 1, 9 (2001).
2. Z. Wang, M. Kuok, S. Ng, D. Lockwood, M. Cottam, K. Nielsch, R. Wehrspohn, and U. Gösele, *Physical Review Letters*, **89**, 2 (2002).
3. J. Park, E. Kang, S. U. Son, H. M. Park, M. K. Lee, J. Kim, K. W. Kim, H.-J. Noh, J.-H. Park, C. J. Bae, J.-G. Park, and T. Hyeon, *Advanced Materials*, **17**, 429 (2005).
4. C. Boeglin, E. Beaurepaire, V. Halté, V. López-Flores, C. Stamm, N. Pontius, H. A. Dürr, and J.-Y. Bigot, *Nature*, **465**, 458 (2010).
5. A. S. Edelstein and R. C. Cammarata, *Nanomaterials: Synthesis, Properties and Applications*, New York: Taylor & Francis Group, 1996.
6. S. Talapatra, P. Ganesan, T. Kim, R. Vajtai, M. Huang, M. Shima, G. Ramanath, D. Srivastava, S. Deevi, and P. Ajayan, *Physical Review Letters*, **95**, 9 (2005).
7. P. K. Kulriya, B. R. Mehta, D. K. Avasthi, D. C. Agarwal, P. Thakur, N. B. Brookes, A. K. Chawla, and R. Chandra, *Applied Physics Letters*, **96**, 053103 (2010).
8. J. P. Nozières, M. Ghidini, N. M. Dempsey, B. Gervais, D. Givord, G. Suran, and J. M. D. Coey, *Nuclear Instruments and Methods in Physics Research Section B: Beam Interactions with Materials and Atoms*, **146**, 250 (1998).
9. P. Esquinazi, D. Spemann, R. Höhne, A. Setzer, K.-H. Han, and T. Butz, *Physical Review Letters*, **91**, 22 (2003).
10. N. Nita, R. Schaeublin, and M. Victoria, *Journal of Nuclear Materials*, **329–333**, 953 (2004).
11. C. M. Wang, D. R. Baer, J. E. Amonette, M. H. Engelhard, J. J. Antony, and Y. Qiang, *Ultramicroscopy*, **108**, 43 (2007).
12. A. H. Latham and M. E. Williams, *Langmuir*, **24**, 14195 (2008).
13. C. D'Orléans, J. P. Stoquert, C. Estournès, J. J. Grob, D. Muller, J. L. Guille, M. Richard-Plouet, C. Cerruti, and F. Haas, *Nuclear Instruments and Methods in Physics Research Section B: Beam Interactions with Materials and Atoms*, **216**, 372 (2004).
14. C. Gavade, N. L. Singh, D. K. Avasthi, and A. Banerjee, *Nuclear Instruments and Methods in Physics Research Section B: Beam Interactions with Materials and Atoms*, **268**, 19, 3127 (2010).
15. L. G. Jacobsohn, J. D. Thompson, Y. Wang, A. Misra, R. K. Schulze, and M. Nastasi, *Nuclear Instruments and Methods in Physics Research Section B: Beam Interactions with Materials and Atoms*, **250**, 201 (2006).



16. J. Ferré, C. Chappert, H. Bernas, J.-P. Jamet, P. Meyer, O. Kaitasov, S. Lemerle, V. Mathet, F. Rousseaux, and H. Launois, *Journal of Magnetism and Magnetic Materials*, **198–199**, 191 (1999).
17. W. Jiang, J. McCloy, A. Lea, J. Sundararajan, Q. Yao, and Y. Qiang, *Physical Review B*, **83**, 13 (2011).
18. J. S. McCloy, W. Jiang, T. C. Droubay, T. Varga, L. Kovarik, J. A. Sundararajan, M. Kaur, Y. Qiang, E. C. Burks, and K. Liu, *J. Appl. Phys.*, **114**, 083903 (2013).
19. J. S. McCloy, W. Jiang, J. A. Sundararajan, Y. Qiang, E. Burks, and K. Liu, *AIP Conference Proceedings*, **1525**, 659 (2013).
20. J. A. Sundararajan, D. T. Zhang, Y. Qiang, W. Jiang, and J. S. McCloy, *J. Appl. Phys.*, **109**, 07E324 (2011).
21. Y. Qiang, J. Antony, A. Sharma, J. Nutting, D. Sikes and D. Meyer, *J. of Nanoparticle Research* **8**, 489 (2006).
22. J. Antony, Y. Qiang, D. R. Baer, and C. M. Wang, *J. Nanoscience and Nanotechnology* **6**, 568 (2006).
23. M. Kaur, J.S. McCloy, W. Jiang, Q. Yao, and Y. Qiang, *J. Phys. Chem. C*, **116**, 12875 (2012).
24. R. Tarumi, K. Takashima and Y. Higo, *Appl. Phys. Lett.* **81**, 4610 (2002)
25. F. X. Redl, C. T. Black, G. C. Papaefthymiou, R. L. Sandstrom, M. Yin, H. Zeng, C. B. Murray, and S. P. O'Brien, *J. Am. Chem. Soc.* **126**, 14583 (2004).
26. G. Ketteler, W. Weiss, W. Ranke and R. Schlögl, *Phys. Chem. Chem. Phys.* **3**, 1114 (2001)
27. K. J. Kim, D. W. Moon, S. K. Lee, and K.-H. Jung, *Thin Solid Films*, **360**, 118 (2000).
28. M. Stir, K. Ishizaki, S. Vaucher, and R. Nicula, *J. Appl. Phys.*, **105**, 124901 (2009).
29. G.S. Was, *Fundamentals of radiation materials science* (Springer, New York, 2007).
30. R. R. Egerton, P. Li, M. Malac, *Micron*, **35**, 399 (2004).
31. A. D. Smigellkas, E. O. Kirkendall, *AIME*, **171**, 130 (1947).
32. S. J. Randolph, J. D. Fowlkes, P. D. Rack, *J. Appl. Phys.*, **97**, 124312 (2005).
33. C. A. Grimes, D. Qian, E. C. Dickey, J. L. Allen and P. C. Eklund, *J. Appl. Phys.* **87**, 5642 (2000)

## **Chapter 9: In-situ Study of Nanostructure and Electrical Resistance of Nanocluster Films Irradiated with Ion Beams**

### **9.1 Abstract**

In this chapter, an in-situ study is reported on the structural evolution in nanocluster films under  $\text{He}^+$  ion irradiation using an advanced helium ion microscope. The films consist of loosely interconnected crystalline nanoclusters of magnetite or iron-magnetite ( $\text{Fe-Fe}_3\text{O}_4$ ) core-shells. The nanostructure is observed to undergo a dramatic change under ion-beam irradiation, featuring grain growth, phase transition, particle aggregation, and formation of nanowire-like network and nanopores. Major structural evolution is discovered to be activated by elastic nuclear collisions, while both electronic and thermal processes may also play key roles once the evolution starts. The electrical resistance of the  $\text{Fe-Fe}_3\text{O}_4$  films measured in situ exhibits a super-exponential decay with dose. The behavior suggests that the material possesses an intrinsic merit for development of an advanced online monitor for neutron radiation with high-sensitivity detection and long-term applicability, which enhances safety measures in many nuclear operations.

### **9.2 Introduction**

Among all sources of near-zero carbon-emission energies, nuclear energy is the only available, proven and affordable large-power electricity generation to date.<sup>1</sup> According to recent reports,<sup>2</sup> nearly 15% of the electricity needs worldwide were provided by nuclear power plants, and even larger percentages in France (80%) and U.S. (20%). With increasing demand for electricity, nuclear energy must be one of the essential parts in the diversity of various energy sources, especially at the current stage of undeveloped renewable energy. New nuclear power plants are being built and more are planned over the next decades.<sup>2</sup> However, severe nuclear accidents<sup>3</sup> that occurred in Three Mile Island, USA (1979), Chernobyl, USSR (1986), and more recently in Fukushima, Japan (2011) have decreased the public confidence of using the nuclear power, which greatly underscores

the importance to meet the highest standards of safety in operation of the existing nuclear power plants and in new designs of advanced nuclear reactors.<sup>4</sup> To date, many of the existing reactors are approaching to their designed operation lifetime. As a priority, research is critically needed to develop technologies that will sustain the safety of current reactors, including advanced monitoring systems that can quantify the “state of health” of structural materials in the current reactor fleet and predict their residual safe operating life. In addition, the monitoring system can be integrated into advanced reactors and new builds for inspectability and safety enhancement. Fast neutron monitors have been developed for application in various fields, including a spallation neutron source,<sup>5</sup> material testing reactors,<sup>6</sup> a subcritical facility,<sup>7</sup> and an accelerator-based neutron generator.<sup>8</sup> Many of the designs involve a coating of polyethylene<sup>5,7,9</sup> or fissile materials,<sup>6</sup> interacting with fast neutrons to create proton recoils or fission products that ionize gas and form electrical signals. In nuclear plants and neutron irradiation facilities, small online fast neutron flux monitors are much needed for effective assessment of material degradation in critical areas as well as for measurement of fast neutron dose in irradiated samples. Nanostructured materials are of both scientific interest and technological importance.<sup>10</sup> Their potential as an advanced sensor material for nuclear radiation needs to be explored. So far, very few reports have been published in the research field. Our recent studies<sup>11</sup> indicate that highly porous films of loosely interconnected magnetite ( $\text{Fe}_3\text{O}_4$ ) nanoparticles, composed of a few crystalline grains ( $\sim 3$  nm in size) each, undergo a dramatic change in nanostructure after 5.5 MeV  $\text{Si}^{2+}$  ion irradiation to a fluence of  $10^{16}$   $\text{Si}^{2+}/\text{cm}^2$  at nominal room temperature (RT). The structural change leads to magnetic domain growth, occurrence of magnetic anisotropy, and transition from superparamagnetic to ferromagnetic behavior. Similar films of  $\text{SmCo}_5$  nanoparticles with an average size of 3.5 nm were also shown to be superparamagnetic.<sup>12</sup> More recently, nanocluster films of iron-magnetite ( $\text{Fe}-\text{Fe}_3\text{O}_4$ ) core-shells were found<sup>13</sup> to reduce Fe valence in the oxide shell after ion irradiation in addition to similar nanostructural changes. In general, energy deposition by ion irradiation modifies material structure and its physical/chemical

properties through defect generation and accumulation (atomic displacements, defect clustering, etc.), amorphization, material decomposition, phase transition, phase segregation, formation of second-phase precipitates and gas species, grain growth, particle aggregation, volumetric change, micro-crack formation, etc. Material resistance or susceptibility to nuclear radiation depends on its structural stability. It is crucial to study structural changes induced by nuclear irradiation, in particular, evolution of nanostructures examined by in-situ methods that provide data to gain physical insights of the basic processes involved in the structural changes. Previous in-situ studies of microstructural evolution under ion irradiation have employed a transmission electron microscope (TEM) interfaced with an ion implanter or accelerator,<sup>14</sup> including facilities at Argonne National Laboratory in US,<sup>15</sup> National Institute for Materials Science in Japan,<sup>16</sup> Center of Nuclear Spectrometry and Mass Spectrometry in France,<sup>17</sup> Wuhan University in China,<sup>18</sup> and more recently at Sandia National Laboratory,<sup>19</sup> to just list a few. By using the in-situ capabilities over the past decades, major advances have been achieved in understanding defect formation, defect interactions and nanostructural evolution in various ion-beam irradiated materials.<sup>15, 20</sup> Other in-situ methods have also been developed and applied to study behavior of battery materials under different conditions.<sup>21</sup>

One of the foci of this study is the in-situ examination of nanostructural evolution with dose in nanocluster films of  $\text{Fe}_3\text{O}_4$  and  $\text{Fe-Fe}_3\text{O}_4$ . Recent technological advances have led to emergence of Helium Ion Microscope (HIM).<sup>22</sup> Compared to conventional scanning electron microscope (SEM), HIM has demonstrated a greatly improved imaging capability with a better surface sensitivity, a higher spatial resolution, a larger depth of field, and a sharper Z contrast. Although HIM was developed and employed in research only recently (since 2007), it has produced impactful results in various fields, including precision graphene cutting,<sup>23</sup> imaging of nanostructural and biological samples,<sup>11,24</sup> patterning and lithography,<sup>25</sup> and elemental analysis with sub-nanometer spatial resolution.<sup>26</sup> While imaged using secondary electrons or backscattered  $\text{He}^+$  ions, the material is simultaneously under  $\text{He}^+$  ion irradiation, which produces atomic displacements in the material. This

unique characteristic allows HIM to be applied for in-situ examinations of nanostructural evolution under  $\text{He}^+$  ion irradiation at a sub-nanometer resolution within the beam dwelling time, typically on the order of tens to hundreds of microseconds per pixel. It should be noted that under HIM, the structural change is observed from the near-surface only, where the dose is smaller than at the damage peak. Subsurface lattice damage from energetic  $\text{He}^+$  ions can be investigated through cross-sectional views.<sup>27</sup> Compared to the TEM-accelerator system, HIM provides a complementary in-situ capability for near real-time examination of bulk samples. Some samples (e.g., nanocluster films in this study) that are not very convenient to study under TEM may be examined in situ using HIM with a comparable spatial resolution.

The other focus of this study is the in-situ measurement of the electrical resistance of the nanocluster films irradiated with MeV ions using van der Pauw four-probe method.<sup>28</sup> The method is particularly effective for films whose electrical resistance decreases with increasing dose, while the substrate maintains a high value of resistance. This condition ensures that a higher dose does not lead to a higher leak current through the substrate, which would otherwise result in a larger error in the measurement of the film resistance. In contrast to a dramatic increase in the electrical resistivity of many metals and ceramics, including Al, Cu and Si upon irradiation due to defect accumulation,<sup>29</sup> our preliminary tests of a nanocluster film showed a significant decrease in the electrical resistance of the film with little alteration of the high resistance of the substrate after ion irradiation. This property makes the nanocluster films attractive as a candidate radiation sensor material for irradiation study of electrical resistivity.

### **9.3 Sample Preparation and Experimental Details**

Highly porous films of  $\text{Fe}_3\text{O}_4$  and Fe- $\text{Fe}_3\text{O}_4$  core-shell nanoclusters on surface-oxidized Si used in this study were prepared using a third-generation cluster-beam deposition system that consists mainly of three components: a cluster source, an e-beam evaporation chamber and a deposition chamber. Iron atoms from an ultra-high iron target sputtered by a high-pressure

magnetron-sputtering gun are decelerated through their collisions with Ar gas injected continuously into the cluster growth chamber cooled by chilled water. The formed Fe clusters are ejected from a small nozzle by differential pumping. When oxygen gas is introduced into the aggregation chamber or deposition chamber during processing, fully oxidized Fe clusters or uniform oxide shells on the core Fe clusters are formed prior to their deposition onto a surface-oxidized Si (100) substrate at room temperature. The resulting film is composed of loosely assembled nanoclusters. Measurements of the film thickness were performed using Rutherford backscattering spectrometry (RBS). The actual linear thickness is larger because of the large porosity. Si substrates with square electrodes at the four corners were also prepared prior to nanocluster deposition. A two-layer structure of Ti and Cu for the electrodes was used to enhance adhesion with the surface-oxidized Si surface.

Helium ion microscopy (HIM, Orion Plus, Carl Zeiss SMT, Peabody, MA) was employed to investigate nanostructural evolution during  $\text{He}^+$  ion irradiation. While imaged using secondary electrons, the material is simultaneously under  $\text{He}^+$  ion irradiation, which produces atomic displacements in the material. This process provides an unprecedented capability that allows for an in-situ study of nanostructural evolution in as-synthesized bulk samples at a sub-nanometer resolution (0.35 nm). In this study, irradiation of 25 keV  $\text{He}^+$  ions was performed near room temperature over a scanning area of  $1 \mu\text{m} \times 1 \mu\text{m}$ , corresponding to  $1024 \times 1024$  pixels with a dwelling time of 200  $\mu\text{s}$  at each pixel. The beam current at the sample was reduced to typically 0.5 pA, leading to an ion flux of  $3.1 \times 10^{14}$  ( $\text{He}^+/\text{cm}^2$ )/sec. The ion fluence for each image is taken as the arithmetic average of the initial and final fluences. The procedure was repeated in the same scanning area to obtain a sequence of image frames with increasing ion fluence. Movies showing the nanostructural evolution as a function of ion fluence or dose in displacements per atom (dpa) were made from the image frames. Similar in-situ study using 20 keV electrons at 0.96 nA under an SEM was performed.

Additional ion irradiation was performed using a 3.0 MV electrostatic tandem accelerator (NEC 9SDH-2 pelletron, Middleton, WI). The granular film was irradiated at normal incidence with 5.5 MeV  $\text{Si}^{2+}$  ions to a fluence up to  $4 \times 10^{15}$  ions/cm<sup>2</sup> or 2.0 MeV  $\text{He}^+$  ions up to  $8 \times 10^{15}$  ions/cm<sup>2</sup> at room temperature or 473 K. A beam rastering system was used to ensure uniform irradiation over an area of  $5.1 \times 5.1$  mm<sup>2</sup> covering the entire film area. Typical ion flux was on the order of 0.01 ( $\text{Si}^{2+}/\text{nm}^2$ )/sec and 0.01 ( $\text{He}^+/\text{nm}^2$ )/sec, and the increase of the sample temperature was less than 50 K during the irradiation. In-situ electrical resistivity measurement of the nanocluster films during ion irradiation was conducted based on reciprocal van der Pauw four-probe method, where arithmetic average of the resistance was obtained by two reversed polarity measurements. After each irradiation dose, in-situ measurements were followed. The irradiation and measurement were conducted intermittently. However, a test to measure the electrical resistance was also attempted under continuous ion irradiation with data recording and a similar dependence of the resistance with ion fluence was observed. In all events, ion energy was high enough to penetrate the films in this study, leaving no or negligible amount of implanted ions in the film materials of interest.

The crystal structure of the nanocluster films without electrodes before and after ion irradiation was analyzed using the Philips X'pert Multi-Purpose Diffractometer (MPD, PAN analytical, Almelo, The Netherlands) based on fixed Cu K $\alpha$  radiation ( $\lambda = 0.154187$  nm). Grazing-angle incidence x-ray diffraction (GIXRD) was employed to study the crystallographic phase and average size of the crystalline grains at room temperature. This technique eliminates the strong diffraction peaks from the single-crystal substrate. In addition, to avoid peak overlapping of diffraction peaks from electrodes, the in-situ samples with Cu/Ti electrodes and Ag paste after irradiation were also analyzed with micro-beam GIXRD.

### 9.3.1 Van der Pauw Sample Preparation

Si (100) substrates with an area of 10 mm  $\times$  10 mm and a SiO surface layer of  $\sim$ 300 nm in thickness were used for van der Pauw sample preparation (Figure 9.1). To enhance adhesion strength

between  $\text{SiO}_2$  on the Si surface and electrode Cu, a Ti buffer layer ( $3 \text{ mm} \times 3 \text{ mm}$  in area and 100 nm in thickness) was deposited onto the substrate in each of the four corners using a magnetron sputtering deposition system. Titanium layer has been known to be a good adhesive layer, particularly at the interfaces with Si or  $\text{SiO}_2$ . Four Cu electrodes of  $3 \text{ mm} \times 3 \text{ mm}$  in area and 1  $\mu\text{m}$  in thickness were deposited on the top of the Ti layers. Highly porous films of  $\text{Fe}_3\text{O}_4$  or Fe- $\text{Fe}_3\text{O}_4$  core-shell nanoclusters with a dimension of about  $5 \text{ mm} \times 5 \text{ mm}$  were deposited at the center of the substrate with the four corners touching the Cu electrodes.

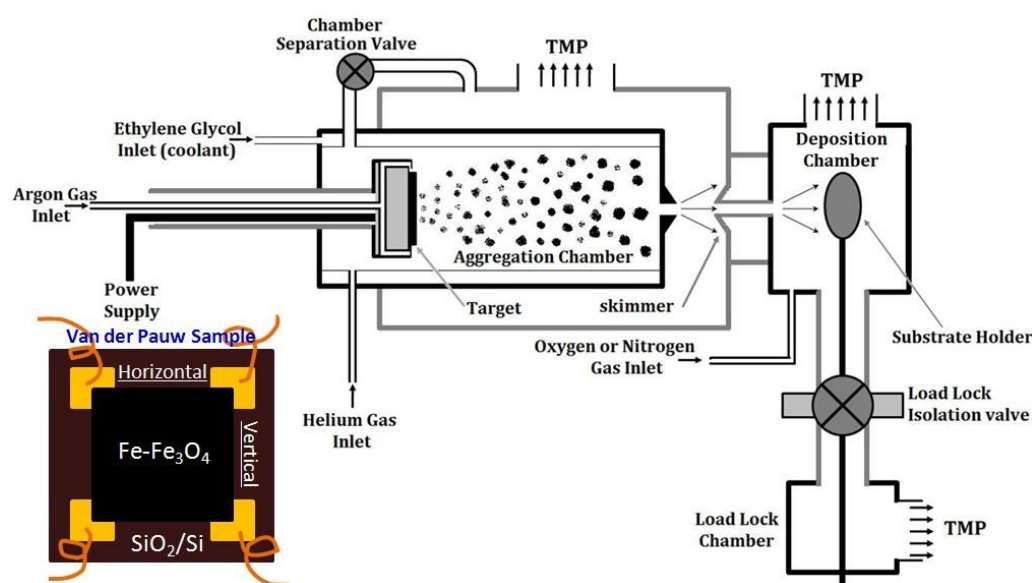


**Figure 9.1** Cluster-beam deposition system and a schematic drawing for a van der Pauw sample of Fe- $\text{Fe}_3\text{O}_4$  core-shell nanocluster film on a surface-oxidized Si substrate with four Cu/Ti electrodes and Cu leads prepared and used in this study is also shown.

A third-generation cluster-beam deposition system<sup>39</sup> was used for the nanocluster film deposition, which consists mainly of three components: a cluster source, a mass-selection chamber and a deposition chamber. Iron atoms from an ultra-high purity iron target sputtered by a high-pressure magnetron-sputtering gun are decelerated through their collisions with Ar gas injected continuously into the cluster growth chamber cooled by chilled water. Iron clusters are generated by Fe atomic interaction and condensation. The formed Fe clusters are ejected from a small nozzle by



differential pumping. When oxygen gas is introduced into the source chamber or deposition chamber during processing, fully oxidized Fe clusters or uniform oxide shells on the core Fe clusters are formed prior to their soft landing onto the substrate near RT. The cluster size can be controlled to a narrow size distribution (5%) using the mass selector. Measurement of the film thickness was performed using in-situ quartz crystal microbalance and ex-situ 2.0 MeV  $\text{He}^+$  Rutherford backscattering spectrometry (RBS) (based on  $5.197 \text{ g/cm}^3$ ). Conducting Cu wires (0.14 mm in diameter) were bonded to each of the four Cu/Ti electrodes using PELCO high-performance silver paste (Product No. 16047).

### 9.3.2 In-situ HIM Examination

As shown in figure 9.2 a helium ion microscope (Orion Plus, Carl Zeiss SMT, Peabody, MA) was employed to investigate nanostructural evolution during  $\text{He}^+$  ion irradiation. Irradiation of 25 or 30 keV He performed at nominally RT over a scanning area of  $1 \mu\text{m} \times 1 \mu\text{m}$  with  $1024 \times 1024$  pixels at a dwelling time of 200  $\mu\text{s}$  for each pixel. The beam current at the sample was reduced to typically 0.5 pA, leading to an ion flux of  $3.1 \times 10^{14} \text{ He}^+$  ions/ $\text{cm}^2/\text{sec}$ .

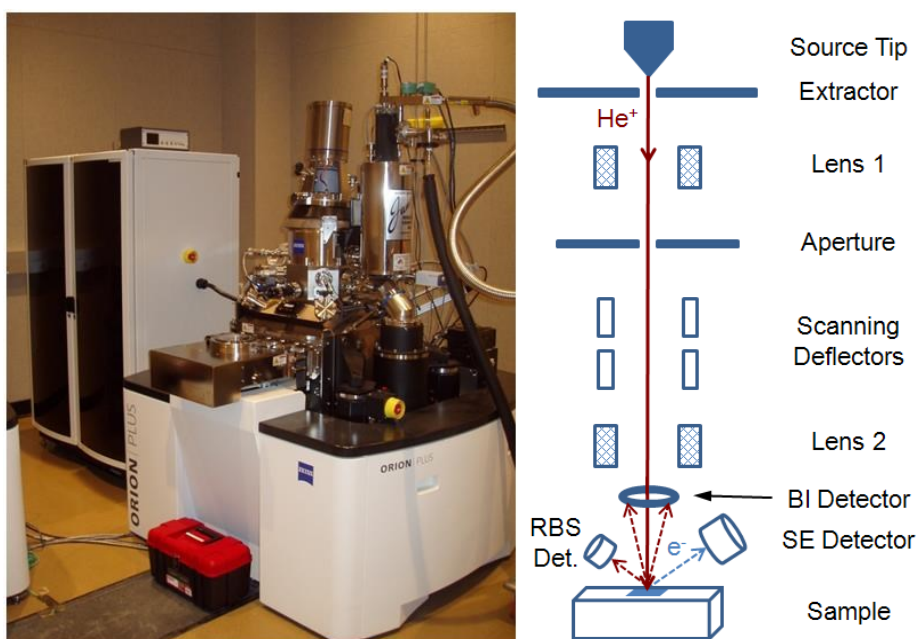


**Figure 9.2** Helium ion microscope and its working principle.

The ion fluence for each image is taken as the arithmetic average of the initial and final fluences. Scans were repeated in the same area for 30 times to obtain consecutive image frames. Movies showing the nanostructural evolution as a function of ion fluence or dose in dpa at the surface were made from the image frames. The frames in the movie have been cropped in the same irradiated area to minimize sample drift effect for better visualization. Similar in-situ study of the nanostructures was performed under 20 keV electron irradiation (at 0.96 nA over a scanning area of  $2.5 \mu\text{m} \times 2.3 \mu\text{m}$ ) using a FIB/SEM system (FEI Quanta 3D FEG).

### 9.3.3 In-situ Resistance Measurement

Ion irradiation was performed using a 3.0 MV electrostatic tandem ion accelerator (NEC 9SDH-2 pelletron, Middleton, WI). Cluster films were irradiated at normal incidence with 5.5 MeV  $\text{Si}^{2+}$  ions to a fluence up to  $10^{16} \text{Si}^{2+}/\text{cm}^2$  or 2.0 MeV  $\text{He}^+$  ions up to  $8 \times 10^{15} \text{He}^+/\text{cm}^2$  at nominally RT or 473 K. A beam rastering system was used to ensure uniform irradiation covering the entire film area of  $5 \text{mm} \times 5 \text{mm}$ . Typical ion flux was on the order of  $0.01 (\text{Si}^{2+}/\text{nm}^2)/\text{sec}$  and  $0.01 (\text{He}^+/\text{nm}^2)/\text{sec}$ . The increase of the sample temperature was less than 50 K during the ion irradiation. In-situ electrical resistance measurement of the nanocluster films was conducted based on reciprocal van der Pauw four-probe method, where arithmetic average of the resistance was obtained from two reversed polarity measurements. After each irradiation dose, a measurement was followed with beam off. The irradiation and measurement were conducted intermittently. In all events, ion energy was selected to be high enough to penetrate the films, leaving negligible amounts of implanted ions in the films. The pictures of accelerator, four probe set up for in-situ measurement and the conductivity data output are shown in Figure 9.3.

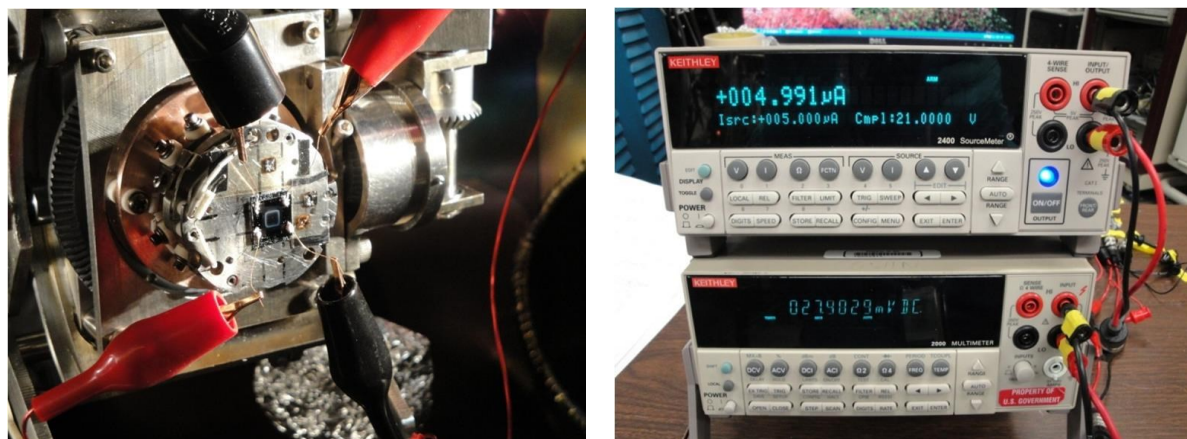
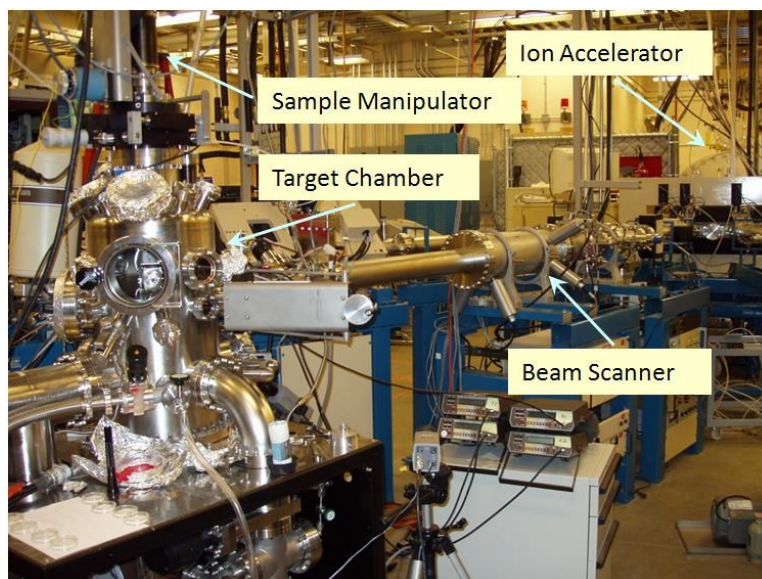


**Figure 9.3** NEC 3.0 MV tandem ion accelerator and +15° beam line for in-situ resistance measurements of nanocluster films under 5.5 MeV  $\text{Si}^{2+}$  and 2.0 MeV  $\text{He}^+$  ion irradiation at nominally room temperature and 473 K using van der Pauw four-probe method. The film resistance was determined from the arithmetic average from two reversed-polarity and reciprocal measurements along the horizontal and vertical directions.

### 9.3.4 XRD analysis

The crystal structures of nanocluster films without electrodes before and after ion irradiation were analyzed using the Philips X'pert Multi-Purpose Diffractometer (MPD, ANalytical, Almelo, The Netherlands) based on fixed  $\text{Cu K}\alpha$  radiation ( $\lambda = 0.154187 \text{ nm}$ ). GIXRD was employed to study the crystallographic phase and average size of the crystalline grains at RT. This technique

eliminates the strong diffraction peaks from the single-crystal substrate. In addition, to eliminate interfering diffraction peaks from the Cu/Ti electrodes and Ag paste, in-situ samples were analyzed with micro-beam GIXRD on the nanocluster film. The data were collected using a Rigaku D/Max Rapid II instrument with a 2D image plate detector. X-rays were generated with a MicroMax 007HF generator fitted with a rotating Cr anode ( $\lambda = 0.22897$  nm), focused on the specimen through a 300 mm diameter collimator. The samples were secured onto a flat reflection sample holder and fitted onto the sample stage. 2DP, Rigaku 2D Data Processing Software (version 1.0, Rigaku, 2007) was used to integrate the diffraction rings captured by the 2D image plate detector. The analysis of diffraction data was carried out using JADE 9.5.1 (Materials Data Inc.), TOPAS 4.2 (Bruker AXS GmbH, Karlsruhe, Germany), and PDF4+ 2012 database (ICSD).

## **9.4 Results and Discussion**

### **9.4.1 Structural Evolution in Fe<sub>3</sub>O<sub>4</sub> Nanocluster Film**

An in-situ study of structural evolution in a magnetite Fe<sub>3</sub>O<sub>4</sub> nanocluster film on a surface-oxidized Si substrate at nominal RT has been performed under 25 keV He<sup>+</sup> ion irradiation using HIM. According to the full-damage cascade simulation based on the Stopping and Range of Ions in Matter (SRIM) code,<sup>30</sup> where the threshold displacement energy for each of the sub lattices in Fe<sub>3</sub>O<sub>4</sub> was assumed to be 25 eV, sputtering rate under the irradiation conditions is negligible; atomic displacement rate corresponds to  $\sim 0.26$  displ./nm/ion at the surface and  $\sim 0.64$  displ./nm/ion at the damage peak that is located at the depth of  $\sim 120$  nm (assuming the theoretical specific gravity of  $5.197$  g/cm<sup>3</sup> and hereafter). The electronic and nuclear stopping powers at the surface are 139 and 12 keV/ $\mu$ m, respectively. The dose in dpa was estimated near the surface for HIM examinations and an average value of the entire film thickness for the grazing-angle incidence x-ray diffraction (GIXRD) and resistivity measurements. In all events of this study, the film thickness is much smaller than the

respective ion projected range so that a great majority of ions penetrated the films and implanted in the Si substrate.

Three individual HIM snapshots of the surface nanostructures from a movie are shown in Figure 9.4 at ion fluences of  $3.3 \times 10^{16}$ ,  $7.6 \times 10^{17}$  and  $1.9 \times 10^{18}$  He<sup>+</sup>/cm<sup>2</sup>, corresponding to doses of 0.9, 20 and 51 dpa (displacements per atom) at the surface, respectively, where the dose rate is  $8.6 \times 10^{-3}$  dpa/sec. Apparently, with increasing dose, nanoclusters aggregate to form larger particles while nanostructure shrinks, resulting in formation of a nanowire-like network accompanied with nano-pores. It has been clearly observed the nanostructural evolution with increasing dose.

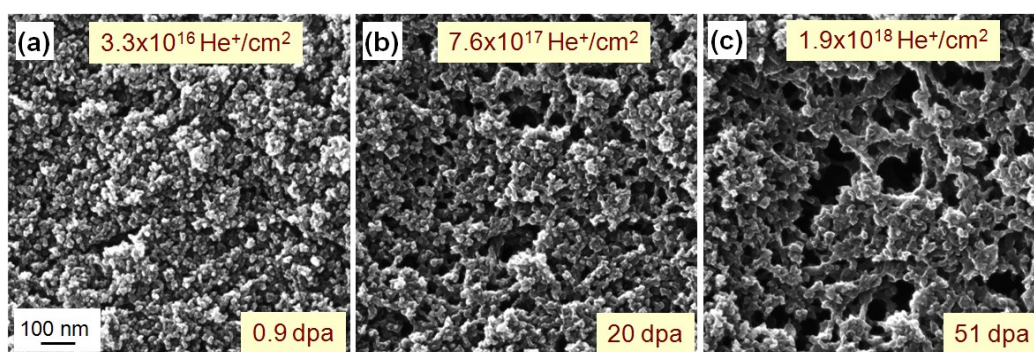


**Figure 9.4** Selected HIM (operating at 25 kV) snapshots of a nanocluster magnetite Fe<sub>3</sub>O<sub>4</sub> film on a surface-oxidized Si substrate irradiated to various ion fluences: (a)  $3.3 \times 10^{16}$ , (b)  $7.6 \times 10^{17}$  and (c)  $1.9 \times 10^{18}$  He<sup>+</sup>/cm<sup>2</sup> at nominal RT. The images have the same scalar bar and show a significant change in the nanostructure (same area).

Upon irradiation, loosely interconnected nanoparticles tend to aggregate. With increasing dose, small particles are absorbed by larger ones, resulting in an overall increase of the particle size. Larger particles interconnect themselves and gradually form a nanowire-like network with concurrent formation of nano-pores. Previous GIXRD for a Si<sup>2+</sup> ion irradiated Fe<sub>3</sub>O<sub>4</sub> nanocluster film to  $10^{16}$  Si<sup>2+</sup>/cm<sup>2</sup>, or an average dose of  $\sim 4$  dpa in the film thickness, indicates<sup>11</sup> a significant increase in grain size. Grain growth took place likely at an expense of the surrounding amorphous material through irradiation-induced interfacial epitaxy and/or of smaller crystalline grains through coalescence. Each grain is a single-domain magnet; irradiation-assisted reorientation of their magnetic moments to reduce the overall system energy could facilitate coalescence to occur.



Irradiation with energetic ions provides three stimuli to promote nanostructural changes, i.e., nuclear elastic collision induced atomic displacements, electronic energy deposition induced atomic excitation and ionization, and heat production induced thermal processes. Experiments were designed and performed to study the individual roles. While  $\text{He}^+$  irradiation was conducted at nominal RT, the temperature within the beam spot is expected to be higher than RT. The actual temperature within the beam spot depends on ion energy, flux, material thermal conductivity, etc. Accurate measurement of the temperature within the small beam spot ( $\sim 1 \mu\text{m} \times 1 \mu\text{m}$ ) was not possible in the study. Calculations<sup>31</sup> also have a great challenge because of the porous nature and structural evolution. Irradiation of similar  $\text{Fe}_3\text{O}_4$  nanocluster films at nominal RT with 5.5 MeV  $\text{Si}^{2+}$  ions at a flux of  $\sim 10^{12} \text{Si}^{2+}/\text{cm}^2/\text{sec}$  indicated<sup>11</sup> a temperature increase of less than 50 K near the beam spot. To study thermal effects on the nanostructural evolution, the as-deposited  $\text{Fe}_3\text{O}_4$  nanocluster film used in Figure 9.4, was annealed in flowing Ar gas environments at 473 and 773 K for 10 hours each. Figure 9.5 shows the surface nanostructures of the film before and after the thermal annealing steps. The nanostructures from different areas of the sample appear to be similar without showing a noticeable change. The data in Figure 9.5 do not suggest an observable modification in the nanostructure after the thermal treatments at temperatures up to 773 K.

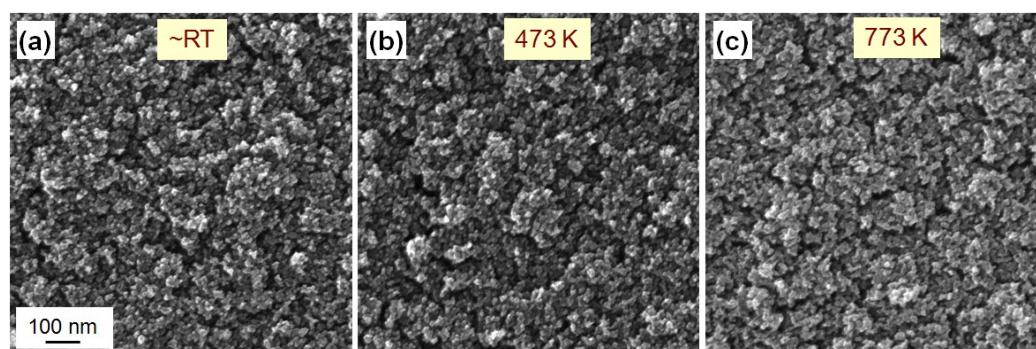


**Figure 9.5** HIM (operating at 25 kV) micrographs of the same nanocluster magnetite  $\text{Fe}_3\text{O}_4$  film in Fig. 1: (a) as-deposited at nominal RT, (b) annealed at 473 K and (c) at 773 K for 10 hours each in flowing Ar gas environments. The images have the same scalar bar and show a similar nanostructure (different areas).

In-situ electron irradiation was also carried out using a scanning electron microscope (SEM) operating at a voltage of 20 kV and a high electron current of 0.96 nA. At the electron energy of 20 keV, permanent atomic displacements cannot be produced in  $\text{Fe}_3\text{O}_4$  crystal due to the limited kinetic energy transfer from electrons to target atoms in the elastic collision process, which is well below the threshold displacement energy (presumably on the order of tens of eV). The primary electrons lose energy in the material mainly through excitation and ionization of the target atoms with multiple interactions. As a result, secondary electrons, photons and phonons are generated in the energy loss process. It should be noted that the electronic energy deposition can influence kinetic process due to sample temperature increase and possible modifications of diffusion energy barriers. Figure 9.6 shows SEM micrographs of nanostructures of a  $\text{Fe}_3\text{O}_4$  nanocluster film before and after electron irradiation to  $4.4 \times 10^{19}$ ,  $1.3 \times 10^{21}$  and  $2.6 \times 10^{21}$   $\text{e}/\text{cm}^2$  at nominal RT. Although the SEM images show a worse resolution and a weaker contrast as compared to HIM images in Figure 9.4, they provide clear evidence that the nanostructure at the surface of the nanocluster film does not change noticeably up to  $2.6 \times 10^{21}$   $\text{e}/\text{cm}^2$ .

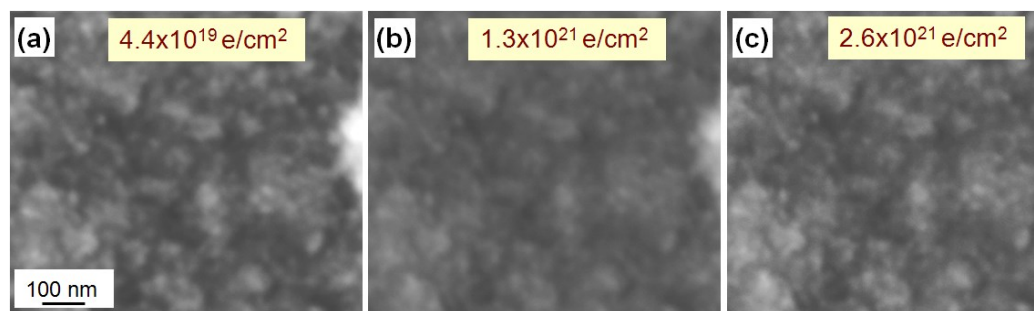


**Figure 9.6** Selected SEM (operating at 20 kV) snapshots of the same nanocluster magnetite  $\text{Fe}_3\text{O}_4$  film in Fig. 1 irradiated to various electron fluences: (a)  $4.4 \times 10^{19}$ , (b)  $1.3 \times 10^{21}$  and (c)  $2.6 \times 10^{21}$   $\text{e}/\text{cm}^2$  at nominal RT. The images have the same scalar bar and show a similar nanostructure (same area).

The density of the electronic energy deposition  $\rho_e$  is the product of ion/electron fluence  $F$  and electronic stopping power  $(dE/dx)_e$ , i.e.,

$$\rho_e = F \times (dE/dx)_e. \quad (9.1)$$

Similarly, the rate of the electronic energy deposition  $\gamma_e$  is the product of ion/electron flux  $f$  and  $(dE/dx)_e$ :

$$\gamma_e = f \times (dE/dx)_e. \quad (9.2)$$

According to the NIST ESTAR database,<sup>33</sup> the electronic stopping powers for 20 keV electrons in Fe and O are 8.468 and 11.38 MeV cm<sup>2</sup>/g, respectively. Using Bragg's rule,<sup>34</sup> the electronic stopping power of 20 keV electrons in Fe<sub>3</sub>O<sub>4</sub> is estimated to be 10.13 MeV cm<sup>2</sup>/g. Similarly, using ASTAR database,<sup>33</sup> the electronic stopping power for 25 keV He<sup>+</sup> ions in Fe<sub>3</sub>O<sub>4</sub> is 412.8 MeV cm<sup>2</sup>/g. As a rough estimation from Eq. (9.1), we obtain a density ratio [ $\rho_e(e)/\rho_e(\text{He}^+)$ ] of ~30 for 20 keV electron irradiation to  $2.6 \times 10^{21}$  e/cm<sup>2</sup> to 25 keV He<sup>+</sup> ion irradiation to  $1.9 \times 10^{18}$  He<sup>+</sup>/cm<sup>2</sup>. This represents a significantly higher energy density deposited by the electrons [Figure 9.6(c)] than that by the He<sup>+</sup> ions [Figure 9.4(c)] at the surface. From Eq. (9.2), the rate ratio [ $\gamma_e(e)/\gamma_e(\text{He}^+)$ ] for the electron irradiation (0.96 nA over an area of 2.5  $\mu\text{m} \times 2.3 \mu\text{m}$ ) versus He<sup>+</sup> ion irradiation (0.5 pA over 1  $\mu\text{m} \times 1 \mu\text{m}$ ) is ~8, which suggests that the temperature within the beam spot of the electrons in SEM should be higher than that of the He<sup>+</sup> ions in HIM. Although both the density and rate ratios are higher, electron irradiation shown in Figure 9.6 does not suggest an observable change in the surface nanostructure up to the highest fluence applied ( $2.6 \times 10^{21}$  e/cm<sup>2</sup>). The result indicates that the combined effects from the electronic energy deposition and elevated temperature are not a major contributor to activate major structural evolution in the Fe<sub>3</sub>O<sub>4</sub> nanocluster film.

Because both thermal and electronic processes can hardly alter the initial nanostructure of the Fe<sub>3</sub>O<sub>4</sub> nanocluster film, nuclear elastic collision is concluded to be primarily responsible for the activation of the dramatic nanostructural evolution at high doses. It should be noted that despite their inactivity for structural evolution, both thermal and electronic processes could play a significant role once the nanostructural evolution starts. The results from Figures 9.4 to 9.6 suggest that the structure of the nanocluster films is likely to be sensitive to fast neutron irradiation, where the first-order



electronic process is absent, but both atomic displacements and heat production processes are active. Further investigations of this type of films under neutron irradiation are planned and the results from the effort will be reported in future publications.

#### 9.4.2 Nanostructural Evolution and Phase Transition in Fe-Fe<sub>3</sub>O<sub>4</sub> Core-shell Nanocluster Film

Figure 9.7 shows the surface structure of a Fe-Fe<sub>3</sub>O<sub>4</sub> core-shell nanocluster film on a surface-oxidized Si irradiated with 30 keV He<sup>+</sup> ions to  $5.2 \times 10^{16}$ ,  $1.1 \times 10^{18}$  and  $2.8 \times 10^{18}$  He<sup>+</sup>/cm<sup>2</sup> at nominal RT, corresponding to 1.2, 25 and 65 dpa at the surface, respectively.

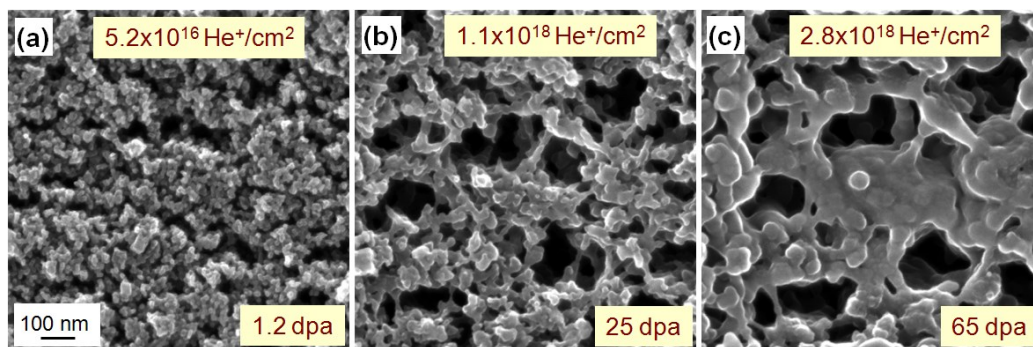


**Figure 9.7** Selected HIM (operating at 30 kV) snapshots of a Fe-Fe<sub>3</sub>O<sub>4</sub> core-shell nanocluster film on a surface-oxidized Si substrate irradiated to various ion fluences: (a)  $5.2 \times 10^{16}$ , (b)  $1.1 \times 10^{18}$  and (c)  $2.8 \times 10^{18}$  He<sup>+</sup>/cm<sup>2</sup> at nominal RT. The images have the same scalar bar and show a dramatic change in the nanostructure (same area).

The nanoclusters have a Fe core of  $\sim 8$  nm in diameter and a Fe<sub>3</sub>O<sub>4</sub> at nominally RT, shell of  $\sim 2$  nm in thickness. Typical TEM micrographs showing the nanoclusters, nano-grains and core-shell structure are provided in the supporting information (Figure 9.8). As an approximation for the core-shell structure, magnetite Fe<sub>3</sub>O<sub>4</sub> was used for SRIM simulation. The results indicate that the atomic displacement rate and electronic stopping power at the surface are 0.22 displ./nm/ion and 155 keV/ $\mu$ m, respectively, which are comparable to those from 25 keV He ion irradiation of Fe<sub>3</sub>O<sub>4</sub>. Similar to the structural evolution in the Fe<sub>3</sub>O<sub>4</sub> nanocluster film shown in Figure 9.4, loosely interconnected small nanoparticles in the Fe-Fe<sub>3</sub>O<sub>4</sub> core-shell nanocluster film aggregate to form larger particles as ion fluence increases, followed by formation of nanowire-like network and nano-

pores. The nanostructure shrinks gradually till the dose reaches to the fluence of  $2 \times 10^{18}$   $\text{He}^+/\text{cm}^2$  or a dose of 45 dpa at the surface, where the nanoparticle at the image center and the surrounding structure begin to expand in volume.

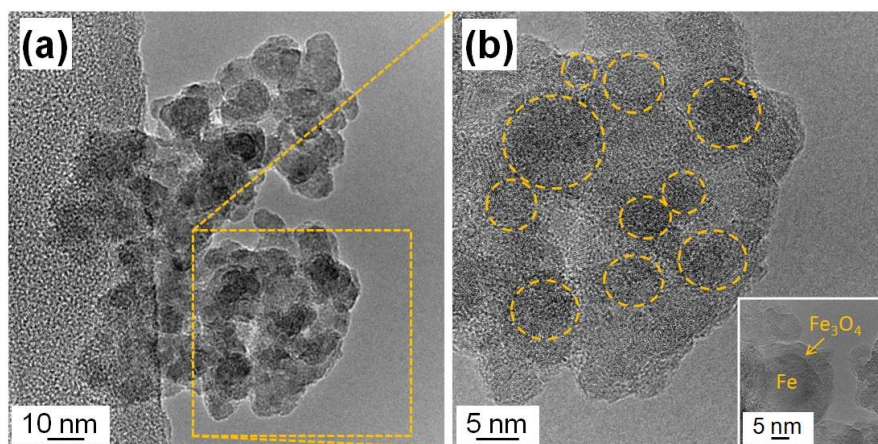


**Figure 9.8** Typical TEM micrographs of Fe-Fe<sub>3</sub>O<sub>4</sub> core-shell nanoclusters: (a) loosely interconnected nanoparticles and (b) a particle containing a number of grains (circled) surrounded by amorphous material; a grain has a Fe core and Fe<sub>3</sub>O<sub>4</sub> shell, as shown in the inset

The surface morphology of the resulting material appear to be similar to that of a similar core-shell film after irradiation with Si<sup>2+</sup> ions to a lower dose at nominal RT, where phase transition of the oxide shell was observed (see below). This volumetric expansion is not yet understood at this stage, but might be associated with helium accumulation, phase transition, defect induced swelling, combination of those or other processes. Further studies are needed for clarification.

To study crystalline phase and grain size, a 3.0 MV ion accelerator was used for a larger-area irradiation that covers the entire surface ( $8 \times 8 \text{ mm}^2$ ) of a Fe-Fe<sub>3</sub>O<sub>4</sub> core-shell nanocluster film ( $\sim 0.9 \mu\text{m}$  in thickness determined by RBS analysis for magnetite Fe<sub>3</sub>O<sub>4</sub>) with 5.5 MeV Si<sub>2+</sub> ions at nominal RT. The irradiation was performed in the low vacuum range of  $10^{-7}$  Torr to  $10^{16}$  Si<sup>2+</sup>/cm<sup>2</sup>, corresponding to an average dose of  $\sim 0.95$  dpa in the film thickness. Figure 9.9 (a) shows the grazing-angle incidence x-ray diffraction (GIXRD) pattern for the film before and after irradiation. The results indicate that prior to irradiation, the crystalline grains consisted of a Fe core of 8 nm in diameter with a shell Fe<sub>3</sub>O<sub>4</sub> of 2 nm in thickness on the average. After irradiation, the average size of

the Fe core decreased slightly to 7 nm. The oxide shell transformed from cubic magnetite  $\text{Fe}_3\text{O}_4$  to cubic Wüstite  $\text{FeO}$  with the average shell thickness increased to 13 nm. The weight ratio of Fe in the film decreased from 81% to 36%. The process might involve creation of O interstitials in  $\text{Fe}_3\text{O}_4$  by ion irradiation, followed by O diffusion, oxidation of Fe, and phase transition to cubic  $\text{FeO}$  in the shell. Epitaxial growth of  $\text{FeO}$  from interface could not be ruled out. Evidently, cubic Wüstite is the preferred phase over the cubic magnetite under the ion irradiation conditions at nominal RT. Similar behavior of Fe valence reduction in the oxide shell of a  $\text{Fe}-\text{Fe}_3\text{O}_4$  nanocluster film was also observed after ion irradiation.<sup>11</sup> A previous study<sup>35</sup> has indicated that a large fraction of nanophase  $\text{FeO}$  can be grown on sapphire when the growth rate is high. Although Wüstite is known as a high-pressure phase,<sup>36</sup> thin epitaxial  $\text{FeO}$  films on Fe have been found to be stable even in vacuum at RT.<sup>37</sup> The cross-sectional view of the film nanostructures before and after  $\text{Si}^{2+}$  ion irradiation is shown in Figure 9.9a and 9.9c, respectively. As a result of the irradiation, the highly porous film becomes a columnar structure that is aligned with the irradiation direction (surface normal). Nano-cracks in the irradiated film also appear, as shown in Figure 9.9c, which could be attributed to accumulation and redistribution of nano-pores that are formed during ion irradiation, similar to those observed in Figure 4.

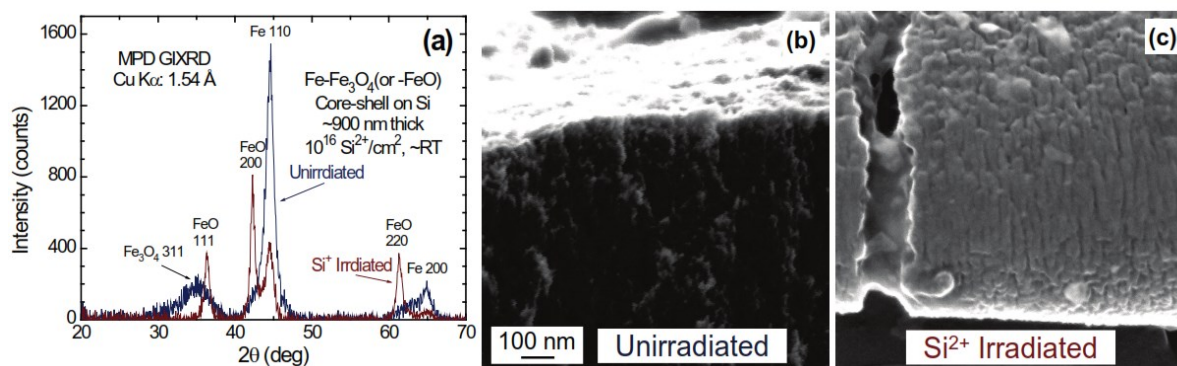


**Figure 9.9** (a) Background subtracted GIXRD patterns for a  $\text{Fe}-\text{Fe}_3\text{O}_4$  core-shell nanocluster film on Si before and after 5.5 MeV  $\text{Si}^+$  ion irradiation to  $10^{16} \text{Si}^+/\text{cm}^2$  ( $\sim 0.95$  dpa in the film) at nominal RT. Also shown are the corresponding cross-sectional HIM images of the film (b) before and (c) after the irradiation. The two images have the same scalar bar.

### 9.4.3 Response of Fe-Fe<sub>3</sub>O<sub>4</sub> Nanocluster Film Resistivity to Ion Irradiation

In-situ resistivity measurements of Fe-Fe<sub>3</sub>O<sub>4</sub> core-shell nanocluster films at nominal RT and 473 K were performed based on van der Pauw four-probe method. The behavior from the reciprocal measurements of the resistivity along the horizontal and vertical directions is found to be similar in this study and only vertical resistivity is shown for clarity. The supporting document available online provides some details about the experimental facilities and procedures. Figure 9.10 shows the average resistance of a 200 nm thick Fe-Fe<sub>3</sub>O<sub>4</sub> nanocluster film at nominal RT as a function of Si<sup>2+</sup> ion fluence (bottom axis) and average dpa dose in the film (top axis).

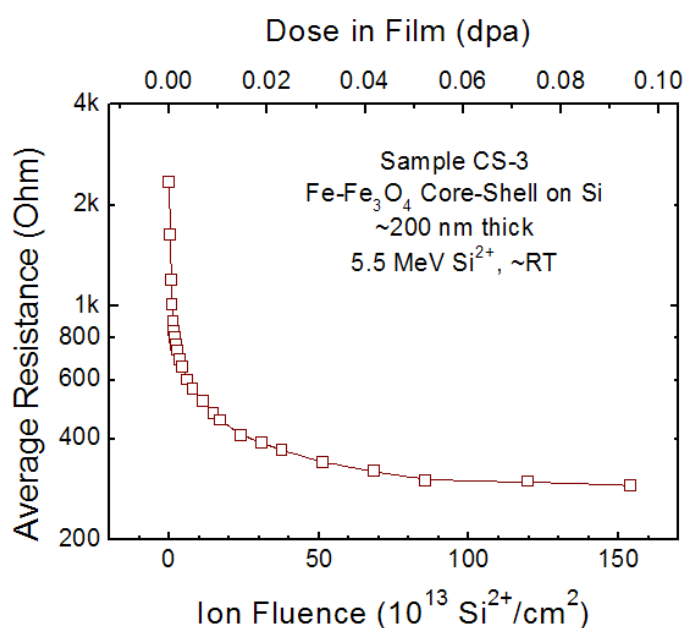


**Figure 9.10** Electrical resistance of a Fe-Fe<sub>3</sub>O<sub>4</sub> core-shell nanocluster film on surface-oxidized Si measured in situ using van der Pauw method as a function of ion fluence during 5.5 MeV Si<sup>2+</sup> ion irradiation at nominal RT. A super exponential decay behavior of the resistance is observed.

The in-situ results reveal that under the ion irradiation there is a super-exponential decay dependence of the electrical resistance on dose in the Fe-Fe<sub>3</sub>O<sub>4</sub> nanocluster film. The electrical resistance decreases from ~2.3 kΩ for the as-deposited film to ~290 Ω at a dose of ~0.1 dpa. The resistance in the entire dose range is much smaller than that of the blank substrate (without film) that has a value on the order of 10 MΩ with a weak dependence on dose. The leak current through the

substrate is negligible at all doses in the measurement. Thus the resistance behavior shown in Figure 9.10 suggests that the nanocluster film has a potential as a sensor material for neutron detection and monitoring. In the low-dose regime ( $< 0.01$  dpa), the material is extremely susceptible to nuclear irradiation, providing a potential for high-sensitivity detection. The resistance decreases more gradually in the higher-dose regime, allowing for a long-term use for neutron monitoring. Note that according to SRIM simulation, the sputtering rate for 5.5 MeV  $\text{Si}^{2+}$  ions incident on  $\text{Fe}_3\text{O}_4$  is 0.12 atoms/ion, resulting in less than 1 nanometer removal of the surface material for the highest accumulated fluence of  $1.6 \times 10^{15} \text{ Si}^{2+}/\text{cm}^2$ , which is negligible compared to the film thickness ( $\sim 200$  nm).

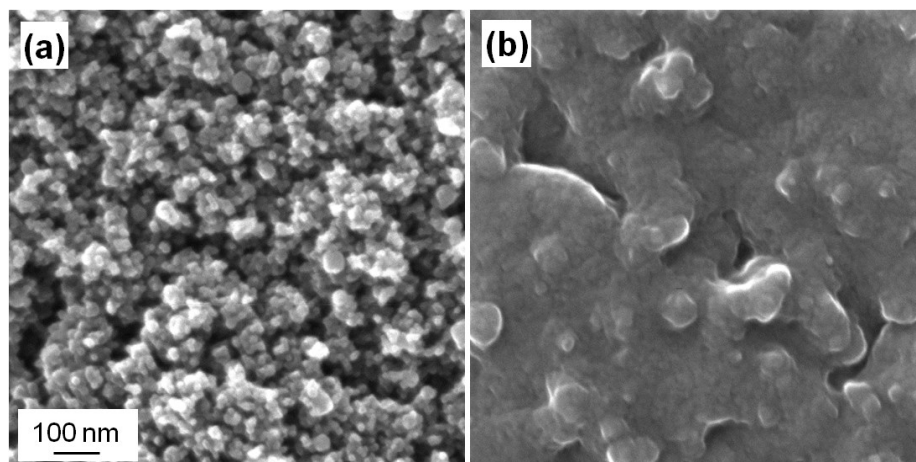


**Figure 9.11** HIM micrographs of the same sample in Fig. 6 (a) before and (b) after 5.5 MeV  $\text{Si}^{2+}$  ion irradiation to  $1.5 \times 10^{15} \text{ Si}^{2+}/\text{cm}^2$  (0.08 dpa at the surface) at nominal RT. The images have the same scalar bar and show a dramatic change in the nanostructure.

The nanostructures of the in-situ sample in Figure 9.10 before and after irradiation are shown in Figure 9.11. At the highest accumulated fluence of  $\sim 1.5 \times 10^{15} \text{ Si}^{2+}/\text{cm}^2$  (or 0.08 dpa at the surface) at nominal RT, a dramatic change in the nanostructure is exhibited, featuring nanoparticle aggregation and formation of large particles and nano-pores. The overall nanostructure is different from that irradiated to a low dose with  $\text{He}^+$  ions [such as that shown in Figure 9.7 (a)], but more similar to that of the nanoparticle resulted from a much higher dose  $\text{He}^+$  ion irradiation of the core-shell film shown in Figure 9.7 (c). According to SRIM simulation, the dose rate for 5.5 MeV  $\text{Si}^{2+}$  ion

irradiation is  $\sim 2$  times as high as that for 30 keV  $\text{He}^+$  ion irradiation at the surface. The result in Figure 9.11 indicates that there is a significant mass effect of ion irradiation on nanostructural modifications. Consistent with the data in Figure 9.9, phase transition of the oxide shell from cubic magnetite  $\text{Fe}_3\text{O}_4$  to cubic Wüstite  $\text{FeO}$  is evident in the irradiated sample, as shown in Figure 9.12, where micro-beam GIXRD was used to eliminate overlapping diffraction peaks from the Cu/Ti electrodes and Ag paste. Data analysis from the whole-peak fitting reveals that the average grain size increases from 5.3 to 9.4 nm for Fe and from 4.8 nm for  $\text{Fe}_3\text{O}_4$  to 5.5 for  $\text{FeO}$  after the  $\text{Si}^{2+}$  ion irradiation to an average dose of only 0.09 dpa in the film. The weight ratio of Fe crystal remains nearly the same (82 vs. 84 wt.%). Except for the size variations that could depend on the initial cluster states (e.g., size) and irradiation conditions (e.g., ion fluence), there is an overall agreement on the irradiation behavior of the films shown in Figures. 9.12 and 9.9 (a).

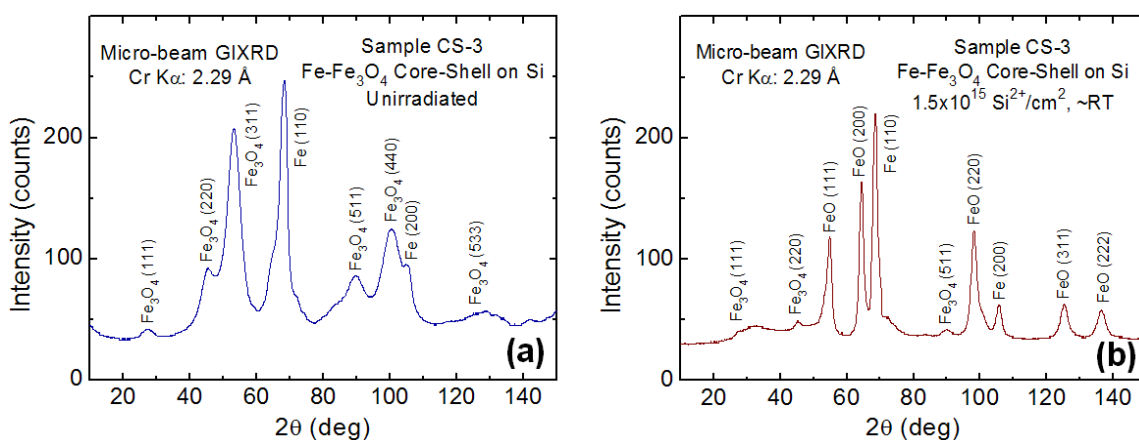


**Figure 9.12** GIXRD patterns for the same sample in Fig. 6 (a) before and (b) after 5.5 MeV  $\text{Si}^{2+}$  ion irradiation to  $1.5 \times 10^{15} \text{Si}^{2+}/\text{cm}^2$  (0.09 dpa in the film) at nominal RT. A phase transition from cubic magnetite  $\text{Fe}_3\text{O}_4$  to cubic Wüstite  $\text{FeO}$  is observed.

A similar super-exponential decay behavior is observed for a Fe-Fe<sub>3</sub>O<sub>4</sub> core-shell nanocluster films irradiated with 5.5 MeV  $\text{Si}^{2+}$  ions at 473 K, as shown in Figure 9.13. Thermal annealing of the film was conducted at the elevated temperature for an extended time prior to ion irradiation and in-situ resistance measurement. An initial rapid decrease followed by nearly invariance in resistance was observed during the thermal annealing process in the absence of ion



irradiation. The in-situ result shown in Figure 9.13 indicates that the resistance also has a super-exponential decay dependence on dose up to 0.21 dpa, similar to that from irradiation at nominally RT (Figure 9.10). However, irradiation of the annealed sample leads to a relatively smaller slope in the low-dose regime. A reduction of resistance by 80% from the initial value requires a dose of  $\sim 0.04$  dpa at 473 K versus  $\sim 0.01$  dpa at nominally RT. Again, the decrease in the electrical resistance of the nanocluster film is due to the grain growth and a tighter connection between the agglomerated conducting particles, which leads to a larger effective cross-sectional area for more efficient electron transport. The corresponding surface nanostructure and diffraction pattern for the irradiated sample are shown in Figure 9.14.

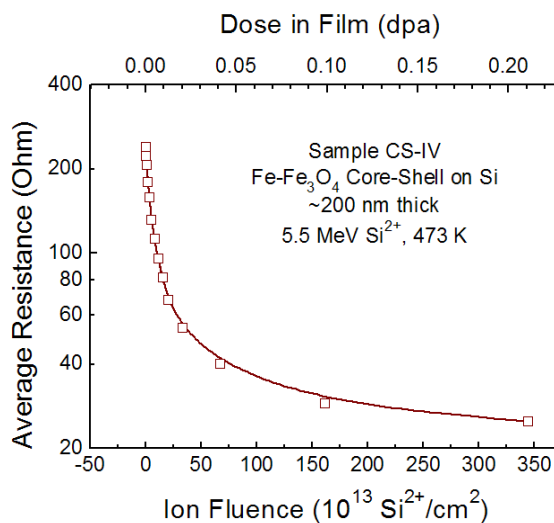


**Figure 9.13** Electrical resistance of a Fe-Fe<sub>3</sub>O<sub>4</sub> core-shell nanocluster film on surface-oxidized Si measured *in situ* using van der Pauw method as a function of ion fluence during 5.5 MeV Si<sup>2+</sup> ion irradiation at 473 K. A super exponential decay behavior of the resistance is observed.

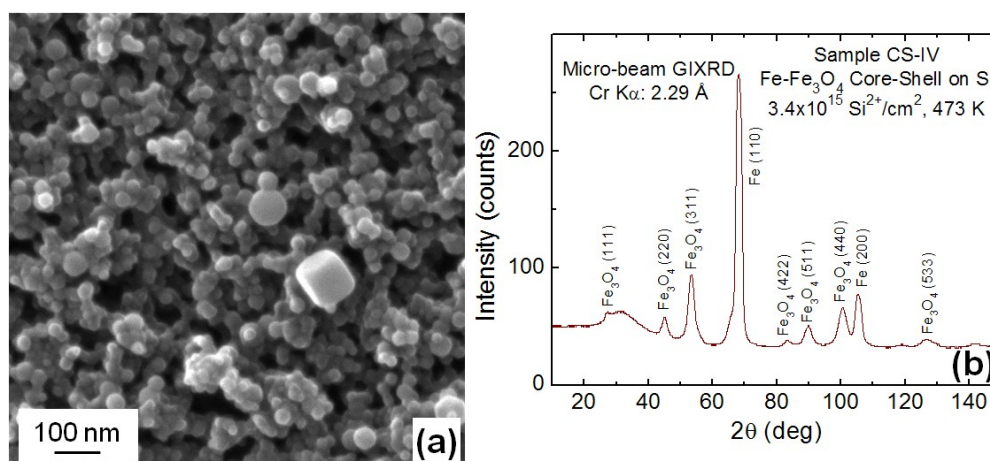


**Figure 9.14** (a) HIM micrograph and (b) GIXRD pattern for the same sample in Fig. 9 after 5.5 MeV  $\text{Si}^{2+}$  ion irradiation to  $3.4 \times 10^{15} \text{ Si}^{2+}/\text{cm}^2$  ( $\sim 0.2$  dpa at the surface and in the film) at 473 K. Phase transition is not observed.

Interestingly, even at a higher dose, the nanostructure of the irradiated film at 473 K (Figure 9.14a) appears to be changed less dramatically than that irradiated at nominally RT (Figure 9.11b). There is also a noticeable difference in the shell, which does not undergo a phase transition to FeO at 473 K (Figure 9.14b). Compared to RT, the elevated temperature leads to a higher rate for simultaneous recombination of Frankel pairs created during ion irradiation, which should be responsible in part for more irradiation resistance of the  $\text{Fe}_3\text{O}_4$  shell to structural modification and phase transition. From Figure 9.10 and 9.13, the resistance changes in the low-dose regime are very rapid. A smaller step of dose was also applied to study the behavior quantitatively based on 2 MeV  $\text{He}^+$  ion irradiation at a significantly lower dose rate. Figure 9.15 shows the data for an 800 nm thick Fe- $\text{Fe}_3\text{O}_4$  nanocluster film; this thickness is small compared to the ion projected range of  $\sim 4 \mu\text{m}$  in the material under the irradiation conditions.



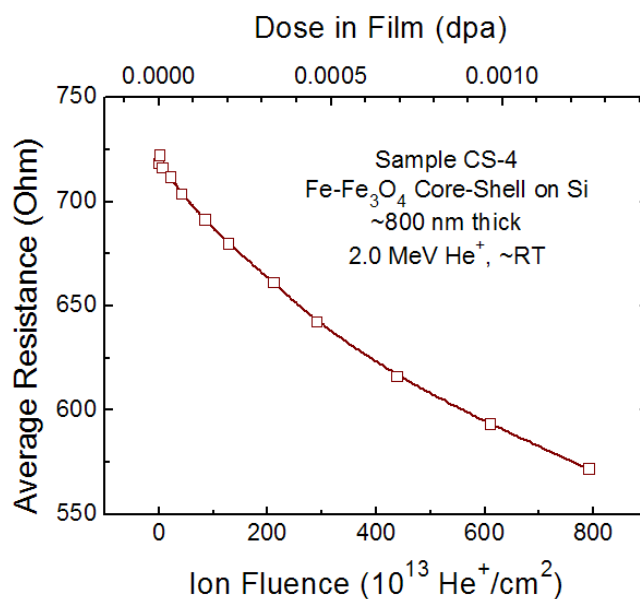


**Figure 9.15** Electrical resistance of a Fe-Fe<sub>3</sub>O<sub>4</sub> core-shell nanocluster film on surface-oxidized Si measured *in situ* using van der Pauw method as a function of ion fluence during 2.0 MeV He<sup>+</sup> ion irradiation at nominal RT. A significant decrease of the resistance is observed within a narrow dose window in the low-dose regime.

At the highest applied ion fluence of  $8 \times 10^{15} \text{ He}^+/\text{cm}^2$ , the corresponding dose in the film is only  $\sim 1.3 \times 10^{-3}$  dpa. Figure 9.15 suggests that even at a dose as low as 10 ion irradiation at nominally RT, there is a considerable decrease in the resistance by  $\sim 15\%$  in the Fe-Fe core-shell nanocluster film. However, at the highest dose applied to the film, a noticeable change in the surface nanostructure is not observed (Figure 9.16) and phase transition also does not occur (Figure 9.17). This is probably because the dose is still too low to produce any major visible effects on the nanostructure, yet quite significant on the electrical resistance already.

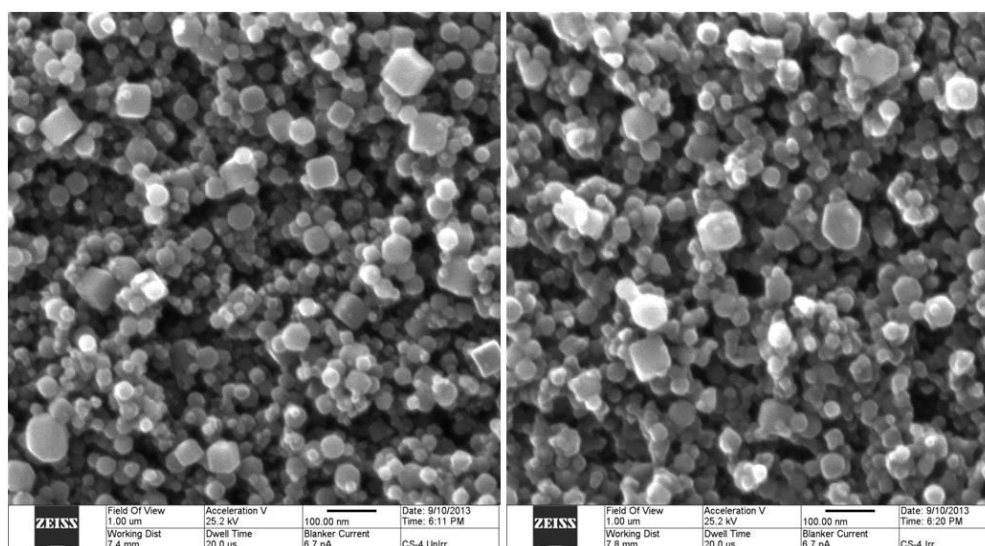


**Figure 9.16** HIM micrographs for the sample in Figure 9.15 (a) before and (b) after 2.0 MeV  $\text{He}^+$  ion irradiation to  $8 \times 10^{15} \text{ He}^+/\text{cm}^2$  at nominally RT. A dramatic change in the surface morphology does not occur.

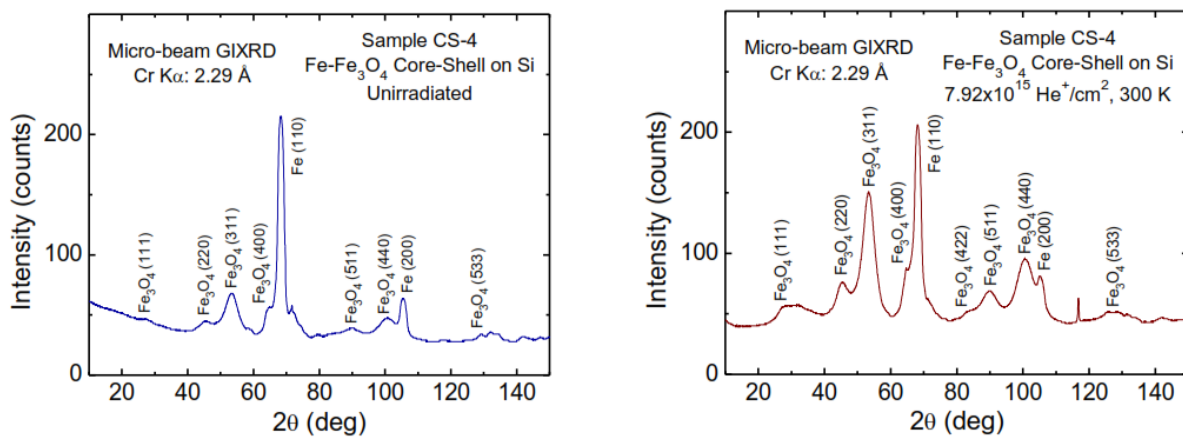


**Figure 9.17** GIXRD patterns for the sample in Figure 9.15 (a) before and (b) after 2.0 MeV  $\text{He}^+$  ion irradiation to  $8 \times 10^{15} \text{ He}^+/\text{cm}^2$  at nominally RT. Phase transition does not occur.

## 9.5 Future Studies

The nanocluster films used in this study has an inhomogeneous and anisotropic nature; their behavior of electrical resistance is complex under ion irradiation. Further studies are needed to better understand the basic mechanisms associated with the irradiation-induced microstructure changes, to develop an accurate interpretation to the observed dose dependence of the electrical resistance, and

to establish the relationship between the nanostructural evolution and the super-exponential decay of the electrical resistance with dose. Meso-scale modeling will be performed and the results will be compared to the experimental data to identify the dominant mechanisms in the structural evolution and its impact on the electrical resistance. The improved understanding, along with the verification of the material susceptibility to neutron irradiation, will help to lay a solid foundation for development of an advanced online, small neutron flux monitor based on nanocluster films as sensing materials.

## 9.6 Conclusion

It has been demonstrated that HIM provides a new, unprecedented capability for in-situ study of nanostructural evolution of bulk materials under He<sup>+</sup> ion irradiation. Nanocluster films of Fe<sub>3</sub>O<sub>4</sub> and Fe-Fe<sub>3</sub>O<sub>4</sub> core-shells are found to undergo a dramatic change in nanostructures under ion irradiation. Crystalline grains grow likely through interfacial epitaxy from the surrounding amorphous material or through coalescence of smaller neighboring grains. A nanoparticle containing several crystalline grains aggregates and forms larger particles under ion irradiation. As dose increases, a nanowire-like network is formed along with nano-pores. The nanostructural evolution is activated by elastic nuclear collisions that produce atomic displacements. Both electronic and thermal processes can play a significant role once the evolution is activated. In-situ study of the nanocluster Fe-Fe<sub>3</sub>O<sub>4</sub> films indicates that the electrical resistance has a super-exponential decay dependence with ion fluence or dose in dpa. The behavior may be attributed to tighter interconnections between nanoparticles, leading to an increase in the cross-sectional area for more efficient electron transport and orders of magnitude decrease in the electrical resistance. The observed phase transition of grain shells from cubic magnetite Fe<sub>3</sub>O<sub>4</sub> to cubic wustite FeO at a higher dose could change intrinsic conductivity of the nanoclusters. The results from this study suggest that the nanocluster core-shell films may have a great potential as a candidate neutron sensor material for development of an advanced online neutron monitor that has high-sensitivity detection and long-term

applicability at RT or elevated temperatures. These monitors would be of great value and critical importance in many nuclear operations to enhance safety, such as those in existing and future nuclear power plants.

## 9.7 References

1. C. D. Ferguson, L. E. Marburger, J. Doayne Farmer, A. Makhijani, *Nature* 2010, 467, 391.
2. a) Y. Guérin, G. S. Was, S. J. Zinkle, *MRS Bulletin* 2009, 34, 10; b) C. Ferguson, *Nature* 2011, 471, 411.
3. P. C. Burns, R. C. Ewing, A. Navrotsky, *Science* 2012, 335, 1184.
4. a) D. A. Clayton, R. T. Wood, *Nuclear News* 2011, 54(13), 42; b) S. Chu, A. Majumdar, *Nature* 2012, 488, 294.
5. F. Murtas, G. Croci, A. Pietropaolo, G. Claps, C. D. Frost, E. Perelli Cippo, D. Raspino, M. Rebai, N. J. Rhodes, E. M. Schooneveld, M. Tardocchi, G. Gorini, *J. Inst.* 2012, 7, p07021.
6. P. Filliatre, C. Jammes, L. Oriol, B. Geslot, L. Vermeeren, *Proc. 1st Int. Conf. Advancements in Nuclear Instrumentation, Measurement Methods and Their Applications (ANIMMA), Marseille, France, 2009*, p. 1.
7. L. Birstein, P. Martinez, A. Filevich, F. Li, *Nucl. Instr. Meth.* 1974, 116, 615.
8. S. Bishnoi, T. Patel, M. Shukla, P. S. Adhikari, A. Sinha, *Proc. DAE Symp. Nucl. Phys.* 2012, 57, 880.
9. D. Mouhssine, A. Nourreddine, A. Nachab, A. Pape, F. Fernandez, *Nucl. Instr. Meth. Phys. Res. B* 2005, 227, 609.
10. a) A. S. Aricò, P. Bruce, B. Scrosati, J.-M. Tarascon, W. Van Schalkwijk, *Nat. Mater.* 2005, 4, 366; b) W. Jiang, W. J. Weber, C. M. Wang, J. S. Young, L. A. Boatner, J. Lian, L. M. Wang, R. C. Ewing, *Adv. Mater.* 2005, 17, 1602; c) G. Wang, X. Sun, F. Lu, H. Sun, M. Yu, W. Jiang, C. Liu, J. Lian, *Small* 2012, 3, 452.
11. W. Jiang, J. S. McCloy, A. S. Lea, J. A. Sundararajan, Q. Yao, Y. Qiang, *Phys. Rev. B* 2011, 83, 134435.
12. O. Akdogan, W. Li, B. Balasubramanian, D. J. Sellmyer, G. C. Hadjipanayis, *Adv. Funct. Mater.* 2013, 23, 3262.
13. J. S. McCloy, W. Jiang, T. C. Droubay, T. Varga, L. Kovarik, J. A. Sundararajan, M. Kauer, Y. Qiang, E. C. Burks, K. Liu, *J. Appl. Phys.* 2013, 114, 083903.
14. J. A. Hinks, *Nucl. Instrum. Meth. Phys. Res. A* 2009, 267, 3652.
15. R. C. Birtcher, M. A. Kirk, K. Furuya, G. R. Lumpkin, M-O. Ruault, *J. Mater. Res.* 2005, 20, 1654.
16. K. Furuya, K. Mitsuishi, M. Song, T. Saito, *J. Electron Microsc.* 1999, 48, 511.

17. P. Trocellier, Y. Serruys, S. Miro, E. Bordas, S. Pellegrino, S. Vaubaillon, M. O. Ruault, S. Henry, O. Kaïtasov, Nucl. Instrum. Meth. Phys. Res. B 2008, 266, 3178.
18. L. P. Guo, C. S. Liu, M. Li, B. Song, M. S. Ye, D. J. Fu, X. J. Fan, Nucl. Instrum. Meth. Phys. Res. A 2008, 586, 143.
19. P. Hosemann, Rev. Accelerator Sci. Tech. 2011, 4, 161.
20. M-O. Ruault, F. Fortuna, H. Bernas, J. Chaumont, O. Kaïtasov, V. A. Borodin, J. Mater. Res. 2005, 20, 1654.
21. a) J. Y. Huang, L. Zhong, C. M. Wang, J. P. Sullivan, W. Xu, L. Q. Zhang, S. X. Mao, N. S. Hudak, X. H. Liu, A. Subramanian, H. Fan, L. Qi, A. Kushima, J. Li, Science 2010, 330, 1515; b) K.-W. Nam, S.-M. Bak, E. Hu, X. Yu, Y. Zhou, X. Wang, L. Wu, Y. Zhu, K.-Y. Chung, X.-Q. Yang, Adv. Funct. Mater. 2013, 23, 1047; c) X. Tao, J. Du, Y. Sun, S. Zhou, Y. Xia, H. Huang, Y. Gan, W. Zhang, X. Li, Adv. Funct. Mater. 2013, 23, 4745; d) M. Gu, L. R. Parent, B. L. Mehdi, R. R. Unocic, M. T. McDowell, R. L. Sacci, W. Xu, J. G. Connell, P. Xu, P. Abellan, X. Chen, Y. Zhang, D. E. Perea, J. E. Evans, L. J. Lauhon, J.-G. Zhang, J. Liu, N. D. Browning, Y. Cui, I. Arslan, C. M. Wang, Nano Lett. 2013, 13, 6106.
22. a) J. Morgan, J. Notte, R. Hill, B. Ward, Microscopy Today 2006, 14, 24; b) M. Ananth, L. Scipioni, J. Notte, American Laboratory 2008, 40, 42; c) L. Scipioni, L. A. Stern, J. Notte, S. Sijbrandij, B. Griffin, Adv. Mater. Process 2008, 166, 27; d) R. Hill, J. A. Notte, L. Scipioni, Advances in Imaging and Electron Physics (Edited by P. W. Hawkes) Elsevier Inc., Amsterdam, 2012, p.p. 65-148.
23. a) D. C. Bell, M. C. Lemme, L. A. Stern, J. R. Williams, C. M. Marcus, Nanotechnology 2009, 20, 455301; b) M. C. Lemme, D. C. Bell, J. R. Williams, L. A. Stern, B. W. H. Baugher, P. J.-Herrero, C. M. Marcus, ACS Nano 2009, 3, 2674.
24. a) M. T. Postek, A. E. Vladár, Scanning 2008, 30, 457; b) B. P. Danysh, T. P. Patel, K. J. Czymmek, D. A. Edwards, L. Wang, J. Pande, M. K. Duncan, Matrix Biology 2010, 29, 228; c) W. Jiang, R. Devanathan, C. J. Sundgren, M. Ishimaru, K. Sato, T. Varga, S. Manandhar, A. Benyagoub, Acta Mater. 2013, 61, 7904.
25. V. Sidorkin, E. van Veldhoven, E. van der Drift, P. Alkemade, H. Salemink, D. Maas, J. Vac. Sci. Tech. B, 2009, 27, L18.
26. S. Sijbrandij, B. Thompson, J. Notte, B. W. Ward, N. P. Economou, J. Vac. Sci. Technol. B 2008, 26, 2103.
27. R. Livengood, S. Tan, Y. Greenzweig, J. Notte, S. McVey, J. Vac. Sci. Technol. B 2009, 27, 3244.
28. a) L. J. Van der Pauw, Philips Research Reports 1958, 13, 1; b) L. J. Van der Pauw, Philips Technical Review 1958, 20, 220.
29. G. J. Dienes, Annu. Rev. Nucl. Sci. 1953, 2, 187.

30. J. F. Ziegler, J. P. Biersack, U. Littmark, *The Stopping and Range of Ions in Solids*, Pergamon, New York, 1985; available at: <http://www.srim.org>.
31. M. N. Özışık, *Boundary Value Problems of Heat Conduction*, Dover Publications, Inc., Mineola, New York, 2002, p. 311.
32. a) S. J. Zinkle, C. Kinoshita, *J. Nucl. Mater.* 1997, 251, 200; b) E. A. kotomin, A. I. Popov, *Nucl. Instrum. Meth. Phys. Res. B* 1998, 141, 1.
33. M. J. Berger, J. S. Coursey, M. A. Zuker, J. Chang, *Stopping Power and Range Tables for Electrons, Protons, and Helium Ions*, December 9, 2011. Available at: <http://www.nist.gov/pml/data/star/index.cfm>
34. W. H. Bragg, R. Kleeman, *Philos. Mag.* 1905, 10, S318.
35. R. F. C. Farrow, P. M. Rice, M. F. Toney, R. F. Marks, J. A. Hedstrom, R. Stephenson, M. J. Carey, A. J. Kellock, *J. Appl. Phys.* 2003, 93, 5626.
36. Z. Fang, K. Terakura, H. Sawada, T. Miyazaki, I. Solovyev, *Phys. Rev. Lett.* 1998, 81, 1027.
37. A. J. Pignocco, G. E. Pellissier, *J. Electrochem Soc.* 1965, 112, 1188.
38. a) I. P. Koutsaroffa, M. Zelnera, P. Wooo, L. Mcneila, M. Buchbindera, A. Cervin-Lawrya, *Integrated Ferroelectrics* 2002, 45, 97; b) Y. K. Ko, S. Lee, H. M. Lee, H. J. Yang, J. Y. Kim, J. Kim, J. H. Lee, H. J. Shin, W. J. Nam, J. G. Lee, *Journal of the Korean Physical Society* 2005, 47, S467; c) B. Lahiri, R. Dylewicz, R. M. D. L. Rue, N. P. Johnson, *Optics Express* 2010, 18, 11202.
39. a) Y. Qiang, J. Antony, A. Sharma, J. Nutting, D. Sikes, D. Meyer, *J. Nanoparticle Res.* 2006, 8, 489; b) M. Kaur, J.S. McCloy, W. Jiang, Q. Yao, Y. Qiang, *J. Phys. Chem. C*, 2012, 116, 12875.

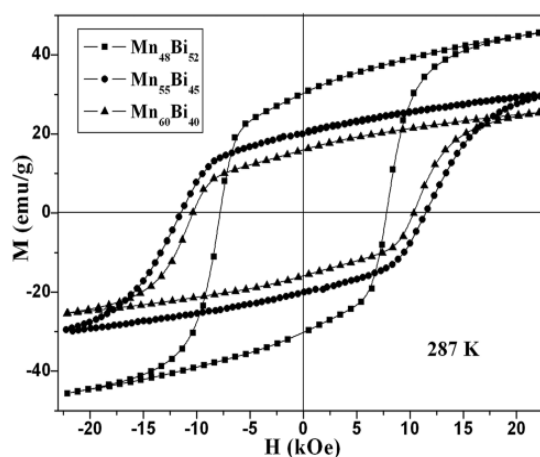
## Chapter 10: Nanoclusters Embedded Thin Film Matrices and Multi-Layered Films

### 10.1 Introduction

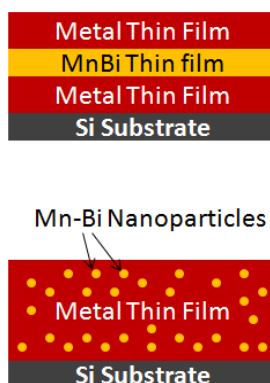
Although studying the heat treatment and irradiation effects on nanoparticles gives insight to the mechanisms behind property changes and its direct use as radiation sensors and monitors in nuclear reactors, in order to find their applications in radiation resistant materials it becomes essential to embed these nanoclusters in the nuclear grade materials or other type of materials to form oxide dispersion strengthened (ODS) or nano-Ferritic alloy (NFA) type materials and study the effects. This chapter deals with the magnetic properties of Ni thin films and the effect of Mn & Bi on the Ni thin films as multilayer films and nanoclusters embedded thin films matrices in order to study the change in magnetic interaction. To alter the magnetic coercivity a layer of MnBi thin film was deposited between two layers of Ni thin films. There has been considerable interest in understanding the magnetic, optical, and magneto-transport properties of Manganese-Bismuth (Mn-Bi)-based materials because of their substantial magneto-optical and permanent magnet properties.<sup>1</sup> By nature Manganese (Mn) exhibits paramagnetic behavior and Bismuth (Bi) exhibit diamagnetic behavior. When combined together in right proportion, Mn-Bi tends to exhibit high coercivity and other interesting properties. Due to such significance, Mn-Bi has become more popular and a good candidate for the replacement of certain widely used rare-earth magnetic materials, which are available rare in nature and can be used as a hybrid metal to enhance certain metal properties. Mn-Bi poses great material property like thermal stability, magnetic anisotropy, structural stability, spin polarization and high coercivity. Such properties give hopes for using Mn-Bi as an alternative for the rare earth elements and opens doors for further investigation on Mn-Bi. Our research finding in the past proved that the bulk low-temperature-phase (LTP) Mn-Bi permanent magnet of hexagonal Ni-As structure prepared by spark plasma sintering (SPS) technique have better magnetic properties (Figure 10.1) at an optimal composition of Mn<sub>48</sub>Bi<sub>52</sub> than compared with the other compositional ratios of Mn & Bi.<sup>2,3</sup> It has also been reported that using MnBi thin films as a sandwich in a



multilayer film or as dopant in hybrid magnets has benefits in altering the magnetic properties to a great extent and by using this technique property changes can be controlled to a certain level.<sup>4,5</sup> Therefore in order to implement these findings at the micro and nano level, in our research we are focused on synthesizing and studying the structural, magnetic and electrical properties of this composition of  $Mn_{48}Bi_{52}$  when it is used as a thin film sandwich layer in multilayered films and as dopants of nanoparticles embedded or dispersed in a metal matrix of thin film as shown in Figure 10.2. In addition to this we focus on the thermal annealing effect on these thin film structures.



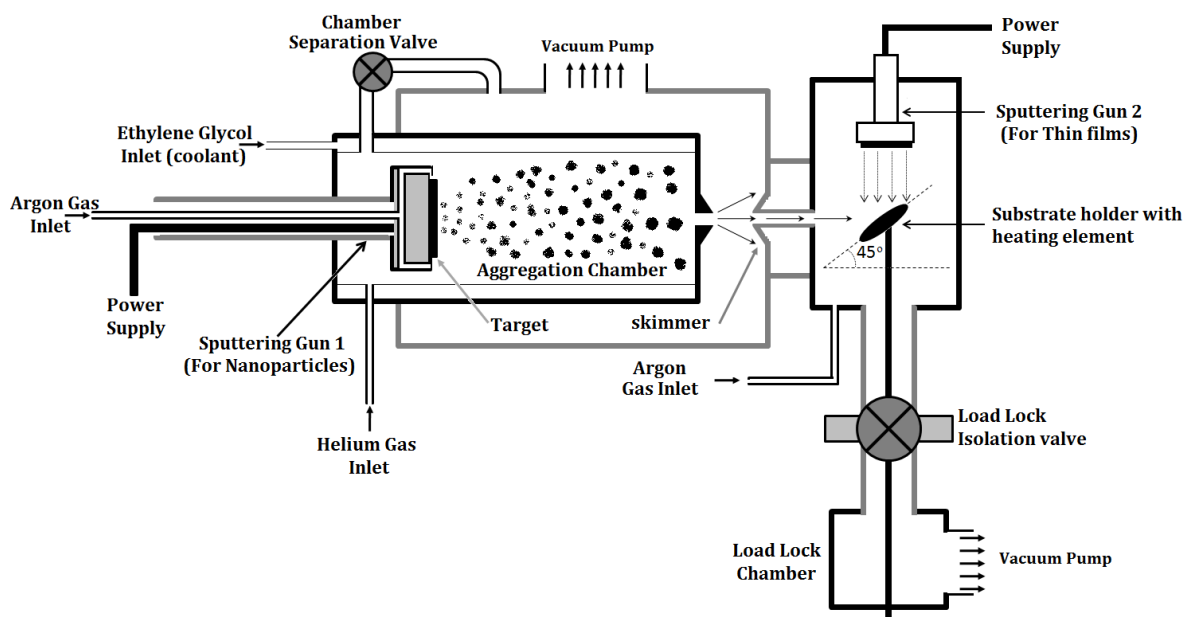
**Figure 10.1** Room temperature hysteresis loops of  $Mn_{100-x}Bi_x$  ( $x=40, 45, 52$ ) magnets sintered at 287 K. Max. field 2.2 T.<sup>2,3</sup>



**Figure 10.2** Mn-Bi thin film sandwiched in a multilayered metal film (Top). Mn-Bi nanoparticles embedded in a metal thin film matrix (Bottom)

## 10.2 Experimental Details

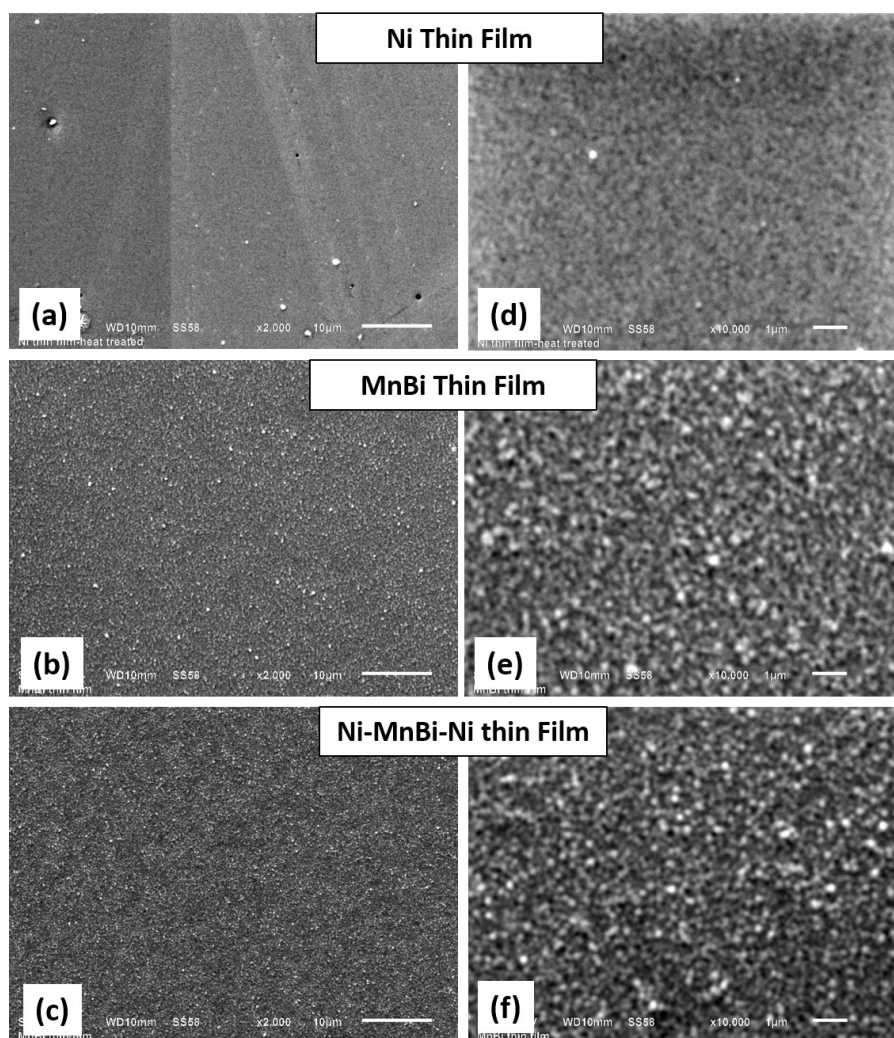
Thin films and multilayered thin films were prepared by the thin film deposition system built in the cluster deposition system as shown in Figure 10.3. It involves a magnetron sputtering gun (gun 2) where a 2-inch diameter target of particular metal is placed and sputtered at the supply of Argon gas. The sputtered atoms are allowed to deposit on a silicon substrate to form thin films. The heating element placed underneath the substrate holder can be used to control the deposition temperature and to perform vacuum annealing after deposition if required. The thickness of the thin films is measured simultaneously during deposition by a quartz sensor, which is placed adjacent to the substrate holder and measured by the INFICON XTC/2 deposition controller. Unlike the multilayer deposition of Mn/Bi followed by annealing to form the NiAs type low temperature phase (LTP) MnBi, the Mn-Bi thin films involved here were deposited directly from  $\text{Mn}_{50}\text{Bi}_{50}$  target by sputtering. Further annealing of the deposited film was not done to form the LTP MnBi, instead the as-deposited Mn-Bi thin film which is a mixed solid solution of Mn and Bi was involved to study its impact on the magnetic properties of Ni thin films. Likewise, the Mn-Bi nanoparticles (NP) were not of the LTP MnBi instead directly sputtered from the three inch  $\text{Mn}_{50}\text{Bi}_{50}$  target placed in the sputtering gun. The Mn-Bi nanoparticles were prepared by the state-of-the-art nanocluster deposition system, which combines magnetron sputtering with gas aggregation technique to form the desired NP. The Mn-Bi NP dispersed in a thin film matrix can be prepared by depositing both the nanoparticles (from gun 1) and thin films (from gun 2) simultaneously on the substrate placed at 45 degree angle as shown in Figure 10.3 and by controlling the respective deposition rates. Scanning Electron Microscopy (SEM) images were taken in Zeiss Supra 35 variable-pressure SEM having 1 nm resolution. The magnetic measurements were carried out in the DMS 1660 Vibrating Sample Magnetometer (VSM) at magnetic fields between -1.35 to 1.35 Tesla. The surface morphology and magnetic domain images were taken by Atomic Force Microscope (AFM), Magnetic Force Microscope (MFM).



**Figure 10.3** Schematic representation of the nanocluster deposition system with provisions for the synthesis of both thin film and nanoclusters.

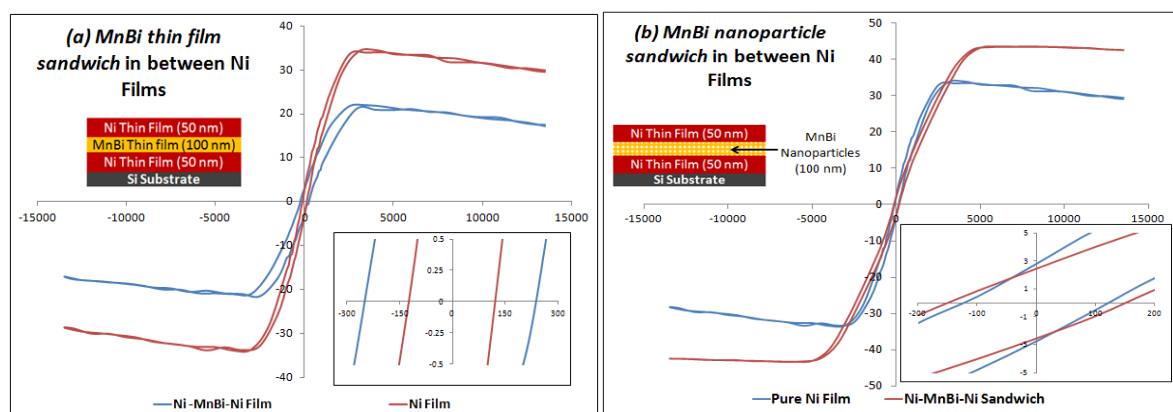
### 10.3 Result and Discussion

Figure 10.4 shows the Scanning electron microscopy (SEM) image of the Mn-Bi thin films as-deposited on silicon substrate at two different scales. Minute grains of particles appear to be at the surface of this thin film, which makes the surface rough. These minute particles were formed due to the grouping of some atoms at the surface of the film due to the heat from the plasma of the gun. In order to study the enhancement of magnetic properties in metal and the change in magnetic interaction due to the Mn-Bi sandwiching in multilayered thin films, both Mn-Bi thin films and Mn-Bi nanoparticles were sandwiched in between nickel thin films. In this study, Ni metal is chosen first as an initiative and since we have previously studied the other dopant effect (Cr doping) in Ni. In this thin film sandwich, the bottom Ni thin film layer thickness was 50 nm, the in-between Mn-Bi thin film layer and Mn-Bi nanoparticle layer thickness was 100 nm and the top Ni thin film layer thickness was 50 nm. The effect of thin film sandwiching is very effective compared with the nanoparticle sandwiching as shown in Figure 10.5 (a) and (b).



**Figure 10.4** SEM images of Ni, Mn-Bi and multilayer Ni/Mn-Bi/Ni thin film deposited on Si substrate at two different scales, 10 $\mu$ m (a,b,c) and 1 $\mu$ m (d,e,f)

It is clearly evident from the magnetic hysteresis of Figure 10.5 that the coercivity almost doubled after sandwiching Mn-Bi thin film in between Ni thin film layers while there was no notable change in the nanoparticle sandwich. This is because the nanoparticle size is so small such that they get oxidized when exposed to the atmosphere and are unable to retain the same magnetic properties of the bulk Mn-Bi. The drop in magnetic saturation after sandwiching is attributed to the presence of Mn-Bi layer.



**Figure 10.5** Hysteresis loop of (a) Mn-Bi thin film sandwiched between Ni thin films and (b) Mn-Bi nanoparticle sandwiched between Ni thin films

Therefore the nanoparticles sandwiched between Ni thin films have less effect on altering the magnetic properties of the metal. On the other hand, Mn-Bi nanoparticles dispersed or embedded in the 50 nm Ni thin film matrix seem to have similar prominent effect like that of the Mn-Bi thin films. As shown in the Figure 10.6, by increasing the concentration of Mn-Bi nanoparticles in the Ni thin film matrix the coercivity increases. The concentration of Mn-Bi nanoparticles was controlled by controlling the time of deposition of Mn-Bi nanoparticles in the matrix. As each nanoparticle is completely surrounded by the Ni film matrix there are fewer chances for the particles to get oxidized and thus they were able to bring the expected changes unlike the nanoparticle sandwich. Thus, both Mn-Bi thin films and Mn-Bi nanoparticles can enhance magnetic properties of a metal based on their respective multilayering or embedding technique.

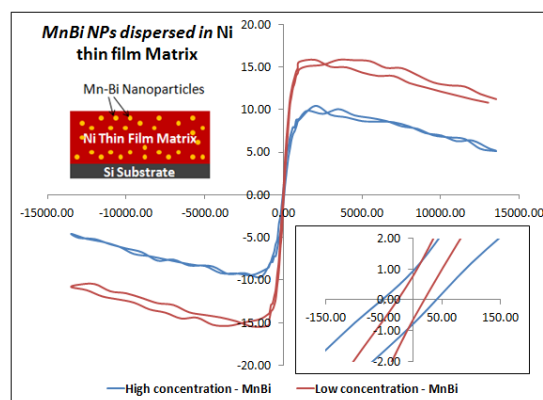


**Figure 10.6** Hysteresis loop of Mn-Bi nanoparticles embedded in Ni thin film matrix.

In order to have more insight on the magnetic effect due to sandwiching Mn-Bi in between Ni thin films, AFM and MFM measurements were done and the results are shown in the Figure 10.7.

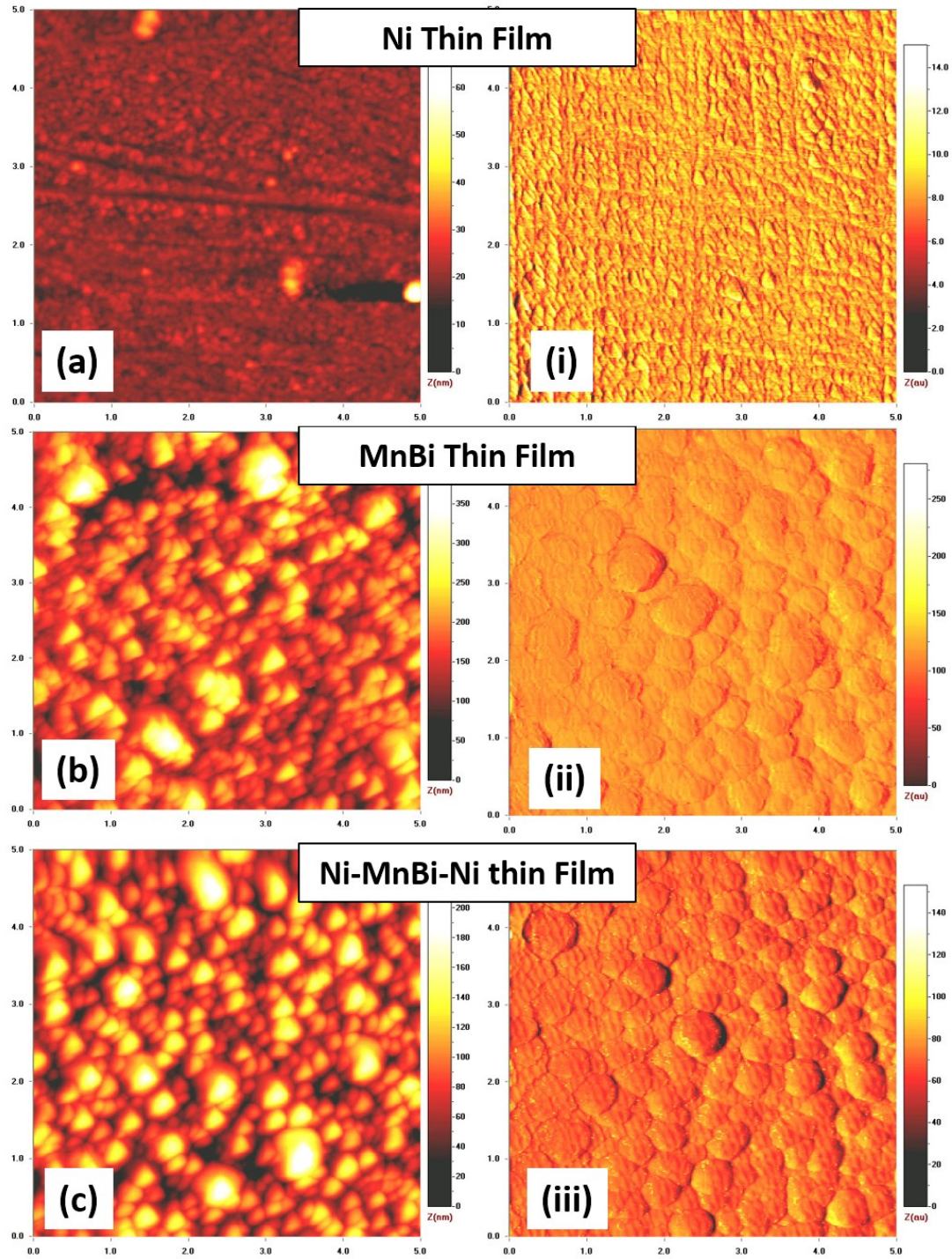


**Figure 10.7** AFM (a, b, c) & MFM (i, ii, iii) images of MnBi Thin film and Ni-MnBi-Ni thin film sandwich.



It is evident from this measurement that the SEM, AFM and MFM images are pretty consistent with the hysteresis data. After sandwiching MnBi layer between Ni layers there is no change in magnetic domain. However the interaction between the domains has a slight reduction as there is increase in the dark spots of MFM as shown in Figure 10.7 (b) and (d). After depositing Ni layers over the Mn-Bi thin film layer, the size of minute grains on the surface of the Mn-Bi film had increased due to the 50 nm Ni layer coating over these grains as shown in Figure 10.7 (a) & (c).

### **10.3 Conclusion**

The effect of Mn-Bi thin films and nanoparticles in the enhancement of the magnetic properties of metals is real and possible as it is evident from the coercivity changes after sandwiching Mn-Bi thin films in-between Ni thin films and embedding Mn-Bi nanoparticles in Ni thin film matrix. Although the presence of Mn and Bi as thin film sandwich layer tend to affect the coercivity of Ni films, the presences of Mn and Bi as nanoparticle-sandwich-layer tend to have no effect on the coercivity of Ni films, when the Mn-Bi nanoparticles were deposited as a sandwich layer. The dispersion technique where the Mn and Bi nanoparticles are dispersed uniformly throughout the Ni thin film matrix has an effect on the magnetic properties. Right proportion of Mn-Bi thin film sandwiching and Mn-Bi nanoparticle embedding along with the combined effect of heat treatment can bring elevated structural and magnetic property changes. Since the preliminary results are promising, it calls for more investigation in this area in the future.

#### 10.4 References

1. Di Chen, G. Otto, and F. Schmit, "MnBi films for magneto-optic recording," *IEEE Transactions on Magnetics*, vol. 9, pp. 66-83, Jun. 1973
2. D. T. Zhang, S. Cao, M. Yue, W. Q. Liu, J. X. Zhang, and Y. Qiang, "Structural and magnetic properties of bulk MnBi permanent magnets," *J. Appl. Phys.*, vol. 109, no. 7, p. 07A722, 2011.
3. D. T. Zhang, W. T. Geng, M. Yue, W. Q. Liu, J. X. Zhang, J. A. Sundararajan, and Y. Qiang, "Crystal structure and magnetic properties of  $Mn_xBi_{100-x}$  ( $x=48, 50, 55$  and  $60$ ) compounds," *J. Magn. Mater.*, vol. 324, no. 11, pp. 1887-1890, Jun. 2012.
4. U. Rüdiger, G. Güntherodt, P. Fumagalli, L. Thomas, S. S. P. Parkin, and A. D. Kent, "Micromagnetism and high temperature coercivity of MnBi/Al multilayers," *Journal of Applied Physics*, vol. 88, p. 4221, 2000
5. S. Cao et al., "Magnetic properties and thermal stability of MnBi/NdFeB hybrid bonded magnets," *Journal of Applied Physics*, vol. 109, p. 07A740, 2011.



## Chapter 11: Summary and Conclusion

This study contributes to the research in the area of identifying the irradiation effects on nanomaterials, which induces changes in magnetic, structural and electrical conductive properties. In regard to this, investigations were conducted on magnetic nanomaterials to study the underlying mysteries behind irradiation-induced property changes in nuclear materials, which plague the current generation nuclear reactor and to create materials that can have controlled property change under irradiation. In order to meet the objective, research was mainly focused on the study of magnetic, structural and electrical conductive property changes in nanomaterials due to irradiation. As this field of research is directly related to Nano Nuclear Technology (NNT), a literature review was done and presented in this dissertation, which unveils the ongoing research and research so far in this field. Results obtained from the previous researches and from this research, convey the message that nanomaterials are good candidates for the radiation impact analysis, radiation applications and for the further studies in the same genre. Nanoparticle-granular films chosen for this study were prepared using the third generation cluster deposition system. These granular films were prepared and exposed to irradiation at the ion accelerator facility at the Pacific Northwest national laboratory (PNNL), Richland, WA.

Some of the granular films like the  $\text{Fe}_3\text{O}_4$  films showed extreme sensitivity of irradiation with the increase of magnetization, growth in cluster size, growth in magnetic domain when exposed to 5.5 MeV  $\text{Si}^{2+}$  ion irradiation to a fluence of  $10^{16}$  ions/cm<sup>2</sup> at room temperature. Such kind of materials opens doors for application of in nuclear reactor sensors, monitor and detectors. On the other hands, materials like the  $\text{FeO}+\text{Fe}_3\text{N}$  granular films when irradiated with 2 MeV  $\text{He}^+$  ions to a fluence of  $3 \times 10^{15}$  ions/cm<sup>2</sup> at room temperature showed magnetic and structural stability proving their robust nature against irradiation. Similarly, Core-shell Fe nanoparticle shows magnetic stability under  $\text{Si}^{2+}$  ion irradiation. These results open new doors for applications in advanced data storage and material usage in extreme condition. Core-shell iron nanoparticles exposed to ion beam

irradiation showed phase change and reduction behavior. Upon further investigation it was revealed that such a behavior occur due the presence of Fe nanocrystals. Grain growth and increase in the thickness of the oxide layer in fully oxidized nanoparticles and core-shell nanoparticles are very common phenomenon observed under irradiation. The investigations done to explore such behavior reveal that the combined effect of vacancy/interstitial formation, diffusion under radiation-induced local temperature increase are the reason for the irradiation-induced particle size growth and oxide layer thickening, which ultimately results in structural and electrical conductivity changes.

In addition to this, it has been confirmed from the research that the radiation stability or tolerance comes when the grain boundaries and interfaces in a material are enhanced. The core-shell Fe nanoparticles affirm this phenomenon as it proved the stability of Fe core when it had a oxide shell, which promoted grain boundary and interface effect. This also shows the importance of using nanomaterials in the future nuclear reactor grade material. The in-situ studies conducted on the core-shell and fully oxidized nanoparticles under irradiation gave more insight in determining the contributors for the radiation induced property changes. Elastic scattering leading to atomic displacement was found to be a major reason behind the structural evolution in nanomaterials under irradiation. However, once the atomic displacement is initiated, the electron energy deposition and thermal effect works hand-in-hand to promote the furthering of the nanostructural evolution. In-situ studies on the sensing ability of these nanostructural materials shows that these materials are capable of avoiding background noises and at the same time remain highly sensitive. Studies on Ni and Cr doped Ni nanoparticles show that the combined effects of doping and heat treatment are excellent ways of bringing controlled property changes in materials. The results from Mn-Bi NP dispersion in Ni thin films show that dispersion only affects the magnetic properties, but not the surface morphologies. On the whole, the results obtained from this research positively contribute in terms of radiation sensing and radiation tolerance to the assurance of enhanced safety of the future nuclear reactors or the Generation IV nuclear reactors, which are expected to be in use sooner or later.

**Appendix A: Sputter yield for different materials**

<b>Material</b>	<b>Sputter Yield</b>
Al	0.77
Al <sub>2</sub> O <sub>3</sub>	0.16
Ag	2.24
Au	1.90
Be	0.19
Bi	1.76
C	0.05
Co	0.62
Cr	0.65
Cu	1.00
Dy	1.27
Er	1.08
Fe	0.52
GaAs	1.83

<b>Material</b>	<b>Sputter Yield</b>
Ge	1.10
Ir	0.66
Mo	0.51
Mn	1.07
Nb	0.48
Ni	0.70
Os	0.54
Pb	3.76
Pd	1.41
Pt	0.97
Rb	4.89
Re	0.57
Rh	0.97
Ru	0.71

<b>Material</b>	<b>Sputter Yield</b>
Sb	3.96
Si	0.38
SiC	0.39
SiO <sub>2</sub>	0.49
Sm	1.21
Su	1.41
Ta	0.46
Th	0.90
Ti	0.41
U	0.81
V	0.41
W	0.42
Y	1.023
Zr	0.70